



Electrical characterization of interface properties in nano-scaled MOSFET devices based on low-frequency fluctuations

Masahiro Koyama

► To cite this version:

Masahiro Koyama. Electrical characterization of interface properties in nano-scaled MOSFET devices based on low-frequency fluctuations. Micro and nanotechnologies/Microelectronics. Université Grenoble Alpes, 2015. English. NNT: 2015GREAT036 . tel-01216463

HAL Id: tel-01216463

<https://theses.hal.science/tel-01216463>

Submitted on 16 Oct 2015

HAL is a multi-disciplinary open access archive for the deposit and dissemination of scientific research documents, whether they are published or not. The documents may come from teaching and research institutions in France or abroad, or from public or private research centers.

L'archive ouverte pluridisciplinaire **HAL**, est destinée au dépôt et à la diffusion de documents scientifiques de niveau recherche, publiés ou non, émanant des établissements d'enseignement et de recherche français ou étrangers, des laboratoires publics ou privés.

THÈSE

Pour obtenir le grade de

DOCTEUR DE L'UNIVERSITÉ DE GRENOBLE

Spécialité : **Nano Électronique et Nano Technologies (NENT)**

Arrêté ministériel : 7 août 2006

Présentée par

Masahiro KOYAMA

Thèse dirigée par **Gérard GHIBAUDO**
et codirigée par **Mikaël CASSÉ**

préparée au sein du **Laboratoire CEA-LETI**
dans l'**École Doctorale EEATS**

**Caractérisation électrique des
propriétés d'interface dans les
MOSFET nanométriques par des
mesures de bruit basse
fréquence**

Thèse soutenue publiquement le **26 mars 2015**
devant le jury composé de :

M. Abdelkader SOUIFI

PR, INSA de Lyon, Président

M. Cor CLAEYS

Professeur étranger, Université Catholique de Leuven, Rapporteur

Mme. Nathalie MALBERT

PR, Université de Bordeaux, Rapporteur

M. Hiroshi IWAI

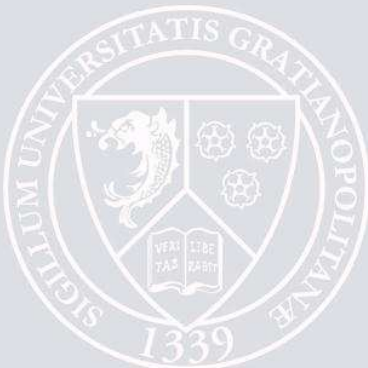
Professeur étranger, Tokyo Institute of Technology, Examinateur

M. Mikaël CASSÉ

ING, CEA-LETI, Co-encadrant de thèse

M. Gérard GHIBAUDO

DR, CNRS Alpes, IMEP-LAHC, INPG-MINATEC, Directeur de thèse



Dissertation for the degree of Doctor of Philosophy

Electrical characterization of interface properties in nano-scaled MOSFET devices based on low-frequency fluctuations

By **Masahiro KOYAMA**

CEA-LETI, MINATEC Campus, 17 rue des Martyrs, 38054 Grenoble, France

January 2015

Supervisor: **Gérard GHIBAUDO**

IMEP-LAHC, Grenoble INP-MINATEC, 3 Parvis Louis Néel, 38016 Grenoble, France

Co-supervisor: **Mikaël CASSÉ**

CEA-LETI, MINATEC Campus, 17 rue des Martyrs, 38054 Grenoble, France

Résumé

Dans cette thèse, les propriétés électriques de transistors à nanofils de silicium liées à l'interface oxyde de grille/canal ont été étudiées par le biais de mesures de bruit basse fréquence (bruit 1/f) et de transport dans le canal. Ces transistors nanofils dont les dimensions ont été réduites jusqu'à quelques nanomètres pour la section, représentent une alternative sérieuse pour les futurs nœuds technologiques CMOS. Cependant, la qualité de l'interface oxyde de grille/canal pose question pour transistors dont l'architecture s'étend dans les 3 dimensions, en raison du fort rapport surface/volume inhérent à ces transistors, des différentes orientations cristallographiques de ces interfaces, ou encore des matériaux contraints utilisés pour améliorer les performances électriques. La compréhension des liens entre les propriétés de transport des porteurs dans le canal, qui garantissent en grande partie les performances électriques des transistors, et la qualité de l'interface avec l'oxyde de grille est fond primordiale pour optimiser les transistors nanofils. Les mesures de bruit, associées à l'étude du transport dans le canal, sont un outil puissant et adapté à ces dispositifs tridimensionnels, sans être limité par la taille ultra-réduite des transistors nanofils.

Les transistors nanofils étudiés ont été fabriqués à partir de substrats minces SOI, et intègrent un empilement de grille HfSiON/TiN, qui permet de réduire les dimensions tout en conservant les mêmes propriétés électrostatiques. Pour gagner en performances, des contraintes mécaniques ont été introduites dans le canal en silicium : en tension pour les NMOS, par le biais de substrat constraint (sSOI), et en compression pour les PMOS. Un canal en compression uni-axiale peut être obtenu par l'intégration de source/drain en SiGe et/ou par l'utilisation de couches contraintes de type CESL. Des transistors à canal SiGe sur isolant en compression ont également été fabriqués et étudiés.

Les caractéristiques électriques des divers transistors nanofils (courbes Id-V_g, compromis Ion-Ioff, mobilité des porteurs) démontrent l'excellent contrôle électrostatique dû à l'architecture 3D, ainsi que l'efficacité de l'ingénierie de contraintes dans les nanofils jusqu'à de faibles longueurs de grilles (~17nm).

Des mesures de bruit basse fréquence ont été réalisées sur ces mêmes dispositifs et analysées en fonction des paramètres géométriques de l'architecture nanofils (largeur W,

forme de la section, longueur de grille L), et des diverses variantes technologiques. Nous avons démontré que le bruit 1/f dans les transistors nanofils peut être décrit par le modèle de fluctuations du nombre de porteurs (CNF) corrélées aux fluctuations de mobilité (CMF). Le bruit associé aux régions S/D a pu également être intégré dans ce modèle en ajoutant une contribution, en particulier pour les PMOS.

Alors que les différentes variantes technologiques ont peu d'effet sur le bruit 1/f, les variations de géométrie en L et W changent la composante de bruit liée aux fluctuations du nombre de porteurs (CNF) de manière inversement proportionnelle à la surface totale ($\sim 1/WL$). Cette augmentation du bruit est le reflet du transport qui se produit à proximité des interfaces avec l'oxyde. Les différentes orientations des interfaces supérieures et latérales (110) ou (100) présentent la même quantité de pièges d'interface (extrait à partir des mesures de bruit 1/f, en séparant les contributions des différentes faces du nanofil) bien qu'ayant une rugosité différente essentiellement liée au process. En revanche la composante CMF n'est pas altérée par la réduction des dimensions contrairement à la mobilité des porteurs qui décroît fortement avec L.

Finalement, les mesures de bruit 1/f ont été comparées aux spécifications ITRS 2013 pour les transistors multi-grilles en vue des futurs nœuds technologiques de la logique CMOS, et démontrent que nos transistors nanofils satisfont les exigences en matière.

Mots-clés

MOSFET, Nanofils, Bruit basse fréquence, Caractérisation

Abstract

In this thesis, electrical properties of gate oxide/channel interface in ultra-scaled nanowire (NW) MOSFETs were experimentally investigated by carrier transport and low-frequency noise (LFN) characterizations. NW FETs, which have aggressively downscaled cross-section of the body, are strong candidates for near future CMOS node. However, the interface quality could be a critical issue due to the large surface/volume ratio, the multiple surface orientations, and additional strain technology to enhance the performance. Understanding of carrier transport and channel interface quality in NW FETs with advanced high-k/metal gate is thus particularly important. LFN provides deep insights into the interface properties of MOSFET without lower limit of required channel size. LFN measurement thus can be a powerful technique for ultra-scaled NW FETs. Also, fitting mobility (such as low-field mobility) extraction by Y-function method is an efficient method.

Omega-gate NW FETs were fabricated from FD-SOI substrates, and with Hf-based high-k/metal gate (HfSiON/TiN), reducing detrimental effects by device downscaling. In addition, strain technologies to the channel were additively processed. Tensile strained-SOI substrate was used for NMOS, whereas compressive stressors were used for PMOS devices. Strained Si channel for PMOS was processed by raised SiGe S/D and CESL formations. Strained SiGe channel (SGOI) was also fabricated for further high-performance PMOS FETs.

Firstly, the most common $Id-Vg$ was characterized in single-channel NW FETs as the basic performance. Reference SOI NWs provided the excellent static control down to short channel of 17nm. Stressors dramatically enhanced on-current owing to a modification of channel energy-band structure. Then, extracted low-field mobility in NWs also showed large improvement of the performance by stressors. The mobility extraction effectively evaluated FET performance even for ultra-scaled NWs.

Next, LFN investigated for various technological and architectural parameters. Carrier number fluctuations with correlated mobility fluctuations (CNF+CMF) model described 1/f noise in all our FETs down to the shortest NWs. Drain current noise behavior was basically similar in both N- and PMOS FETs regardless of technological splits. Larger 1/f noise stemming from S/D regions in PMOS FETs was perfectly

interpreted by the CNF+CMF model completed with Rsd fluctuations. This observation highlighted an advantage of SGOI NW with the lowest level of S/D region noise.

Geometrical variations altered the CNF component with simple impact of device scaling (reciprocal to both Wtot and Lg). No large impact of surface orientation difference between the channel (100) top and (110) side-walls in [110]-oriented NWs was observed. Scaling regularity with both Wtot and Lg, without much quantum effect, could be attributed to the use of HfSiON/TiN gate and carrier transport occurring mostly near top and side-wall surfaces even in NW geometry. Meanwhile, the CMF factor was not altered by decreasing dimensions, while the mobility strongly depends on the impact.

Extracted oxide trap density was roughly steady with scaling, structure, and technological parameter impacts. Simple separation method of the contributions between channel top surface and side-walls was demonstrated in order to evaluate the difference. It revealed that oxide quality on (100) top and (110) side-walls was roughly comparable in all the [110]-devices. The density values lie in similar order as the recent reports. An excellent quality of the interface with HfSiON/TiN gate was thus sustained for all our technological and geometrical splits.

Finally, our NWs fulfilled 1/f LFN requirements stated in the ITRS 2013 for future MG CMOS logic node. Consequently, we concluded that appropriate strain technologies powerfully improve both carrier transport and LFN property for future CMOS circuits consisting of NW FETs, without any large concern about the interface quality.

Keywords

MOSFET, Nanowire, Low-frequency noise, Characterization

Acknowledgments

I would like to thank profoundly my supervisors, Professor Gérard Ghibaudo at IMEP-LAHC and Dr. Mikaël Cassé at CEA LETI, for their passionate tutelage, encouragement, and thoughtful supports not only throughout my study but also for life.

I am also deeply grateful to Dr. Simon Deleonibus, Dr. Gilles Reimbold, Dr. Sylvain Barraud, Dr. Rémi Coquand, and Ms. Estelle Brague at CEA LETI for their fruitful collaboration and great help. All researchers and engineers at CEA LETI and IMEP-LAHC with whom I have worked are also gratefully acknowledged. The life in Grenoble, France, was exciting and beautiful experiences. I really appreciate and will never forget the wonderful days, friendship with a lot of people, and their kindness.

And I would like to thank Professor Hiroshi Iwai, Professor Takeo Hattori, Professor Kenji Natori, Professor Yoshinori Kataoka, Professor Akira Nishiyama, Professor Nobuyuki Sugii, Professor Kazuo Tsutsui, Professor Hitoshi Wakabayashi, and Professor Kuniyuki Kakushima at Tokyo Institute of Technology for their worthwhile advisements. I am also thankful to research colleagues of Iwai-Kakushima laboratory for their friendship, and to secretaries of the laboratory, Ms. Akiko Matsumoto and Ms. Masako Nishizawa, for their kind assistance.

This work was partially carried out in the frame of the STMicroelectronics/IBM/CEA-LETI joint program and by the French Public Authorities through NANO 2017 program.

Acknowledgments

*To my family
for everything to date*

Table of Contents

Résumé & Abstract	2
Acknowledgements	6
List of Tables	12
List of Figures	13
List of Symbols, Acronyms, and Abbreviations	21
Chapter 1. Introduction	27
1.1 General Context	28
1.2.1 MOSFET downscaling -Moore's law-	28
1.2.2 Power consumption of CMOS logic circuits	30
1.2.3 End of scaling era?	33
1.2 Purposes and scopes of this work	37
1.3 References	44
Chapter 2. Nanowire MOSFETs	50
2.1 Introduction to MOSFETs for the next technological nodes	51
2.1.1 Fundamentals of MOSFET	51
2.1.1.1 MOSFET as a switch	
2.1.1.2 Threshold voltage	
2.1.1.3 Subthreshold swing	
2.1.1.4 Short-channel effects	
2.1.2 Key concepts for advanced MOSFET	58
2.1.2.1 FD-SOI devices	
2.1.2.2 Multi-gate devices	
2.1.2.3 High- κ dielectric/metal gate system	
2.1.2.4 Strain technology	
2.2 Our nanowire devices	73
2.2.1 Process step overview	73

Table of Contents

2.2.2 Key device parameters	74
2.2.2.1 Architectural splits	
2.2.2.2 High- κ /metal gate stack	
2.2.2.3 Additional H ₂ anneal	
2.2.2.4 Tensile strained-SOI (sSOI) devices for NMOS	
2.2.2.5 Compressively strained SiGe-on-insulator (SGOI) for PMOS	
2.2.2.6 Additional strain sources: SiGe source/drain and CESL	
2.2.3 Descriptions of all the device parameters	81
2.3 References	84
 Chapter 3. Carrier transport characterizations	95
3.1 Methodology	96
3.1.1 I _d -V _g measurement	96
3.1.2 C _{gc} -V _g measurement	97
3.1.3 Mobility extraction	98
3.1.3.1 Effective mobility	
3.1.3.2 Low-field mobility	
3.2 Experimental results	101
3.2.1 I _d -V _g characteristics	101
3.2.1.1 Threshold voltage	
3.2.1.2 Drain induced barrier lowering	
3.2.1.3 Subthreshold swing	
3.2.1.4 Challenge of I _{ON} enhancement	
3.2.2 Temperature dependent Effective mobility	114
3.2.2.1 Extraction of contributions of side-wall and top surfaces	
3.2.2.2 Tri-gate vs. omega-gate	
3.2.2.3 Impact of tensile strain	
3.2.3 Low-field mobility	125
3.2.3.1 Extracted low-field mobility	
3.2.3.2 Mobility degradation factor	
3.2.3.3 Evaluation of source/drain series resistance	
3.3 References	132

Table of Contents

Chapter 4. Low-frequency noise characterizations	137
4.1 Fundamentals	138
4.1.1 Introduction to main noise sources	138
4.1.1.1 Thermal noise	
4.1.1.2 Shot noise	
4.1.1.3 Generation-recombination (g-r) noise	
4.1.1.4 Random-telegraph-signal (RTS) noise	
4.1.1.5 1/f noise	
4.1.2 Low-frequency noise in MOSFET	145
4.1.2.1 LFN measurements as a diagnostic tool	
4.1.2.2 Hooge empirical model - Mobility fluctuations	
4.1.2.3 McWhorter model - Carrier number fluctuations	
4.1.2.4 CNF+CMF model	
4.1.3 Measurement set-up	153
4.2 Experimental results	155
4.2.1 1/f noise behavior and CNF+CMF model	155
4.2.1.1 Comparison between experimental data and CNF+CMF model	
4.2.1.2 Impact of resistance from source/drain regions	
4.2.1.3 Evaluation of Hooge parameter	
4.2.2 Flat-band voltage noise	166
4.2.2.1 Extraction	
4.2.2.2 Influence of scalability	
4.2.3 Coulomb scattering parameter	169
4.2.3.1 General feature	
4.2.3.2 Comparison with transport parameter: low-field mobility	
4.2.4 Oxide trap density	170
4.2.4.1 General tendency	
4.2.4.2 Assessment of the contribution of different surface orientations	
4.2.4.3 Interface quality comparison with charge pumping measurement	
4.2.5 Drain bias influence	177
4.2.6 Comparison with ITRS requirements for 1/f LFN	178
4.3 References	183

Table of Contents

Chapter 5. Conclusions	192
5.1 Carrier transport characterizations	193
5.2 Low-frequency noise characterizations	195
5.3 Feature of strain technologies in advanced NW MOSFETs	196
5.4 Future perspectives	196
5.5 References	198
 Résumé de la thèse en français	 201
Introduction générale	201
Partie I : Les transistors nanofils et la caractérisation du transport	203
Partie II: Les mesures de bruit basse fréquence	211
Conclusion générale	221
 List of publications and presentations	 223

List of Tables

Chapter 1

Tab.1-1. Scaling MOSFET device and circuit parameters [1-9].

Chapter 2

Tab.2-1. Summary of all our technological and architectural parameters for NMOS devices.

Tab.2-2. Summary of all our technological and architectural parameters for PMOS devices.

Chapter 3

Tab.3-1. Brief summary of strain effect on carrier transport along [110]-oriented channel for various stress configurations.

Tab.3-2. Extracted power law exponent γ in the temperature dependence of maximum mobility $\mu_{\max} \sim T^{-\gamma}$.

Chapter 4

Tab. 4-1. Summary of the extracted $\alpha_{sc}\mu_{eff}$ and S_{Rsd} values in Fig.4-15 with the extracted S/D series resistance RSD for NWs in Fig.3-33.

Tab. 4-2. ITRS requirements data of L_g , V_{dd} , and V_d conditions for high performance (HP) and low standby power (LSTP) logic circuits consisting of MG FETs [4-95].

List of Figures

Chapter 1

- Fig. 1-1. The evolution of MOSFET minimum feature size (gate length) and the density of MOSFETs in microprocessors over time [1-10].
- Fig. 1-2. (a) Circuit schematic of CMOS inverter. Equivalent circuits of (b) pull-up and (c) pull-down conditions.
- Fig. 1-3. Total chip dynamic and static power dissipation trends based on the International Technology Roadmap for Semiconductors [1-14].
- Fig. 1-4. Recent MOSFET architectures and process nodes released by Intel Corporation [1-15].
- Fig. 1-5. Schematic of MOSFET structure based on silicon-on-insulator (SOI) technology [1-18].
- Fig. 1-6. ITRS 2011 “equivalent scaling” process technologies timing compared to overall roadmap technology characteristics (ORTC) and industry “node” naming [1-19].
- Fig. 1-7. ITRS requirements for future high performance (HP) and low standby power (LSTP) logic circuits consisting of MG FETs [1-21].
- Fig. 1-8. Low-frequency noise of Si and c-strained SiGe NWs. Inserted figure is a comparison of oxide trap density (N_t). L_G and W_{NW} are $\sim 290\text{nm}$ and $\sim 20\text{nm}$, respectively [1-39].
- Fig. 1-9. Effective trap density versus gate voltage overdrive for the 30-fin triple-gate devices ($W_{FIN}=60\text{nm}$, $L=1\mu\text{m}$) and planar devices ($W \times L = 1\mu\text{m} \times 1\mu\text{m}$) [1-23].
- Fig. 1-10. Averaged noise spectral densities (symbols) $\langle S_{Id}/I_d^2 \rangle$ and (lines) $\langle (g_m/I_d)^2 \rangle$ versus I_d at $V_d=0.1\text{V}$ and $f=10\text{Hz}$ for 7-, 9-, and 12-nm d_{NW} , respectively. All the left axes represent $\langle S_{Id}/I_d^2 \rangle$, whereas all the right axes (red colored) represent $\langle (g_m/I_d)^2 \rangle$ multiplied by a constant [1-43].
- Fig. 1-11. Relationship between equivalent oxide traps per unit area N_t and scattering parameter α and with different Ge content of SRB layers. [1-54].
- Fig. 1-12. Outline diagram in this work on electrical characteristics of the gate oxide/channel interface in ultra-scaled NW MOSFETs.

Chapter 2

- Fig. 2-1. A schematic view of a classical bulk n-channel MOSFET [2-1].
- Fig. 2-2. A schematic of three regions in the V_g and V_d both dependent MOSFET operation.

List of Figures

- Fig. 2-3. Band diagram of an ideal n-type metal-insulator-semiconductor capacitor under strong inversion [2-2].
- Fig. 2-4. The drain current as a function of the gate voltage in a MOSFET [2-1].
- Fig. 2-5. Illustration of short-channel effects [2-1]. (a) The DIBL and (b) the SS increase impacts are shown in the relationship between the drain current I_d and the gate voltage V_g .
- Fig. 2-6. Process flow schematics of SOI substrate fabrication by Smart CutTM technology [2-8].
- Fig. 2-7. Equivalent circuits of (a) bulk Si and (b) FD-SOI MOSFETs for capacitance.
- Fig. 2-8. Illustration of C_{tot} - V_g characteristic in bulk Si NMOS FET [2-17].
- Fig. 2-9. Types of MG MOSFETs. (a) SOI DG FinFET, (b) SOI tri-gate FET, (c) SOI Π -gate FET, (d) SOI Ω -gate FET, (d) SOI quadruple-GAA FET, and (e) bulk tri-gate FET [2-1].
- Fig. 2-10. Dependence of DIBL and SS on the scaling parameter [2-21].
- Fig. 2-11. Array of Si NW on oxide ($\times 50$ channels) obtained by SEM [2-32].
- Fig. 2-12. Conduction and valence band offsets for various dielectrics [2-43~2-45].
- Fig. 2-13. Band gap energy as a function of relative permittivity for various dielectrics [2-43~2-45].
- Fig. 2-14. Diagram of degenerate conduction and valence bands splitting owing to strain effect.
- Fig. 2-15. Process integration schematic of our MOSFETs.
- Fig. 2-16. Schematic representation of the different strain-engineering approaches [2-86].
- Fig. 2-17. The lattice arrangement of strained Si layer on the virtual $Si_{1-x}Ge_x$ substrate structures with increasing the Ge concentration in steps or linearly [2-61].
- Fig. 2-18. Process schematics of sSOI substrate preparation [2-89].
- Fig. 2-19. Schematic of lateral strain relaxation occurred in sSOI TGNW structure.
- Fig. 2-20. Schematic of SGOI substrate preparation by Ge condensation technique.

List of Figures

Fig. 2-21. Cross-sectional TEM picture of final SiO₂/SiGe/BOX structure after Ge condensation process [2-95].

Fig. 2-22. Cross-sectional TEM image of a perfect interface between Si_{0.8}Ge_{0.2} channel and raised Si_{0.7}Ge_{0.3} S/D with doped B in Ω-gate NW FET [2-95].

Fig. 2-23. Schematic and cross-sectional TEM image of Ω-gate NW MOSFETs.

Chapter 3

Fig. 3-1. I_d-V_g characteristics of the narrowest NW FETs with L_g≈110nm for all the technological parameters in (a) NMOS and (b) PMOS devices.

Fig. 3-2. C_{gc}-V_g characteristics of the widest FET and narrowest multiple 50-channel NW with L_g=10μm in both SOI N- and PMOS devices.

Fig. 3-3. Schematic exhibiting the three dominant scattering mechanisms which limit carrier mobility of MOSFET, and the temperature dependent mobility behavior from 300 K down to 20 K on 10μm-wide NMOS FET.

Fig. 3-4. Illustration of the relationship between μ_{eff} and μ₀ on (a) NMOS and (b) PMOS cases.

Fig. 3-5. I_d-V_g characteristics as a function of L_g in the narrowest NWs for (a,b) SOI and (c,d) sSOI NMOS devices with comparison between (a,c) linear (V_d=40mV) and (b,d) saturation (V_d=0.9V) regions.

Fig. 3-6. I_d-V_g characteristics as a function of L_g in the narrowest NWs for (a,b) SOI and (c,d) nSGOI PMOS devices with comparison between (a,c) linear (V_d=-40mV) and (b,d) saturation (V_d=-0.9V) regions.

Fig. 3-7. Threshold voltage V_t as a function of L_g extracted at linear (|V_d|=40mV) and saturation (|V_d|=0.9V) regions in the widest and the narrowest NW FETs for SOI (a) NMOS and (b) PMOS devices.

Fig. 3-8. Threshold voltage V_t as a function of L_g in the narrowest NMOS NWs at (a) linear (V_d=40mV) and (b) saturation (V_d=0.9V) regions for all the technological parameters.

Fig. 3-9. Threshold voltage V_t as a function of L_g in the narrowest PMOS NWs at (a,c) linear (V_d=-40mV) and (b,d) saturation (V_d=-0.9V) regions for all the technological splits.

Fig. 3-10. Extracted DIBL as a function of L_g in the widest and the narrowest NW FETs for SOI (a) NMOS and (b) PMOS devices.

Fig. 3-11. Extracted DIBL as a function of L_g in the narrowest NMOS NWs for all the technological parameters.

List of Figures

- Fig. 3-12. Extracted DIBL as a function of L_g in the narrowest PMOS NWs for all the technological splits.
- Fig. 3-13. Subthreshold swing SS as a function of L_g in the widest and the narrowest NW FETs for SOI (a) NMOS and (b) PMOS devices.
- Fig. 3-14. Subthreshold swing SS as a function of L_g in the narrowest NMOS NWs at (a) linear ($V_d=40\text{mV}$) and (b) saturation ($V_d=0.9\text{V}$) regions for all the technological parameters.
- Fig. 3-15. Subthreshold swing SS as a function of L_g in the narrowest PMOS NWs at (a,c) linear ($V_d=-40\text{mV}$) and (b,d) saturation ($V_d=-0.9\text{V}$) regions for all the technological splits.
- Fig. 3-16. (a) Extracted I_{ON} and (b) the gain compared with reference SOI as a function of L_g in the narrowest NMOS NWs for all the technological parameters.
- Fig. 3-17. (a) Extracted I_{ON} and (b) the gain compared with reference SOI as a function of L_g in the narrowest PMOS NWs for all the technological splits.
- Fig. 3-18. I_{ON} - I_{OFF} performance in the narrowest NW (a) NMOS and (b) PMOS FETs with comparison of stressor impacts.
- Fig. 3-19. Effective mobility μ_{eff} extracted as a function of N_{inv} in SOI TGNW and wide FETs at varying temperatures (from 300 K down to 20 K) for (a) NMOS and (b) PMOS devices.
- Fig. 3-20. Effective mobility μ_{eff} extracted as a function of N_{inv} in SOI TGNW NMOS FETs with $W_{top}=10\text{nm}$ and $W_{top}=30\text{nm}$ at varying temperatures (from 300 K down to 20 K).
- Fig. 3-21. Extraction of the (100) top and (110) side-wall mobility contributions at 300K in SOI TGNW FETs as a function of N_{inv} for (a) NMOS with $W_{top}=10\text{nm}$ and (b) PMOS with $W_{top}=30\text{nm}$.
- Fig. 3-22. Extraction of the μ_{top} and $\mu_{side-wall}$ contributions at 50K in SOI TGNW FETs with $W_{top}=10\text{nm}$ as a function of N_{inv} for (a) NMOS and (b) PMOS devices.
- Fig. 3-23. Effective mobility μ_{eff} as a function of N_{inv} extracted at varying temperatures for SOI TG and ΩG NW (a) NMOS and (b) PMOS devices.
- Fig. 3-24. Effective mobility μ_{eff} as a function of N_{inv} extracted at varying temperatures in SOI wide FET with or without additional H_2 anneal process for (a) NMOS and (b) PMOS devices.

List of Figures

- Fig. 3-25. Effective mobility μ_{eff} as a function of N_{inv} extracted at varying temperatures, showing (a) comparison between sSOI wide FET and TGNW devices, and (b) comparison between SOI and sSOI TGNW FETs.
- Fig. 3-26. Effective mobility μ_{eff} at high N_{inv} as a function of W_{top} for SOI and sSOI (a,b) NMOS and (c,d) PMOS FETs at room temperature (300K) with comparison between (a,c) TG and (b,d) Ω G devices.
- Fig. 3-27. Effective mobility μ_{eff} extracted at high N_{inv} as a function of temperature in (a,c) SOI and (b,d) sSOI devices for (a,b) NMOS and (c,d) PMOS FETs.
- Fig. 3-28. Maximum mobility μ_{max} extracted as a function of temperature in SOI and sSOI (a) NMOS and (b) PMOS TGNW FETs.
- Fig. 3-29. Low-field mobility μ_0 as a function of L_g with comparison between the widest FETs and narrowest NWs in reference SOI (a) NMOS and (b) PMOS devices.
- Fig. 3-30. Low-field mobility μ_0 as a function of L_g with comparison among NMOS technological splits in (a) the widest FET and (b) the narrowest NW devices. (c,d) Summary of μ_0 gain compared with reference SOI case.
- Fig. 3-31. Low-field mobility μ_0 as a function of L_g with comparison among PMOS technological splits in (a,b) the widest FET and (c,d) the narrowest NW devices. (e,f) Summary of μ_0 gain compared with reference SOI case.
- Fig. 3-32. Mobility degradation factor α_μ in the widest FETs and narrowest NWs for all the technological parameters.
- Fig. 3-33. Source/drain resistivity ρ_{SD} in the widest FETs and narrowest NWs for all the technological splits.

Chapter 4

- Fig. 4-1. An illustration of typical noise waveform [4-1].
- Fig. 4-2. A Lorentzian shaped PSD, plotted for the RTS noise waveform in Fig.4-3 [4-1].
- Fig. 4-3. Schematic description of RTS noise, exemplified for a MOSFET [4-1].
- Fig. 4-4. Superposition of 4 Lorentzians giving a total spectrum that approximately exhibits a 1/f dependence over several decades of frequency [4-1].
- Fig. 4-5. The PSD for low-frequency noise and white noise plotted vs. frequency [4-1].

List of Figures

- Fig. 4-6. Schematic illustration of electrons in the channel of a MOSFET moving in and out of traps, giving rise to fluctuations in the inversion charge density and thereby the drain current [4-1].
- Fig. 4-7. Simulation of the mobility fluctuation noise and carrier number fluctuation noise from subthreshold to the strong inversion regime [4-1].
- Fig. 4-8. Energy band diagram showing the tunneling transitions of electrons between the conduction band and traps in the gate oxide, (i) corresponds to direct tunneling and (ii) to indirect tunneling via interface traps [4-1].
- Fig. 4-9. A schematic of the LFN measurement system 3PNMS with PBA2 and DUT.
- Fig. 4-10. S_{Id}/I_d^2 as a function of frequency in the (a) SOI and (b) sSOI narrowest Ω -gate NW NMOS FETs with $L_g \sim 110\text{nm}$, showing good $1/f$ behavior at threshold voltage ($V_g = V_t$) up to strong inversion region.
- Fig. 4-11. S_{Id}/I_d^2 as a function of frequency in the SOI and nSGOI narrowest Ω -gate NW PMOS FETs with $L_g = 107\text{-}108\text{nm}$, showing good $1/f$ behavior at threshold voltage ($V_g = V_t$).
- Fig. 4-12. (a) S_{Id}/I_d^2 as a function of frequency in the narrowest SOI Ω -gate NW NMOS FETs with $L_g = 113\text{nm}$, showing large $1/f^2$ noise components at threshold voltage ($V_g = V_t$). I_d fluctuation as a function of time for sampling frequency of (b) $f = 1\text{kHz}$, (c) $f = 40\text{kHz}$, and (d) $f = 1\text{MHz}$.
- Fig. 4-13. (a) S_{Id}/I_d^2 as a function of frequency in the narrowest SOI Ω -gate NW NMOS FETs with $L_g = 28\text{nm}$, showing large $1/f^2$ noise components at threshold voltage ($V_g = V_t$). I_d fluctuation as a function of time for sampling frequency of (b) $f = 1\text{kHz}$, (c) $f = 40\text{kHz}$, and (d) $f = 1\text{MHz}$.
- Fig. 4-14. S_{Id}/I_d^2 as a function of frequency in the narrowest SOI Ω -gate NW NMOS FETs with (a) $L_g = 113\text{nm}$ and (b) short channel $L_g = 23\text{-}28\text{nm}$, showing $1/f$ behavior in low-frequency region at threshold voltage ($V_g = V_t$).
- Fig. 4-15. I_d dependent (symbols) S_{Id}/I_d^2 and (lines) corresponding $(g_m/I_d)^2$ curve characteristics normalized by channel size parameters (W_{tot} and L_g) in reference SOI wide FETs and the narrowest NWs compared with (a) [100]-oriented SOI, (b) SOI with additional H_2 anneal, and (c) sSOI for NMOS devices.
- Fig. 4-16. I_d dependent (symbols) S_{Id}/I_d^2 and (lines) corresponding $(g_m/I_d)^2$ curve characteristics normalized by channel size parameters (W_{tot} and L_g) in wide FETs and the narrowest NWs for (a) SOI, (b) nSG-S/D, and (c) nSGOI for PMOS devices.

List of Figures

- Fig. 4-17. Comparison of 3-types of PMOS device variants; SOI, nSG-S/D, and nSGOI, in I_d dependent (symbols) S_{Id}/I_d^2 and (lines) corresponding $(g_m/I_d)^2$ curve characteristics normalized by W_{tot} and L_g for (a) wide FETs and (b) the narrowest NWs.
- Fig. 4-18. Schematic of defects in spacers 1 and 2 and/or in Si film contributing to R_{SD} fluctuations in SOI MOSFET architecture.
- Fig. 4-19. I_d dependent (symbols) S_{Id}/I_d^2 and (lines) corresponding $(g_m/I_d)^2$ curves with consideration of the $\alpha_{sc}\mu_{eff}$ and S_{Rsd} term shown in Eq. (4-28), showing (a) the narrowest NW vs. wide FETs in SOI devices, and SiGe S/D vs. SGOI devices in (b) NWs, and in (c) wide FETs.
- Fig. 4-20. Hooge parameter α_H as a function of gate voltage overdrive V_{gt} for various technological splits in the narrowest (a) NMOS and (b) PMOS NW FETs.
- Fig. 4-21. (Symbols) $S_{Vg}^{1/2}$ versus I_d/g_m characteristics and (lines) the linear regression for extraction of S_{Vfb} and $\alpha_{sc}\mu_{eff}$ in (a) wide and (b) 1ch-TGNW both N- and PMOS FETs.
- Fig. 4-22. S_{Vfb} as a function of (a) W_{tot} and (b) L_g for all the technological splits in NMOS devices.
- Fig. 4-23. S_{Vfb} as a function of (a) W_{tot} and (b) L_g for all the technological parameters in PMOS devices.
- Fig. 4-24. Coulomb scattering parameter $\alpha_{sc}\mu_{eff}$ as a function of the channel area $W_{tot}L_g$ in all the devices with single-channel for (a) NMOS and (b) PMOS FETs.
- Fig. 4-25. Coulomb scattering parameter $\alpha_{sc}\mu_{eff}$ as a function of low-field mobility μ_0 extracted in [Figs.3-30b and 3-31d](#) for the narrowest NW (a) NMOS and (b) PMOS FETs.
- Fig. 4-26. N_t as a function of (a) W_{tot} and (b) L_g for all the technological splits in NMOS devices.
- Fig. 4-27. N_t as a function of (a) W_{top} and (b) L_g for all the technological parameters in PMOS devices.
- Fig. 4-28. N_t averaged for L_g in wide and NW FETs for (a) NMOS and (b) PMOS devices, with comparison between SOI and sSOI for NMOS, and among SOI, cSG-S/D, and nSGOI for PMOS.
- Fig. 4-29. (a) Demonstration of the extraction and (b) the extracted N_t contribution of top surface and side-walls by the N_t separation method for all the NMOS devices

List of Figures

Fig. 4-30. (a) Demonstration of the extraction and (b) the extracted N_t contribution of top surface and side-walls by the N_t separation method for all the PMOS devices.

Fig. 4-31. Schematics of the experimental set-up used for charge pumping spectroscopy [4-94].

Fig. 4-32. Mean D_{it} obtained by CP measurement as a function of W_{top} in wide gated P-i-N diode and 75-multiple channel NW devices.

Fig. 4-33. V_d impact for $S_{Id}/I_d^2 - I_d$ characteristics of the narrowest NW NMOS FETs in (a) SOI ($L_g=113\text{nm}$) and (b) sSOI ($L_g=107\text{nm}$).

Fig. 4-34. V_d impact for $S_{Id}/I_d^2 - I_d$ characteristics of the narrowest NW PMOS FETs with short channel in (a) SOI ($L_g=17\text{nm}$) and (b) nSGOI ($L_g=23\text{nm}$).

Fig. 4-35. (Symbols) S_{Vg} with normalization by channel size parameters (W_{tot} and L_g) and frequency as a function of V_d in the (a) SOI and (b) sSOI narrowest NW NMOS FETs.

Fig. 4-36. Comparison of the normalized S_{Vg} between our experimental data and ITRS requirements in 2015 and 2026 in NMOS MG FETs [4-95].

Fig. 4-37. (Symbols) S_{Vg} with normalization by channel size parameters (W_{tot} and L_g) and frequency as a function of V_d in the narrowest NW PMOS FETs for (a) SOI, (b) cSG-S/D, and (c) nSGOI devices.

Fig. 4-38. Comparison of the normalized S_{Vg} between our experimental data and ITRS requirements in 2015 and 2026 for PMOS MG FETs [4-95].

List of Symbols, Acronyms, and Abbreviations

Symbol	Unit	Meaning
C_{acc}	F (F/cm^2)	Accumulation layer capacitance (per channel area)
C_{BOX}	F (F/cm^2)	Buried-oxide capacitance
C_{dep}	F (F/cm^2)	Depletion layer capacitance
C_{gb}	F (F/cm^2)	Gate-to-body capacitance
C_{gc}	F (F/cm^2)	Gate-to-channel capacitance
C_{in}	F	Input capacitance
C_{inv}	F (F/cm^2)	Inversion layer capacitance
C_{it}	F (F/cm^2)	Capacitance of interfacial traps
C_{it_BOX}	F (F/cm^2)	Capacitance of traps at Si/BOX interface
C_{load}	F	Total load capacitance
C_{out}	F	Output capacitance
C_{ox}	F (F/cm^2)	Gate oxide capacitance
C_{tot}	F (F/cm^2)	Total capacitance
C_{wire}	F	Wiring capacitance
D_{it}	$\text{eV}^{-1}\text{cm}^{-2}$	Density of interface traps
E_C	eV	Conduction band edge energy
E_{eff}	V/cm	Effective electric field
E_F	eV	Fermi level
E_i	eV	Intrinsic Fermi level
E_V	eV	Valence band edge energy
f	Hz	Frequency (operating frequency = clock frequency)
f_{max}	Hz	Maximum operating frequency
f_p	Hz	Frequency of pulse signal in CP technique
g_m	S	Transconductance
h	Js	Planck's constant ($=6.626 \times 10^{-34}$)
H_{NW}	cm	Channel height of nanowire
I	A	Current
I_{CP}	A	Maximum charge pumping current
I_d	$\text{A} (\mu\text{A}/\mu\text{m})$	Drain current (normalized by channel width)
I_{d_lin}	A	Drain current in linear region
I_{d_sat}	A	Drain current in saturation region
I_{d_sub}	A	Drain current in subthreshold region
I_{leak}	A	Off-state leakage current
I_{ON}	$\text{A} (\mu\text{A}/\mu\text{m})$	On-state drain current
I_{ox}	A	Leakage current due to gate oxide tunneling
I_{sat}	$\text{A} (\mu\text{A}/\mu\text{m})$	Saturated on-current in short channel devices
I_{sc}	A	Direct short-circuit current
I_{sub}	A	Subthreshold leakage current
$I(t)$	A	Time dependent fluctuating current
$i(t)$	A	Randomly fluctuating component of current
k	J/K	Boltzmann's constant ($=1.38 \times 10^{-23}$)
K		Proportional constant
L	cm	Channel length
L_g	cm	Gate length
m		Body-effect coefficient
m^*	g	Carrier effective mass

List of Symbols, Acronyms, and Abbreviations

Symbol	Unit	Meaning
n	cm^{-2}	Electron density
n		Effective number of gate
N		Number of conducting carriers
N_A	cm^{-2}	Acceptor (hole) doping density
N_{ch}		Number of parallel channel finger
n_i		Intrinsic carrier density in the substrate
N_{inv}	cm^{-2}	Inversion carrier density
N_t	$\text{eV}^{-1}\text{cm}^{-3}$	Oxide trap density
$N_{t_side-walls}$	$\text{eV}^{-1}\text{cm}^{-3}$	Oxide trap density in the channel side-walls
N_{t_top}	$\text{eV}^{-1}\text{cm}^{-3}$	Oxide trap density in the channel top
p	cm^{-2}	Hole density in the substrate
P_{all}	W	Overall power consumption
P_{sc}	W	Direct short-circuit power consumption
P_{st}	W	Static power consumption
P_{sw}	W	Dynamic switching power consumption
q	C	Elementary charge ($=1.602 \times 10^{-19}$)
Q_{dep}	C/cm^2	Depletion charge density
Q_{inv}	C/cm^2	Inversion charge density
Q_{ox}	C/cm^2	Oxide charge density
R	Ω	Resistance
$R(s)$		Autocorrelation function
R_{SD}	Ω	Source/drain series resistance
S(f)		Power spectral density
S_I	A^2/Hz	Power spectral density of current noise
$S_{I\text{d}}$	A^2/Hz	Power spectral density of the drain current noise
S_R	Ω^2/Hz	Power spectral density of the resistance fluctuations
$S_{R\text{sd}}$	Ω^2/Hz	Power spectral density of the R_{SD} fluctuations
S_V	V^2/Hz	Power spectral density of voltage noise
$S_{V\text{fb}}$	V^2/Hz	Power spectral density of the flat-band voltage noise
S_{Vg}	V^2/Hz	Power spectral density of the gate voltage noise
t	s	Time
T	K	Absolute temperature
$T_{\text{high-k}}$	cm	High- κ gate dielectric thickness
T_{ox}	cm	Gate oxide (insulator) thickness
t_{sc}	s	Duration of direct short-circuit
T_{Si}	cm	Si film thickness
T_{SiO_2}	cm	Gate silicon dioxide thickness
t_{sw}	s	Duration of switching
V	V	Voltage
V_{base}	V	Base level of gate voltage pulse in CP technique
V_{ch}	V	Potential along the channel
V_d	V	Drain (-to-source) voltage
V_{dd}	V	Power supply voltage
V_{d_lin}	V	Drain voltage in linear region
V_{d_sat}	V	Drain voltage in saturation region
V_{fb}	V	Flat-band voltage

List of Symbols, Acronyms, and Abbreviations

Symbol	Unit	Meaning
V_g	V	Gate voltage
V_{gt}	V	Gate voltage overdrive ($= V_g - V_t $)
V_{in}	V	Input voltage
v_{inj}	cm/s	Injection velocity of carriers
v_{lim}	cm/s	Limiting velocity of carriers
V_{out}	V	Output voltage
v_{sat}	cm/s	Saturation velocity of carriers
V_t	V	Threshold voltage
V_{t_lin}	V	Threshold voltage in linear region
V_{t_sat}	V	Threshold voltage in saturation region
W	cm	Channel width
W_{dep}	cm	Depletion layer width
W_{Si}	cm	Si body width
W_{top}	cm	Top-view channel width
W_{tot}	cm	Total effective channel width
$x(t)$		Variable in time domain
$X(f)$		Fourier-transformed variable in frequency domain
z	cm	Oxide trap location from the channel interface
ΔE	J, eV	Energy splitting
ΔE_{g_Si}	eV	Band gap energy of Si (=1.12)
Δf	Hz	Loss of operating frequency by DIBL effect
ΔI	A	Difference between two current levels in RTS
ΔI_d	A	Fluctuating (AC) component of drain current
ΔN^2		Variance of the fluctuating number of carriers
ΔV_g	V	Constant amplitude of trapezoidal gate voltage pulse in CP technique
α		Generalized scaling factor of electric field
α_H		Hooge parameter
α_{sc}	Vs/C	Coulomb scattering coefficient
α_{sw}		Switching activity rate
α_μ	nmVs/cm ²	Mobility degradation factor
β		Proportionality constant
β_0	$\mu\text{A}/\text{V}^2$	Transistor (transconductance) gain
γ		Frequency or temperature exponent
δQ_{ox}		Fluctuation of oxide charge
δV_{fb}		Fluctuation of flat-band voltage
$\delta \mu_{eff}$		Fluctuation of carrier effective mobility
ϵ_0	F/cm	Permittivity in vacuum ($=8.854 \times 10^{-10}$)
ϵ_{ox}		Relative permittivity of gate oxide
ϵ_{Si}		Relative permittivity of silicon (=12)
ϵ_{SiO2}		Relative permittivity of silicon dioxide (=3.9)
ϵ_{high-k}		Relative permittivity of high-k dielectric
ζ		Current exponent in 1/f noise definition

List of Symbols, Acronyms, and Abbreviations

Symbol	Unit	Meaning
η		Empirical parameter for E_{eff} definition
κ		Scaling factor of MOSFET or chip size
λ	cm	Attenuation length of carrier wave function in oxide
λ_n	cm	Natural length (parameter with respect to SCE)
μ_0	cm^2/Vs	Low-filed mobility
μ_c	cm^2/Vs	Mobility limited by Coulomb scattering
μ_{const}	cm^2/Vs	Assumed constant mobility along the channel
μ_{eff}	cm^2/Vs	Effective mobility
μ_{max}	cm^2/Vs	Peak mobility
μ_n	cm^2/Vs	Electron mobility
μ_p	cm^2/Vs	Mobility limited by phonon scattering
μ_{sat}	cm^2/Vs	Effective mobility in saturation region
$\mu_{side-wall}$	cm^2/Vs	Effective mobility in the channel side-walls
μ_{SR}	cm^2/Vs	Mobility limited by surface roughness scattering
μ_{TG}	cm^2/Vs	Effective mobility in tri-gate nanowire devices
μ_{top}	cm^2/Vs	Effective mobility in the channel top
μ_Y	cm^2/Vs	Mobility approximated by Y-function method
π_L	Pa^{-1}	Longitudinal piezoresistive coefficient
$\theta_1, \theta_{1,0}$	V^{-1}	First order mobility attenuation factor
θ_2	V^{-1}	Second order mobility attenuation factor
ρ	C/cm^2	Local charge density
ρ_{SD}	$\Omega\mu\text{m}$	Source-drain series resistivity
σ	S/cm	Conductivity
σ_{stress}	Pa	Applied stress in the longitudinal direction
τ	s	Time constant of carrier transitions
τ_0	s	Time constant based on SRH process (often $=10^{-10}$)
τ_h	s	Duration for higher current state in RTS
τ_l	s	Duration for lower current state in RTS
τ_{phonon}	s	Relaxation time due to intervalley phonon scattering
τ_{trap}	s	Relaxation time due to intervalley phonon scattering
ϕ_{ms}	eV	Work function difference between gate and channel materials
Φ_B	eV	Tunneling energy barrier height
Ψ_B	V	Difference between E_F and E_i potentials ($= E_F-E_i /q$)
Ψ_{Bp}	V	Ψ_B in p-type substrate (NMOS)
Ψ_S	V	Surface potential (band bending of substrate)
3PNMS		Programmable Point Probe Noise Measuring System
AC		Alternate current
ALD		Atomic layer deposition
BEOL		Back-end of line
BOX	cm	Buried oxide
CESL		Contact etch stop layer
CMF		Correlated mobility fluctuations
CMOS		Complementary metal-oxide-semiconductor

List of Symbols, Acronyms, and Abbreviations

Symbol	Unit	Meaning
CNF		Carrier number fluctuations
C-V		Capacitance-voltage
CVD		Chemical vapor deposition
DC		Direct current
DG		Double gate
DIBL	mV/V	Drain induced barrier lowering
DUT		Device-under-test
DUV		Deep ultraviolet
e-beam		Electron beam
CMP		Chemical mechanical polishing
CP		Charge pumping
EOT	cm	Equivalent oxide thickness
FD		Fully depleted
FET		Field-effect transistor
GAA		Gate-all-around
g-r		Generation-recombination
high- κ		High dielectric constant (permittivity)
HDD		Highly doped drain
HH		Heavy holes
HP		High performance
IC		Integrated circuit
IL		Interfacial layer
ITRS		International Technology Roadmap for Semiconductors
LCR		Inductance (L) - capacitance (C) - resistance (R)
LDD		Lightly doped drain
LFN		Low frequency noise
LH		Light holes
LNA		Low noise amplifier
LSTP		Low standby power
MF		Mobility fluctuations
MG		Multi-gate
MOSFET		Metal-oxide-semiconductor field-effect transistor
NMOS		N-channel MOS
NW		Nanowire
PBA		Programmable biasing amplifier
PD		Partially depleted
PDP	J	Power-delay product
PMOS		P-channel MOS
poly-		Polycrystalline
PR		Piezoresistance
PSD		Power spectral density
QM		Quantum-mechanical
RF		Radio frequency
RTS		Random-telegraph-signal
SCE		Short-channel effects
S/D		Source and drain

List of Symbols, Acronyms, and Abbreviations

Symbol	Unit	Meaning
SEM		Scanning electron microscopy
SGOI		SiGe-on-insulator
SOI		Silicon-on-insulator
SRB		Strained-relaxed buffer
SS	mV/dec	Subthreshold swing
sSi		Strained-Si
sSOI		Strained-Si-on-insulator
TEM		Transmission electron microscopy
Tri-gate (TG)		Triple-gate
Ω -gate (Ω G)		Omega-gate
Π -gate		Pi-gate

Chapter 1

Introduction

1.1 General Context

- 1.2.1 MOSFET downscaling -Moore's law-**
- 1.2.2 Power consumption of CMOS logic circuits**
- 1.2.3 End of scaling era?**

1.2 Purposes and scopes of this work

1.3 References

Chapter 1. Introduction

1.1 General Context

1.2.1 MOSFET downscaling -Moore's law-

Metal-oxide-semiconductor field-effect transistor (MOSFET) is the core technology of today's microelectronics. MOSFETs are mainly used as switches in logic microcircuits, and the devices can also fulfill other purposes. A modern microprocessor can contain more than 7 billion MOSFETs. Moreover, 128-gigabyte memory card contains 1024 billion (over 1 trillion) MOSFETs, while the card only weighs approximately 0.4g. 1 trillion is comparable to the number of fixed stars in the Andromeda Galaxy, which is the largest galaxy in the local group of galaxies included the Milky Way Galaxy, the solar system, and the earth where we live.

The concept of MOSFET was first invented around 1925-30 by Julius Lilienfeld [1-1,1-2]. After the development of point-contact transistor in 1947 by William Shockley, John Bardeen, and Walter Brattain [1-3], Martin Atalla and Dawon Kahng developed first MOSFET in 1959 [1-4]. The MOSFET technology was combined with the invention of integrated circuit (IC) in 1958 by Jack Kilby (and also by Robert Noyce) [1-5,1-6], and the growth has been accelerated and continued over 50 years up to the present days. The huge growth of semiconductor industry mainly based on silicon devices has lead to the miniaturization, the price drop, and the performance enhancement for lots of appliances and multimedia applications, such as computers and mobile phones.

In 1965, Gordon Moore published a paper [1-7], in which he predicted that density of MOSFETs on a chip would increase twice every 18 months. Although this "Moore's law" is empirically based on data within only 6 years between 1959 when the first Si IC was fabricated and 1965, the law has held amazingly up to the present, over 45 years (Fig.1-1). This clearly means that size reduction of MOSFETs allows increase of the density in an IC chip. The circuit capability thus increases for a constant chip size. However, there are other motivations for downscaling of MOSFET size. Double increase of MOSFETs density in a chip provides reduction of the chip dimensions, which are the length and width, divided by $2^{1/2}$. This scaling rate is usually represented

Chapter 1. Introduction

as a factor of κ . In 1974, Dennard *et al.* published a paper [1-8], and he expressed the scaling benefits. Based on the ideal supposition for maintaining a constant electric field inside the MOSFET, device scaling by the factor κ (*i.e.* twice the integration density) increases the switching speed by κ and reduces the power dissipation by κ^2 . Table 1-1 shows the scaling MOSFET and circuit parameters under the constant field scaling and the generalized scaling rules [1-9]. The generalized scaling rule assumes that the electric field intensity changes by a factor of α . Dennard's law was suitable for the chip scaling until around 2005. After, the conventional scaling ended, and the performance enhancement originating from the device scaling, such as microprocessor clock frequency, has been saturated. This performance saturation has been caused by short-channel effects (SCE), which appeared in MOSFETs with aggressively shortened distance between the source and drain regions. Unfortunately, it is anticipated that SCE becomes more salient as the length is downscaled.

Table 1-1. Scaling MOSFET device and circuit parameters [1-9].

	MOSFET device and circuit parameters	Multiplicative factor ($\kappa > 1$)		
		Constant-field scaling	Generalized scaling	
			Long Ch.	Short Ch.
Scaling assumptions	Device dimensions (t_{ox} , W, L)	1/ κ	1/ κ	
	Doping concentration (N_A , N_D)	κ	$\alpha\kappa$	
	Voltage (V)	1/ κ	α/κ	
Derived scaling behavior of device parameters	Electric field (E)	1	α	
	Carrier velocity (v)	1	α	1
	Depletion-layer width (W_{dep})	1/ κ	1/ κ	
	Capacitance ($C = \epsilon A/t$)	1/ κ	1/ κ	
	Inversion-layer charge density (Q_{inv})	1	α	
	Drift current (I)	1/ κ	α^2/κ	α/κ
	Channel resistance (R_{ch})	1	$1/\alpha$	1
Derived scaling behavior of circuit parameters	Circuit delay time ($\tau \sim CV/I$)	1/ κ	1/ $\alpha\kappa$	1/ κ
	Power dissipation per circuit ($P \sim VI$)	1/ κ^2	α^3/κ^2	α^2/κ^2
	Power-delay product per circuit ($P\tau$)	1/ κ^3	α^2/κ^3	
	Circuit density ($\sim 1/A$)	κ^2	κ^2	
	Power density (P/A)	1	α^3	α^2

Chapter 1. Introduction

As shown in Fig.1-1 [1-10], minimum feature size of MOSFETs, which corresponds to the gate length, has been downscaled from 10 μ m down to 28nm (yellow circles; right y axis) between 1970 and 2011. In parallel, the number of MOSFETs per square millimeter (mm^{-2}) increased from 200 to over 1 million (other objects show data for the four main microprocessor manufacturers; left y axis). The gate length in the current MOSFET generation lies between 22nm and 17nm. In practice, the distance between the source and the drain is approximately 50% shorter than the gate length, resulting in an effective channel length of only ~10nm. It is predicted that the effective channel length will approach about 5nm in 2020, which is only ten-fold size of the lattice parameter of a silicon crystal.

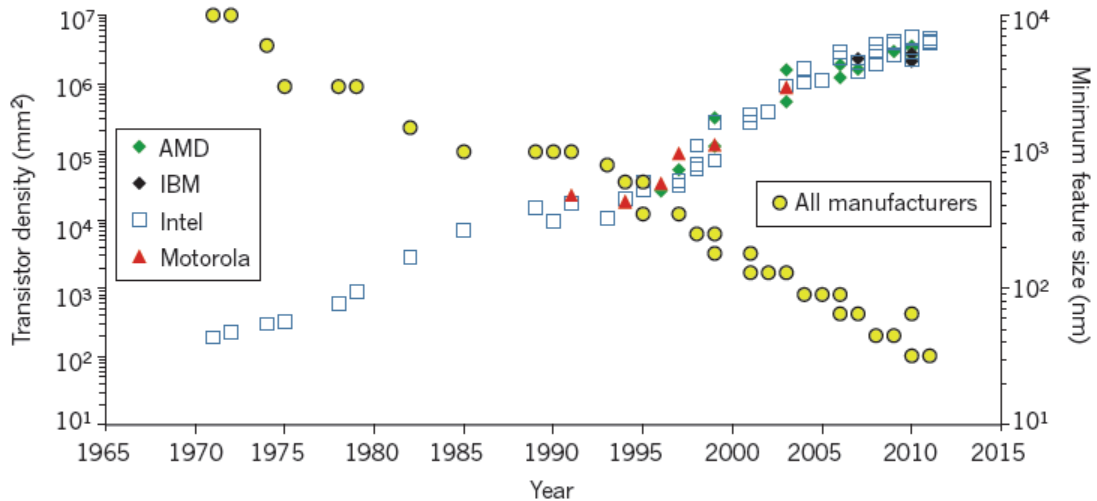


Fig. 1-1. The evolution of MOSFET minimum feature size (gate length) and the density of MOSFETs in microprocessors over time [1-10].

1.2.2 Power consumption of CMOS logic circuits

The most basic component of digital logic microcircuits is a complementary-MOS (CMOS) inverter as a switch. The CMOS configuration was first invented in 1963 by Frank Wanlass [1-11,1-12]. It consists of a symmetrical pairs of two types of MOSFETs, which are an n-channel MOSFET (NMOS FET) and a p-channel MOSFET (PMOS FET), as shown in Fig.1-2a. The source terminal of the NMOS FET is grounded, while the supply voltage V_{dd} is applied to the PMOS FET source. The gates of both MOSFETs are connected and common signal is input to the gates. The drains are also connected as

Chapter 1. Introduction

the output node. The C_{load} is the total load capacitance including the output capacitance C_{out} , the input capacitance C_{in} , and the wiring capacitance C_{wire} .

The current through the PMOS FET (I_P) flows from the source into the drain and charges up the output voltage to V_{dd} (pull-up), meanwhile the current through the NMOS FET (I_N) flows from the drain into the grounded source and discharges the output voltage to zero (pull-down), as shown in Fig.1-2b and c. In CMOS system, the complementary essence allows only one of the MOSFETs to be switched-on (*i.e.* one FET of the pair is always switched-off). In principle, the power dissipation thus occurs only during momentary switching when the charging or discharging current flows through the inverter. Therefore, CMOS system dissipates significantly less static power and has higher noise immunity than other logic circuits with resistive loads, such as transistor-transistor logic (TTL) and NMOS logic. Moreover, CMOS process allows a high-density integration of logic functions on an IC. Since these advantages have been efficiently improved, the huge majority of modern IC manufacturing is based on CMOS processes.

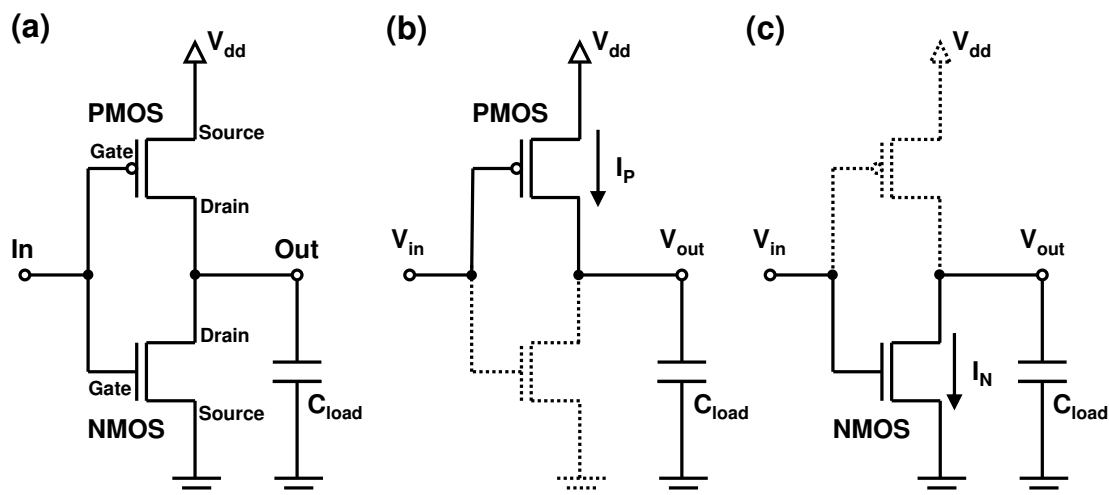


Fig. 1-2. (a) Circuit schematic of CMOS inverter. Equivalent circuits of (b) pull-up and (c) pull-down conditions.

Overall power consumption P_{all} in a CMOS logic IC is defined by the sum of dynamic switching power P_{sw} , direct short-circuit power P_{sc} , and static power P_{st} as [1-13,1-14]:

Chapter 1. Introduction

$$P_{all} = P_{sw} + P_{sc} + P_{st} \quad (1-1)$$

$$\text{with } P_{sw} = \alpha_{sw} C_{load} V_{dd}^2 f \quad (1-2)$$

$$P_{sc} = \alpha_{sw} t_{sc} I_{sc} V_{dd} f \quad (1-3)$$

$$P_{st} = (1 - \alpha_{sw}) \cdot I_{leak} V_{dd} = (1 - \alpha_{sw}) \cdot (I_{sub} + I_{ox}) \cdot V_{dd} \quad (1-4)$$

where α_{sw} is the switching activity rate, f is the operating frequency (clock frequency), t_{sc} is the required short-circuit time, I_{sc} is the short-circuit current flowing directly from the V_{dd} line to the ground line, and I_{leak} is the off-state leakage current. The I_{leak} is divided into two components: the subthreshold leakage current I_{sub} and the tunneling current in the gate oxide I_{ox} . Generally, the power consumption P_{all} is dominated by the dynamic component P_{sw} and is reduced by the scaling factor κ^2 . Furthermore, the average energy consumed per switching operation can be reduced by κ^3 . The average switching energy, also known as the power-delay product (PDP), is a figure of merit about energy efficiency in logic circuits. It is the product of dynamic power consumption and duration of the switching t_{sw} ($=1/f$), thus the PDP is expressed as:

$$PDP = P_{sw} t_{sw} = \frac{P_{sw}}{\alpha_{sw} f} = C_{load} V_{dd}^2 \quad (1-5)$$

As mentioned above, the P_{st} leakage is negligible in theory since CMOS circuits dissipate power only during switching, and it is the primary advantage of CMOS system. In practice, however, the continuing MOSFET scaling and the resulting circuit density growth has recently caused an unacceptable level of the P_{st} . Figure 1-3 shows the power consumption trends in CMOS logic IC chips [1-14]. As the size of MOSFETs is decreased with each advanced process technology, the clock frequency of CMOS circuits is increased. As a result, the dynamic switching power P_{sw} has been increased year by year. On the other hand, the static power consumption P_{st} , which is the sum of the subthreshold leakage and the gate oxide leakage components, is exponentially increased by shortening the gate length of MOSFET. Particularly, the P_{st} exceeds the P_{sw} after 2005 in the prediction. Therefore, reduction of the P_{st} has been a major challenge for recent CMOS technology node.

Increase of the I_{sub} is mainly due to short-channel effects (SCE). Meanwhile I_{ox} is increased owing to the aggressively scaled gate oxide thickness for enhancement of the

Chapter 1. Introduction

electrostatic gate control. This gate oxide leakage can be reduced by replacing the conventional gate insulator, silicon dioxide (SiO_2), with materials with higher dielectric constant (high- κ). For the issue of I_{sub} increase, change of the gate architecture has been proposed in order to effectively enhance the electrostatic gate control.

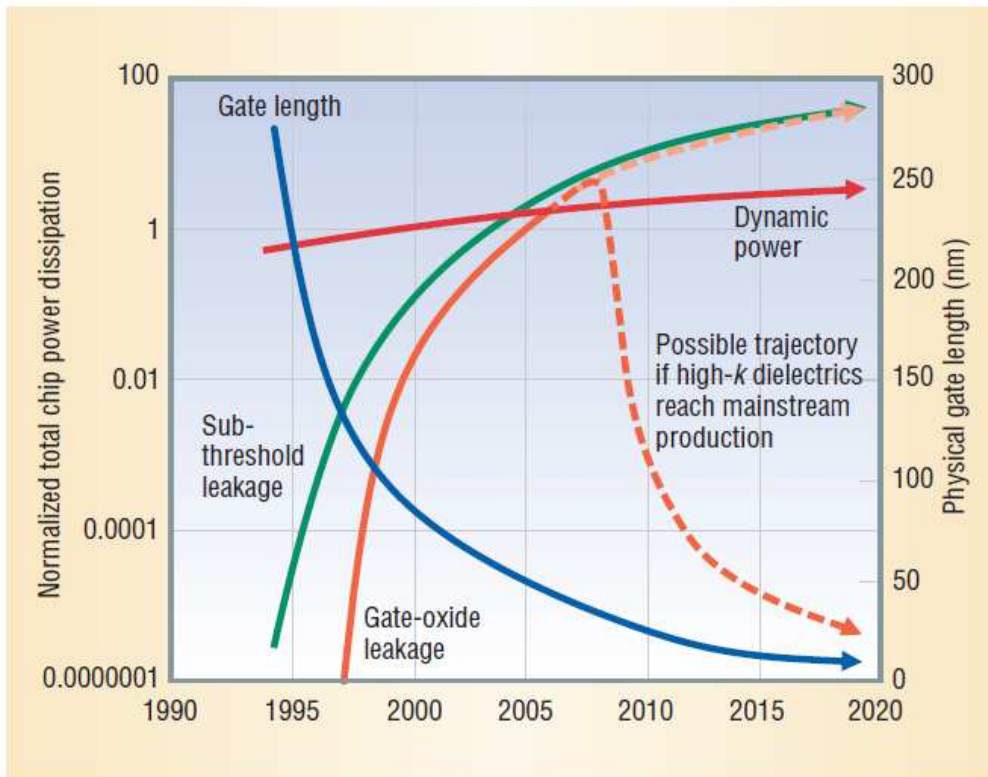


Fig. 1-3. Total chip dynamic and static power dissipation trends based on the International Technology Roadmap for Semiconductors. [1-14].

1.2.3 End of scaling era?

Unfortunately, MOSFETs are thus not perfect switches. The off-current is not zero, the on-current is limited by semiconductor resistance, and the switching takes longer time. Moreover, the switching does not occur suddenly at exact gate voltage bias but needs some voltage range and the gradual change. Furthermore, the switching behavior and the leakage power consumption are degraded by SCE as the size of MOSFET is downscaled, and it has been a serious issue for recent and future technology nodes.

For continuous MOSFET downscaling *i.e.* the performance enhancement, huge efforts have been actually made to solve various issues mainly stemming from SCE. For

Chapter 1. Introduction

instance, recent MOSFET structures released by Intel are shown in Fig.1-4 [1-15]. Some solutions to overcome the deterioration of the switching properties have been considered by using novel technologies, such as silicon-on-insulator (SOI) substrate [1-16,1-17] (Fig.1-5 [1-18]) and 3D multi-gate (MG) structures [1-10] (such as Tri-Gate device in Fig.1-4). For further performance improvement, solutions to the resolution limit of optical lithography, alternative oxide/metal gate, and high-performance channel materials have been also investigated as well.

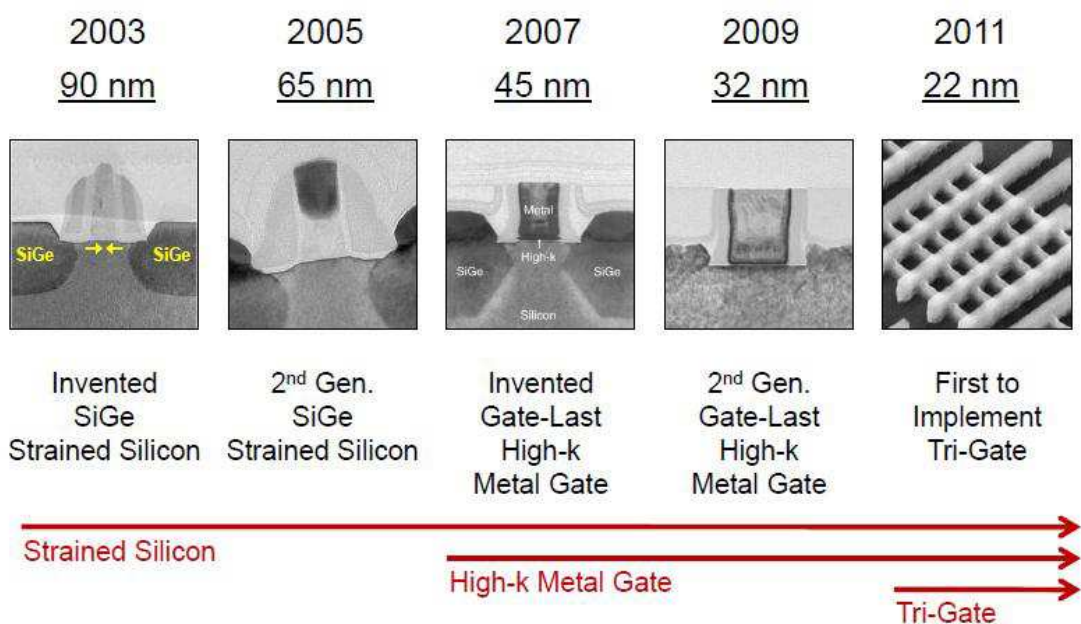


Fig. 1-4. Recent MOSFET architectures and process nodes released by Intel Corporation [1-15].

Chapter 1. Introduction

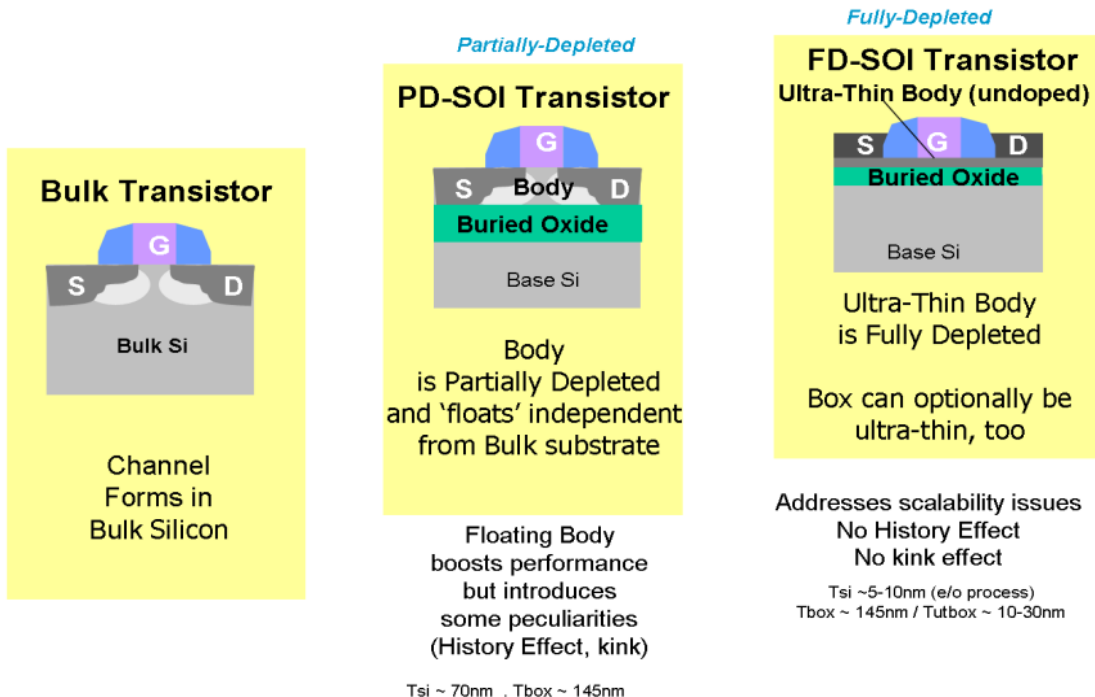


Fig. 1-5. Schematic of MOSFET structure based on silicon-on-insulator (SOI) technology [1-18].

Figure 1-6 shows the schematic of future device technology as reported by the international technology roadmap for semiconductors (ITRS) in 2011 [1-19]. The gate-stack, composed of high- κ dielectric/metal gate materials instead of $\text{SiO}_2/\text{Poly-Si}$, has been practically introduced from the 45nm process node in 2007 by Intel (Fig.1-4). This technology is going to be maintained and the materials will be further optimized to obtain better gate control and lower gate leakage current I_{ox} . For high-speed operating devices, strained Si channel exhibiting higher carrier mobility has been intensively investigated. Moreover, substitute materials, such as Ge and III-V compounds, have been also studied to achieve much higher mobility. As mentioned above, SOI and MG technologies have been proposed to improve electrostatic control by the gate and strongly reduce the SCE (*i.e.* I_{sub}). First commercial MG MOSFET was released in 2011 by Intel, using the structure of a bulk FinFET [1-20] (Fig.1-4). For the next device generation, MG with extremely shrunk body (nanowire) on bulk or SOI substrates has been intensely expected. The gate length of MOSFET should become sub-10nm within 10 years, and approach 6-7nm in 2026. It is awaited that performance requirements could be achieved by MG architectures (Fig.1-7) [1-21].

Chapter 1. Introduction

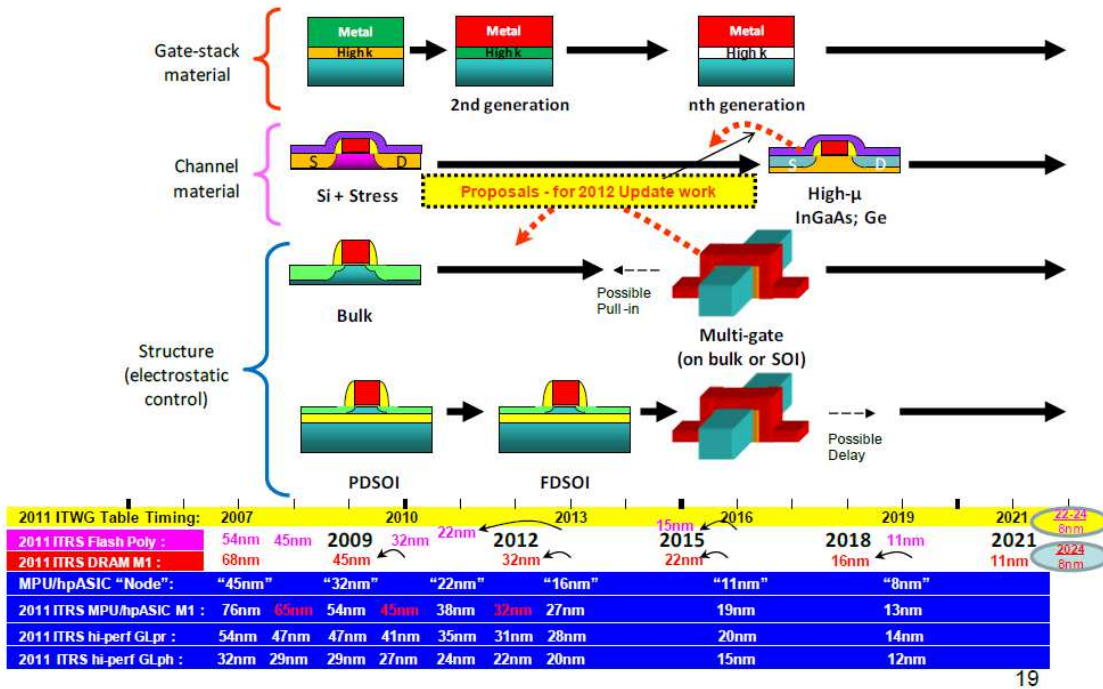


Fig. 1-6. ITRS 2011 “equivalent scaling” process technologies timing compared to overall roadmap technology characteristics (ORTC) and industry “node” naming [1-19].

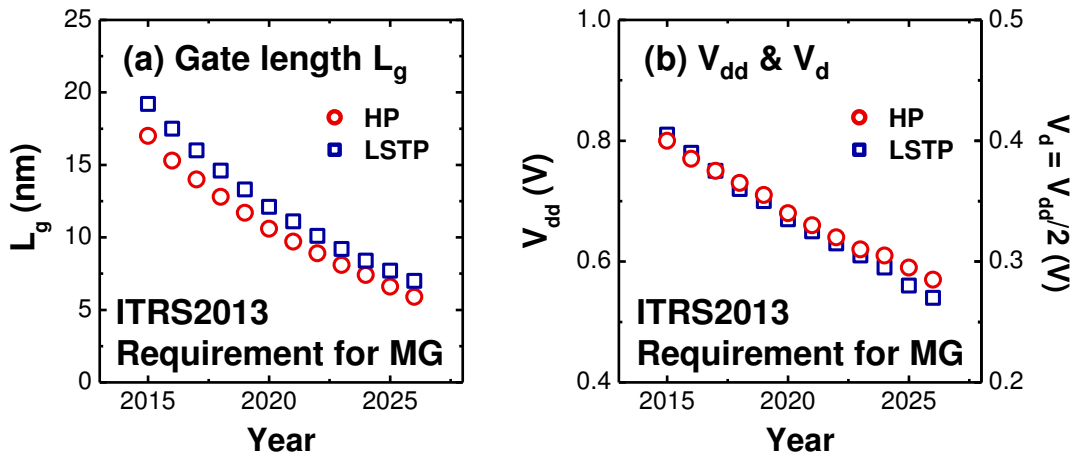


Fig. 1-7. ITRS requirements for future high performance (HP) and low standby power (LSTP) logic circuits consisting of MG FETs. (a) MOSFET gate length L_g , and (b) circuit supply voltage V_{dd} and MOSFET drain voltage V_d are plotted as a function of year between 2015 and 2026 (sourced from ITRS 2013 data in Table RFAMS1 CMOS technology requirements [1-21]).

Chapter 1. Introduction

1.2 Purposes and scopes of this work

Future MOSFET technology node should require MG architectures. However, it became difficult to rigorously examine the electrical characterizations of MG FETs, especially for NW devices, with general characterization method based on capacitance measurement (such as split C-V). Low-frequency noise (LFN) also provides deep insights into electrical properties of the gate oxide/channel interface in MOSFETs [1-22]. LFN characterization has no lower limit of the necessary MOSFET channel area. Therefore, LFN measurement can be a powerful characterization technique for ultra-scaled NW MOSFETs. From engineering point of view, LFN can be a problem in RF/analog circuits. LFN cannot be completely eliminated and sets a lower limit on signal detection in analog devices and circuits. For instance, when excess LFN (1/f noise) stemming from MOSFET appears in phase noise of voltage-controlled-oscillators (VCO), the signal-to-noise ratio (SNR) in mixers for homodyne receivers is degraded. Consequently, measurements and understanding of LFN are highly important in order to evaluate the electrical interface properties and the performance in MOSFETs.

Nowadays, a large number of reports for LFN measurement even in MG devices (for FinFETs [1-23~1-35] and for NW FETs [1-36~1-45]) have been published. Concerning LFN characterizations in recent MG devices, the origin of 1/f noise is mainly attributed to unified carrier number fluctuations with correlated fluctuations (CNF+CMF). Hung *et al.* suggested the CNF+CMF model in 1990 [1-46], and then Ghibaudo *et al.* proposed a more popular definition [1-47]. In practice, the model is mainly suitable for MG devices and have been discussed in previous reports [1-23~1-25,1-28,1-32~1-34,1-36,1-38~1-45]. However, few reports of comprehensive study on each parameter defined in the CNF+CMF model as functions of MOSFET channel size (W_{top} and L_g), architectural difference (planar vs. MG), and technological parameters (channel orientation, strain, etc...), have been published.

In intensive investigations of high- κ /metal gate stack, a number of researches for Hf-based gate dielectric have been reported in MG FinFETs [1-25,1-28~1-34]. But, there are few reports of LFN study in NW FETs with high- κ /metal gate stack. Tachi *et*

Chapter 1. Introduction

al. reported a figure exhibiting LFN behavior of vertically-stacked GAA NWs in 2009, as shown in Fig.1-8 [1-39]. They found that the trap density of Si NWs is higher than the value of planar FD FET. Therefore, there is a concern about the degraded interface quality in NW FETs with Hf-based high- κ /metal gate.

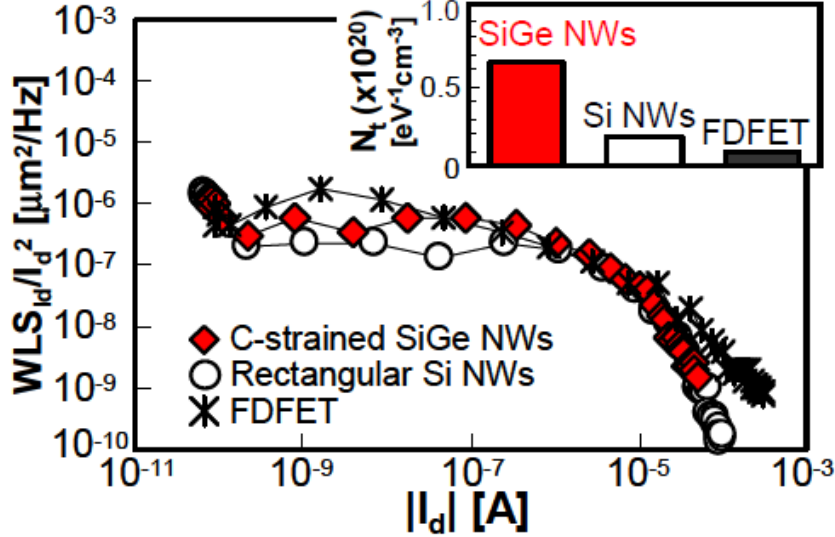


Fig. 1-8. Low-frequency noise of Si and c-strained SiGe NWs. Inserted figure is a comparison of oxide trap density (N_t). L_G and W_{NW} are ~290nm and ~20nm, respectively [1-39].

Similarly with the report by Tachi *et al.*, Zhuge *et al.* reported LFN characterization of GAA NW with thermal Si oxide (SiO_2) with higher oxide trap density than conventional $\text{SiO}_2/\text{poly-Si}$ gate stack in 2009 [1-36]. They considered that the degradation could be caused by various surface orientations and small diameter of GAA NW. On the other hand, Crupi *et al.* reported similar values of oxide trap density between tri-gate and planar NMOS FETs with $\text{SiON}/\text{poly-Si}$ gate stack in 2006, as shown in Fig.1-9 [1-23]. Contributions of different crystallographic orientations of channel surface among the interfaces (*i.e.* MG top (and bottom) surface vs. side-walls) into oxide trap density should be thus evaluated in detail.

Chapter 1. Introduction

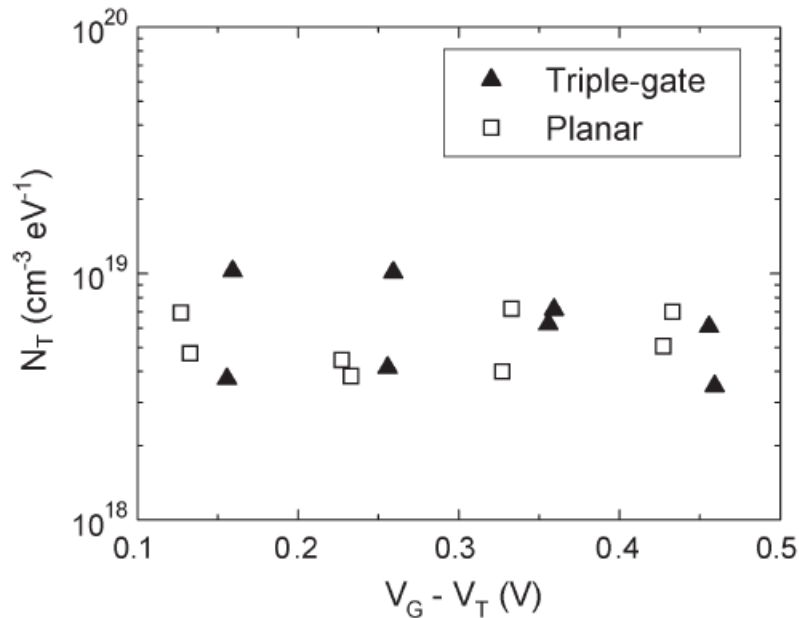


Fig. 1-9. Effective trap density versus gate voltage overdrive for the 30-fin triple-gate devices ($W_{FIN}=60\text{nm}$, $L=1\mu\text{m}$) and planar devices ($W \times L=1\mu\text{m} \times 1\mu\text{m}$). No significant difference between the two structures is observed. [1-23].

Meanwhile, LFN level decrease was observed in SOI tri-gate NW FETs with SiO₂/poly-Si by Feng *et al.* in 2011 [1-42], and in GAA Si NWFETs with SiO₂/TiN by Lee *et al.* in 2012 as shown in Fig.1-10 [1-43]. It could be ascribed to quantum confinement of carriers due to large surface/volume ratio of NW. This volume inversion impact may also be observed in aggressively scaled NWs with Hf-based high-k/metal gate stack.

Chapter 1. Introduction

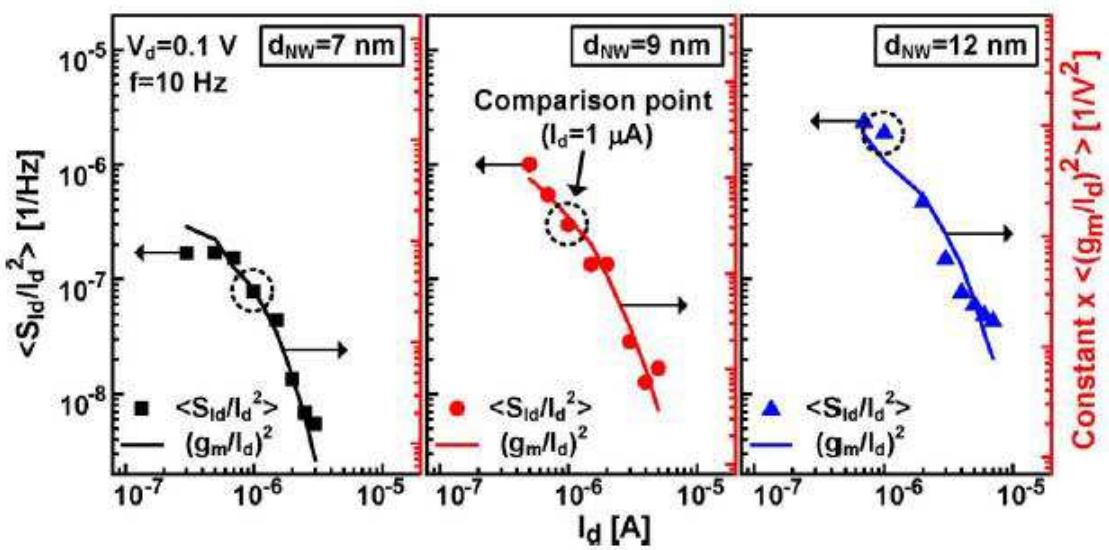


Fig. 1-10. Averaged noise spectral densities (symbols) $\langle S_{Id}/I_d^2 \rangle$ and (lines) $\langle (g_m/I_d)^2 \rangle$ versus I_d at $V_d=0.1\text{V}$ and $f=10\text{Hz}$ for 7-, 9-, and 12-nm d_{NW} , respectively. All the left axes represent $\langle S_{Id}/I_d^2 \rangle$, whereas all the right axes (red colored) represent $\langle (g_m/I_d)^2 \rangle$ multiplied by a constant. The symbols within the dotted circle at the same current level ($1\mu\text{A}$) are for the comparison of $\langle S_{Id}/I_d^2 \rangle$ for each d_{NW} . [1-43].

Influence of strain technology into the interface quality has also been a significant concern and has been studied. For improvement of NMOS performance, tensile strained Si fabricated on SiGe virtual layers has been used and reported the LFN characteristics mostly for planar FETs [1-22,1-48~1-54]. The upgraded [1-48~1-50], constant [1-22], and degraded [1-51~1-54] LFN results compared with reference Si devices. For example, Fig.1-11 shows a deteriorated oxide trap density with increase of Ge content in strained-relaxed-buffer (SRB) SiGe virtual layer reported by Wang *et al.* in 2007 [1-54]. LFN data of sSi NW is necessary for future CMOS node.

Chapter 1. Introduction

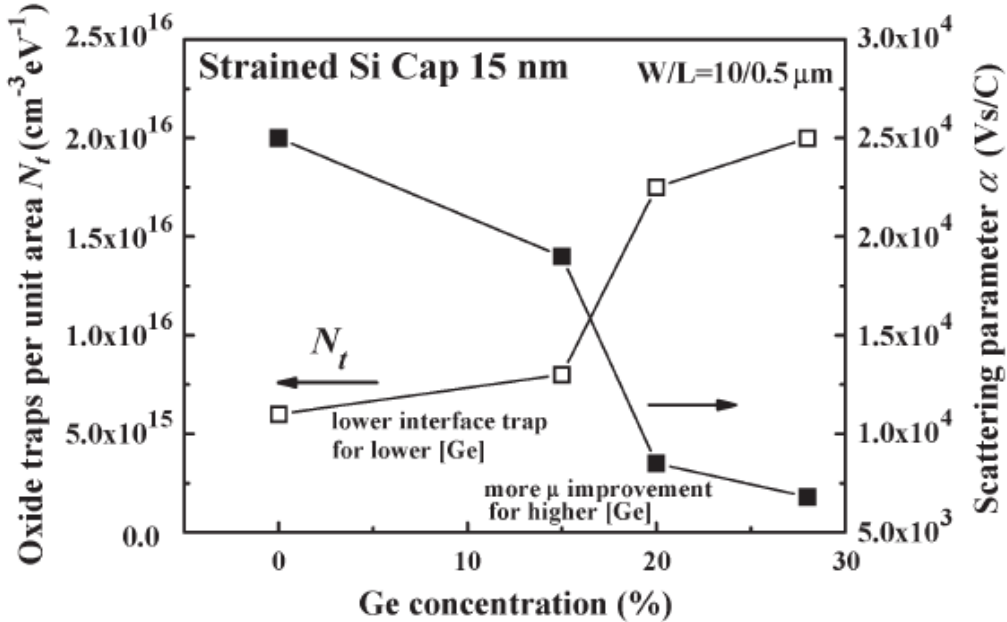


Fig. 1-11. Relationship between equivalent oxide traps per unit area N_t and scattering parameter α and with different Ge content of SRB layers. [1-54].

For PMOS enhancement, compressive strained channel has been fabricated by SiGe source/drain (S/D) and SiGe channel formations. There are few reports of LFN study for SiGe S/D technique in planar [1-55~1-57] and NW [1-45] FETs. LFN properties for SiGe channel FinFETs [1-29~1-31] and NWs [1-37,1-38] have been investigated. However, as Tachi *et al.* reported a 3.5 times higher oxide trap density for SiGe NWs than for Si NWs (Fig.1-8 [1-39]), there is still a concern about the interface quality.

As a consequence, important concerns for ultra-scaled NW MOSFETs should be discussed in detail as follows;

- (i) CNF+CMF model parameters as a function of channel size down to NW
- (ii) NW FETs with advanced Hf-based high- κ /metal gate stack
- (iii) Contributions of different crystallographic orientations of channel surface
- (iv) Large channel surface/volume ratio in NW
- (v) Strained NW technology;

NMOS - tensile strain

PMOS - compressive strain

Chapter 1. Introduction

Accordingly, the purpose of this work is experimental and comprehensive investigation of electrical characteristics in gate oxide/channel interface by LFN and carrier transport measurements in ultra-scaled NW MOSFETs with Hf-based high- κ /metal gate stack, in order to evaluate the significant concerns of (i)-(v).

Our silicon nanowire (NW) MOSFETs were fabricated from advanced fully-depleted SOI (FD-SOI) substrate, and with Hf-based high- κ /metal gate stack (HfSiON/TiN) in order to suppress detrimental SCE and gate leakage. In addition, strain introduction technologies to the channel were additively processed to efficiently improve the MOSFET's performance. Tensile strained-SOI substrate was used for NMOS FETs, whereas compressive stressors were used for PMOS devices. Compressively strained Si channel can be processed by raised SiGe S/D and contact-etch-stop-layer (CESL) formations. In addition, strained SiGe-on-insulator channel was also fabricated for further high-performance PMOS FETs. These fabrication technologies and processes are described in detail in chapter 2.

The gate oxide/channel interface characteristics in the various NW MOSFETs are examined on carrier transport characterizations as the channel properties in chapter 3, and LFN characterizations for the interface properties in chapter 4. In chapter 3, DC gate voltage dependent drain current (I_d - V_g), temperature dependent effective mobility (μ_{eff}), and low-field mobility (μ_0) characteristics are investigated. In chapter 4, drain current noise S_{Id}/I_d^2 behavior, parameter evaluations based on advanced 1/f noise model (involving flat-band voltage noise S_{Vfb} , Coulomb scattering parameter $\alpha_{sc}\mu_{eff}$, and oxide trap density N_t), and drain bias dependent gate voltage noise (S_{Vg} - V_d) behavior compared with the ITRS requirements are characterized.

Finally, our study on electrical characterizations for the oxide/channel interface in NW MOSFETs is concluded in chapter 5. The perspective of LFN investigation on future device nodes is described.

Chapter 1. Introduction

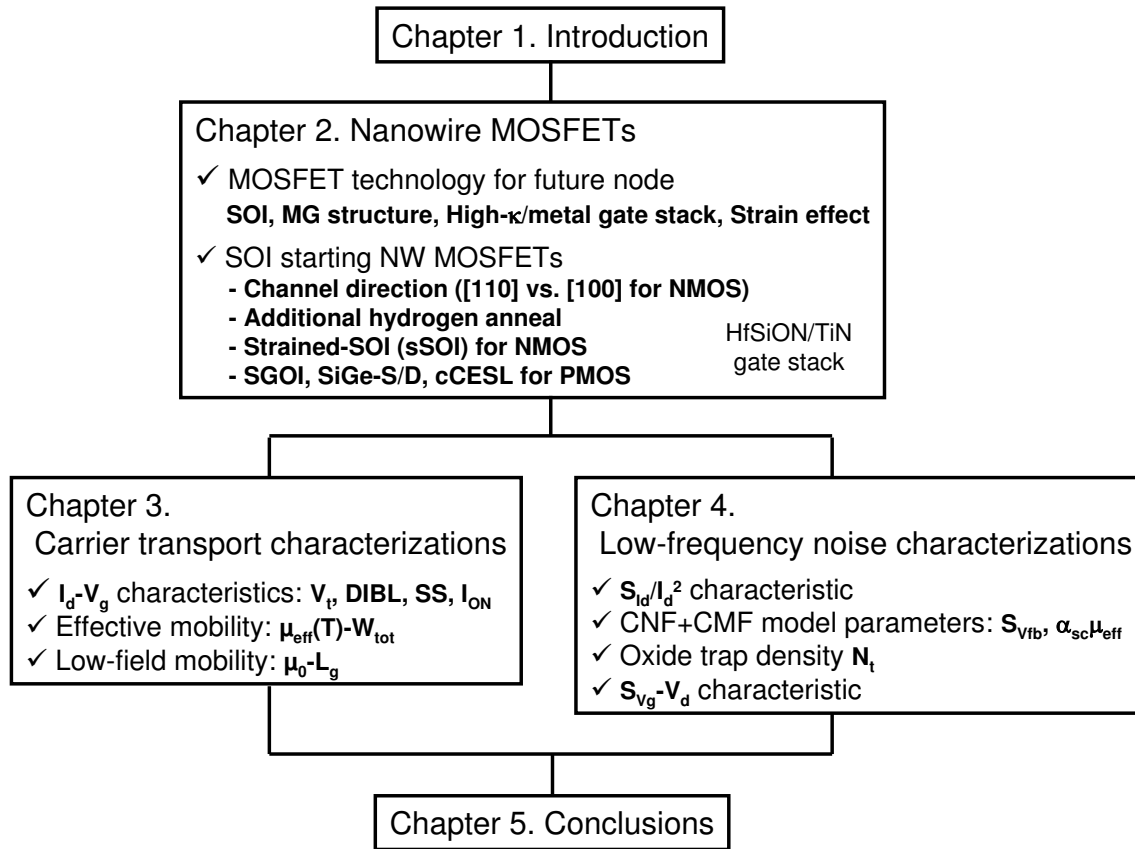


Fig. 1-12. Outline diagram in this work on electrical characteristics of the gate oxide/channel interface in ultra-scaled NW MOSFETs.

Chapter 1. Introduction

1.3 References

- [1-1] J. E. Lilienfeld, "Method and apparatus for controlling electric current," *Canada Patent*, 272437, 1925. and *U.S. Patent*, 1745175, 1926.
- [1-2] J. E. Lilienfeld, "Device for controlling electric current," *U.S. Patent*, 1900018, 1928.
- [1-3] J. Bardeen and W. Brattain, "The transistor, a semi-conductor triode," *Phys. Rev.*, vol. 74, pp. 230-231, 1948.
- [1-4] D. Kahng, "Electric field controlled semiconductor device," *U.S. Patent*, 3102230, 1960.
- [1-5] J. S. Kilby, "Miniaturized electronic circuits," *U.S. Patent*, 3138743, 1959.
- [1-6] R. N. Noyce, "Semiconductor device-and-lead structure," *U.S. Patent*, 2981877, 1959.
- [1-7] G. E. Moore, "Cramming more components onto integrated circuits," *Electronics*, vol. 38, pp. 114-117, 1965. and *Proc. IEEE*, vol. 86, pp. 82-85, 1998.
- [1-8] R. H. Dennard, F. H. Gaensslen, V. L. Rideout, E. Bassous, A. R. LeBlanc, "Design of ion-implanted MOSFET's with very small physical dimensions," *IEEE J. Solid-State Circuits*, vol. 9, pp. 256-268, 1974.
- [1-9] Y. Taur and T. K. Ning: *Fundamentals of modern VLSI devices*, 2nd Edition, Cambridge Univ. Press, Cambridge, 2009.
- [1-10] I. Ferain, C. A. Colinge, and J.-P. Colinge, "Multigate transistors as the future of classical metal-oxide-semiconductor field-effect transistors," *Nature*, vol. 479, pp. 310-316, 2011.
- [1-11] F. M. Wanlass and C. T. Sah, "Nanowatt logic using field-effect metal-oxide semiconductor triodes," *ISSCC Tech. Dig.*, 1963, pp. 32-33.
- [1-12] F. M. Wanlass, "Low stand-by power complementary field effect circuitry," *U.S. Patent*, 3356858, 1963.
- [1-13] T. Sakurai, "Perspectives on power-aware electronics," *ISSCC Tech. Dig.*, 2003, pp. 26-29.
- [1-14] N. S. Kim, T. Austin, D. Baauw, T. Mudge, K. Flautner, J. S. Hu, M. J. Irwin, M. Kandemir, V. Narayanan, "Leakage current: Moore's law meets static power," *Computer*, vol. 36, pp. 68-75, 2003.
- [1-15] M. Bohr and K. Mistry, "Intel's revolutionary 22 nm transistor technology," Intel, 2011. [Online] Available: http://download.intel.com/newsroom/kits/22nm/pdfs/22nm-details_presentation.pdf (accessed on 31 August 2014)

Chapter 1. Introduction

- [1-16] J.-P. Colinge and T. I. Kamins, “CMOS circuits made in thin SIMOX films,” *Electron. Lett.*, vol. 23, pp. 1162-1164, 1987.
- [1-17] K. K. Young, “Short-channel effect in fully depleted SOI MOSFETs”, *IEEE Trans. Electron Devices*, vol. 36, pp. 399-402, 1989.
- [1-18] X. Cauchy, “Forecasted impact of fully depleted SOI technology on design,” SOI industry consortium news, 2010. [Online] Available: http://www.soiconsortium.org/pdf/fullydepletedsoi/SOIconsortium_FDSOI_design.pdf (accessed on 30 June 2014)
- [1-19] “2011 executive summary,” ITRS 2011 edition. [Online] Available: <http://www.itrs.net/Links/2011itrs/2011Chapters/2011ExecSum.pdf> (accessed on 31 August 2014).
- [1-20] C. Auth, C. Allen, A. Blattner, D. Bergstrom, M. Brazier, M. Bost, M. Buehler, V. Chikarmane, T. Ghani, T. Glassman, R. Grover, W. Han, D. Hanken, M. Hattendorf, P. Hentges, R. Heussner, J. Hicks, D. Ingerly, P. Jain, S. Jaloviar, R. James, D. Jones, J. Jopling, S. Joshi, C. Kenyon, H. Liu, R. McFadden, B. Mcintyre, J. Neirynck, C. Parker, L. Pipes, I. Post, S. Pradhan, M. Prince, S. Ramey, T. Reynolds, J. Roesler, J. Sandford, J. Seiple, P. Smith, C. Thomas, D. Towner, T. Troeger, C. Weber, P. Yashar, K. Zawadzki, and K. Mistry, “A 22nm high performance and low-power CMOS technology featuring fully-depleted tri-gate transistors, self-aligned contacts and high density MIM capacitors,” *Symp. VLSI Tech. Dig.*, 2012, pp. 131-132.
- [1-21] “RF and analog/mixed-signal technologies (RFAMS) 2013 tables,” ITRS 2013 edition. [Online] Available: http://www.itrs.net/Links/2013ITRS/2013Tables/RFAMS_2013Tables.xlsx (accessed on 30 June 2014).
- [1-22] M. von Haartman and M. Östling: *Low-frequency noise in advanced MOS devices*, Springer, Dordrecht, 2007.
- [1-23] F. Crupi, B. Kaczer, R. Degraeve, V. Subramanian, P. Srinivasan, E. Simoen, A. Dixit, M. Jurczak, and G. Groeseneken, “Reliability comparison of triple-gate versus planar SOI FETs,” *IEEE Trans. Electron Devices*, vol. 53, pp. 2351-2357, 2006.
- [1-24] E. Simoen, A. Mercha, C. Claeys, N. Lukyanchikova, “Low-frequency noise in silicon-on-insulator devices and technologies,” *Solid-State Electron.*, vol. 51, pp. 16-37, 2007.
- [1-25] K. Bennamane, T. Boutchacha, G. Ghibaudo, M. Mouis, and N. Collaert, “DC and low frequency noise characterization of FinFET devices,” *Solid-State Electron.*, vol. 53, pp. 1263-1267, 2009.

Chapter 1. Introduction

- [1-26] C. Wei, Y.-Z. Xiong, and X. Zhou, “Investigation of low-frequency noise in n-channel FinFETs from weak to strong inversion,” *IEEE Trans. Electron Devices*, vol. 56, pp. 2800-2810, 2009.
- [1-27] M. G. C. de Andrade, J. A. Martino, E. Simoen, and C. Claeys, “Comparison of the low-frequency noise of bulk triple-gate FinFETs with and without dynamic threshold operation,” *IEEE Electron Device Lett.*, vol. 32, pp. 1597-1599, 2011.
- [1-28] C. G. Theodorou, N. Fasarakis, T. Hoffman, T. Chiarella, G. Ghibaudo, and C. A. Dimitriadis, “Flicker noise in n-channel nanoscale tri-gate fin-shaped field-effect transistors,” *Appl. Phys. Lett.*, vol. 101, 243512, 2012.
- [1-29] B. Rajamohanan, I. Ok, S. Mujumdar, C. Hobbs, P. Majhi, R. Jammy, and S. Datta, “Correlated flicker noise and hole mobility characteristics of (110)/<110> uniaxially strained SiGe FINFETs,” *IEEE Electron Device Lett.*, vol. 33, pp. 1237-1239, 2012.
- [1-30] T. Romeo, L. Pantisano, E. Simoen, R. Krom, M. Togo, N. Horiguchi, J. Mitard, A. Thean, G. Groeseneken, C. Claeys, and F. Crupi, “Low-Frequency Noise Assessment of the Transport Mechanisms in SiGe Channel Bulk FinFETs,” *Proc. ESSDERC*, 2012, pp. 330-333.
- [1-31] E. Simoen, T. Romeo, L. Pantisano, A. Luque Rodríguez, J. A. Jiménez Tejada, M. Aoulaiche, A. Veloso, M. Jurczak, R. Krom, J. Mitard, Ch. Caillat, P. Fazan, F. Crupi, and C. Claeys, “Insights in low frequency noise of advanced and high-mobility channel transistors,” *IEDM Tech. Dig.*, 2012, pp. 661–664.
- [1-32] C. G. Theodorou, N. Fasarakis, T. Hoffman, T. Chiarella, G. Ghibaudo, and C. A. Dimitriadis, “Origin of the low-frequency noise in n-channel FinFETs,” *Solid-State Electron.*, vol. 82, pp. 21-24, 2013.
- [1-33] J. W. Lee, M. J. Cho, E. Simoen, R. Ritzenthaler, M. Togo, G. Boccardi, J. Mitard, L.-Å. Ragnarsson, T. Chiarella, A. Veloso, N. Horiguchi, A. Thean, and G. Groeseneken, “1/f noise analysis of replacement metal gate bulk p-type fin field effect transistor,” *Appl. Phys. Lett.*, vol. 102, 073503, 2013.
- [1-34] J. W. Lee, E. Simoen, A. Veloso, M. J. Cho, H. Arimura, G. Boccardi, L.-Å. Ragnarsson, T. Chiarella, N. Horiguchi, A. Thean, and G. Groeseneken, “1/f noise analysis of replacement metal gate bulk p-type fin field effect transistor,” *IEEE Trans. Electron Devices*, vol. 60, pp. 2960-2962, 2013.

Chapter 1. Introduction

- [1-35] H. Sakai, S. O'uchi, K. Endo, T. Matsukawa, Y. Liu, Y. Ishikawa, J. Tsukada, T. Nakagawa, T. Sekigawa, H. Koike, M. Masahara, and H. Ishikuro, “1/f noise characteristics of fin-type field-effect transistors in saturation region,” *Jpn. J. Appl. Phys.*, vol. 52, 04CC23, 2013.
- [1-36] J. Zhuge, R. Wang, R. Huang, Y. Tian, L. Zhang, D.-W. Kim, D. Park, Y. Wang, “Investigation of low-frequency noise in silicon nanowire MOSFETs,” *IEEE Electron Device Lett.*, vol. 30, pp. 57-60, 2009.
- [1-37] C. Wei, Y.-Z. Xiong, X. Zhou, N. Singh, S. C. Rustagi, G. Q. Lo, and D.-L. Kwong, “Investigation of low-frequency noise in silicon nanowire MOSFETs in the subthreshold region,” *IEEE Electron Device Lett.*, vol. 30, pp. 668-671, 2009.
- [1-38] C. Wei, Y. Jiang, Y.-Z. Xiong, X. Zhou, N. Singh, S. C. Rustagi, G. Q. Lo, and D.-L. Kwong, “Impact of gate electrodes on 1/f noise of gate-all-around silicon nanowire transistors,” *IEEE Electron Device Lett.*, vol. 30, pp. 1081-1083, 2009.
- [1-39] K. Tachi, M. Cassé, D. Jang, C. Dupré, A. Hubert, N. Vulliet, V. Maffini-Alvaro, C. Vizioz, C. Carabasse, V. Delaye, J. M. Hartmann, G. Ghibaudo, H. Iwai, S. Cristoloveanu, O. Faynot, and T. Ernst, “Relationship between mobility and high-k interface properties in advanced Si and SiGe nanowires,” *IEDM Tech. Dig.*, 2009, pp. 313-316.
- [1-40] D. Jang, J. W. Lee, K. Tachi, L. Montes, T. Ernst, G. T. Kim, and G. Ghibaudo, “Low-frequency noise in strained SiGe core-shell nanowire p-channel field effect transistors,” *Appl. Phys. Lett.*, vol. 97, 073505, 2010.
- [1-41] R.-H. Baek, C.-K. Baek, H.-S. Choi, J.-S. Lee, Y. Y. Yeoh, K. H. Yeo, D.-W. Kim, K. Kim, D. M. Kim, and Y.-H. Jeong, “Characterization and modeling of 1/f noise in Si-nanowire FETs: effects of cylindrical geometry and different processing of oxides,” *IEEE Trans. Nanotechnol.*, vol. 10, pp. 417-423, 2011.
- [1-42] W. Feng, R. Hettiarachchi, Y. Lee, S. Sato, K. Kakushima, M. Sato, K. Fukuda, M. Niwa, K. Yamabe, K. Shiraishi, H. Iwai, and K. Ohmori, “Fundamental origin of excellent low-noise property in 3D Si-MOSFETs ~Impact of charge-centroid in the channel due to quantum effect on 1/f noise~,” *IEDM Tech. Dig.*, 2011, pp. 630–633.
- [1-43] S.-H. Lee, C.-K. Baek, S. Park, D.-W. Kim, D. K. Sohn, J.-S. Lee, D. M. Kim, and Y.-H. Jeong, “Characterization of channel-diameter-dependent low-frequency noise in silicon nanowire field-effect transistors,” *IEEE Electron Device Lett.*, vol. 33, pp. 1348-1350, 2012.

Chapter 1. Introduction

- [1-44] M. Saitoh, K. Ota, C. Tanaka, and T. Numata, “Systematic understanding of channel-size dependence of low-frequency noise in 10nm-diameter tri-gate nanowire MOSFETs,” *Symp. VLSI Tech. Dig.*, 2013, pp. T228-T229.
- [1-45] S.-H Lee, Y.-R. Kim, J.-H. Hong, E.-Y. Jeong, J.-S. Yoon, C.-K Baek, D.-W. Kim, J.-S. Lee, and Y.-H Jeong, “Investigation of low-frequency noise in p-type nanowire FETs: Effect of switched biasing condition and embedded SiGe layer,” *IEEE Electron Device Lett.*, vol.35, pp. 702-704, 2014.
- [1-46] K. K. Hung, P. K. Ko, C. Hu, and Y. C. Cheng, “A physics-based MOSFET noise model for circuit simulators,” *IEEE Trans. Electron Devices*, vol. 37, pp. 1323-1333, 1990.
- [1-47] G. Ghibaudo, O. Roux, Ch. Nguyen-Duc, F. Balestra, and J. Brini, “Improved analysis of low frequency noise in field-effect MOS transistors,” *Phys. Status Solidi A*, vol. 124, pp. 571-581, 1991.
- [1-48] E. Simoen, G. Eneman, P. Verheyen, R. Delhougne, R. Loo, K. De Meyer, and C. Claeys, “On the beneficial impact of tensile-strained silicon substrates on the low-frequency noise of n-channel metal-oxide-semiconductor transistors,” *Appl. Phys. Lett.*, vol. 86, 223509, 2005.
- [1-49] E. Simoen, G. Eneman, P. Verheyen, R. Loo, K. De Meyer, and C. Claeys, “Processing aspects in the low-frequency noise of nMOSFETs on strained-silicon substrates,” *IEEE Trans. Electron Devices*, vol. 53, pp. 1039-1047, 2006.
- [1-50] E. Simoen, and C. Claeys, “Impact of strain-engineering on the low-frequency noise performance of advanced MOSFETs,” *Proc. ICSICT*, 2006, pp. 120-123.
- [1-51] M. H. Lee, P. S. Chen, W.-C. Hua, C.-Y. Yu, Y. T. Tseng, S. Maikap, Y. M. Hsua, C. W. Liu, S. C. Lu, W.-Y. Hsieh, and M.-J. Tsai, “Comprehensive low-frequency and RF noise characteristics in strained-Si NMOSFETs,” *IEDM Tech. Dig.*, 2003.
- [1-52] W.-C. Hua, M. H. Lee, P. S. Chen, S. Maikap, C. W. Liu, and K. M. Chen, “Ge outdiffusion effect on flicker noise in strained-Si nMOSFETs,” *IEEE Electron Device Lett.*, vol. 25, pp. 693-695, 2004.
- [1-53] W.-C. Hua, M. H. Lee, P. S. Chen, M.-J. Tsai, and C. W. Liu, “Threading dislocation induced low frequency noise in strained-Si nMOSFETs,” *IEEE Electron Device Lett.*, vol. 26, pp. 667-669, 2005.
- [1-54] Y. P. Wang, S. L. Wu, and S. J. Chang, “Low-frequency noise characteristics in strained-Si nMOSFETs,” *IEEE Electron Device Lett.*, vol. 28, pp. 36-38, 2007.

Chapter 1. Introduction

- [1-55] G. Giusi, E. Simoen, G. Eneman, P. Verheyen, F. Crupi, K. de Meyer, C. Claeys, and C. Ciofi, “Low-frequency (1/f) noise behavior of locally stressed HfO₂/TiN gate-stack pMOSFETs,” *IEEE Electron Device Lett.*, vol. 27, pp. 508-510, 2006.
- [1-56] E. Simoen, P. Verheyen, A. Shickova, R. Loo, and C. Claeys, “On the low-frequency noise of pMOSFETs with embedded SiGe source/drain and fully silicided metal gate,” *IEEE Electron Device Lett.*, vol. 28, pp. 987-989, 2007.
- [1-57] B. C. Wang, S. L. Wu, C. W. Huang, Y. Y. Lu, S. J. Chang, Y. M. Lin, K. H. Lee, and O. Cheng, “Correlation between random telegraph noise and 1/f noise parameters in 28-nm pMOSFETs with tip-shaped SiGe source/drain,” *IEEE Electron Device Lett.*, vol. 33, pp. 928-930, 2012.

Chapter 2

Nanowire MOSFETs

2.1 Introduction to MOSFETs for the next technological nodes

2.1.1 Fundamentals of MOSFET

2.1.2 Key concepts for advanced MOSFET

2.2 Our nanowire devices

2.2.1 Process step overview

2.2.2 Key device parameters

2.2.3 Descriptions of all the device parameters

2.3 References

Chapter 2. Nanowire MOSFETs

2.1 Introduction to MOSFETs for the next technological nodes

2.1.1 Fundamentals of MOSFET

2.1.1.1 MOSFET as a switch

A schematic view of classical bulk silicon MOSFET is shown in Fig.2-1 [2-1]. The NMOS FET basically consists of p-type silicon substrate and two opposite n-type regions called the source and drain (S/D). On the other hand, PMOS FET has the n-type substrate and the p-type S/D. The n^+ -p- n^+ type structure (source-substrate-drain) can be seen as two p-n diodes connected back-to-back, and the structure normally prevents flow of current between the S/D regions except small diffusion current. The S/D regions are heavily doped in order to reduce the S/D resistances as small as possible. The substrate is typically silicon in current MOSFET technology, but other semiconductor materials with capability for faster transport of inversion carriers are also being considered for future microelectronics. A thin insulator layer, such as silicon dioxide, covers the substrate region between the S/D regions. This insulating layer is capped by a metal or heavily doped poly-Si called gate electrode, and is called gate oxide.

Under distinctive bias conditions; a positive voltage is applied to the drain, the source is grounded, and an enough large positive voltage is applied to the gate. As a result, electrons flow from the n-type source to the drain regions through a formed thin electron-rich layer called channel in the substrate beneath the gate oxide. The gate bias with a positive voltage increases the surface potential and repels holes from the surface. If the gate bias surpasses the threshold voltage, the substrate type near the surface inverts and the electrons, which are opposite type carriers for p-type substrate, can largely flow between the S/D regions. When the channel, which behaves as a minority carrier path, is formed, then the MOSFET is turned on and the state corresponds to a closed switch. If the gate voltage bias is much smaller than the on-state, the channel is dissolved and electrons do not flow except by diffusion effect. This means that the MOSFET is turned off and the state equals an open switch.

Chapter 2. Nanowire MOSFETs

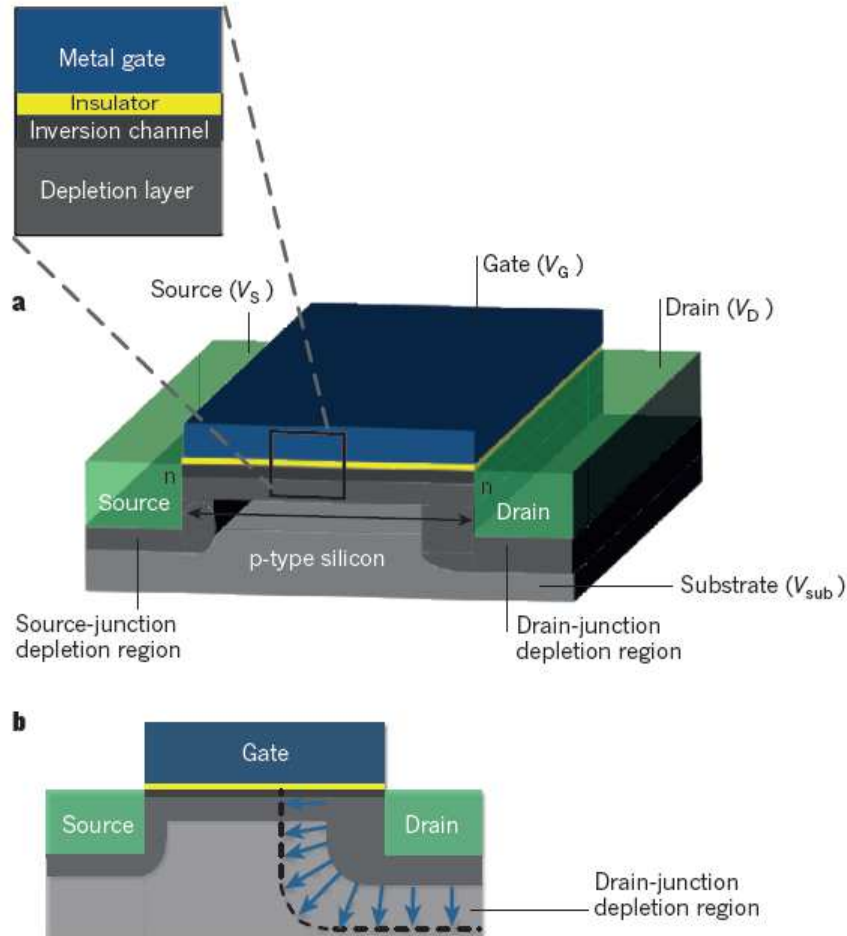


Fig. 2-1. A schematic view of a classical bulk n-channel MOSFET [2-1].

As mentioned above, the gate voltage V_g controls the conductivity between the S/D regions. The drain current I_d between S/D regions therefore depend on the conductivity and the applied electric field along the channel. The I_d in linear region of drain voltage V_d bias (V_{d_lin}) can be expressed as [2-2,2-3]:

$$I_{d_lin} = \mu_{eff} C_{ox} \frac{W}{L} \left\{ (V_g - V_t) \cdot V_{d_lin} - \frac{m}{2} V_{d_lin}^2 \right\} \quad (2-1)$$

where W is the channel width, L is the channel length, V_t is the threshold voltage, μ_{eff} is the effective mobility of carriers in the channel, C_{ox} is the gate oxide capacitance, and m is the body-effect coefficient. If the V_{d_lin} is enough small, this equation can be simplified as:

Chapter 2. Nanowire MOSFETs

$$I_{d_lin} \approx \mu_{eff} C_{ox} \frac{W}{L} (V_g - V_t) \cdot V_{d_lin} = \mu_{eff} C_{ox} \frac{W}{L} V_{gt} V_{d_lin} \quad (2-2)$$

where V_{gt} is the gate voltage overdrive ($=V_g - V_t$).

The I_d increases with the V_d until the I_d reaches a maximum, and then the saturation occurs. The V_d at the saturation region (V_{d_sat}) can be derived by a relationship of $dI_d/dV_d=0$ in Eq. (2-1) and is written as:

$$V_{d_sat} = \frac{V_{gt}}{m} \leftarrow \frac{dI_d}{dV_d} \Big|_{V_d=V_{d_sat}} = \mu_{eff} C_{ox} \frac{W}{L} (V_{gt} - mV_{d_sat}) = 0 \quad (2-3)$$

At this V_d point, the channel at the end of the drain region is vanished, and this phenomenon is called pinch-off. The electric field along the channel between the source and the pinch-off point is steady with the V_d increase over V_{d_sat} , and thus this basically results in the saturated I_d . By substituting the $V_{d_sat}=V_{gt}/m$ into Eq. (2-1), the I_d in the saturation region can be derived as:

$$I_{d_sat} = \mu_{eff} C_{ox} \frac{W}{L} \cdot \frac{(V_g - V_t)^2}{2m} = \mu_{eff} C_{ox} \frac{W}{L} \cdot \frac{V_{gt}^2}{2m} \quad (2-4)$$

Actually, the pinch-off point approaches slightly the source region in the condition of $V_d > V_{d_sat}$, and that results in slight decrease of the channel length. This is called channel length modulation and causes a little increase of I_d in the saturation region in practice. It should be noticed that the pinch-off occurs for long device only. If the electric field ($E \propto L^{-1}$) is higher than 10^4V/m , here is saturation of the carrier velocity before the pinch-off. The V_g and the V_d both dependent MOSFET operations are classified as three regions; linear, saturation, and subthreshold regions as shown in Fig.2-2.

Chapter 2. Nanowire MOSFETs

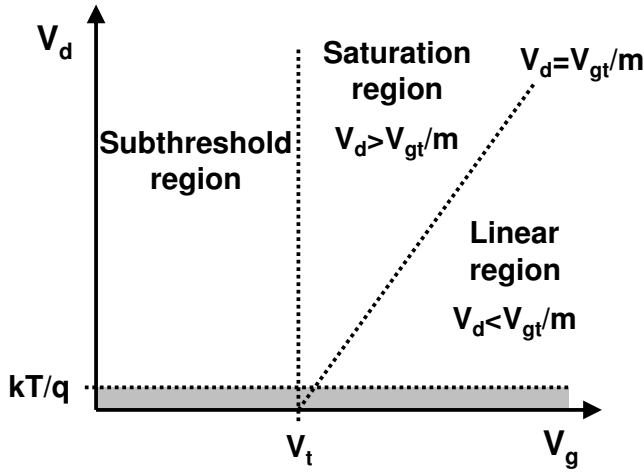


Fig. 2-2. A schematic of three regions in the V_g and V_d both dependent MOSFET operation.

2.1.1.2 Threshold voltage

Threshold voltage V_t is one of the most important and fundamental device parameters for the MOSFET characterization. Precise control of the V_t is a major issue in CMOS applications. It represents the V_g value which is the transition point between weak and strong inversion regions of the MOSFET operation. The definition of V_t was first suggested in 1953 [2-4], and is commonly understood that the V_t provides a bend of the semiconductor energy band at the substrate-insulator interface (surface potential Ψ_S) equaling twice the energy difference between the Fermi level E_F and the intrinsic Fermi level E_i (Ψ_{Bp}) [2-5], as shown in Fig.2-3 [2-2]. The surface potential Ψ_S for NMOS FET comprised of p-type substrate at the V_t can be expressed as:

$$\Psi_S|_{V_g=V_t} = 2\Psi_{Bp} = 2 \frac{kT}{q} \ln\left(\frac{p}{n_i}\right) \approx 2 \frac{kT}{q} \ln\left(\frac{N_A}{n_i}\right) \quad (2-5)$$

where q is the elementary charge, k is the Boltzmann's constant, T is the absolute temperature, also kT is defined as the thermal energy, n_i is the intrinsic carrier density, p is the hole density, and N_A is the acceptor doping density. The threshold voltage V_t in bulk Si NMOS FET can be given by:

$$V_t = V_{fb} + 2\Psi_{Bp} + \frac{2\sqrt{q\varepsilon_0\varepsilon_{Si}N_A\Psi_{Bp}}}{C_{ox}} \quad (2-6)$$

Chapter 2. Nanowire MOSFETs

where V_{fb} is the flat-band voltage, ϵ_0 is the permittivity in vacuum, and ϵ_{Si} is the relative permittivity of silicon. The flat-band voltage V_{fb} depends on the work function difference between the gate and substrate materials ϕ_{ms} and the equivalent oxide charge density Q_{ox} including the fixed and trapped charges, and is described as:

$$V_{fb} = \phi_{ms} - \frac{Q_{ox}}{C_{ox}} \quad (2-7)$$

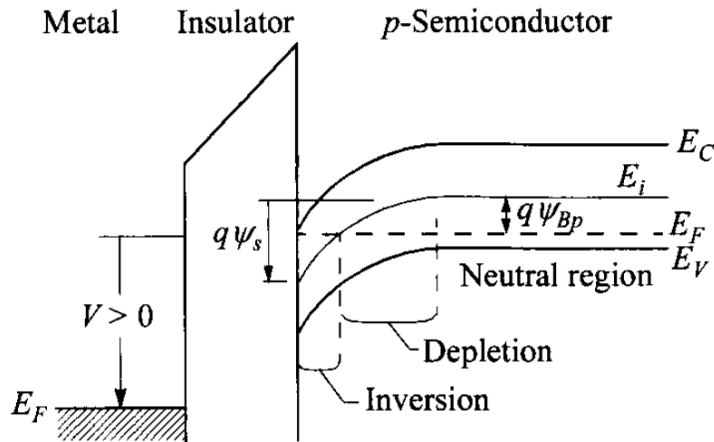


Fig. 2-3. Band diagram of an ideal n-type metal-insulator-semiconductor capacitor under strong inversion [2-2].

In strong inversion mode of MOSFET operation, minority carriers are confined in a potential well near the substrate surface, which is illustrated in Fig.2-3 as an inversion layer. The inversion layer corresponds to the channel region, and thus is formed by a strong bending of substrate energy band in the vicinity of interface between the dielectric barrier and the substrate conduction or valence bands, respectively for electrons or holes as the minority carriers. Consequently, a large number of the carriers can flow from the source toward the drain through the nearly 2D-like channel region in the physical device dimension.

In a MOSFET characteristic of the I_d as a function of the V_g , the I_d seems to approach zero rapidly below the V_t on the linear scale, whereas on the logarithmic scale, the I_d abruptly drops to the off-state, but does not reach zero (Fig.2-4 [2-1]). The V_t corresponds to the beginning point of the on-state, and region where $V_g < V_t$ is called subthreshold (below threshold) region.

Chapter 2. Nanowire MOSFETs

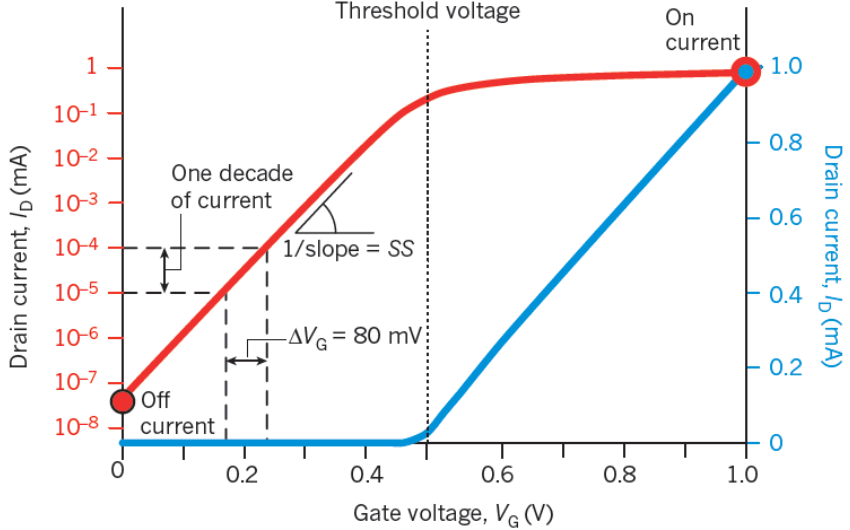


Fig. 2-4. The drain current as a function of the gate voltage in a MOSFET [2-1].

2.1.1.3 Subthreshold swing

In MOSFET operation, when the applied V_g is below V_t (*i.e.* in subthreshold region), a small I_d exists whereas the channel is not formed yet. Once larger V_d than kT/q is applied to MOSFET in subthreshold region, the current transport is occurred independently of the V_d . The subthreshold current is dominated by the diffusion current and is exponentially increased by V_g . The small I_d in subthreshold region is expressed as [2-2,2-3]:

$$I_{d_sub} = \mu_{eff} C_{ox} \frac{W}{L} (m-1) \left(\frac{kT}{q} \right)^2 \exp\left(\frac{qV_{gt}}{mkT} \right) \left\{ 1 - \exp\left(-\frac{qV_d}{kT} \right) \right\} \quad (2-8)$$

Subthreshold swing (SS) corresponds to the inverse slope of steep and nearly straight I_d - V_g curve in subthreshold region on logarithmic scale as shown in Fig.2-4. This indicates the MOSFET performance of switching steepness between off-state and on-state. The SS value is defined as the reciprocal of the slope and given by:

$$SS = \left(\frac{d(\log_{10} I_{d_sub})}{dV_g} \right)^{-1} = \ln(10) \frac{mkT}{q} = 2.3 \frac{mkT}{q} \quad (2-9)$$

The value thus exhibits the necessary V_g range to increment I_d by one decade on logarithmic scale, and the steep slope is desirable. The SS has a lower boundary of

Chapter 2. Nanowire MOSFETs

59.6mV/decade at room temperature, and the limit cannot be altered by any device parameters of MOSFETs [2-6].

2.1.1.4 Short-channel effects

Short-channel effects (SCE) result from the sharing of the electrical charges in the channel region between the gate and the S/D. The S/D junctions with the body form depletion regions encroaching laterally to the channel region from both sides underneath the gate, thus the effective channel length is shortened. The depletion layers overlaid on the channel region deteriorate the channel controllability by the gate, thereby the control loss is amplified as the V_d increases. This effect is schematically illustrated in Fig.2-1b. The channel control thus does not only depend on the V_g and is also influenced from the V_d bias and the distance between the S/D regions as shown in Fig.2-5. Consequently, the off-current is increased and threshold voltage V_t is decreased, as the channel length is shrunk and high V_d is applied. These could impede the normal operation as MOSFET. Two effects indicating the charge control degradation are mainly observed; drain induced barrier lowering (DIBL) and SS increase. These effects additively increase the gate leakage current, which is a serious obstruction to further downscaling of MOSFETs. Degradation of the maximum operating frequency f_{\max} (*i.e.* deterioration of the maximum switching speed) originated from DIBL effect is expressed by [2-1]:

$$\Delta f = -f_{\max} \frac{2DIBL}{V_{dd} - V_t} \quad (2-10)$$

Therefore, the DIBL and SS are important properties characterizing SCE and electrostatic controllability in MOSFET operation.

Chapter 2. Nanowire MOSFETs

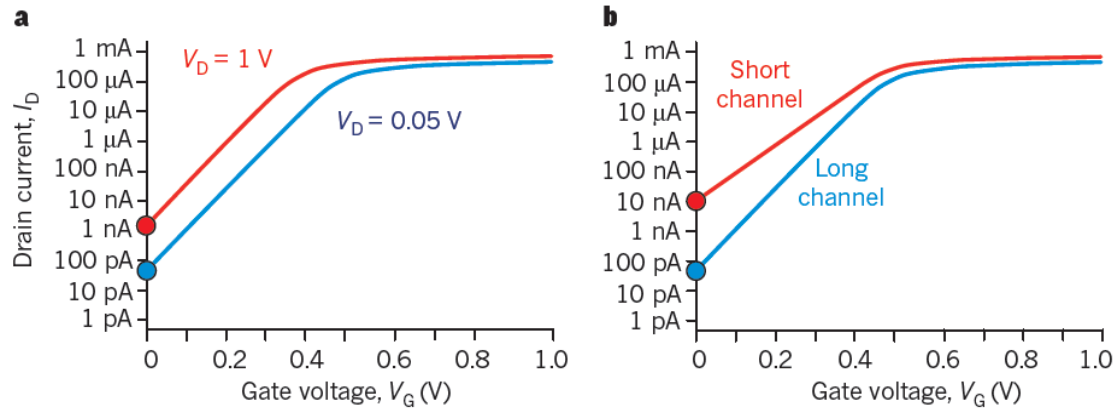


Fig. 2-5. Illustration of short-channel effects [2-1]. (a) The DIBL and (b) the SS increase impacts are shown in the relationship between the drain current I_d and the gate voltage V_g .

2.1.2 Key concepts for advanced MOSFET

2.1.2.1 FD-SOI devices

Silicon-on-insulator (SOI) substrate consists of a thin single-crystalline Si layer placed on an insulator, which is generally silicon dioxide (SiO_2) and is called buried oxide (BOX). The SOI technology was first introduced to military and space applications in the 1970s. For general fabrication of SOI wafers, the founders of Soitec pioneered a new wafer bonding technique, Smart CutTM [2-7,2-8], which was developed at CEA-LETI and ramped up in mid 1990s. Figure 2-6 illustrates the Smart CutTM technology. At first, a donor Si wafer A is thermally oxidized to obtain SiO_2 layer as a BOX in SOI structure. The transferred Si thickness is settled by cleavage layer creation by ion implantation of hydrogen. After surface cleaning and wafer bonding between the donor wafer A and handle wafer B, the cleavage layer is split. As a result, the structure with thin Si film on BOX layer is achieved. The process is finished with polishing, annealing, and treatment of the thin Si film to ensure the targeted Si thickness.

Chapter 2. Nanowire MOSFETs

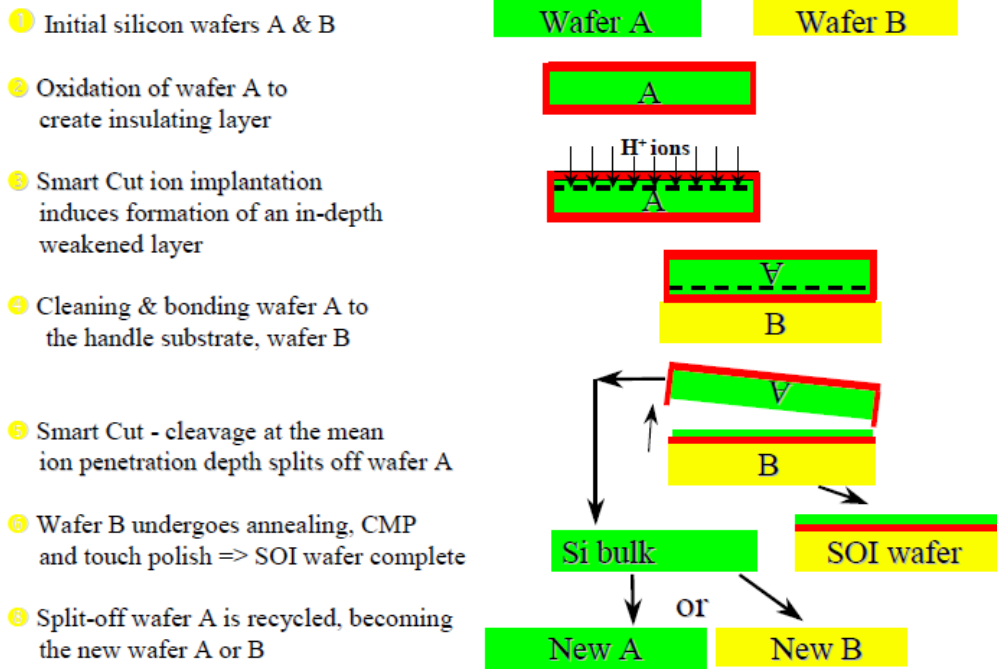


Fig. 2-6. Process flow schematics of SOI substrate fabrication by Smart Cut™ technology [2-8].

The SOI is classified into two categories; partially depleted (PD) or fully depleted (FD) substrates depending on the targeted Si film thickness T_{Si} [2-9~2-11]. In general, FD-SOI structure with thinner T_{Si} (typically, $T_{Si} < 20\text{nm}$) is more advantageous for high- or low-speed digital and analog applications, and also in the mixed-mode IC. The extremely thin body film and dielectric isolation permitting undoped channel provides several advantages: suppression of random dopant fluctuation (RDF), reduced parasitic capacitances, reduction of leakage currents and power consumption, better switching, suitability for low power operation, suppressed latch-up, and simplified lateral isolation process [2-7~2-16].

In addition, body-effect suppression is well known as an important advantage in FD-SOI. The body-effect coefficient, m , is an image of the coupling inefficiency (usually for bulk FET) between the gate and the channel of MOSFET. Impact of the body-effect is discussed with comparison between conventional bulk Si and FD-SOI MOSFETs in the following. The equivalent circuit capacitance in bulk Si and FD-SOI MOSFETs is shown in Fig.2-7. The total capacitance C_{tot} in bulk MOSFET is given as:

Chapter 2. Nanowire MOSFETs

$$\frac{1}{C_{tot_bulk}} = \frac{1}{C_{ox}} + \frac{1}{(C_{acc} \text{ or } C_{dep} \text{ or } C_{inv}) + C_{it}} \quad (2-11)$$

where C_{acc} , C_{dep} , and C_{inv} are the capacitances in accumulation, depletion, and inversion layers, and C_{it} is the capacitance of traps at gate oxide/channel interface. Figure 2-8 illustrates the C_{tot} - V_g characteristics in bulk Si NMOS FETs [2-17]. Focusing on the ideal curve (metal gate case without quantum-mechanical (QM) effect), the three modes correspond to; upper saturation region on negative bias is accumulation mode, upper saturation region on positive bias is inversion mode, and in-between lower saturation region is depletion mode. Great amount of majority or minority carries, respectively in accumulation and inversion modes, screens the dielectric from the substrate. Thus, in these regions, measured C_{tot} corresponds to C_{ox} (*i.e.* C_{acc} and $C_{inv} \gg C_{ox}$). In depletion region, depletion layer has the width W_{dep} towards the substrate body. Now C_{tot} and C_{dep} in bulk MOSFETs are written as:

$$\frac{1}{C_{tot_bulk}} = \frac{1}{C_{ox}} + \frac{1}{C_{dep} + C_{it}} \quad (2-12a)$$

$$\text{with } C_{dep} = \frac{\epsilon_0 \epsilon_{Si}}{W_{dep}} \quad (2-12b)$$

For FD-SOI case, the C_{tot} is modified as following:

$$\frac{1}{C_{tot_SOI}} = \frac{1}{C_{ox}} + \frac{1}{(C_{acc} \text{ or } C_{dep_SOI} \text{ or } C_{inv}) + C_{it}} \quad (2-13a)$$

$$\text{with } \frac{1}{C_{dep_SOI}} = \frac{1}{C_{dep}} + \frac{1}{C_{BOX} + C_{it_BOX}} \quad (2-13b)$$

where C_{BOX} is the capacitance in BOX, and C_{it_BOX} is the capacitance of traps at Si/BOX interface. Here, the W_{dep} equals the Si film thickness T_{Si} , thereby $C_{dep} = \epsilon_0 \epsilon_{Si} / T_{Si}$ is obtained.

Chapter 2. Nanowire MOSFETs

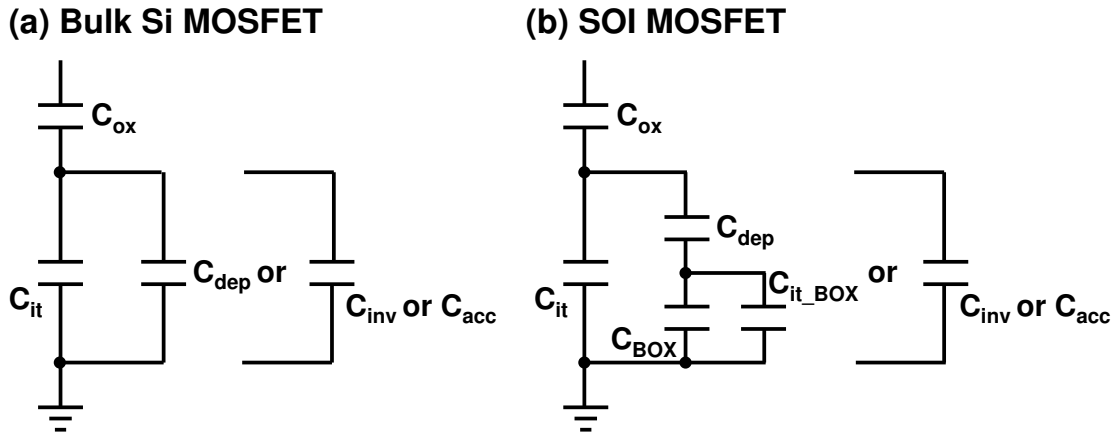


Fig. 2-7. Equivalent circuits of (a) bulk Si and (b) FD-SOI MOSFETs for capacitance.

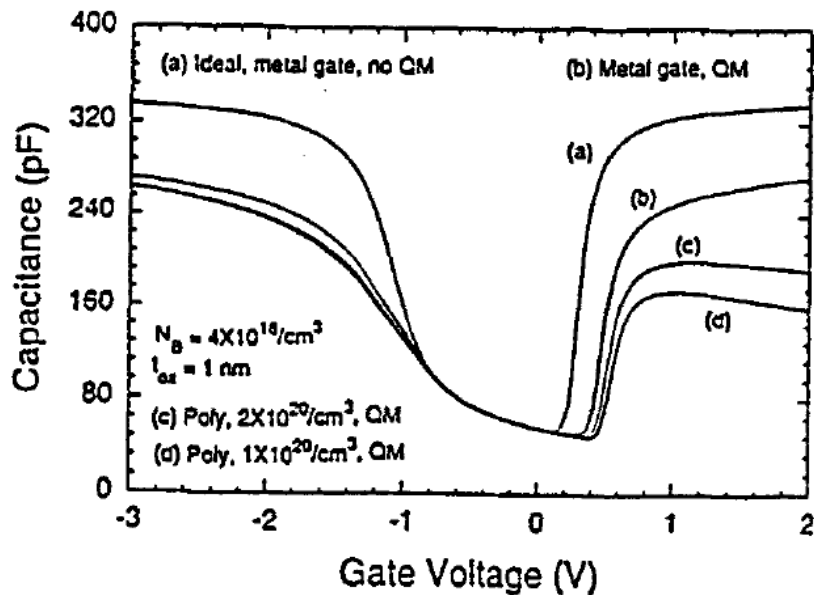


Fig. 2-8. Illustration of C_{tot} - V_g characteristic in bulk Si NMOS FET (Illustration of QM and poly-silicon depletion effects on C-V) [2-17].

Body-effect coefficient m is defined as the capacitance divider ratio, and the coefficient in bulk MOSFET is expressed as:

$$m_{bulk} = 1 + \frac{C_{dep} + C_{it}}{C_{ox}} \quad (2-14)$$

On the other hand, the coefficient in FD-SOI case is given by:

Chapter 2. Nanowire MOSFETs

$$m_{SOI} = 1 + \frac{C_{it}}{C_{ox}} + \frac{C_{dep}(C_{BOX} + C_{it_BOX})}{C_{ox}(C_{dep} + C_{BOX} + C_{it_BOX})} \quad (2-15)$$

Here, assuming that the ideal circuits exclude C_{it} and C_{it_BOX} , the two equations are simplified as:

$$m_{bulk} \approx 1 + \frac{C_{dep}}{C_{ox}} \quad (2-16)$$

$$m_{SOI} \approx 1 + \frac{C_{dep}C_{BOX}}{C_{ox}(C_{dep} + C_{BOX})} \quad (2-17)$$

The coefficient is typically $m \approx 1.05\text{-}1.1$ in FD-SOI devices with thick BOX ($C_{BOX} \ll C_{ox}$ and C_{dep}), thus the body-effect is roughly unity, meanwhile the effect is non-negligible with $m \approx 1.2\text{-}1.5$ in bulk FETs [2-1,2-12]. Therefore, higher on-state current I_{ON} is achievable by using FD-SOI technology, as mentioned above in Eq. (2-4). Furthermore, nearly ideal SS in Eq. (2-9) *i.e.* sharper switching property is also provided.

2.1.2.2 Multi-gate devices

3D architectures are also key features for further MOSFET performance improvement. These multi-gate (MG) architectures provide a better electrostatic integrity, thus limiting the SCE [2-1,2-14~2-16]. The innovative structures allow the continuing enhancement of device performance and offer advantages for both the node downscaling and reduction of power consumption. First commercial MG MOSFET based on bulk FinFET technology was released in 2011 by Intel [2-18,2-19] (cf. Fig.1-4). For future CMOS technology nodes, the MG device with aggressively shrunk channel cross-section, which is called nanowire (NW) MOSFET, is thought to be a strong candidate. Various MG structures are schematically shown in Fig.2-9 [2-1].

Chapter 2. Nanowire MOSFETs

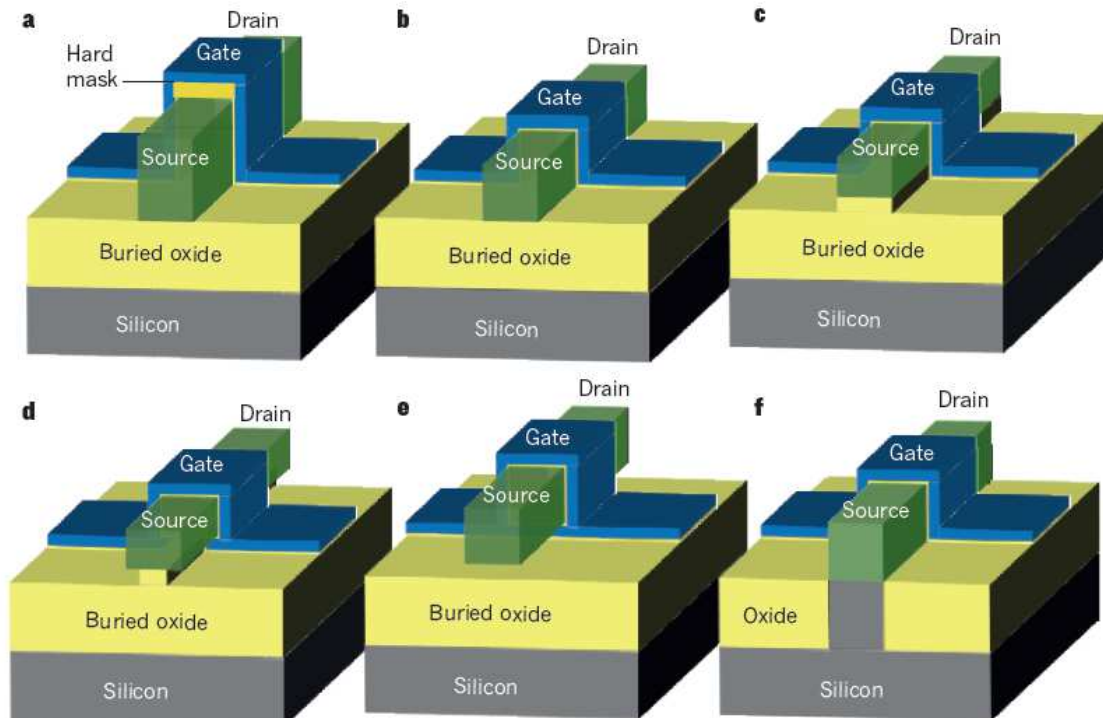


Fig. 2-9. Types of MG MOSFETs. (a) SOI DG FinFET, (b) SOI tri-gate FET, (c) SOI Π -gate FET, (d) SOI Ω -gate FET, (d) SOI quadruple-GAA FET, and (e) bulk tri-gate FET [2-1].

Advantage of the immunity against SCE in MG architecture is discussed in the following. SS degradation and DIBL are caused by lateral penetration of the electric field from the S/D regions into the channel. The distribution of electrical potential in the channel of a Si MOSFET is described by Poisson equation, which is one of the Maxwell's equations as:

$$\nabla \bullet \mathbf{E} = \frac{dE_x}{dx} + \frac{dE_y}{dy} + \frac{dE_z}{dz} = -\frac{\rho}{\epsilon_0 \epsilon_{Si}} = Const. \quad (2-18)$$

where \mathbf{E} is the vector of the electric field, ρ is the local density of electrical charge. In MG devices, increased gate control is exerted in the z (by the top and/or bottom gates) and/or y (by the left- and right-hand side gates) directions, and this decrease the electric field penetration from S/D regions to the channel (x direction). Based on the 3D Poisson equation, a parameter, natural length λ_n which represents the lateral extension of the electrical field, can be introduced [2-16,2-20]. This describes that a MOSFET is free

Chapter 2. Nanowire MOSFETs

from SCE, if the L_g is six-fold longer than the λ_n ($L_g > 6\lambda_n$). If the MG FET has a square cross-section ($T_{Si} = W_{Si}$, where T_{Si} is the Si body thickness and W_{Si} is the Si body width), then the λ_n value is given by:

$$\lambda_n = \sqrt{\frac{\epsilon_{Si}}{n\epsilon_{ox}}} T_{Si} T_{ox} \quad (2-19)$$

where T_{ox} is the gate oxide thickness, ϵ_{ox} is the relative permittivity of the gate oxide, and n is the effective gate number. By extensive numerical simulations, the value of n is defined as shown in [Fig.2-10](#), and this figure shows the universal dependence of DIBL and SS on the scaling parameter $L/2\lambda_n$ for the various MG configurations [\[2-21\]](#). In addition, these explanations indicate that SCE can be reduced by using the thinner gate oxide, the shallower S/D regions, and the gate oxide material with the higher dielectric constant.

Chapter 2. Nanowire MOSFETs

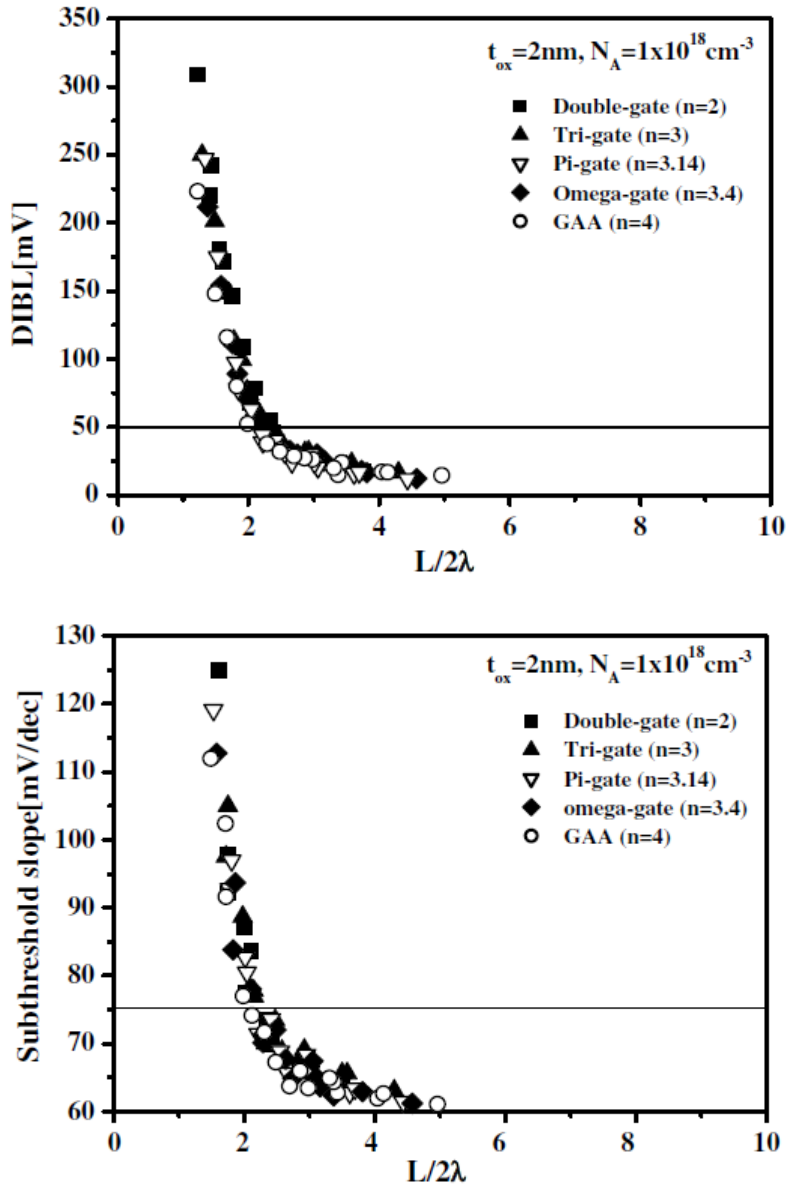


Fig. 2-10. Dependence of DIBL and SS on the scaling parameter [2-21].

In the history of MG devices, a double-gate (DG) structure was first proposed in 1984 [2-22]. The DG architecture was invented based on laterally positioned Si film (similar to FD-SOI structure) and the additional bottom gate. The first DG MOSFET, the fully depleted lean-channel transistor (DELTA), was actually fabricated in 1989 [2-23]. The DG FET consisted of a vertically positioned Si film, and the vertical channel technology continued later to DG FinFETs [2-24]. In the DG FinFET (Fig.2-9a),

Chapter 2. Nanowire MOSFETs

channel conduction is exerted only in both side-walls of Si fin structure. The top has no contribution to the conduction, since the top is covered with hard mask, which is a thick dielectric.

Other MG MOSFET structures have been then excogitated in a stream, such as triple-gate (tri-gate) ([Fig.2-9b](#)) [[2-25,2-26](#)], pi-gate (Π -gate) ([Fig.2-9c](#)) [[2-27](#)], omega-gate (Ω -gate) ([Fig.2-9d](#)) [[2-28](#)], and gate-all-around (GAA) architectures. In tri-gate FETs, gate control is exerted from three surfaces of the channel; the top and two side-walls. Π -gate and Ω -gate FETs improve gate control over tri-gate FET because of better lateral electric field at the bottom, and of increased channel region, respectively. The names of Π -gate and Ω -gate reflect that the gate shapes resemble each Greek character. First GAA device was reported in 1990 [[2-29](#)], and consisted of quadruple-gate which has rectangular channel cross-section shape ([Fig.2-9e](#)). The all four sides contribute to the channel conduction. In addition, a circular-GAA structure, which has the circularly surrounded channel shape and the aggressively scaled diameter, has been investigated in [Refs. \[2-30,2-31\]](#). The MG FETs with aggressively downscaled body cross-section are called NW devices. In practice, NW FETs are usually designed with several channel fingers aligned parallel and with a common gate electrode. This configuration allows simple increase of the drive current and the total effective channel area by increasing the number of fingers (*e.g.* tri-gate array structure with the 50-multiple fingers is shown in [Fig.2-11 \[2-32\]](#)). Especially, increment of the total effective channel width is important technology to perform accurate measurements (*e.g.* capacitance, charge pumping, etc.) in actively miniaturized MG architectures, such as NW FETs. Moreover, 3D-stacked MG devices have been also contrived with a concept of the finger multiplication in the vertical direction [[2-33~2-36](#)].

Chapter 2. Nanowire MOSFETs

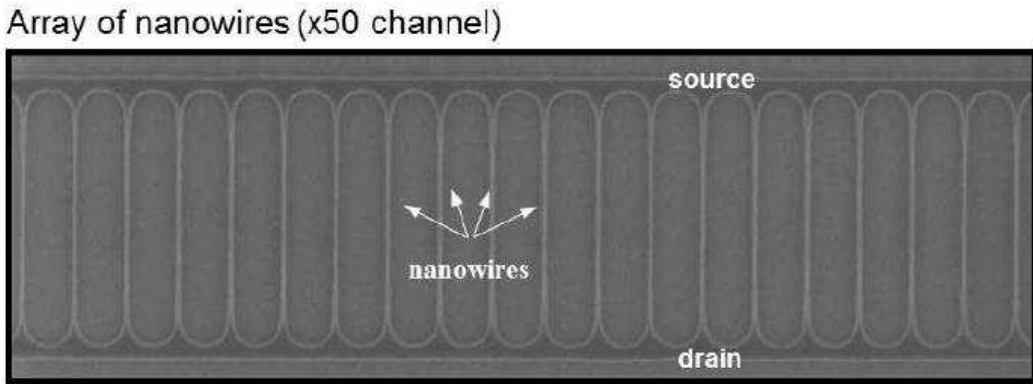


Fig. 2-11. Array of Si NW on oxide ($\times 50$ channels) obtained by SEM [2-32].

SOI substrates have good compatibility with MG device fabrication. Particularly, most of the advanced MG devices mentioned above were fabricated by using FD-SOI substrates. FD-SOI substrate is more beneficial than bulk Si case for fabrication of miniaturized MG devices, such as NW FETs, due to the intrinsic device isolation by BOX layer. Although more complicated process are required, bulk DG FinFET and tri-gate devices have been also investigated (Fig.2-9f), and good SCE immunity has been reported [2-18,2-19,2-37]. Basically, MG fabrication process is same as conventional planar device process. Furthermore, the advanced technologies are also applicable, though more process optimization is required.

However, the channel interface quality is often considered in MG FETs as a critical issue, due to the large surface/volume ratio and multiple surface orientations of MG body. In fact, the ultra-scaled dimensions with the diameter of NW below sub-10nm can lead to QM confinement of inversion carriers, and change the transport properties of the carriers in NW FETs [2-38~2-40]. Moreover, the difference of crystallographic orientation between the top (equal to bottom) and side-wall planes may also change the carrier transport property compared to conventional planar Si MOSFETs [2-32,2-41,2-42]. Thus, the understanding of carrier transport behavior and oxide/channel interface quality is particularly important and needs experimental and theoretical investigations.

Chapter 2. Nanowire MOSFETs

2.1.2.3 High- κ dielectric/metal gate system

Success of Si MOSFET has proceeded from the excellent MOS structure with the interface of Si/SiO₂. However, as a consequence of aggressively MOSFET downscaling, the replacement of SiO₂ by dielectric with higher permittivity (high- κ) is imperative in order to prevent the excess gate leakage current by enlarged quantum-mechanical tunneling effect. A relationship of physical thickness between SiO₂ (T_{SiO_2}) and the alternative high- κ dielectric (T_{high-k}) with same gate capacitance C_{ox} is described as:

$$C_{ox} = \frac{\epsilon_0 \epsilon_{SiO_2}}{T_{SiO_2}} = \frac{\epsilon_0 \epsilon_{high-k}}{T_{high-k}} \quad (2-20)$$

where ϵ_{SiO_2} is the relative permittivity of silicon dioxide, and ϵ_{high-k} is the relative permittivity of high- κ dielectric. A high dielectric constant thereby allows physically thicker layer to obtain the same C_{ox} than the required T_{SiO_2} . The required T_{SiO_2} is called the equivalent oxide thickness (EOT), and is given by:

$$EOT = \frac{\epsilon_{SiO_2}}{\epsilon_{high-k}} T_{high-k} \quad (2-21)$$

Effectiveness of the high- κ dielectric is interpreted by using the EOT, *i.e.* the gate leakage current is reduced with the high- κ dielectric due to thicker T_{high-k} , while a small EOT is maintained.

To select a good alternative, a number of considerations are required; high dielectric constant, large band gap and band offset to channel material, thermodynamic stability, process compatibility, reliability, and interface quality. SiO₂ is an excellent gate dielectric in terms of band gap and band offset to Si, since the band gap is 9eV and is roughly intermediately placed around Si band gap with 1.1eV thus forming high barriers for both electrons and holes. Most of high- κ dielectric candidates has smaller band gap than the 9eV of SiO₂, and some indicates considerably worse band offsets and symmetry as shown in Fig.2-12 [2-43~2-45]. Moreover, excessively high dielectric constant is ineligible because of a trade-off relationship between the dielectric constant and the band gap as shown in Fig.2-13 [2-43~2-45].

Chapter 2. Nanowire MOSFETs

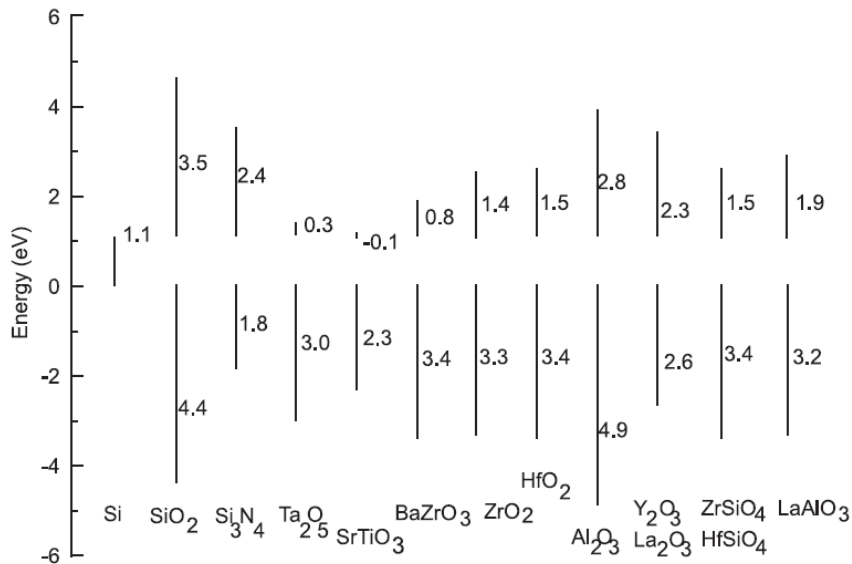


Fig. 2-12. Conduction and valence band offsets for various dielectrics [2-43~2-45].

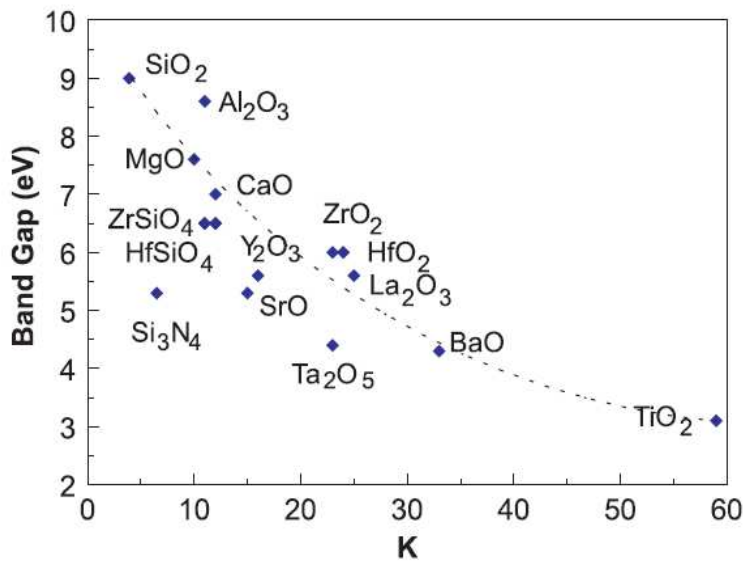


Fig. 2-13. Band gap energy as a function of relative permittivity for various dielectrics [2-43~2-45].

Hf-based oxides have been widely and intensively investigated as attractive high- κ dielectrics due to the good trade-off between the dielectric constant and the band gap, as shown in Figs.2-12 and 2-13. Firstly, Hafnium dioxide (HfO₂) has been focused significantly, but the oxide is difficult to etch [2-46], and reacts with the gate electrode

Chapter 2. Nanowire MOSFETs

[2-47,2-48]. Furthermore, HfO_2 is typically amorphous like SiO_2 , however through thermal process in the FET fabrication, the oxide becomes crystalline or poly-crystalline. The poly-crystalline oxide is undesirable, since the dielectric is composed of grains [2-49]. The grains can generate large dispersion of the dielectric property, due to the randomly varied size, orientation, and number in each oxide film. In addition, boundary of the grains possibly makes defects trapping/de-trapping carriers and large leakage current path. These drawbacks can be suppressed by forming hafnium silicate ($\text{Hf}_x\text{Si}_{1-x}\text{O}_2$ or HfSiO). To achieve more thermal stability, nitrogen-incorporated hafnium silicate, hafnium silicon oxy-nitride (HfSiON), has been proposed. Both reliability and dielectric constant enhancements by the Hf-N bonds were reported [2-46,2-50,2-51].

In conventional gate stack with SiO_2 , highly-doped poly-Si gate is used due to good compatibility in device fabrication process. The poly-Si gate similarly behaves as metal due to modulated Fermi level near conduction or valence bands by ion implantation. This technique is greatly advantageous for tuning of threshold voltage V_t of MOSFET. However, depletion of the poly-Si gate leading to the spurious C_{ox} measurement (smaller than the net value) is non-negligible with FET downscaling (cf. Fig.2-8). The dopant penetration to gate dielectric is also a problem. Therefore, an appropriate metal gate is also necessary to further scaled MOSFET. For integration, not only metal work function corresponding to Fermi level, which is basically intrinsic property in each metal, but also thermodynamic stability and process compatibility must be taken into account.

Large efforts to integrate high- κ dielectrics and metals as the gate stack system in CMOS devices have been made. Today TiN metal gate has been applied worldwide due to the good stability and compatibility [2-51~2-53]. Moreover, the TiN work function can be adjusted by different deposition process or thickness [2-54,2-55]. Consequently, the work function can be roughly conformed to mid-gap of Si band structure. Thus, as one of the most optimized high- κ /metal gate stack, the Hf-based oxide/TiN system is utilized. Negative impacts of high- κ /metal gate integration in MOSFETs (degraded inversion carrier mobility and reliability [2-56~2-58]) and the solutions have been also investigated. Most detrimental effects in advanced Hf-based high- κ /TiN devices are ascribed to nitridation processes such as the TiN deposition rather than high- κ dielectric

Chapter 2. Nanowire MOSFETs

processes [2-59].

2.1.2.4 Strain technology

Strain introduction to the channel material has been considered as one of the most attractive solutions to improve the I_{ON}/I_{OFF} ratio, transconductance, and carrier mobility against the downscaling limits of MOSFETs [2-60,2-61]. For NMOS, largely improved electron mobility and lower threshold voltage V_t are achieved by introducing in plane tensile strain in the channel [2-62,2-63]. The enhancement of electron mobility and the V_t lowering results from splitting of the conduction band [2-64~2-69], as shown in Fig.2-14. The tensile strain separates the six-fold degenerate valleys in unstrained Si into two groups; four-fold ($\Delta 4$) valleys with higher energy and two-fold ($\Delta 2$) valleys with lower energy. The $\Delta 2$ valleys lead to decrease of the averaged conductivity mass owing to the preferential occupancy with lighter conductivity mass than $\Delta 4$ valleys. Furthermore, intervalley phonon scattering between the $\Delta 2$ and $\Delta 4$ valleys is suppressed due to the energy splitting. The latter contribution can be expressed as follows:

$$\frac{1}{\tau_{phonon}} \propto \Delta E \quad (2-22)$$

where τ_{phonon} is relaxation time due to intervalley phonon scattering and ΔE is the energy splitting between the $\Delta 2$ and $\Delta 4$ valleys of the Si conduction band. The scattering rate decreases as the energy splitting enlarges due to the applied tensile stress in NMOS case. Recently, tensile strained SOI (sSOI) has been proposed as a powerful technology for enhancement of NMOS FET performance with combination of each advantage in SOI and tensile strain technologies [2-8,2-70].

For PMOS, significantly higher hole mobility and lower V_t are obtained from introduction of in plane compressive strain in the channel [2-71~2-73]. The improvement stems from unraveled $\Delta 2$ degeneracy to heavy and light holes (HH and LH) bands in the valence band [2-74] (Fig.2-14). The light hole band provides reduced conductivity mass. In addition, intervalley (interband) phonon scattering is suppressed by the degeneracy resolution. Uniaxially compressive strained Si channel has been obtained by embedded SiGe-S/D formation [2-75] (cf. Fig.1-4). For future high-performance CMOS node, strained SiGe-on-insulator (SGOI) structure is a serious

Chapter 2. Nanowire MOSFETs

alternative technology [2-76,2-77]. In addition, a contact-stop-etch-layer (CESL) deposition has been also used as a uniaxial stressor for either tensile or compressive strain depending on the deposition conditions [2-78].

As a consequence, the use of strain technology is thought as an efficient booster to reduce power consumption by lowering the supply voltage without losing circuit performance. At the same time, influence to the oxide/channel interface quality and reliability from the stress technologies would be an issue. Thus, the understanding of comprehensive oxide/channel interface characteristics is absolutely imperative.

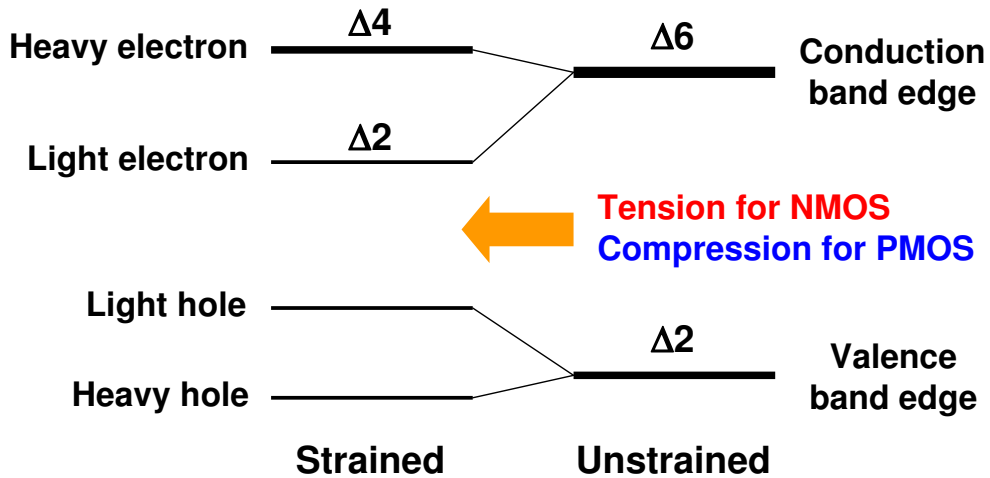


Fig. 2-14. Diagram of degenerate conduction and valence bands splitting owing to strain effect.

Chapter 2. Nanowire MOSFETs

2.2 Our nanowire devices

2.2.1 Process step overview

Our NW FETs were fabricated starting from 300nm (001) SOI or sSOI wafers with \approx 10-15nm Si layer and 145nm BOX, and following the process steps given in [Fig.2-15](#). FD-SOI-based device fabrication results in an undoped *i.e.* high purity channel. For PMOS enhancement, a process to form SGOI was performed in some SOI wafers. The devices have been patterned by using the top-down approach, consisting of mesa isolation and hybrid DUV/e-beam lithography followed by a resist trimming process [2-32,2-79~2-83]. It was carried out in order to achieve NW structures as narrow as 10nm (top-view width). A Hf-based high- κ /metal gate stack (HfSiON/TiN) was then processed. After the gate patterning, first nitrided spacer (SiN) was formed, and then raised S/D were realized by epitaxial Si (or SiGe for PMOS improvement), in order to get low parasitic resistance. Next, S/D implantation with phosphorus for NMOS and with boron for PMOS, respectively, was performed in twice. By the first lightly doped drain (LDD) and second highly doped drain (HDD) implantation processes, SCE and hot-carrier generation are effectively reduced. Compressive CESL was deposited to enhance the performance in some PMOS devices. After dopants activation and silicidation of S/D regions, the fabrication ended with a standard back-end of line (BEOL) process.

Chapter 2. Nanowire MOSFETs

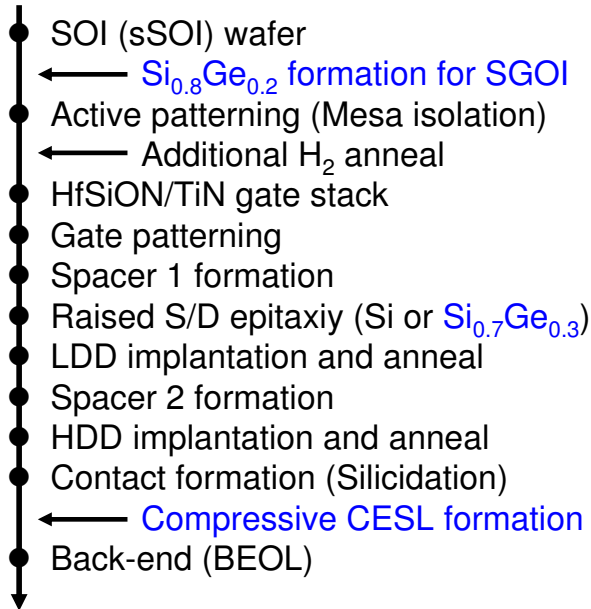


Fig. 2-15. Process integration schematic of our MOSFETs.

2.2.2 Key device parameters

2.2.2.1 Architectural splits

FET structures with varied top-view width W_{top} were fabricated from $10\mu\text{m}$ (the widest FET) down to $\approx 10\text{nm}$ (NW FET). The thickness of Si, strained-Si, and SiGe layers under the gate oxide is equivalent to the NW height (H_{NW}), which is also equal to all the device heights in each technology configuration. For the investigations, the total effective width W_{tot} is given by:

$$W_{tot} = N_{ch} (W_{top} + 2H_{NW}) \quad (2-23)$$

where N_{ch} is number of parallel channel fingers (1 or 50 in this work). The gate length L_g was processed from $10\mu\text{m}$ down to 17nm .

The conduction in [110]-oriented NW takes place in (001) top surface and (-110) left- and right-side surfaces (side-walls), respectively. On the other hand, in [100]-oriented NWs fabricated by 45° -rotated process, both top and side-walls have the same conduction as (100) surface.

Chapter 2. Nanowire MOSFETs

2.2.2.2 High- κ /metal gate stack

All the devices have a high- κ /metal gate (HfSiON/TiN) stack consisting of $\approx 2.5\text{nm}$ HfSiON deposited by chemical vapor deposition (CVD), and 5nm TiN deposited by atomic layer deposition (ALD) with capped 50nm poly-Si. Note that a $\approx 0.8\text{nm}$ SiO_2 interfacial layer (IL) between the body and HfSiON was formed. This leads to $\text{EOT} \approx 1.2\text{-}1.3\text{nm}$ calculated by Eqs. (2-13), (2-20), and (2-21). The EOT value is maintained from conventional 2D FETs down to 50-channel NW FETs for both N- and PMOS cases (cf. Section 3.1.2, “ C_{gc} - V_g measurement”).

2.2.2.3 Additional H_2 anneal

Additional hydrogen anneal has been performed to obtain a circular-like cross-sectional shape of the NW channel. By applying this process, Ω -gate and GAA architectures with rounded corner (semi-circular shape) have been fabricated [2-34,2-84,2-85]. The H_2 annealing was processed before the gate stack formation.

2.2.2.4 Strained-SOI (sSOI) devices for NMOS

To introduce tensile strain in the Si channel, a method using $\text{Si}_{1-x}\text{Ge}_x$ strained-relaxed buffer (SRB) layer has been widely applied in [2-60~2-69]. A schematic of strained Si/SiGe SRB/Si substrate or BOX is illustrated in Fig.2-16a [2-86]. Crystalline Si and crystalline Ge have the same lattice structure (diamond structure), but the size of Ge atoms is larger and the lattice constant is 4.2% greater (5.66\AA) than crystalline Si (5.43\AA). SiGe alloys thus have a lattice constant between those of Si and Ge, and the value can be tuned selectively by adjusting the ratio of Ge content. When a thin Si layer is epitaxially grown on a relaxed SiGe layer, the Si atoms attempt to perfectly align with the SiGe lattice without crystalline defects (Fig.2-17 [2-61]). The lattice constant difference between Si and Ge is too large, and Si epitaxy on Ge is imperfect in practice. As a consequence of parallel stretch of the thin Si layer, tensile strained-Si (sSi) layer can be fabricated on the SiGe virtual substrate. Today, tensile strained SOI (sSOI) without the SiGe SRB layer is being explored in order to achieve the combination of enhanced performances by FD-SOI and tensile sSi [2-8,2-80,2-87~2-89]. It is also known as another name, strained Si directly on insulator

Chapter 2. Nanowire MOSFETs

(SSDOI).

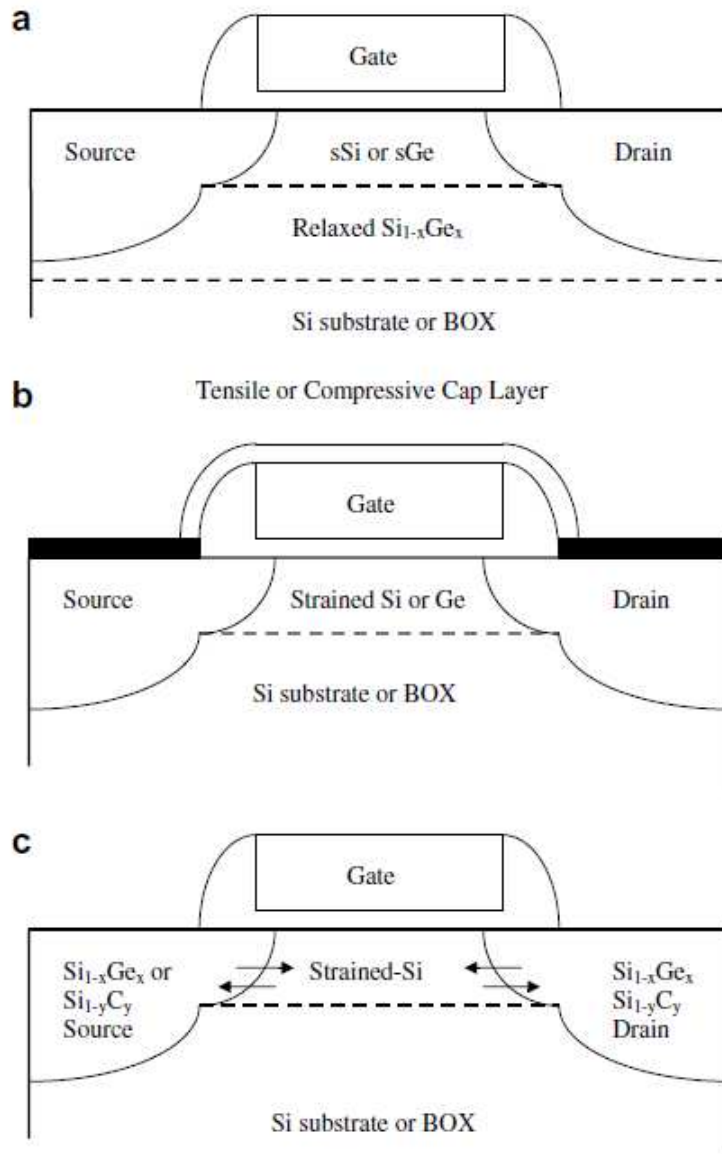


Fig. 2-16. Schematic representation of the different strain-engineering approaches: (a) global strain, using a tensile strained (sSi) ($x<0.5$) or compressively strained-Ge (sGe) ($x>0.5$) fabricated on a silicon or SOI substrate. The sSi or sGe layer may be directly on the BOX; (b) local tensile or compressive stress induced by a SiN cap layer in the Si, Ge or Si_{1-x}Ge_x channel; (c) local tensile or compressive strain induced by embedded Si_{1-y}C_y or Si_{1-x}Ge_x source/drain regions [2-86].

Chapter 2. Nanowire MOSFETs

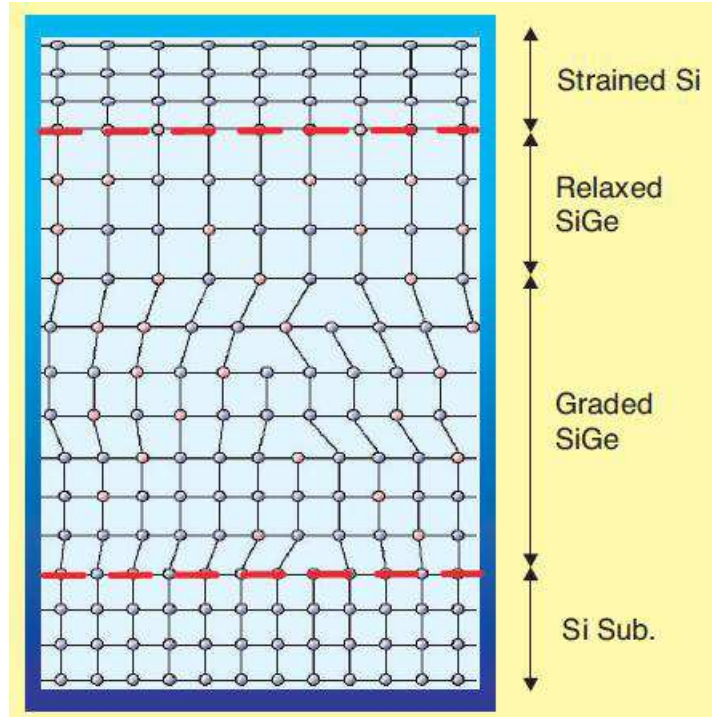


Fig. 2-17. The lattice arrangement of strained Si layer on the virtual $\text{Si}_{1-x}\text{Ge}_x$ substrate structures with increasing the Ge concentration in steps or linearly [2-61].

Our sSOI substrate is based on a standard Smart CutTM technology (cf. Fig.2-6). This can thus be realized with transfer of a strained Si film grown on donor wafer onto handle wafer, and can maintain the strain integrity. Figure 2-18 shows the process flow of sSOI wafer fabrication [2-89]. Oxidation of handle wafer is adjusted as targeted BOX layer thickness. On the other hand, sSi layer is successively created by using SiGe SRB and sSi epitaxy steps in donor wafer. Ge content and relaxation rate of the SiGe allows to tune the stress value in the sSi wafer. The steps, ion implantation, cleaning, bonding, and splitting, are all based on Smart CutTM technology (cf. Section 2.1.2.1, “FD-SOI devices”). The sSOI fabrication process is finished with removal of the SiGe layer by selective etching.

Chapter 2. Nanowire MOSFETs

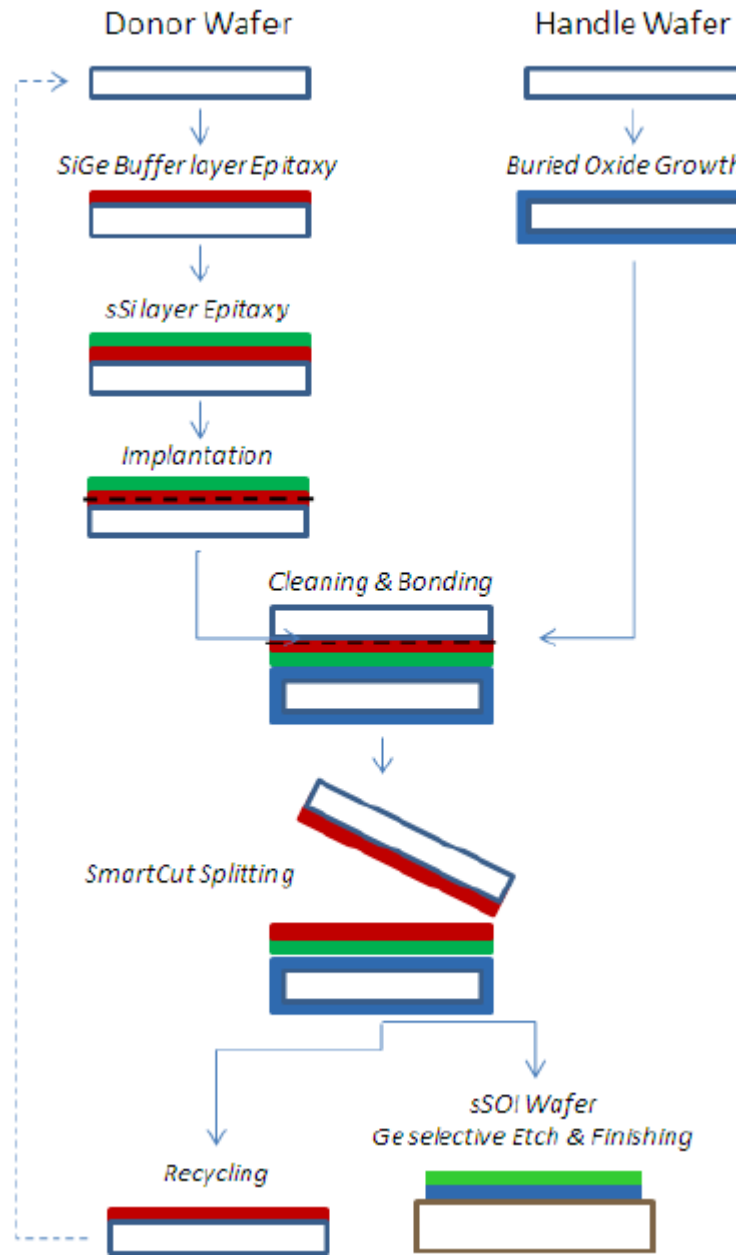


Fig. 2-18. Process schematics of sSOI substrate preparation [2-89].

In sSOI substrate used in this work, a biaxial tensile stress $\sigma_{\text{stress}} \approx 1.4 \text{ GPa}$ has been initially introduced, corresponding to a virtual substrate with 20% Ge. NWs processed on the sSOI wafer have finally a uniaxial tensile strain along the channel direction due to lateral strain relaxation [2-79,2-81,2-82], as illustrated in Fig.2-19.

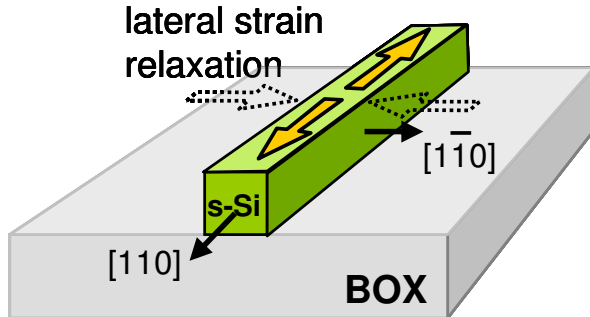


Fig. 2-19. Schematic of lateral strain relaxation occurred in sSOI TGNW structure.

2.2.2.5 SiGe-on-insulator (SGOI) for PMOS

Compressively strained SiGe layer sitting directly on BOX, *i.e.* SiGe-on-insulator (SGOI) [2-76,2-77,2-90~2-95], has been fabricated by Ge condensation technique [2-96,2-97]. The technique enables to achieve thin and fully strained SGOI substrate with low defect rate. Fabrication process of the compressively-strained SGOI starts from $\text{Si}_{1-x}\text{Ge}_x$ film epitaxy by CVD on blanket SOI wafer with 145nm BOX. Then, the SiGe layer is capped by 2nm Si. Next, a dry oxidation is carried out to diffuse Ge atoms towards the bottom of Si film in SOI wafer and consume the Si atoms. As a consequence, the total semiconductor thickness (Si+SiGe layers) decreases while the average Ge content increases when the oxidation duration is prolonged. The oxidation is finally stopped to obtain the enriched unitary $\text{Si}_{1-x}\text{Ge}_x$ layer with initial thickness and Ge concentration x or thinner film with more condensed Ge ratio (Fig.2-20). Our $\text{Si}_{1-x}\text{Ge}_x\text{OI}$ substrates have been fabricated with Ge content of 20% ($x=0.2$). Cross-sectional TEM image of the final $\text{SiO}_2/\text{SiGe}/\text{BOX}$ structure shown in Fig.2-21 exhibits a good crystalline lattice quality [2-95]. The initial biaxial stress in $\text{Si}_{0.8}\text{G}_{0.2}\text{OI}$ sample corresponds to $\sigma_{\text{stress}} \approx -1.2\text{GPa}$ and is laterally relaxed to a uniaxial compressive stress in NW structures.

Chapter 2. Nanowire MOSFETs

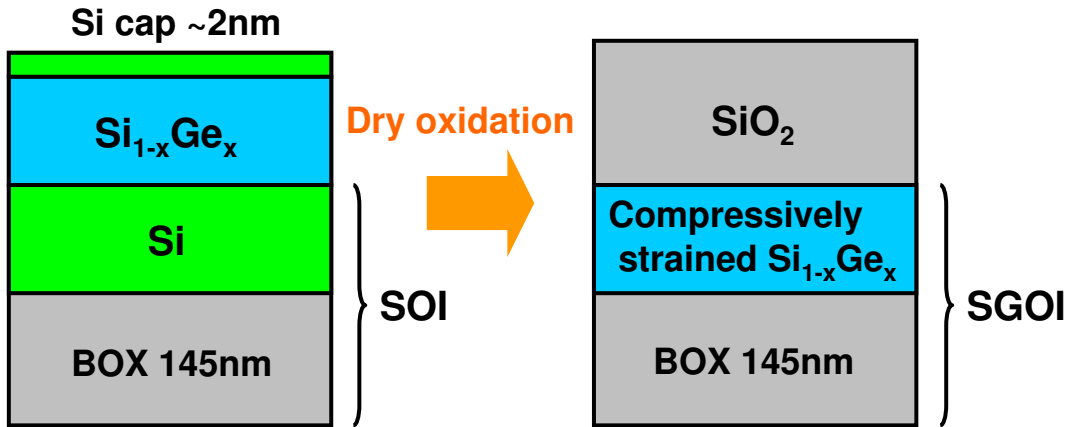


Fig. 2-20. Schematic of SGOI substrate preparation by Ge condensation technique. The initial pre-structure with SiGe on SOI finally becomes enriched and compressive strained SGOI by dry oxidation.

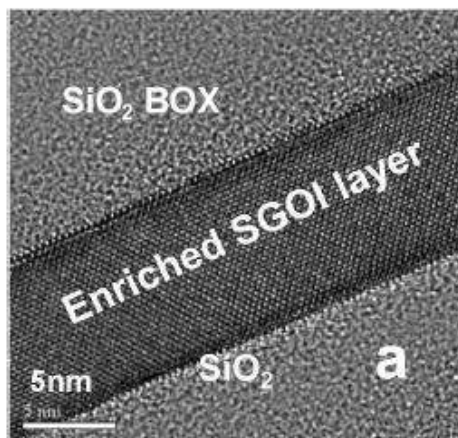


Fig. 2-21. Cross-sectional TEM picture of final SiO₂/SiGe/BOX structure after Ge condensation process [2-95].

2.2.2.6 Additional strain sources: SiGe source/drain and CESL

For some PMOS devices, a longitudinal uniaxial compressive strain by raised SiGe S/D and CESL formations was additionally introduced to the Si channel. [Figure 2-16b and c](#) sketches the use of CESL or embedded SiGe S/D resulting in a uniaxial strain in the channel [2-86].

The CESL consisting of SiN_x is deposited after the S/D formation and silicidation processes. The tensile and compressive CESL deposition is processed on NMOS and

Chapter 2. Nanowire MOSFETs

PMOS FETs, respectively, to effectively enhance the performance in short channel devices [2-98,2-99], even for MG FETs [2-100~2-102].

The use of $\text{Si}_{1-x}\text{Ge}_x$ S/D was firstly proposed for higher boron activation, the abrupt junction profile, and reduced external resistance [2-75]. Meanwhile SiGe S/D provides PMOS performance enhancement owing to significant uniaxial compression in the Si channel [2-103~2-106]. The SiGe S/D in our devices was formed by boron doped $\text{Si}_{1-x}\text{Ge}_x$ epitaxy resulting in $\text{Si}_{0.7}\text{Ge}_{0.3}$ with boron dopant. Figure 2-22 shows a TEM picture of the $\text{Si}_{0.8}\text{Ge}_{0.2}$ channel and raised $\text{Si}_{0.7}\text{Ge}_{0.3}$ S/D with perfect interface in Ω -gate NW FET [2-95].

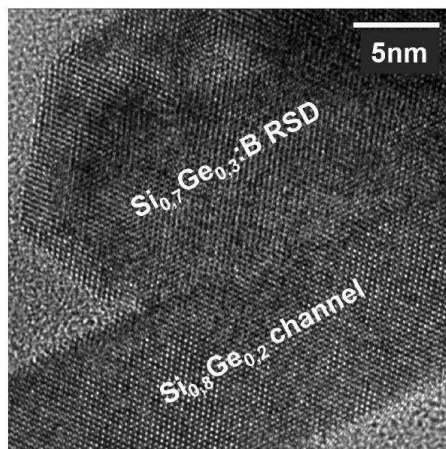


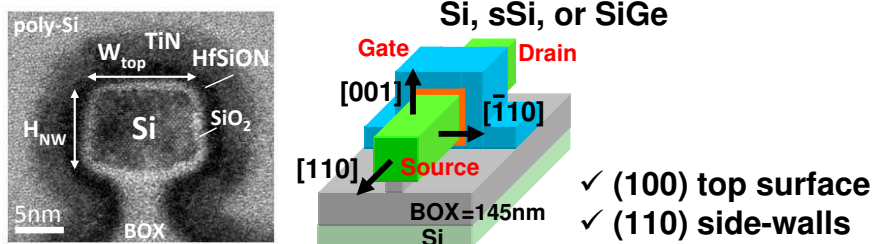
Fig. 2-22. Cross-sectional TEM image of a perfect interface between $\text{Si}_{0.8}\text{Ge}_{0.2}$ channel and raised $\text{Si}_{0.7}\text{Ge}_{0.3}$ S/D with doped B in Ω -gate NW FET [2-95].

2.2.3 Descriptions of all the device parameters

MOSFETs with various structural and technological parameters were fabricated based on FD-SOI technology. Schematic and cross-sectional TEM image of [110]- and [100]-oriented NW MOSFETs are shown in Fig.2-23. Device characterizations were performed on basic carrier transport properties (I_d - V_g , effective mobility, low-field mobility) (cf. Chapter 3) and low-frequency noise measurements (cf. Chapter 4).

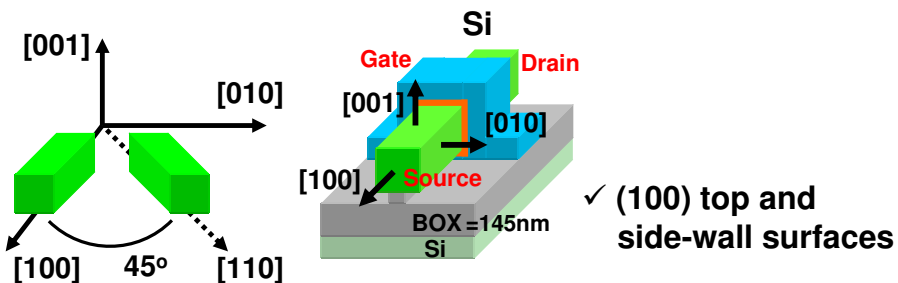
Chapter 2. Nanowire MOSFETs

✓ [110]-oriented Ω-gate nanowire



✓ (100) top surface
✓ (110) side-walls

✓ [100]-oriented Ω-gate nanowire



✓ (100) top and side-wall surfaces

Fig. 2-23. Schematic and cross-sectional TEM image of Ω-gate NW MOSFETs.

NMOS FETs with 4-types of technological device parameters have been studied in this thesis: reference SOI with [110]-oriented channel, [110]-channel SOI with additional H_2 anneal process, SOI with [100]-oriented channel, and tensile strained SOI (sSOI) with [110]-channel. The different splits are summarized in [Table 2-1](#) with architectural parameters, H_{NW} and W_{top} .

On the other hand, 6-types of PMOS FETs have been investigated: reference SOI, SOI with additional H_2 anneal process (SOI- H_2A), SOI with raised $\text{Si}_{0.7}\text{Ge}_{0.3}$ -S/D (nSG-S/D), SOI with SiGe-S/D and additional compressive CESL (cSG-S/D), compressively strained $\text{Si}_{0.8}\text{Ge}_{0.2}\text{OI}$ (nSGOI), and SGOI with compressive CESL (cSGOI). All PMOS FETs have been processed with [110]-oriented channel. Each of the devices was briefly named (noted in brackets), and these are summarized in [Table 2-2](#).

Other multiple-channel tri-gate and Ω-gate NWs, fabricated with a previous process mask, were also used for the purpose of our effective mobility study (cf. Section 3.2.2).

Chapter 2. Nanowire MOSFETs

Table 2-1. Summary of all our technological and architectural parameters for NMOS.

Ω -gate NW NMOS FETs	Channel		H_2 anneal	NW height H_{NW}	Narrowest NW top width W_{top}
	Material	Direction			
Reference SOI	Si	[110]	No	11nm	13nm
SOI with H_2 anneal	Si	[110]	Yes	10nm	11nm
[100]-oriented SOI	Si	[100]	No	10nm	10nm
Strained-SOI (sSOI)	sSi	[110]	No	11nm	11nm

Table 2-2. Summary of all our technological and architectural parameters for PMOS.

[110]-oriented Ω -gate PMOS	Undoped channel	Raised S/D with B dope	C- CESL	H_2 anneal	NW height H_{NW}	Narrowest NW top width W_{top}
SOI	Si	Si	No	No	13.5nm	17nm
SOI- H_2 A	Si	Si	No	Yes	12nm	11nm
nSG-S/D	Si	$Si_{0.7}Ge_{0.3}$	No	No	9.5nm	14nm
cSG-S/D	Si	$Si_{0.7}Ge_{0.3}$	Yes	No	13.5nm	17nm
nSGOI	$Si_{0.8}Ge_{0.2}$	$Si_{0.7}Ge_{0.3}$	No	No	11.5nm	13nm
cSGOI	$Si_{0.8}Ge_{0.2}$	$Si_{0.7}Ge_{0.3}$	Yes	No	11.5nm	13nm

Chapter 2. Nanowire MOSFETs

2.3 References

- [2-1] I. Ferain, C. A. Colinge, and J.-P. Colinge, “Multigate transistors as the future of classical metal-oxide-semiconductor field-effect transistors,” *Nature*, vol. 479, pp. 310-316, 2011.
- [2-2] S. M. Sze and K. K. Ng: *Physics of Semiconductor Devices*, 3rd Edition, Wiley, Hoboken, 2006.
- [2-3] Y. Taur and T. K. Ning: *Fundamentals of modern VLSI devices*, 2nd Edition, Cambridge Univ. Press, Cambridge, 2009.
- [2-4] W. L. Brown, “N-type surface conductivity on p-type germanium”, *Phys. Rev.*, vol. 91, pp. 518-527, 1953.
- [2-5] A. Ortiz-Conde, J. Rodríguez, F. J. García Sánchez, and J. J. Liou, “An improved definition for modeling the threshold voltage of MOSFETs”, *Solid-State Electron.*, vol. 42, pp. 1743-1746, 1998.
- [2-6] J.-P. Colinge, “Subthreshold slope of thin-film SOI MOSFET’s,” *IEEE Electron Device Lett.*, vol. 7, pp. 244-246, 1986.
- [2-7] A. J. Auberton-Hervé, “SOI: materials to systems,” *IEDM Tech. Dig.*, 1996, pp. 3-10.
- [2-8] G. Celler, and M. Wolf, “Smart CutTM; A guide to the technology, the process, the products,” SOITEC, 2003. [Online] Available: http://soitec.com/pdf/SmartCut_WP.pdf (accessed on 30 June 2014)
- [2-9] X. Cauchy, “Forecasted impact of fully depleted SOI technology on design,” SOI industry consortium news, 2010. [Online] Available: http://www.soiconsortium.org/pdf/fullydepletedsoi/SOIconsortium_FDSOI_design.pdf (accessed on 30 June 2014)
- [2-10] X. Cauchy and F. Andrieu, “Questions and answers on fully depleted SOI technology; for next generation CMOS node,” SOI industry consortium, 2010. [Online] Available: http://www.soiconsortium.org/pdf/fullydepletedsoi/SOIconsortium_FDSOI_QA.pdf (accessed on 30 June 2014)
- [2-11] X. Cauchy, H. Mendez, T. Skotnicki, O. Faynot, and C. Mazuré, “Fully depleted SOI; Designed for low power,” SOI industry consortium, 2010. [Online] Available: http://www.soiconsortium.org/pdf/White_paper_FDSOI_Designed_for_low_power.pdf (accessed on 30 June 2014)
- [2-12] J.-P. Colinge, “Fully-depleted SOI CMOS for analog applications,” *IEEE Trans. Electron Devices*, vol. 45, pp. 1010-1016, 1998.

Chapter 2. Nanowire MOSFETs

- [2-13] D. Frandre, J. -P. Colinge, J. Chen, D. De Ceuster, J. P. Eggermont, L. Ferreira, B. Gentinne, P. G. A. Jespers, A. Viviani, R. Gillon, J. P. Raskin, A. Vander Vorst, D. Vanhoenacker-Janvier, and F. Silveira, “Fully-depleted SOI CMOS technology for low-voltage low-power mixed digital/analog/microwave circuits,” *Analog Integrated Circuits and Signal Processing*, vol. 21, pp. 213-228, 1999.
- [2-14] J.-T. Park and J.-P. Colinge, “Multiple-gate SOI MOSFETs: Device design guidelines,” *IEEE Trans. Electron Devices*, vol. 49, pp.2222-2229, 2002.
- [2-15] J.-P. Colinge, “Multiple-gate SOI MOSFETs,” *Solid-State Electron.*, vol. 48, pp. 897-905, 2004.
- [2-16] J.-W. Yang and J. G. Fossum, “On the feasibility of nanoscale triple-gate CMOS transistors,” *IEEE Trans. Electron Devices*, vol. 52, pp. 1159-1164, 2005.
- [2-17] J. R. Hauser, and K. Ahmed, “Characterization of ultra-thin oxides using electrical C-V and I-V measurements,” *Proc. AIP Conf.*, 1998, pp. 235-239.
- [2-18] M. Bohr and K. Mistry, “Intel’s revolutionary 22 nm transistor technology,” Intel, 2011. [Online] Available: http://download.intel.com/newsroom/kits/22nm/pdfs/22nm-details_presentation.pdf (accessed on 31 August 2014)
- [2-19] C. Auth, C. Allen, A. Blattner, D. Bergstrom, M. Brazier, M. Bost, M. Buehler, V. Chikarmane, T. Ghani, T. Glassman, R. Grover, W. Han, D. Hanken, M. Hattendorf, P. Hentges, R. Heussner, J. Hicks, D. Ingerly, P. Jain, S. Jaloviar, R. James, D. Jones, J. Jopling, S. Joshi, C. Kenyon, H. Liu, R. McFadden, B. McIntyre, J. Neirynck, C. Parker, L. Pipes, I. Post, S. Pradhan, M. Prince, S. Ramey, T. Reynolds, J. Roesler, J. Sandford, J. Seiple, P. Smith, C. Thomas, D. Towner, T. Troeger, C. Weber, P. Yashar, K. Zawadzki, and K. Mistry, “A 22nm high performance and low-power CMOS technology featuring fully-depleted tri-gate transistors, self-aligned contacts and high density MIM capacitors,” *Symp. VLSI Tech. Dig.*, 2012, pp. 131-132.
- [2-20] R.-H. Yan, A. Ourmazd, K. F. Lee, “Scaling the Si MOSFET: From bulk to SOI to bulk,” *IEEE Trans. Electron Devices*, vol. 39, 1992, pp. 1704-1710.
- [2-21] C.-W. Lee, S.-R.-N. Yun, C.-G. Yu, J.-T. Park, J.-P. Colinge, “Device design guidelines for nano-scale MuGFETs,” *Solid-State Electron.*, vol. 51, pp. 505-510, 2007.
- [2-22] T. Sekigawa and Y. Hayashi, “Calculated threshold-voltage characteristics of an XMOS transistor having an additional bottom gate,” *Solid-State Electron.*, vol. 27, pp. 827-828, 1984.
- [2-23] D. Hisamoto, T. Kaga, Y. Kawamoto, and E. Takeda, “A fully depleted lean-channel transistor (DELTA): a novel vertical ultra thin SOI MOSFET,” *IEDM Tech. Dig.*, 1989, pp. 833-836.

Chapter 2. Nanowire MOSFETs

- [2-24] X. Huang, W.-C. Lee, C. Kuo, D. Hisamoto, L. Chang, J. Kedzierski, E. Anderson, H. Takeuchi, Y.-K. Choi, K. Asano, V. Subramanian, T.-J. King, J. Bokor, and C. Hu, “Sub 50-nm FinFET: PMOS,” *IEDM Tech. Dig.*, 1999, pp. 67-70.
- [2-25] X. Baie, J.-P. Colinge, V. Bayot, and E. Grivei, “Quantum-wire effects in thin and narrow SOI MOSFETs,” Proc. *IEEE Int. SOI Conf.*, 1995, pp. 66–67.
- [2-26] B. S. Doyle, S. Datta, M. Doczy, S. Hareland, B. Jin, J. Kavalieros, T. Linton, A. Murthy, R. Rios, and R. Chau, “High performance fully-depleted tri-gate CMOS transistors,” *IEEE Electron Device Lett.*, vol. 24, pp. 263-265, 2003.
- [2-27] J. T. Park, J.-P. Colinge, C. H. Diaz, “Pi-gate SOI MOSFET,” *IEEE Electron Device Lett.*, vol. 22, pp. 405-406, 2001.
- [2-28] F.-L. Yang, H.-Y. Chen, F.-C. Chen, C.-C. Huang, C.-Y. Chang, H.-K. Chiu, C.-C. Lee, C.-C. Chen, H.-T. Huang, C.-J. Chen, H.-J. Tao, Y.-C. Yeo, M.-S. Liang, and C. Hu, “25 nm CMOS omega FETs,” *IEDM Tech. Dig.*, 2002, pp. 255-258.
- [2-29] J.-P. Colinge, M. H. Gao, A. Romano, H. Maes, and C. Claeys, “Silicon-on-insulator ‘gate-all-around device’,” *IEDM Tech. Dig.*, 1990, pp. 595-598.
- [2-30] S. D. Suk, S.-Y. Lee, S.-M. Kim, E.-J. Yoon, M.-S. Kim, M. Li, C. W. Oh, K. H. Yeo, S. H. Kim, D. S. Shin, K.-H. Lee, H. S. Park, J. N. Han, C. J. Park, J.-B. Park, D.-W. Kim, D. Park, and B. I. Ryu, “High performance 5 nm radius twin silicon nanowire MOSFET (TSNWFET): Fabrication on bulk Si wafer, characteristics, and reliability,” *IEDM Tech. Dig.*, 2005, pp. 717–720.
- [2-31] N. Singh, A. Agarwal, L. K. Bera, T. Y. Liow, R. Yang, S. C. Rustagi, C. H. Tung, R. Kumar, G. Q. Lo, N. Balasubramanian, and D.-L. Kwong, “High-performance fully depleted silicon nanowire (diameter \leq 5 nm) gate-all-around CMOS devices,” *IEEE Electron Device Lett.*, vol. 27, pp. 383-386, 2006.
- [2-32] R. Coquand, S. Barraud, M. Cassé, P. Leroux, C. Vizioz, C. Comboreou, P. Perreau, E. Ernst, M.-P. Samson, V. Maffini-Alvaro, C. Tabone, S. Barnola, D. Munteanu, G. Ghibaudo, S. Monfray, F. Boeuf, and T. Poiroux “Scaling of high-k/metal-gate trigate SOI nanowire transistors down to 10nm width,” *Proc. ULIS*, 2012.
- [2-33] T. Ernst, C. Dupré, C. Isheden, E. Bernard, R. Ritzenthaler, V. Maffini-Alvaro, J. C. Barbe, F. De Crecy, A. Toffoli, C. Vizioz, S. Borel, F. Andrieu, V. Delaye, D. Lafond, G. Rabille, J. M. Hartmann, M. Rivoire, B. Guillaumot, A. Suhm, P. Rivallin, O. Faynot, G. Ghibaudo, and S. Deleonibus, “Novel 3D integration process for highly scalable Nano-Beam stacked-channels GAA (NBG) FinFETs with HfO₂/TiN gate stack,” *IEDM Tech. Dig.*, 2006.

Chapter 2. Nanowire MOSFETs

- [2-34] E. Dornel, T. Ernst, J. C. Barbé, J. M. Hartmann, V. Delaye, F. Aussenac, C. Vizioz, S. Borel, V. Maffini-Alvaro, C. Isheden, and J. Foucher, “Hydrogen annealing of arrays of planar and vertically stacked Si nanowires,” *Appl. Phys. Lett.*, vol. 91, 233502, 2007.
- [2-35] C. Dupré, A. Hubert, S. Bécu, M. Jublot, V. Maffini-Alvaro, C. Vizioz, F. Aussenac, C. Arvet, S. Barnola, J.-M. Hartmann, G. Garnier, F. Allain, J.-P. Colonna, M. Rivoire, L. Baud, S. Pauliac, V. Loup, T. Chevolleau, P. Rivallin, B. Guillaumot, G. Ghibaudo, O. Faynot, T. Ernst and S. Deleonibus, “15nm-diameter 3D stacked nanowires with independent gates operation: ΦFET,” *IEDM Tech. Dig.*, 2008, pp. 749-752.
- [2-36] K. Tachi, M. Cassé, D. Jang, C. Dupré, A. Hubert, N. Vulliet, V. Maffini-Alvaro, C. Vizioz, C. Carabasse, V. Delaye, J. M. Hartmann, G. Ghibaudo, H. Iwai, S. Cristoloveanu, O. Faynot, and T. Ernst, “Relationship between mobility and high-k interface properties in advanced Si and SiGe nanowires,” *IEDM Tech. Dig.*, 2009, pp. 313-316.
- [2-37] K. Okano, T. Izumida, H. Kawasaki, A. Kaneko, A. Yagishita, T. Kanemura, M. Kondo, S. Ito, N. Aoki, K. Miyano, T. Ono, K. Yahashi, K. Iwade, T. Kubota, T. Matsushita, I. Mizushima, S. Inaba, K. Ishimaru, K. Suguro, K. Eguchi, Y. Tsunashima, and H. Ishiuchi, “Process integration technology and device characteristics of CMOS FinFET on bulk silicon substrate with sub-10nm fin width and 20nm gate length,” *IEDM Tech. Dig.*, 2005, pp. 725-728.
- [2-38] E. Gnani, S. Reggiani, M. Rudan, and G. Baccarani, “Effects of the Band-Structure Modification in Silicon Nanowires with Small Diameters,” *Proc. ESSDERC*, 2006, pp. 170-173.
- [2-39] M. O. Baykan, S. E. Thompson, and T. Nishida, “Strain effects on three-dimensional, two-dimensional, and one-dimensional silicon logic devices: Predicting the future of strained silicon,” *J. Appl. Phys.*, vol. 108, 093716, 2010.
- [2-40] H. Yoshioka, N. Morioka, J. Suda, and T. Kimoto, “Bandgap shift by quantum confinement effect in <100> Si-nanowires derived from threshold-voltage shift of fabricated metal-oxide-semiconductor field effect transistors and theoretical calculations,” *J. Appl. Phys.*, vol. 109, 064312, 2011.
- [2-41] J. Chen, T. Saraya, K. Miyaji, K. Shimizu, and T. Hiramoto, “Experimental study of mobility in [110]- and [100]-directed multiple silicon nanowire GAA MOSFETs on (100) SOI,” *Symp. VLSI Tech. Dig.*, 2008, pp. 32-33.

Chapter 2. Nanowire MOSFETs

- [2-42] M. Saitoh, Y. Nakabayashi, H. Itokawa, M. Murano, I. Mizushima, K. Uchida, and T. Numata, “Short-channel performance and mobility analysis of <110>- and <100>-oriented tri-gate nanowire MOSFETs with raised source/drain extensions,” *Symp. VLSI Tech. Dig.*, 2010, pp. 169-170.
- [2-43] J. Robertson, “Band offsets of wide-band-gap oxides and implications for future electronic devices,” *J. Vac. Sci. Technol. B*, vol. 18, pp. 1785-1791, 2000.
- [2-44] J. Robertson, “High dielectric constant oxides,” *Eur. Phys. J. Appl. Phys.*, vol. 28, pp. 265-291, 2004.
- [2-45] J. Robertson, “High dielectric constant gate oxides for metal oxide Si transistors,” *Rep. Prog. Phys.*, vol. 69, pp. 327-396, 2006.
- [2-46] M. R. Visokay, J. J. Chambers, A. L. P. Rotondaro, A. Shanware, and L. Colombo, “Application of HfSiON as a gate dielectric material,” *Appl. Phys. Lett.*, vol. 80, pp. 3183-3185, 2002.
- [2-47] C. H. Lee, H. F. Luan, W. P. Bai, C. H. Lee, T. S. Jeon, Y. Senzaki, D. Roberts, and D. L. Kwong, “High quality ultra thin CVD HfO₂ gate stack with poly-Si gate electrode,” *IEDM Tech. Dig.*, 2000, pp. 31-34.
- [2-48] T. Ma, S. A. Campbell, R. Smith, N. Hoilien, B. He, W. L. Gladfelter, C. Hobbs, D. Buchanan, C. Taylor, M. Gribelyuk, M. Tiner, M. Coppel, and J. J. Lee, “Group IVB metal oxides high permittivity gate insulators deposited from anhydrous metal nitrates,” *IEEE Trans. Electron Devices*, vol. 48, pp. 2348-2356, 2001.
- [2-49] J. R. Watling, A. R. Brown, G. Ferrari, J. R. Barker, G. Bersuker, P. Zeitzoff, and A. Asenov, “Impact of high-k gate stacks on transport and variability in nano-CMOS devices,” *J. Comput. Theor. Nanosci.*, 2008. vol. 5, pp. 1072-1088, 2008.
- [2-50] M. Koike, T. Ino, Y. Kamimuta, M. Koyama, Y. Kamata, M. Suzuki, Y. Mitani, A. Nishiyama, Y. Tsunashima, “Effect of Hf-N bond on properties of thermally stable amorphous HfSiON and applicability of this material to sub-50nm technology node LSIs,” *IEDM Tech. Dig.*, 2003, pp. 107-110.
- [2-51] M. A. Quevedo-Lopez, S. A. Krishnan, P. D. Kirsch, H. J. Li, J. H. Sim, C. Huffman, J. J. Peterson, B. H. Lee, G. Pant, B. E. Gnade, M. J. Kim, R. M. Wallace, D. Guo, H. Bu, and T. P. Ma, “High performance gate first HfSiON dielectric satisfying 45nm node requirements,” *IEDM Tech. Dig.*, 2005.
- [2-52] F. Lime, K. Oshima, M. Cassé, G. Ghibaudo, S. Cristoloveanu, B. Guillaumot, and H. Iwai, “Carrier mobility in advanced CMOS devices with metal gate and HfO₂ gate

Chapter 2. Nanowire MOSFETs

- dielectric,” *Solid-State Electron.*, pp. 1617-1621, 2003.
- [2-53] T. Ando, M. M. Frank, K. Choi, C. Choi, J. Bruley, M. Hopstaken, M. Copel, E. Cartier, A. Kerber, A. Callegari, D. Lacey, S. Brown, Q. Yang, and V. Narayanan, “Understanding mobility mechanisms in extremely scaled HfO₂ (EOT 0.42 nm) using remote interfacial layer scavenging technique and V_t-tuning dipoles with gate-first process,” *IEDM Tech. Dig.*, 2009.
- [2-54] K. Choi, H.-C. Wen, H. Alshareef, R. Harris, P. Lysaght, H. Luan, P. Majhi, and B.H. Lee, “The effect of metal thickness, overlayer and high-k surface treatment on the effective work function of metal electrode,” *Proc. ESSDERC*, 2005, pp. 101-104.
- [2-55] M. Charbonnier, C. Leroux, V. Cosnier, P. Besson, E. Martinez, N. Benedetto, C. Licitra, N. Rochat, C. Gaumer, K. Kaja, G. Ghibaudo, F. Martin, G. Reimbold, “Measurement of dipoles/roll-off /work functions by coupling CV and IPE and study of their dependence on fabrication process,” *IEEE Trans. Electron Devices*, vol. 57, pp. 1809-1819, 2010.
- [2-56] M. Cassé, L. Thevenod, B. Guillaumot, L. Tosti, F. Martin, J. Mitard, O. Weber, F. Andrieu, T. Ernst, G. Reimbold, T. Billon, M. Mouis, and F. Boulanger, “Carrier transport in HfO₂/metal gate MOSFETs: physical insight into critical parameters,” *IEEE Trans. Electron Devices*, vol. 53, pp. 759-768, 2006.
- [2-57] X. Garros, M. Cassé, G. Reimbold, F. Martin, C. Leroux, A. Fanton, O. Renault, V. Cosnier, and F. Boulanger, “Guidelines to improve mobility performances and BTI reliability of advanced high-k/metal gate stacks,” *Symp. VLSI Tech. Dig.*, 2008, pp. 68-69.
- [2-58] X. Garros, M. Cassé, M. Rafik, C. Fenouillet-Béranger, G. Reimbold, F. Martin, C. Wiemer, and F. Boulanger, “Process dependence of BTI reliability in advanced HK MG stacks,” *Microelectron. Reliab.*, vol. 49, pp. 982-988, 2009.
- [2-59] M. Cassé, X. Garros, O. Weber, F. Andrieu, G. Reimbold, and F. Boulanger, “A study of N-induced traps due to a nitrided gate in high-k/metal gate nMOSFETs and their impact on electron mobility,” *Solid-State Electron.*, vol. 65-66, pp. 139-145, 2011.
- [2-60] M. L. Lee, E. A. Fitzgerald, M. T. Bulsara, M. T. Currie, and A. Lochtefeld, “Strained Si, SiGe, and Ge channels for high-mobility metal-oxide-semiconductor field-effect transistors,” *J. Appl. Phys.*, vol. 97, 011101, 2005.
- [2-61] C. W. Liu, S. Maikap, and C.-Y. Yu, “Mobility - enhancement technologies,” *IEEE Circuits and Devices Magazine*, vol. 21, pp. 21-36, 2005.
- [2-62] F. Schaffler, D. Tobben, H.-J. Herzog, G. Abstreiter, and B. Hollander, “High-electron mobility Si/SiGe heterostructures: Influence of the relaxed SiGe buffer layer,” *Semicond.*

Chapter 2. Nanowire MOSFETs

- Sci. Technol.*, vol. 7, pp. 260-261, 1992.
- [2-63] J. Welser, J. L. Hoyt, and J. F. Gibbons, “NMOS and PMOS transistors fabricated in strained silicon/relaxed silicon-germanium structures,” *IEDM Tech. Dig.*, 1992, pp. 1000-1002.
 - [2-64] D. V. Lang, R. People, J. C. Bean, and A. M. Sergent, “Measurement of the band gap $\text{Ge}_x\text{Si}_{1-x}/\text{Si}$ strained-layer heterostructures,” *Appl. Phys. Lett.*, vol. 47, pp. 1333-1335, 1985.
 - [2-65] Th. Vogelsang and K. R. Hofmann, “Electron mobilities and high-field drift velocities in strained silicon on silicon-germanium substrates,” *Trans. Electron Devices*, vol. 39, pp. 2641-2642, 1992.
 - [2-66] Th. Vogelsang and K. R. Hofmann, “Electron transport in strained Si layers on $\text{Si}_{1-x}\text{Ge}_x$ substrates,” *Appl. Phys. Lett.*, vol. 63, pp. 186-188, 1993.
 - [2-67] J. Welser, J. L. Hoyt, S. Takagi, and J. F. Gibbons, “Strain dependence of the performance enhancement in strained-Si n-MOSFETs,” *IEDM Tech. Dig.*, 1994, pp. 373-376.
 - [2-68] M. V. Fischetti and S. E. Laux, “Comparative study of phononlimited mobility of twodimensional electrons in strained and unstrained Si metal-oxide-semiconductor fieldeffect transistors,” *J. Appl. Phys.*, vol. 80, pp. 1567-1577, 1996.
 - [2-69] M. V. Fischetti and S. E. Laux, “Band structure, deformation potentials, and carrier mobility in strained-Si, Ge, and SiGe alloys,” *J. Appl. Phys.*, vol. 80, pp. 2234-2252, 1996.
 - [2-70] B. Ghyselen, J.-M. Hartmann, T. Ernst, C. Aulnette, B. Osternaud, Y. Bogumilowicz, A. Abbadie, P. Besson, O. Rayssac, A. Tiberj, N. Daval, I. Cayrefourq, F. Fournel, H. Moriceau, C. Di Nardo, F. Andrieu, V. Paillard, M. Cabié, L. Vincent, E. Snoeck, F. Cristiano, A. Rocher, A. Ponchet, A. Claverie, P. Boucaud, M.-N. Semeria, D. Bensahel, N. Kernevez, and C. Mazuré, “Engineering strained silicon on insulator wafers with the Smart CutTM technology,” *Solid-State Electron.*, vol. 48, pp. 1285-1296, 2004.
 - [2-71] E. Kasper and H.-J. Herzog, “Elastic strain and misfit dislocation density in $\text{Si}_{0.92}\text{Ge}_{0.08}$ films on silicon substrates,” *Thin Solid Films*, vol. 44, pp. 357-370, 1977.
 - [2-72] R. People and J. C. Bean, “Band alignments of coherently strained- $\text{Ge}_x\text{Si}_{1-x}/\text{Si}$ heterostructures on $<001>\text{Ge}_y\text{Si}_{1-y}$ substrates,” *Appl. Phys. Lett.*, vol. 48, pp. 538-540, 1986.
 - [2-73] R. People, “Physics and applications of $\text{Ge}_x\text{Si}_{1-x}/\text{Si}$ strained layer heterostructures,” *IEEE J. Quantum Electron.*, vol. 22, pp. 1696-1710, 1986.

Chapter 2. Nanowire MOSFETs

- [2-74] T. Manku and A. Nathan, "Energy-band structure for strained p-type Si_{1-x}Ge_x," *Phys. Rev. B*, vol. 43, pp. 12634-12637, 1991.
- [2-75] S. Gannavaram, N. Pesovic, and C. Ozturk, "Low temperature (800 °C) recessed junction selective silicon-germanium source/drain technology for sub-70 nm CMOS," *IEDM Tech. Dig.*, 2000, pp. 437-440.
- [2-76] T. Tezuka, N. Sugiyama, T. Mizuno, and S. Takagi, "Ultrathin body SiGe-on-insulator pMOSFETs with high-mobility SiGe surface channels," *IEEE Trans. Electron Devices*, vol. 50, pp. 1328-1333, 2003.
- [2-77] T. Tezuka, S. Nakaharai, Y. Moriyama, N. Sugiyama, and S. Takagi, "Selectively-formed high mobility SiGe-on-insulator pMOSFETs with Ge-rich strained surface channels using local condensation technique," *Symp. VLSI Tech. Dig.*, 2004, pp. 198-199.
- [2-78] A. Shimizu, K. Hachimine, N. Ohki, H. Ohta, M. Koguchi, Y. Nonaka, H. Sato, and F. Ootsuka, "Local mechanical-stress control (LMC): A new technique for CMOS-performance enhancement," *IEDM Tech. Dig.*, 2001, pp. 433-436.
- [2-79] R. Coquand, M. Cassé, S. Barraud, P. Leroux, D. Cooper, C. Vizioz, C. Comboroure, P. Perreau, V. Maffini-Alvaro, C. Tabone, L. Tosti, F. Allain, S. Barnola, V. Delaye, F. Aussénac, G. Reimbold, G. Ghibaudo, D. Munteanu, S. Monfray, F. Boeuf, O. Faynot, and T. Poiroux, "Strain-induced performance enhancement of tri-gate and omega-gate nanowire FETs scaled down to 10nm width," *Symp. VLSI Tech. Dig.*, 2012, pp. 13-14.
- [2-80] S. Barraud, R. Coquand, M. Cassé, M. Koyama, J.-M. Hartmann, V. Maffini-Alvaro, C. Comboroure, C. Vizioz, F. Aussénac, O. Faynot, and T. Poiroux, "Performance of omega-shaped-gate silicon nanowire MOSFET with diameter down to 8 nm," *IEEE Electron Device Lett.*, vol. 33, pp. 1526-1528, 2012.
- [2-81] M. Cassé, S. Barraud, C. Le Royer, M. Koyama, R. Coquand, D. Blachier, F. Andrieu, G. Ghibaudo, O. Faynot, T. Poiroux, and G. Reimbold, "Study of piezoresistive properties of advanced CMOS transistors: thin film SOI, SiGe/SOI, unstrained and strained tri-gate nanowires," *IEDM Tech. Dig.*, 2012, pp. 637-640.
- [2-82] R. Coquand, M. Cassé, S. Barraud, D. Cooper, V. Maffini-Alvaro, M.-P. Samson, S. Monfray, F. Boeuf, G. Ghibaudo, O. Faynot, and T. Poiroux, "Strain-induced performance enhancement of tri-gate and omega-gate nanowire FETs scaled down to 10nm width," *IEEE Trans. Electron Devices*, vol. 60, pp. 727-732, 2013.

Chapter 2. Nanowire MOSFETs

- [2-83] S. Barraud, R. Coquand, V. Maffini-Alvaro, M.-P. Samson, J.-M. Hartmann, L. Tosti, M. Cassé, V.-H. Nguyen, F. Triozon, Y.-M. Niquet, C. Tabone, P. Perreau, F. Allain, C. Vizioz, C. Comboroure, F. Aussénac, S. Monfray, G. Ghibaudo, F. Boeuf, B. De Salvo, and O. Faynot, “Scaling of Ω -gate SOI nanowire N- and P-FET down to 10nm gate length: size- and orientation-dependent strain effects,” *Symp. VLSI Tech. Dig.*, 2013, pp. T230-T231.
- [2-84] K. Tachi, M. Cassé, S. Barraud, C. Dupré, A. Hubert, N. Vulliet, M. E. Faivre, C. Vizioz, C. Carabasse, V. Delaye, J. M. Hartmann, H. Iwai, S. Cristoloveanu, O. Faynot, and T. Ernst, “Experimental study on carrier transport limiting phenomena in 10 nm width nanowire CMOS transistors,” *IEDM Tech. Dig.*, 2010, pp. 784-787.
- [2-85] M. Cassé, K. Tachi, S. Thiele, and T. Ernst, “Spectroscopic charge pumping in Si nanowire transistors with a high-k/metal gate,” *Appl. Phys. Lett.*, vol. 96, 123506, 2010.
- [2-86] C. Clayes, E. Simoen, S. Put, G. Giusi, and F. Crupi, “Impact strain engineering on gate stack quality and reliability,” *Solid-State Electron.*, vol. 52, pp. 1115-1126, 2008.
- [2-87] G. Celler, and I. Cayrefourq, “Strained silicon on insulator; A quick guide to the technology, the processes, the products,” SOITEC, 2006. [Online], Available: http://www.soitec.com/pdf/StrainedSOI_WP.pdf (accessed on 30 June 2014)
- [2-88] M. Yoshimi, I. Cayrefourcq, and C. Mazuré, “Strained-SOI (sSOI) technology for high-performance CMOSFETs in 45nm-or-below technology node,” *Proc. ICSICT*, 2006, pp. 96-99.
- [2-89] W. Schwarzenbach, N. Daval, S. Kerdilès, G. Chabanne, C. Figuet, S. Guerroudj, O. Bonnin, X. Cauchy, B.-Y. Nguyen and C. Maleville, “Strained silicon on insulator substrates for fully depleted application,” *Proc. ICICDT*, 2012.
- [2-90] B. Vincent, J.-F. Damlencourt, P. Rivallin, E. Nolot, C. Licitra, Y. Morand, and L. Clavelier, “Fabrication of SiGe-on-insulator substrates by a condensation technique: an experimental and modeling study,” *Semicond. Sci. Technol.*, vol. 22, pp. 237-244, 2007.
- [2-91] L. Hutin, M. Cassé, C. Le Royer, J.-F. Damlencourt, A. Pouydebasque, C. Xu, C. Tabone, J.-M. Hartmann, V. Carron, H. Grampeix, V. Mazzocchi, R. Truche, O. Weber, P. Batude, X. Garros, L. Clavelier, M. Vinet, and O. Faynot, “20nm gate length trigate pFETs on strained SGOI for high performance CMOS,” *Symp. VLSI Tech. Dig.*, 2010, pp. 37-38.

Chapter 2. Nanowire MOSFETs

- [2-92] A. Khakifirooz, K. Cheng, T. Nagumo, N. Loubet, T. Adam, A. Reznicek, J. Kuss, D. Shahrjerdi, R. Sreenivasan, S. Ponoth, H. He, P. Kulkarni, Q. Liu, P. Hashemi, P. Khare, S. Luning, S. Mehta, J. Gimbert, Y. Zhu, Z. Zhu, J. Li, A. Madan, T. Levin, F. Monsieur, T. Yamamoto, S. Naczas, S. Schmitz, S. Holmes, C. Aulnette, N. Daval, W. Schwarzenbach, B.-Y. Nguyen, V. Paruchuri, M. Khare, G. Shahidi, and B. Doris, “Strain engineered extremely thin SOI (ETSOI) for high-performance CMOS,” *Symp. VLSI Tech. Dig.*, 2012, pp. 117-118.
- [2-93] F. Glowacki, C. Le Royer, Y. Morand, J.-M. Pédini, T. Denneulin, D. Cooper, J.-P. Barnes, P. Nguyen, D. Rouchon, J.-M. Hartmann, O. Gourhant, E. Baylac, Y. Campidelli, D. Barge, O. Bonin, and W. Schwarzenbach, “Fabrication and characterization of ultrathin (5nm) SiGe-on-insulator with high compressive strain (-2GPa),” *Proc. EuroSOI Conf.*, 2013.
- [2-94] P. Hashemi, M. Kobayashi, A. Majumdar, L. A. Yang, A. Baraskar, K. Balakrishnan, W. Kim, K. Chan, S. U. Engelmann, J. A. Ott, S. W. Bedell, C. E. Murray, S. Liang, R. H. Dennard, J. W. Sleight, E. Leobandung, and D.-G. Park, “High-performance $\text{Si}_{1-x}\text{Ge}_x$ channel on insulator trigate pFETs featuring an implant-free process and aggressively-scaled fin and gate dimensions,” *Symp. VLSI Tech. Dig.*, 2013, pp. T18-T19.
- [2-95] P. Nguyen, S. Barraud, M. Koyama, M. Cassé, F. Andrieu, C. Tabone, F. Glowacki, J.-M. Hartmann, V. Maffini-Alvaro, D. Rouchon, N. Bernier, D. Lafond, M.-P. Samson, F. Allain, C. Vizioz, D. Delprat, B.-Y. Nguyen, C. Mazuré, O. Faynot, and M. Vinet, “High mobility Ω -gate nanowire p-FET on cSGOI substrates obtained by Ge enrichment technique,” *Proc. IEEE S3S Conf.*, 2014.
- [2-96] T. Tezuka, N. Sugiyama, T. Mizuno, M. Suzuki, and S. Takagi, “A novel fabrication technique of ultrathin and relaxed SiGe buffer layers with high Ge fraction for sub-100 nm strained silicon-on-insulator MOSFETs,” *Jpn. J. Appl. Phys.*, vol. 40, pp. 2866-2874, 2001.
- [2-97] T. Tezuka, N. Sugiyama, and S. Takagi, “Fabrication of strained Si on an ultrathin SiGe-on-insulator virtual substrate with a high-Ge fraction,” *Appl. Phys. Lett.*, vol. 79, pp. 1798-1800, 2001.
- [2-98] S. E. Thompson, M. Armstrong, C. Auth, M. Alavi, M. Buehler, R. Chau, S. Cea, T. Ghani, G. Glass, T. Hoffman, C.-H. Jan, C. Kenyon, J. Klaus, K. Kuhn, Z. Ma, B. Mcintyre, K. Mistry, A. Murthy, B. Obradovic, R. Nagisetty, P. Nguyen, S. Sivakumar, R. Shaheed, L. Shifren, B. Tufts, S. Tyagi, M. Bohr, and Y. El-Mansy, “A 90-nm logic technology

Chapter 2. Nanowire MOSFETs

- featuring strained-silicon,” *IEEE Trans. Electron Devices*, vol. 51, pp. 1790-1797, 2004.
- [2-99] M. Shima, K. Okabe, A. Yamaguchi, T. Sakoda, K. Kawamura, S. Pidin, M. Okuno, T. Owada, K. Sugimoto, J. Ogura, H. Kokura, H. Morioka, T. Watanabe, T. Isome, K. Okoshi, T. Mori, Y. Hayami, H. Minakata, A. Hatada, Y. Shimamune, A. Katakami, H. Ota, T. Sakuma, T. Miyashita, K. Hosaka, H. Fukutome, N. Tamura, T. Aoyama, K. Sukegawa, M. Nakaishi, S. Fukuyama, S. Nakai, M. Kojima, S. Sato, M. Miyajima, K. Hashimoto, and T. Sugii, “High-performance low operation power transistor for 45nm node universal applications,” *Symp. VLSI Tech. Dig.*, 2006, pp. 156-157.
- [2-100] N. Collaert, A. De Keersgieter, K. G. Anil, R. Rooyackers, G. Eneman, M. Goodwin, B. Eyckens, E. Sleenckx, J.-F. de Marneffe, K. De Meyer, P. Absil, M. Jurczak, and S. Biesemans, “Performance improvement of tall triple gate devices with strained SiN layers,” *IEEE Electron Device Lett.*, vol. 26, pp. 820-822, 2005.
- [2-101] K. Shin, C. O. Chui, and T.-J. King, “Dual stress capping layer enhancement study for hybrid orientation FinFET CMOS technology,” *IEDM Tech. Dig.*, 2005.
- [2-102] S. Suthram, M. M. Hussain, H. R. Harris, C. Smith, H.-H. Tseng, R. Jammy, and S. E. Thompson, “Comparison of uniaxial wafer bending and contact-etch-stop-liner stress induced performance enhancement on double-gate FinFETs,” *IEEE Electron Device Lett.*, vol. 29, pp. 480-482, 2008.
- [2-103] S. E. Thompson, G. Sun, K. Wu, J. Lim, and T. Nishida, “A 90-nm logic technology featuring strained-silicon,” *IEDM Tech. Dig.*, 2004, pp. 221-224.
- [2-104] G. Eneman, P. Verheyen, R. Rooyackers, F. Nouri, L. Washington, R. Degraeve, B. Kaczer, V. Moroz, A. De Keersgieter, R. Schreutelkamp, M. Kawaguchi, Y. Kim, A. Samoilov, L. Smith, P. P. Absil, K. De Meyer, M. Jurczak, and S. Biesemans, “Layout impact on the performance of a locally strained PMOSFET,” *Symp. VLSI Tech. Dig.*, 2005, pp. 22-23.
- [2-105] P. Verheyen, N. Collaert, R. Rooyackers, R. Loo, D. Shamiryan, A. De Keersgieter, G. Eneman, F. Leys, A. Dixit, M. Goodwin, Y. S. Yim, M. Caymax, K. De Meyer, P. Absil, M. Jurczak, and S. Biesemans, “25% drive current improvement for p-type multiple gate FET (MuGFET) devices by the introduction of recessed $\text{Si}_{0.8}\text{Ge}_{0.2}$ in the source and drain regions,” *Symp. VLSI Tech. Dig.*, 2005, pp. 194-195.
- [2-106] B. C. Wang, S. L. Wu, C. W. Huang, Y. Y. Lu, S. J. Chang, Y. M. Lin, K. H. Lee, and O. Cheng, “Correlation between random telegraph noise and 1/f noise parameters in 28-nm pMOSFETs with tip-shaped SiGe source/drain,” *IEEE Electron Device Lett.*, vol. 33, pp. 928-930, 2012.

Chapter 3. Carrier transport characterizations

Chapter 3

Carrier transport characterizations

3.1 Methodology

- 3.1.1 I_d - V_g measurement**
- 3.1.2 C_{gc} - V_g measurement**
- 3.1.3 Mobility extraction**

3.2 Experimental results

- 3.2.1 I_d - V_g characteristics**
- 3.2.2 Temperature dependent Effective mobility**
- 3.2.3 Low-field mobility**

3.3 References

Chapter 3. Carrier transport characterizations

3.1 Methodology

3.1.1 I_d - V_g measurement

Gate voltage V_g dependent drain current I_d characteristics (I_d - V_g) were measured by a parameter analyzer Agilent B1500A for all the technological and architectural device parameters. This is the most common measurement to characterize FET performance [3-1,3-2]. DC V_g is applied from negative to positive bias conditions for NMOS (contrary, positive to negative for PMOS) to evaluate the off-state and on-state properties by monitoring the drain current I_d . Figure 3-1 shows one of the results for the narrowest single-channel NW N- and PMOS FETs with $L_g \approx 110\text{nm}$ in linear ($|V_d| = 40\text{mV}$) and saturation ($|V_d| = 0.9\text{V}$) regimes of V_d bias conditions.

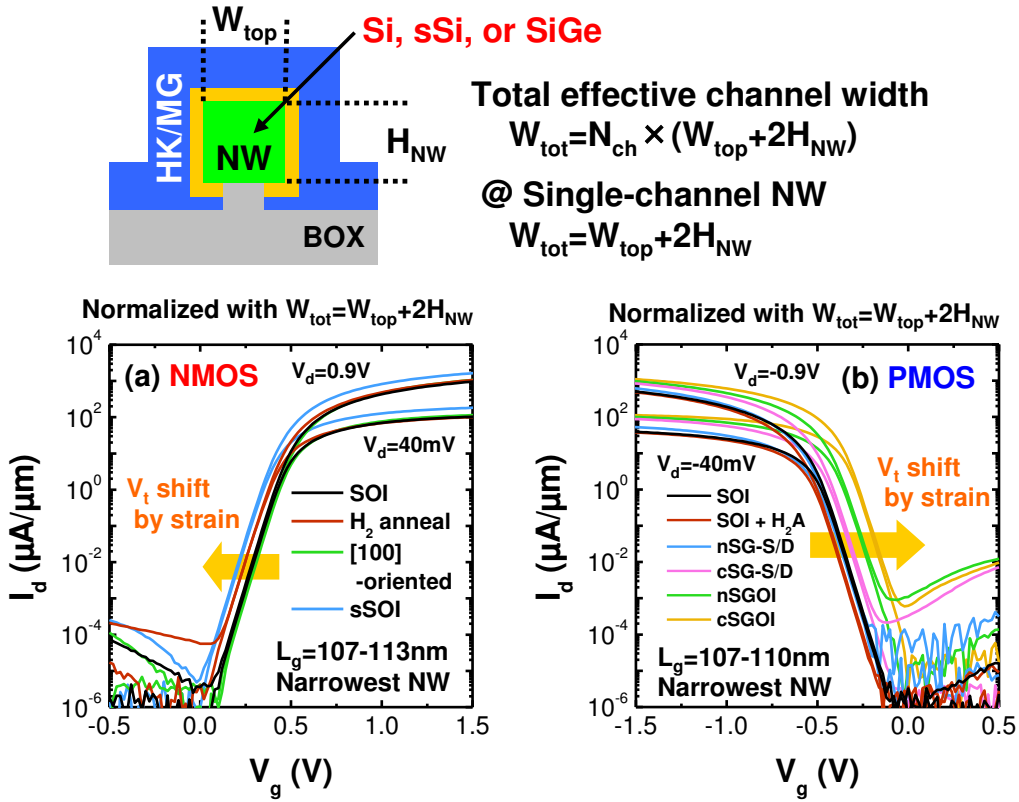


Fig. 3-1. I_d - V_g characteristics of the narrowest NW FETs with $L_g \approx 110\text{nm}$ for all the technological parameters in (a) NMOS and (b) PMOS devices.

Chapter 3. Carrier transport characterizations

3.1.2 C_{gc} - V_g measurement

Gate voltage V_g dependent gate-to-channel capacitance C_{gc} characteristics (C_{gc} - V_g) were measured by a precision LCR (inductance-capacitance-resistance) meter Agilent E4980A. A small AC signal is superimposed to the DC voltage V_g , consequently the capacitance, which is the charge change ΔQ responding to the AC voltage, is measured from AC current signal through S/D. The measurement results in the widest FET and the narrowest 50-channel NW with long $L_g=10\mu m$ is shown in Fig.3-2. The normalized curves by channel area ($W_{tot} \times L_g$) are identical between the widest FET and NW. This means that the equivalent oxide thickness (EOT) and gate oxide capacitance C_{ox} , defined here as a saturated C_{gc} value at strong inversion region, are sustained from the widest FETs down to the narrowest NW FETs. Here C_{ox} is constantly acquired as $C_{ox} \approx 2 \times 10^{-6} F/cm^2$ for both N- and PMOS devices.

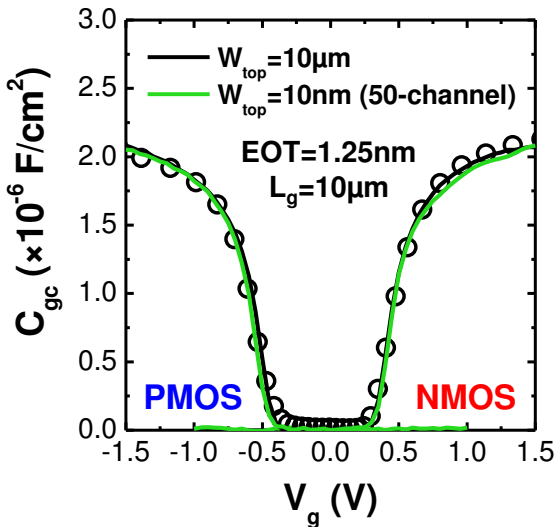


Fig. 3-2. C_{gc} - V_g characteristics of the widest FET and narrowest multiple 50-channel NW with $L_g=10\mu m$ in both SOI N- and PMOS devices. Sustained EOT value of 1.25nm for both wide and NW FETs was extracted by fitting between (lines) measured C_{gc} data and (circles) the simulated curve.

Chapter 3. Carrier transport characterizations

3.1.3 Mobility extraction

3.1.3.1 Effective mobility

Carrier mobility in MOSFET operation is a very important parameter, involved in the I_d definitions (cf. Eqs. (2-2) and (2-4)). Several techniques are available for the mobility extraction [3-3,3-4]. One of the techniques, split C-V technique proposed by J. Koomen [3-5] has been widely applied [3-6~3-8]. The technique needs enough large device channel area to allow accurate C_{gc} - V_g measurement. The split C-V extracts the carrier effective mobility μ_{eff} as a function of the effective field E_{eff} or the inversion carrier density N_{inv} . The μ_{eff} in linear region is obtained as:

$$\mu_{eff} = \frac{L}{W} \cdot \frac{I_d}{Q_{inv} V_d} \quad (3-1)$$

where Q_{inv} is the inversion charge density. The Q_{inv} at a given V_g is obtained by integrating the C_{gc} to the given V_g , and the relationship is written as:

$$Q_{inv} = \int_{-\infty}^{V_g} C_{gc} dV \quad (3-2)$$

For bulk FET case, the depletion charge density Q_{dep} is also necessary, and evaluated from the gate-to-body capacitance C_{gb} measurement. The Q_{dep} is similarly extracted as the Q_{inv} by integrating from flat-band voltage V_{fb} to given V_g , and the equation is shown as:

$$Q_{dep} = \int_{V_{fb}}^{V_g} C_{gb} dV \quad (3-3)$$

For SOI substrates, the C_{gb} measurement cannot be carried out because of the BOX. However, the Q_{dep} is negligible compared with the Q_{inv} in FD-SOI FETs with undoped ultra-thin channel and thick BOX. Therefore, the E_{eff} in our SOI FETs is expressed as:

$$E_{eff} = \frac{\eta Q_{inv} + Q_{dep}}{\epsilon_{Si}} \approx \frac{\eta}{\epsilon_{Si}} Q_{inv} \quad (3-4)$$

where η is an empirical parameter corresponding to 1/2 for electrons and to 1/3 for holes. The carrier density N_{inv} is simply calculated as:

$$N_{inv} = \frac{Q_{inv}}{q} = \frac{1}{q} \int_{-\infty}^{V_g} C_{gc} dV \quad (3-5)$$

Chapter 3. Carrier transport characterizations

The carrier density in the channel under strong inversion condition N_{inv} is often approximated by:

$$N_{inv} = \frac{Q_{inv}}{q} \approx \frac{C_{ox}}{q} (V_g - V_t - mV_{ch}) \quad (3-6)$$

where V_{ch} is the potential along the channel. In general, the equation can be further simplified as:

$$N_{inv} \approx \frac{C_{ox}}{q} (V_g - V_t) = \frac{C_{ox} V_{gt}}{q} \quad (3-7)$$

A well known schematic showing the three dominant scattering mechanisms which limit carrier mobility of MOSFET is shown in Fig.3-3. Mobility limited by phonon scattering μ_P depends on temperature more keenly than others. Phonon scattering influence disappears at low temperature, and below 77K, the mobility is only limited by Coulomb scattering at low N_{inv} regime (μ_C) and surface roughness scattering at higher N_{inv} region (μ_{SR}) [3-9,3-10]. Figure 3-3 shows the mobility extracted on 10μm-wide FET as an illustration of the three scattering mechanisms.

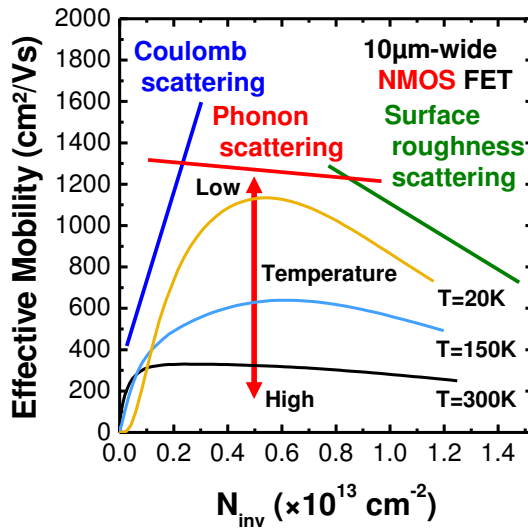


Fig. 3-3. Schematic exhibiting the three dominant scattering mechanisms which limit carrier mobility of MOSFET, and the temperature dependent mobility behavior from 300 K down to 20 K on 10μm-wide NMOS FET.

Chapter 3. Carrier transport characterizations

3.1.3.2 Low-field mobility

Extraction and evaluation of the low-field mobility μ_0 based on Y-function method [3-4,3-11~3-13] is very effective for ultra-scaled FETs, as effective mobility μ_{eff} investigation needs enough large size of the channel area. The μ_0 is extracted as the mobility at low electric field region, in other words, low inversion carrier density region ($N_{inv} \approx 0$), without consideration of Coulomb scattering influence. With this assumption, the relationship between low-field mobility μ_0 and effective mobility μ_{eff} is expressed as:

$$\mu_{eff} = \frac{\mu_0}{1 + \theta_1(V_g - V_t) + \theta_2(V_g - V_t)^2} = \frac{\mu_0}{1 + \theta_1 V_{gt} + \theta_2 V_{gt}^2} \quad (3-8a)$$

$$\text{with } \theta_1 = \theta_{1,0} + R_{SD}\beta_0 \quad (3-8b)$$

where $\theta_1 (\theta_{1,0})$ and θ_2 , are the first and second order mobility attenuation factors, respectively, R_{SD} is the series resistance of source and drain contacts, and β_0 is the transistor gain. The attenuation factors express mobility degradation at strong inversion region, and θ_1 includes mainly phonon scattering impacts, while θ_2 correspond roughly to surface roughness scattering influence. However, Eq. (3-8a) gives only an empirical expression of μ_{eff} , so that θ_1 and θ_2 have no physical meaning [3-13]. In linear region ($V_d \ll V_{d_sat}$), μ_0 can be deduced from the transistor gain β_0 as:

$$\mu_0 = \mu_{eff} (N_{inv} \approx 0) = \frac{\beta_0 L}{C_{ox} W} \quad (3-9)$$

The parameter β_0 is extracted from the slope of the Y-function vs. V_{gt} curve, and the Y-function is given by:

$$Y = \frac{I_d}{\sqrt{g_m}} = V_{gt} \sqrt{\frac{\beta_0 V_{d_lin}}{1 - \theta_2 V_{gt}^2}} \quad (3-10)$$

where g_m is the transconductance and is defined as dI_d/dV_g . This equation can be simplified for $\theta_2 V_{gt}^2 \ll 1$ as:

$$Y = \frac{I_d}{\sqrt{g_m}} \approx V_{gt} \sqrt{\beta_0 V_{d_lin}} \quad (3-11)$$

The method allows to extract V_t , θ_1 , θ_2 , and β_0 after several fitting procedures.

Figure 3-4 shows illustration of the relationships among experimental μ_{eff} , and

Chapter 3. Carrier transport characterizations

computed μ_0 and μ_Y in the widest FET and narrowest 50-channel NWs with $L_g=10\mu\text{m}$. The $\mu_{\text{eff}}-N_{\text{inv}}$ curves can be completely reconstructed by the Y-function method using Eq. (3-8a) by adding Coulomb scattering limitation in small N_{inv} range. Note that μ_0 extracted by this method is free from R_{SD} effect, which limits the I_d especially for short channel device.

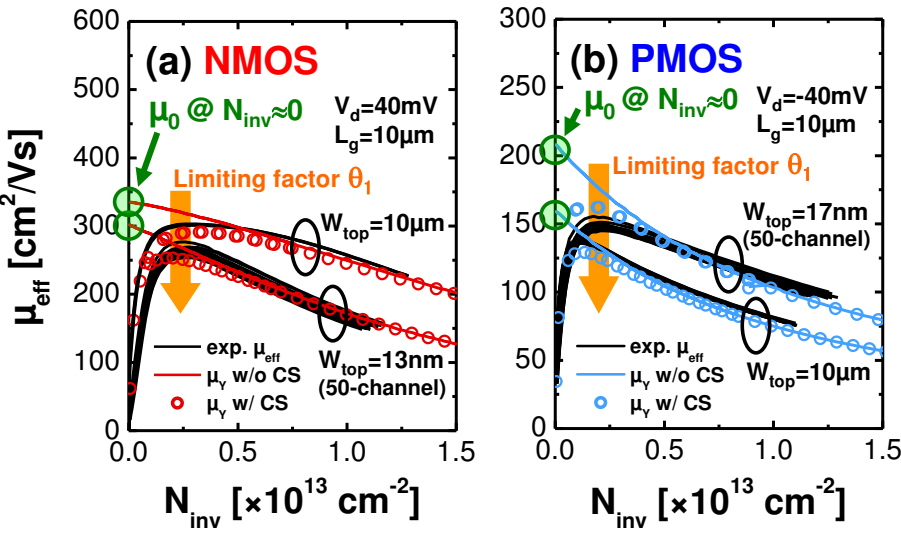


Fig. 3-4. Illustration of the relationship between μ_{eff} and μ_0 on (a) NMOS and (b) PMOS cases. The computed μ_Y curves considering Coulomb scattering (CS) influence show good agreement with experimental μ_{eff} data measured by split C-V in the narrowest 50-channel NW and the widest FETs with $L_g=10\mu\text{m}$.

3.2 Experimental results

3.2.1 I_d - V_g characteristics

I_d - V_g characteristics in the narrowest single-channel NW FETs with varied gate length L_g from $1\mu\text{m}$ down to 17nm are discussed for all the technological parameters. The curves in reference SOI and strained devices (sSOI for NMOS, and nSGOI for PMOS) are shown in Fig.3-5 for NMOS NW, and in Fig.3-6 for PMOS NW FETs, respectively. The curves are parallel and vertically shifted as the L_g is shortened in both linear and saturation regions, and also for both unstrained and strained FETs. In the

Chapter 3. Carrier transport characterizations

following, we discuss the main electrical parameters for all the narrowest NW devices; threshold voltage V_t , drain induced barrier lowering (DIBL), subthreshold swing (SS), and on-state drain current I_{ON} .

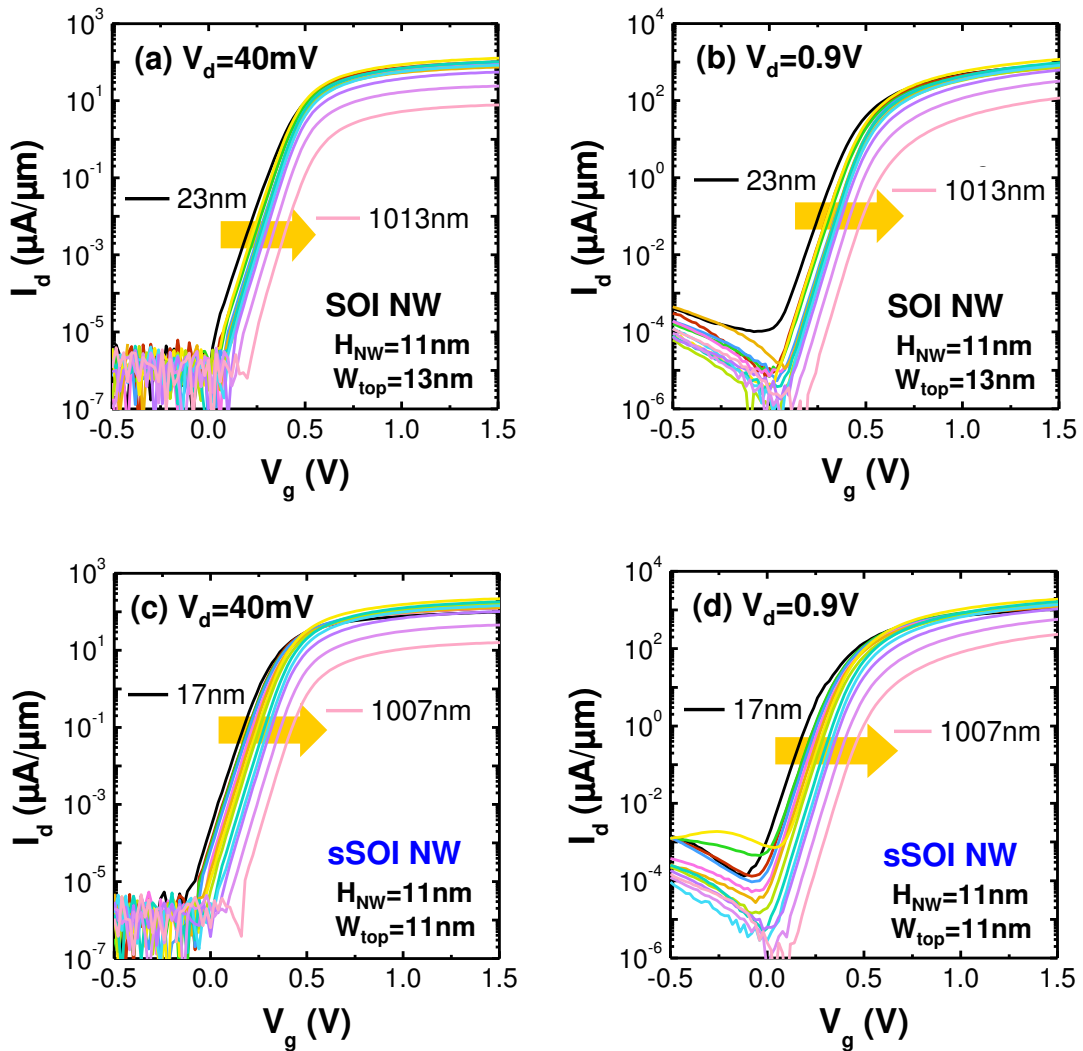


Fig. 3-5. I_d - V_g characteristics as a function of L_g in the narrowest NWs for (a,b) SOI and (c,d) sSOI NMOS devices with comparison between (a,c) linear ($V_d=40\text{mV}$) and (b,d) saturation ($V_d=0.9\text{V}$) regions.

Chapter 3. Carrier transport characterizations

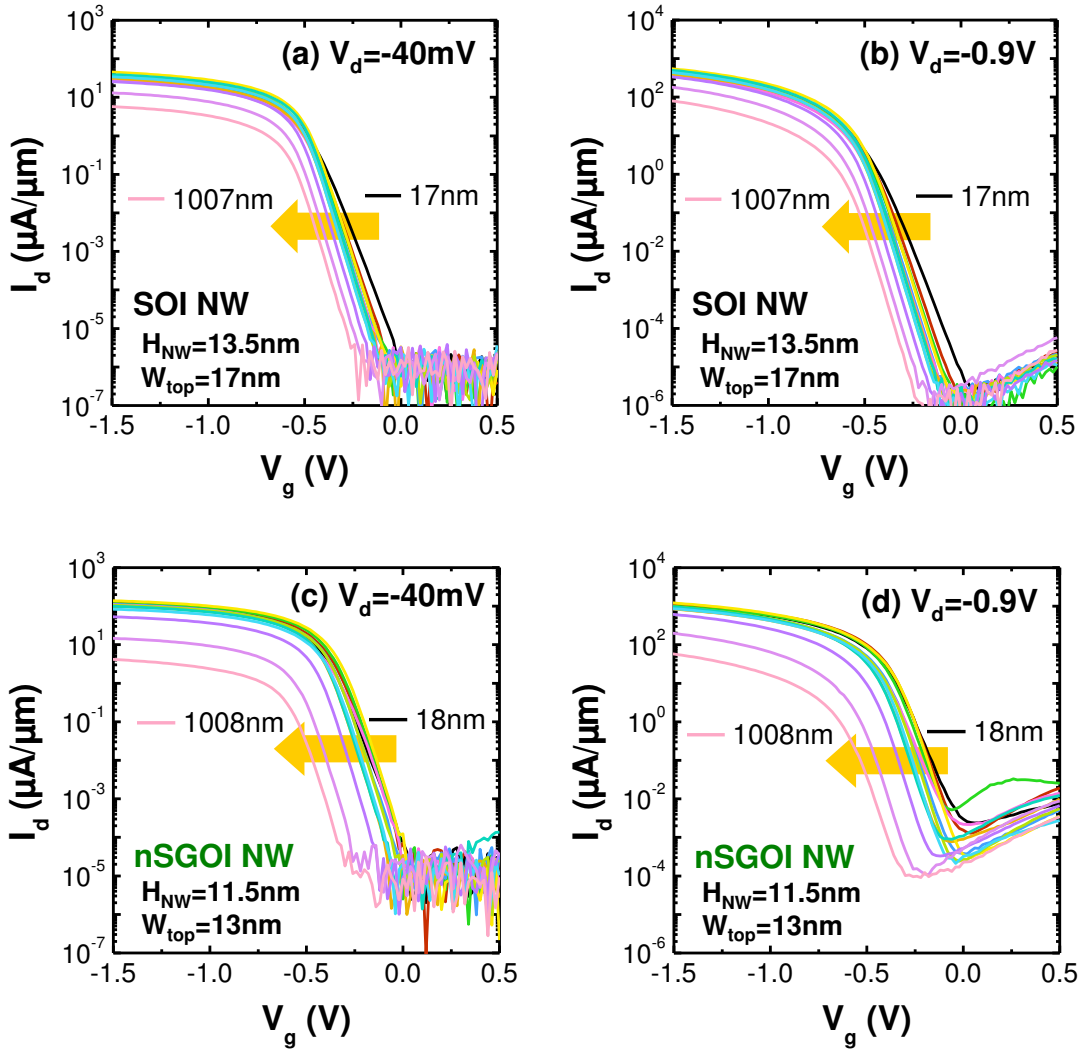


Fig. 3-6. I_d - V_g characteristics as a function of L_g in the narrowest NWs for (a,b) SOI and (c,d) nSGOI PMOS devices with comparison between (a,c) linear ($|V_d|=-40\text{ mV}$) and (b,d) saturation ($|V_d|=0.9\text{ V}$) regions.

3.2.1.1 Threshold voltage

Threshold voltage V_t is extracted by constant-current method, and the arbitrary constant I_d is defined as $(W_{\text{tot}}/L_g) \times 10^{-7}$ [3-3,3-14]. The V_t extracted at linear ($|V_d|=-40\text{ mV}$) and saturation ($|V_d|=0.9\text{ V}$) regions in the widest ($W_{\text{top}}=10\mu\text{m}$) and the narrowest NW FETs for reference SOI N- and PMOS devices is shown in Fig.3-7. The V_t values are dependently shifted on the L_g by SCE [3-2], thus the absolute values ($|V_t|$)

Chapter 3. Carrier transport characterizations

decrease for shorter L_g in both NMOS and PMOS devices [3-15~3-18]. It is noticed that SOI PMOS NWs with shorter $L_g < 50\text{nm}$ exhibit ascending of the $|V_t|$. The decreasing tendency of $|V_t|$ in NWs is much smaller than wide FET cases, and this means that NW devices have better endurance to detrimental SCE.

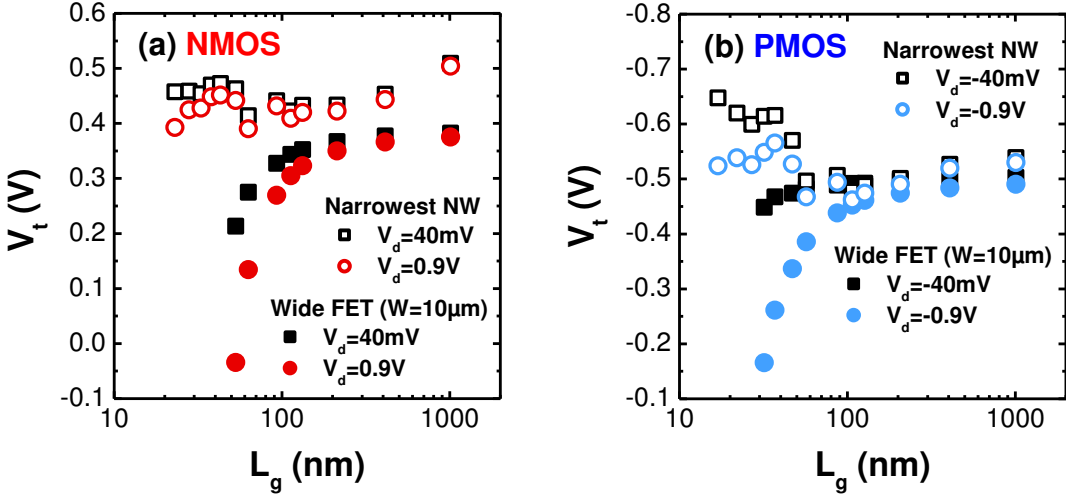


Fig. 3-7. Threshold voltage V_t as a function of L_g extracted at linear ($|V_d|=40\text{mV}$) and saturation ($|V_d|=0.9\text{V}$) regions in the widest and the narrowest NW FETs for SOI (a) NMOS and (b) PMOS devices.

The V_t values for all N- and PMOS NWs are shown in Figs.3-8 and 3-9, respectively. The decreasing tendency of $|V_t|$ is in agreement with all NWs (except shorter range with $L_g < 50\text{nm}$ in PMOS NWs). Moreover, the technological parameters sensitively alter the L_g dependent V_t behavior. For NMOS, [100]-oriented NWs show somewhat higher V_t values, in contrast H_2 annealed NWs exhibit lower V_t values than reference SOI devices. The V_t shifts could be attributed to the interface dipole alteration, which may depend on crystallographic surface orientation and cross-sectional shape of the NW body [3-16]. Strain effect also enlarges the L_g dependent V_t shift indicating the lower values than SOI NWs [3-19,3-20], and this result is in good agreement with tensile strain effect which introduces the significant band offset [3-21~3-23]. In PMOS, SOI- H_2A NW shows higher $|V_t|$ values and more drastic ascending of the $|V_t|$ behavior especially in shorter L_g region than reference SOI NW. This could be also ascribed to the surface dipole

Chapter 3. Carrier transport characterizations

modulation. Similarly to NMOS, the compressive strain impact is appeared with the lower $|V_t|$ values in cSG-S/D [3-20], clearly in both n- and cSGOI devices [3-16~3-18].

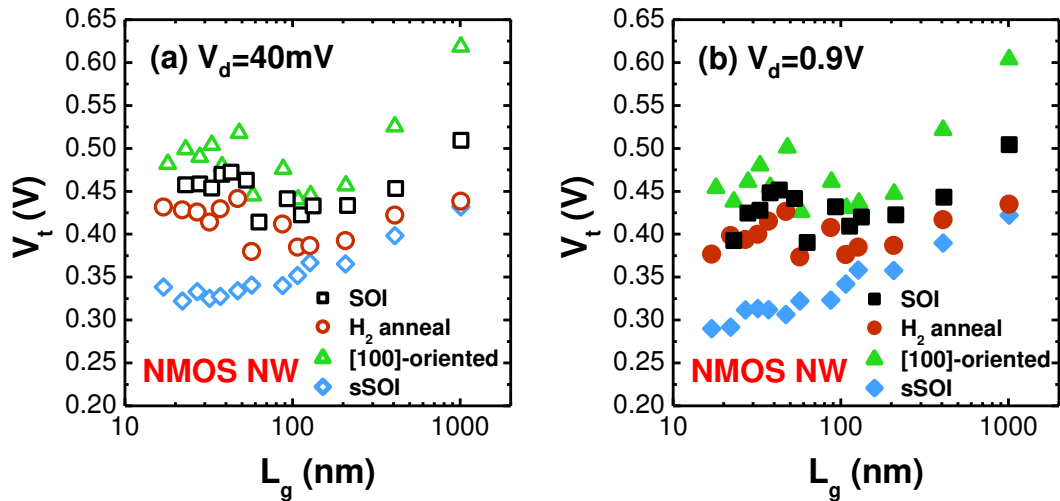


Fig. 3-8. Threshold voltage V_t as a function of L_g in the narrowest NMOS NWs at (a) linear ($V_d=40\text{mV}$) and (b) saturation ($V_d=0.9\text{V}$) regions for all the technological parameters.

Chapter 3. Carrier transport characterizations

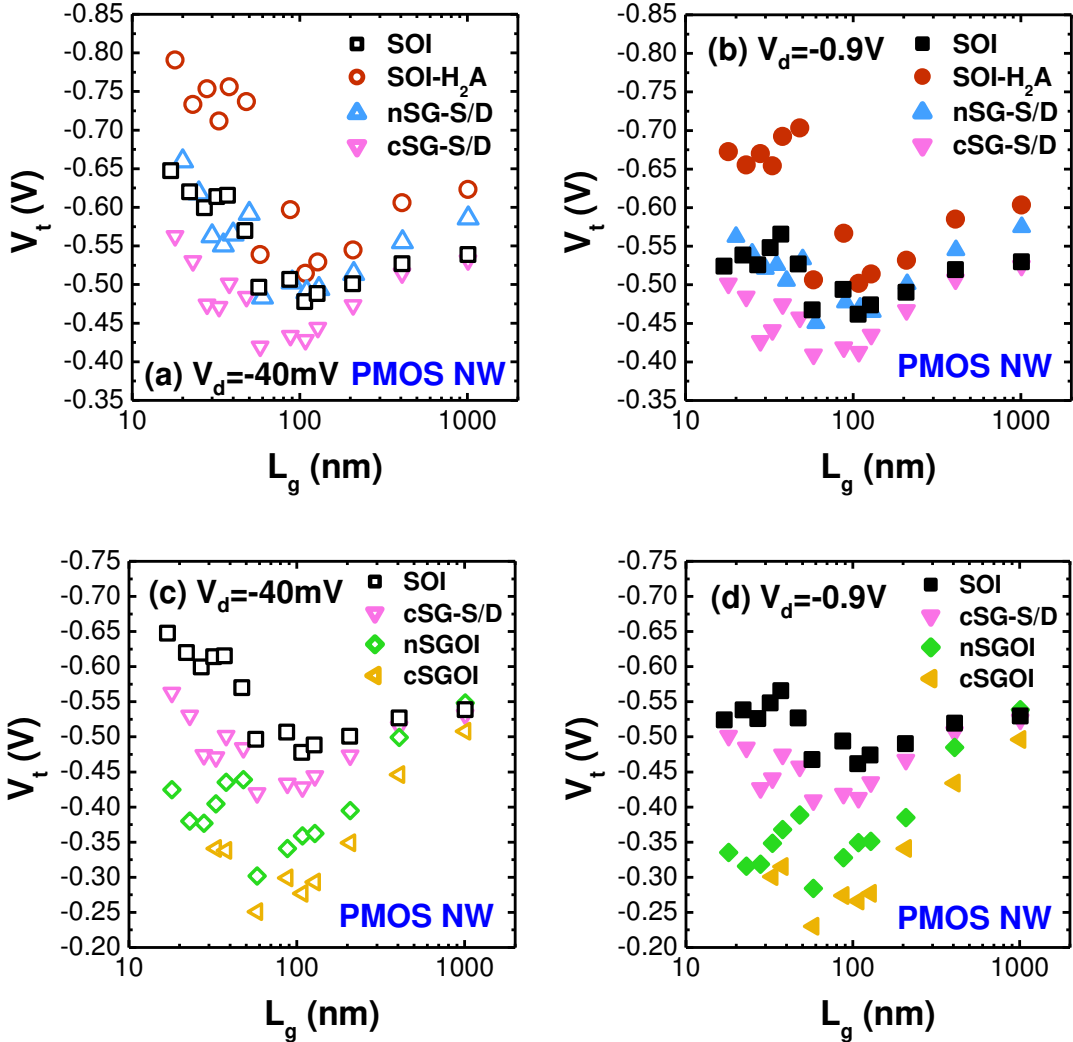


Fig. 3-9. Threshold voltage V_t as a function of L_g in the narrowest PMOS NWs at (a,c) linear ($V_d=-40\text{mV}$) and (b,d) saturation ($V_d=-0.9\text{V}$) regions for all the technological splits.

3.2.1.2 Drain induced barrier lowering

Drain induced barrier lowering (DIBL) causes the threshold voltage V_t decrease as the V_d bias is increased. The DIBL is defined by assigning the extracted V_t values in linear and saturation regimes (V_{t_lin} and V_{t_sat} in Figs.3-7~3-9) as [3-24]:

$$DIBL = \left| \frac{V_{t_sat} - V_{t_lin}}{V_{d_sat} - V_{d_lin}} \right| = \frac{|V_{t_sat} - V_{t_lin}|}{0.86} \quad (3-12)$$

The DIBL in the widest and the narrowest NW FETs for reference SOI N- and PMOS

Chapter 3. Carrier transport characterizations

devices is evaluated in Fig.3-10. The widest FETs exhibit a drastic increase of the DIBL values as the L_g is shortened below 100nm for both N- and PMOS devices, whereas the DIBL are similar with the values in NWs maintained below 30mV/V for the L_g range over 200nm. On the other hand, NWs sustain the much smaller values in entire L_g range, with a maximum DIBL=75.5mV/V at L_g =23nm for NMOS, and with 143.6mV/V at L_g =17nm for PMOS NWs. It is thus reconfirmed that NW devices have much better electrostatic control than planer devices.

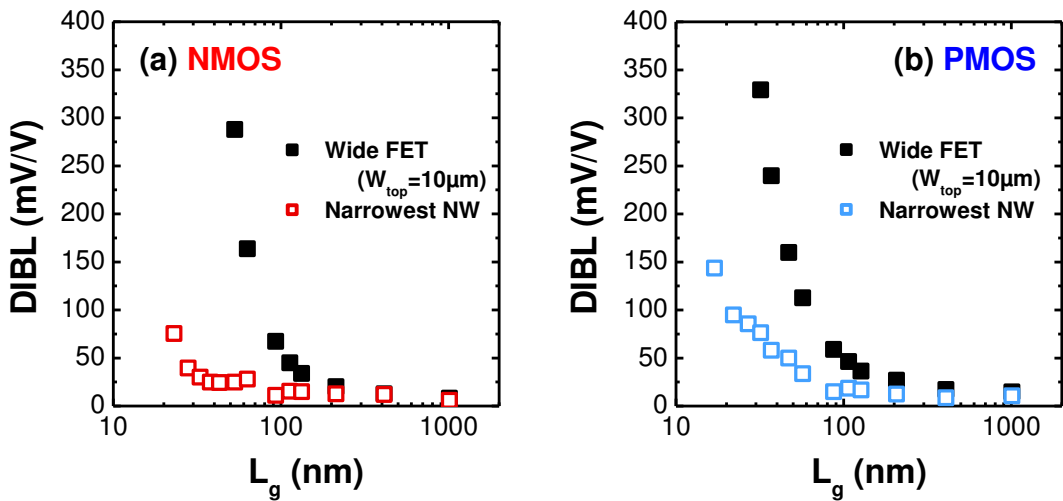


Fig. 3-10. Extracted DIBL as a function of L_g in the widest and the narrowest NW FETs for SOI (a) NMOS and (b) PMOS devices.

Figures 3-11 and 3-12 summarize the DIBL extracted in all N- and PMOS NW devices, respectively. In both NWs, the L_g dependent DIBL behavior draws roughly the same curves. In NMOS, it is observed that additional H₂ anneal process provides slightly better SCE immunity in whole L_g range [3-24]. For PMOS, cSG-S/D shows the best performance. It is found that electrostatic control against detrimental SCE is more effective in NMOS than PMOS NWs for short channel region. Moreover, the tensile and compressive strain technologies do not largely influence the DIBL behaviors. The extracted DIBL behaviors are comparable with our recent studies for NW MOSFETs [3-20,3-24,3-25].

Chapter 3. Carrier transport characterizations

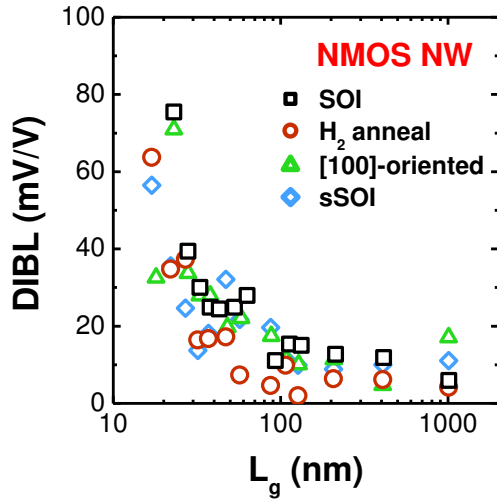


Fig. 3-11. Extracted DIBL as a function of L_g in the narrowest NMOS NWs for all the technological parameters.

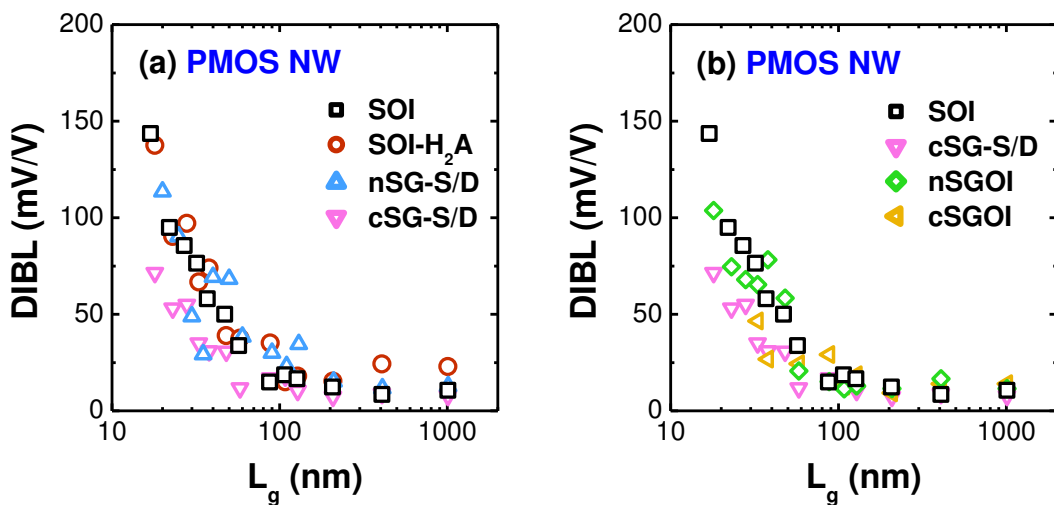


Fig. 3-12. Extracted DIBL as a function of L_g in the narrowest PMOS NWs for all the technological splits.

3.2.1.3 Subthreshold swing

Extracted subthreshold swing (SS) in the widest and the narrowest NW FETs for reference SOI N- and PMOS devices is shown in Fig.3-13. Similarly with DIBL

Chapter 3. Carrier transport characterizations

characterization, the SS in widest FETs drastically increase with decreasing of the L_g below 100nm for both N- and PMOS devices, while the almost ideal $SS \approx 60\text{mV/dec}$ is obtained for the L_g range above 200nm. In contrast, SOI NWs maintain the SS close to the ideal value in whole L_g range even for the shortest devices and at high $|V_d|$ condition. The worst $SS = 69.5\text{mV/dec}$ for NMOS NW with $L_g = 23\text{nm}$ and $SS = 76.7\text{mV/dec}$ for PMOS NW with $L_g = 17\text{nm}$ are extracted. The SOI NWs thus demonstrate the excellent electrostatic control.

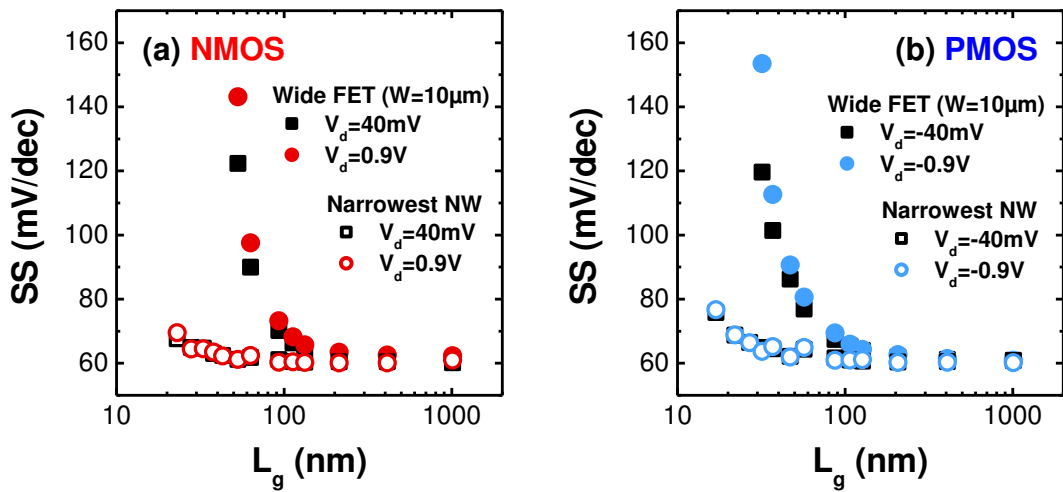


Fig. 3-13. Subthreshold swing SS as a function of L_g in the widest and the narrowest NW FETs for SOI (a) NMOS and (b) PMOS devices.

The SS observed in all NWs is shown in Figs.3-14 and 3-15 for N- and PMOS devices, respectively. For NMOS, the SS is close to the ideal value ($\approx 60\text{mV/dec}$) in longer region of $L_g > 80\text{nm}$, and the value increases below L_g of 70nm . This reflects SCE impact enlarging the body-effect. H₂ anneal processed NWs show the values above the universal value at low $V_d = 40\text{mV}$, even in the longer L_g range. However, the data dispersion roughly disappears at high V_d condition. Therefore, all NMOS NWs show the similar and excellent behavior the SS values sustaining below 69.5mV/V at high $V_d = 0.9\text{V}$.

In PMOS devices, the L_g dependent SS behavior at low $V_d = -40\text{mV}$ is similar to NMOS case, but with the higher SS accession. Furthermore, the control is deteriorated

Chapter 3. Carrier transport characterizations

at high $V_d=-0.9V$ compared to the low V_d case, unlike with NMOS devices. The SiGe strain technologies introduce degraded SS values of 82-85mV/dec compared to reference SOI NW with 76.7mV/dec at the minimum $L_g=17-20nm$ at high V_d regime. These conclude that PMOS NWs, especially SiGe processed devices, are more influenced by SCE than NMOS NWs. The SS behavior is better in NMOS and is comparable in PMOS NW FETs compared to our recent works on NW MOSFETs [3-20,3-24,3-25].

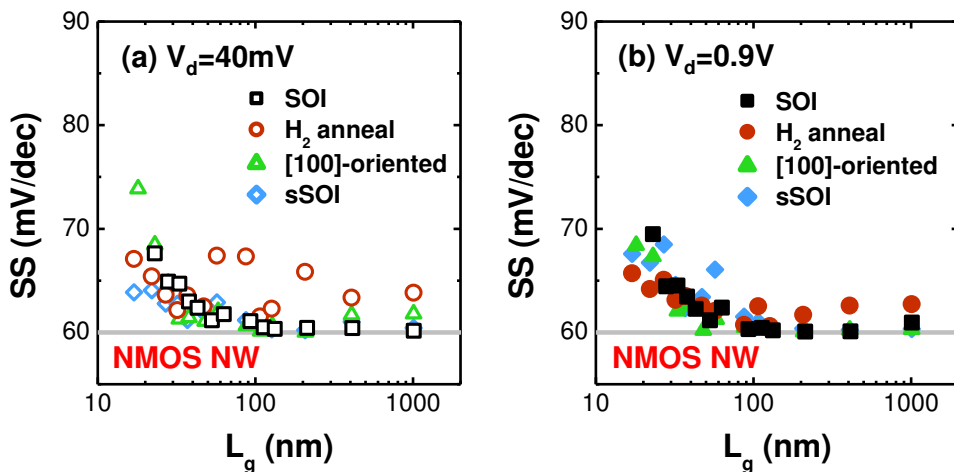


Fig. 3-14. Subthreshold swing SS as a function of L_g in the narrowest NMOS NWs at (a) low $V_d=40mV$ and (b) high $V_d=0.9V$ for all the technological parameters.

Chapter 3. Carrier transport characterizations

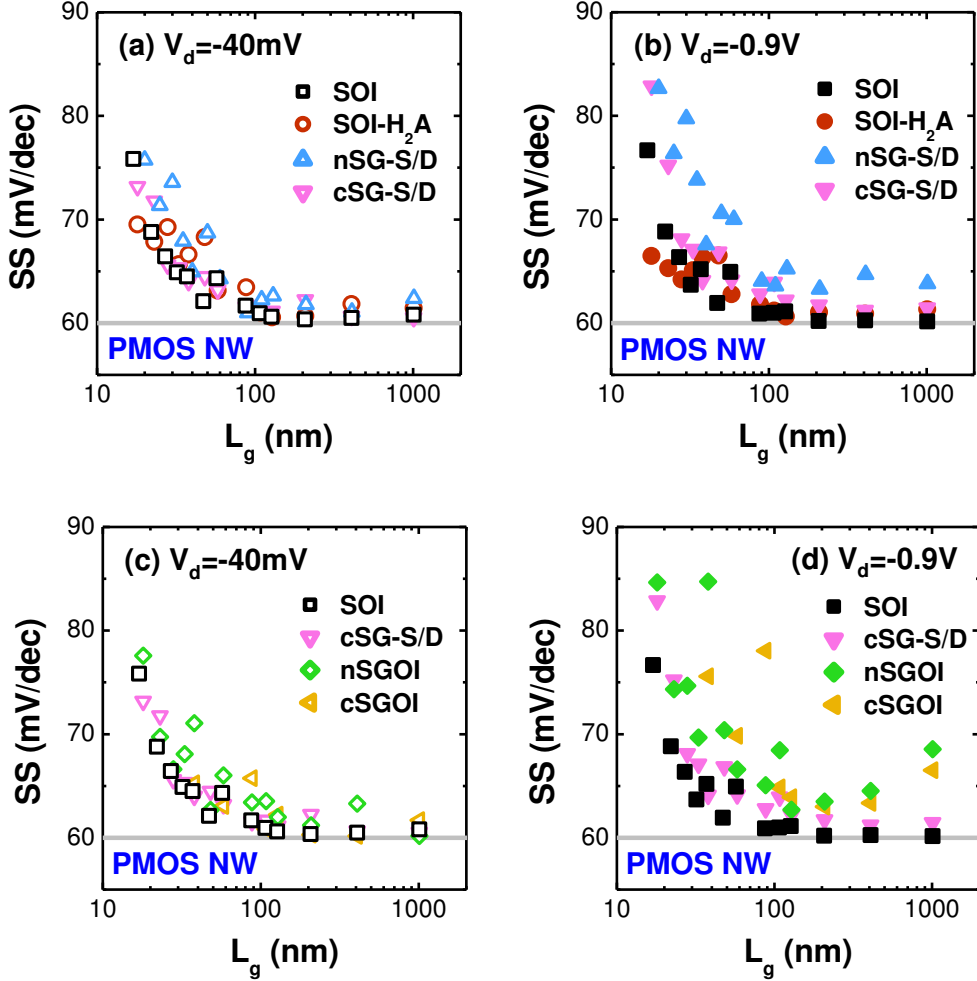


Fig. 3-15. Subthreshold swing SS as a function of L_g in the narrowest PMOS NWs at (a,c) low $V_d = -40\text{mV}$ and (b,d) high $V_d = -0.9\text{V}$ for all the technological splits.

3.2.1.4 Challenge of I_{ON} enhancement

On-state current I_{ON} in saturation region is here defined as I_d measured at $|V_g| = |V_d| = 0.9\text{V}$. The extracted I_{ON} is shown in Figs.3-16 and 3-17 for N- and PMOS FETs, respectively. The I_{ON} in both N- and PMOS NWs over $L_g > 100\text{nm}$ follows the general I_d behavior in saturation region illustrated as straight lines, and the equation without body-effect coefficient m is shown as (cf. Eq. (2-4)):

$$I_{d_sat} = \mu_{eff} C_{ox} \frac{W_{tot}}{L_g} \cdot \frac{V_{gt}^2}{2} \quad (3-13)$$

In contrast, the I_{ON} is saturated below $L_g < 100\text{nm}$, and the limitation is occurred by

Chapter 3. Carrier transport characterizations

carrier velocity limit and is interpreted as:

$$I_{sat} = C_{ox}W_{tot}V_{gt}v_{lim} \quad (3-14)$$

where v_{lim} is the limiting velocity of the carriers during transport. The velocity v_{lim} is limited by the saturation velocity v_{sat} in drift-diffusion transport and the injection velocity v_{inj} in quasi-ballistic transport [3-26].

For NMOS, [110]-SOI with H₂ anneal and [100]-SOI devices show roughly the same values as reference [110]-SOI NWs, except in over L_g>400nm. Beneficial impact of the tensile strain can be clearly seen with the I_{ON} gain of +61% at least in entire L_g range compared with reference SOI NWs. The I_{ON} enhancement over 60% at L_g=22-23nm is higher than previous sSOI devices [3-19,3-27].

For PMOS, SOI-H₂A devices show degraded I_{ON} with the maximum loss of -69% in whole L_g range. This agrees with the prediction for the strange V_t behavior that channel conduction in SOI-H₂A NW could be worse than reference SOI device. On the other hand, the compressive strain provides the huge advantage, especially in shorter L_g region (*e.g.* at minimum L_g of 17-18nm with the gain of +137% for cSG-S/D, and of +323% for nSGOI, respectively). Consequently, it is concluded that the uniaxial strain technologies in ultra-scaled NW N- and PMOS FETs efficiently improve the I_{ON}, especially for PMOS a dramatic enhancement is achieved by SGOI NW architecture.

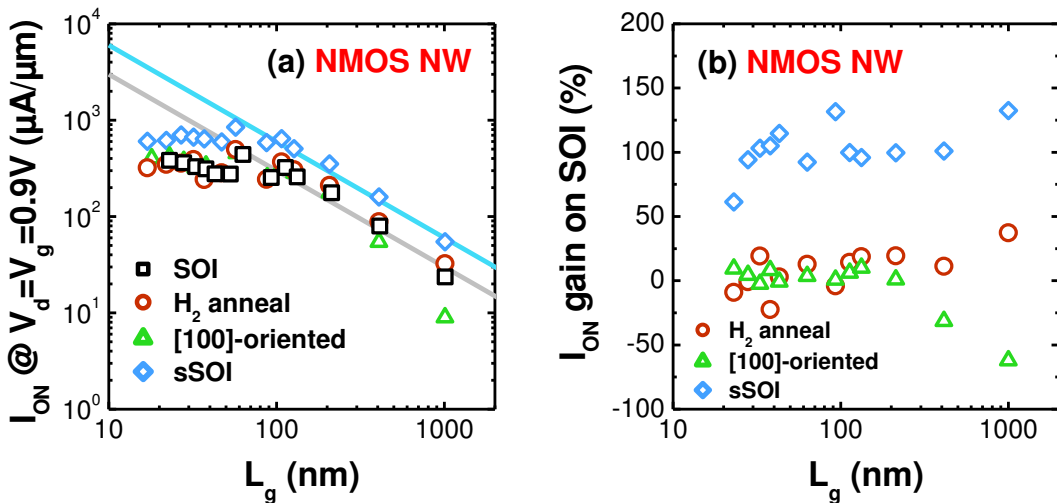


Fig. 3-16. (a) Extracted I_{ON} and (b) the gain compared with reference SOI as a function of L_g in the narrowest NMOS NWs for all the technological parameters.

Chapter 3. Carrier transport characterizations

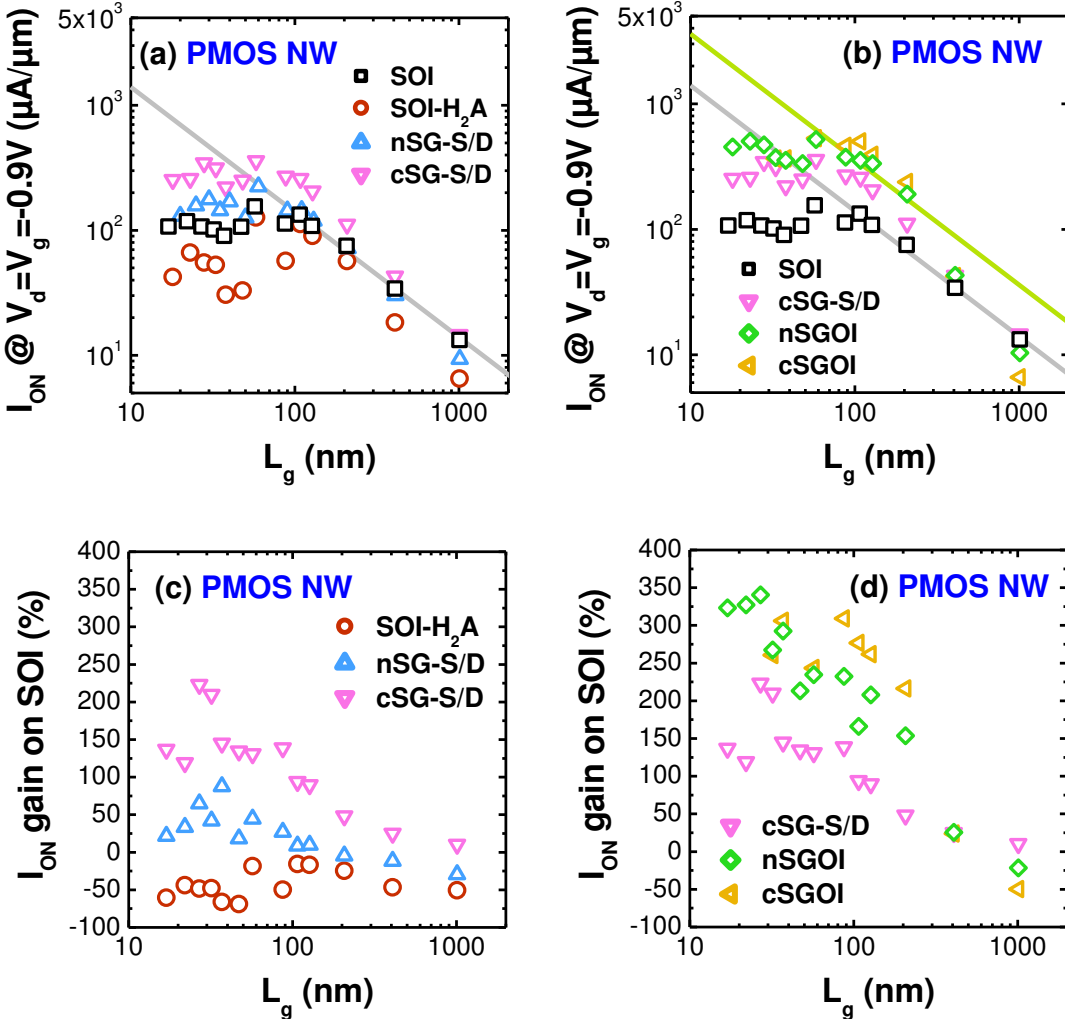


Fig. 3-17. (a,b) Extracted I_{ON} and (c,d) the gain compared with reference SOI as a function of L_g in the narrowest PMOS NWs for all the technological splits.

The I_{ON} - I_{OFF} performance in the narrowest NWs with L_g between $\sim 110\text{nm}$ and 17nm is reported in Fig.3-18. Off-state current I_{OFF} is extracted at $V_g=0\text{V}$ and $|V_d|=0.9\text{V}$. The I_{ON} enhancement and level shift of I_{OFF} by stressors effect are visible.

Chapter 3. Carrier transport characterizations

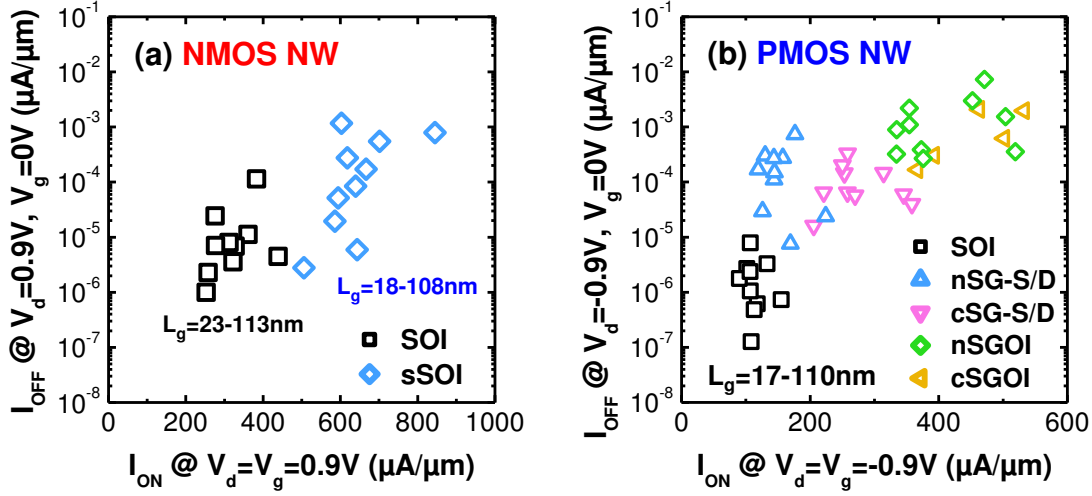


Fig. 3-18. I_{ON} - I_{OFF} performance in the narrowest NW (a) NMOS and (b) PMOS FETs with comparison of stressor impacts.

3.2.2 Temperature dependent Effective mobility

Effective carrier mobility μ_{eff} has been systematically measured as a function of temperature, from room temperature (300K) down to 20 K, in order to investigate the different scattering mechanism involved in carrier transport. Here, the measurements have been performed in 10 μm -long tri-gate (TG) and omega-gate (ΩG) NWs with multiple 50-channel fingers, since sufficient channel area is necessary for μ_{eff} extraction based on split C-V technique. ΩG NW structure was formed with additional H₂ anneal process.

Figure 3-19 shows the μ_{eff} of electron and hole extracted as a function of inversion carrier density N_{inv} for SOI TGNW and wide FETs. For NWs, μ_{eff} was obtained through C_{gc} measurement which takes into account inversion carrier density in the whole structure, involving side-walls and top surface.

NMOS mobility - The electron mobility in NMOS TGNW is degraded as compared to wide FET in the whole range of N_{inv} . In particular, the degradation in NMOS is larger in high N_{inv} region above $0.4 \times 10^{13}\text{cm}^{-2}$, and is more severe at low temperature. The maximum peak mobility μ_{max} is shifted to lower N_{inv} for NMOS TGNW (e.g. $\mu_{max} \approx 650\text{cm}^2/\text{Vs}$ at $N_{inv} \approx 0.2 \times 10^{13}\text{cm}^{-2}$ and $T=100\text{K}$) compared to wide FET ($\mu_{max} \approx 800\text{cm}^2/\text{Vs}$ at $N_{inv} \approx 0.6 \times 10^{13}\text{cm}^{-2}$ and $T=100\text{K}$). The degradation for NMOS in

Chapter 3. Carrier transport characterizations

TGNW is in good agreement with the increasing contribution of the (110)-oriented side-walls as the transistor width is reduced down to NW [3-25,3-28]. Indeed, the electron mobility is degraded in (110)/[110] channel [3-10]. The impact of the 3D architecture for NMOS can be clearly evidenced in TGNWs. Figure 3-20 shows comparison of the μ_{eff} behavior between $W_{\text{top}}=10\text{nm}$ and $W_{\text{top}}=30\text{nm}$ SOI TGNWs. The peak shift of μ_{max} and deep mobility deterioration in the narrowest NW with $W_{\text{top}}=10\text{nm}$ at higher N_{inv} region are visible. Furthermore, below 100K, μ_{max} in the narrowest NW becomes lower than in wider NW.

PMOS mobility - On the other hand, the hole mobility of TGNW is improved in medium-high N_{inv} region. Moreover, there is no significant shift of μ_{max} for PMOS NWs. As for NMOS, the mobility improvement for PMOS TGNW is in good agreement with the increasing contribution of the (110)-oriented side-walls, as the hole mobility in (110)/[110] channel is higher than the one in (100)/[110] channel.

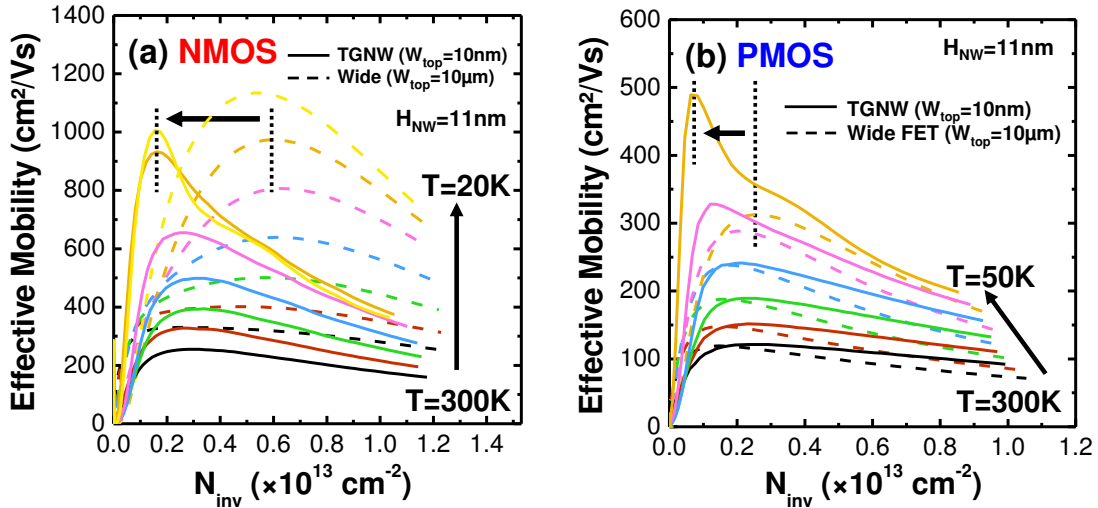


Fig. 3-19. Effective mobility μ_{eff} extracted as a function of N_{inv} in SOI TGNW and wide FETs at varying temperatures (from 300K down to 20K) for (a) NMOS and (b) PMOS devices.

Chapter 3. Carrier transport characterizations

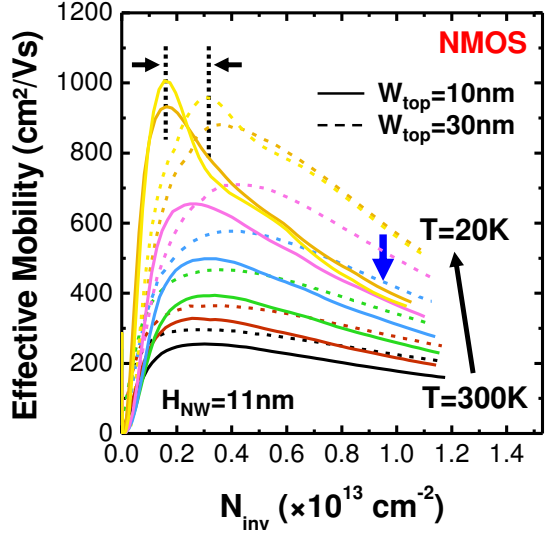


Fig. 3-20. Effective mobility μ_{eff} extracted as a function of N_{inv} in SOI TGNW NMOS FETs with $W_{\text{top}}=10\text{nm}$ and $W_{\text{top}}=30\text{nm}$ at varying temperatures (from 300K down to 20K).

3.2.2.1 Extraction of contributions of side-wall and top surfaces

In the following, the contribution of the top and side-wall surfaces on mobility of TGNW μ_{TG} is discussed, using the total mobility expressed as [3-25,3-28]:

$$\mu_{\text{TG}} = \frac{W_{\text{top}}}{W_{\text{tot}}} \mu_{\text{top}}^{(100)} + \frac{2H_{\text{NW}}}{W_{\text{tot}}} \mu_{\text{side-wall}}^{(110)} \quad (3-15)$$

where μ_{top} and $\mu_{\text{side-wall}}$ are the mobility corresponding to each surface orientation, which is (100) top surface, and (110) side-walls, respectively. Using this equation and making the reliable assumption that the mobility in (100) top surface μ_{top} is simply given by the 10μm-wide FETs, the mobility contributions of the top and the side-walls can be de-correlated for both N- and PMOS TGNWs. The extracted contributions as a function of N_{inv} at 300 K are shown in Fig.3-21. The $\mu_{\text{side-wall}}$ of both N- and PMOS is in good agreement with the experimental data of reference Si(110) wide FET, showing that the transport properties of TGNWs in strong inversion regime are mainly governed by the independent inversion surfaces.

Chapter 3. Carrier transport characterizations

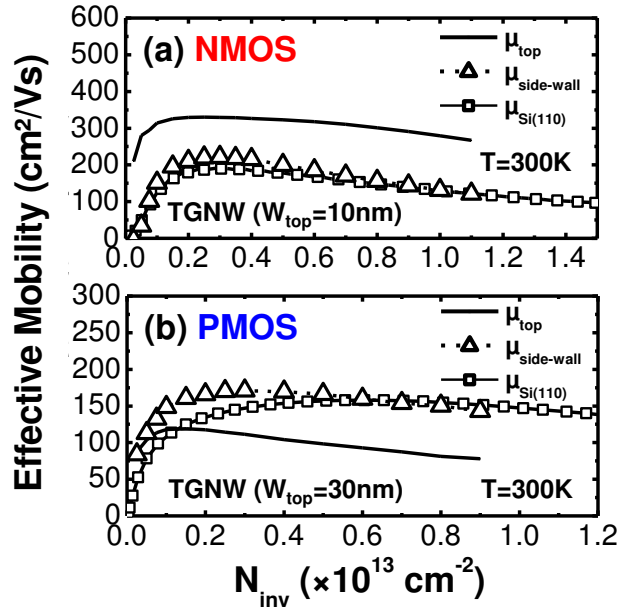


Fig. 3-21. Extraction of the (100) top and (110) side-wall mobility contributions at 300K in SOI TGNW FETs as a function of N_{inv} for (a) NMOS with W_{top}=10nm and (b) PMOS with W_{top}=30nm. The experimental data in Si(110) wide MOSFET μ_{Si(110)} is also shown as a reference.

The different contributions have also been extacted at 50K, and plotted in Fig.3-22. For NMOS, the contribution of surface roughness scattering in NW is drastically increased due to the enhanced side-wall contribution, and is in good agreement with data reported for (110)/[110] electrons in literature [3-10,3-29]. Furthermore, the μ_{max} in NW is shifted to lower N_{inv}, and could indicate a reduced contribution of Coulomb scattering for the side-walls. For PMOS, the mobility limited by surface roughness scattering μ_{SR} in side-walls is slightly enhanced, leading to better mobility at high N_{inv} region for NW compared to the wide FET. Similarly to NMOS, (110) side-walls in PMOS also show dramatically reduced Coulomb scattering contribution.

Chapter 3. Carrier transport characterizations

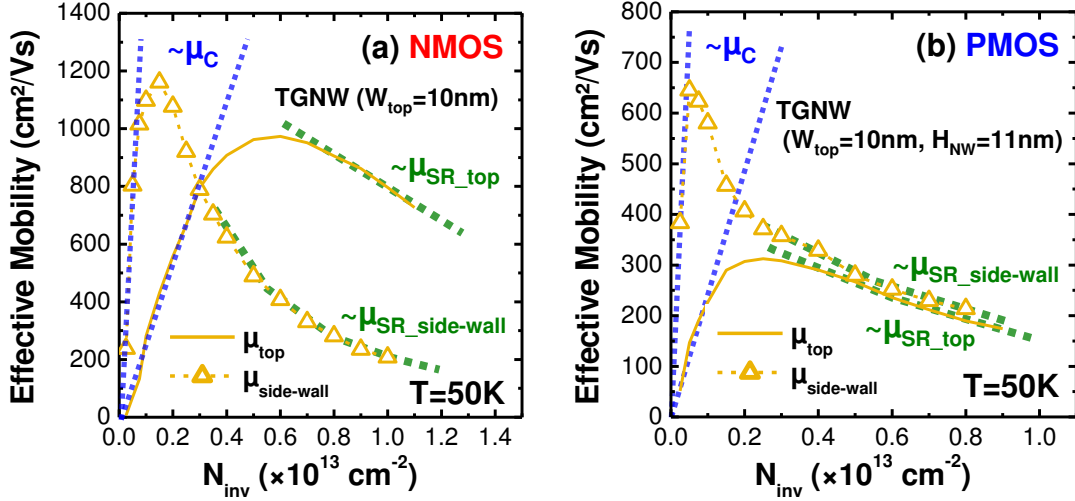


Fig. 3-22. Extraction of the μ_{top} and $\mu_{\text{side-wall}}$ contributions at 50K in SOI TGNW FETs with $W_{\text{top}}=10\text{nm}$ as a function of N_{inv} for (a) NMOS and (b) PMOS devices.

3.2.2.2 Tri-gate vs. Omega-gate

The μ_{eff} of electron and hole is compared for SOI TG and Ω G NW FETs with similar width in Fig.3-23. For PMOS, the mobility in Ω G and TG NWs are very similar in the whole range of N_{inv} and temperature, with a slightly higher mobility at low N_{inv} for Ω GNW. On the other hand, differences appear for NMOS at low temperature: the mobility is higher for Ω GNW at low N_{inv} , while it is deteriorated at high N_{inv} region. A different surface roughness influence due to circular shape can be distinguished below 50K. However, these results show that the shape of the NWs (rectangular vs. semi-circular) has only a little influence on carrier transport for the dimension as small as $10\text{nm} \times 10\text{nm}$ at room temperature. Impact of the (110) side-wall surface can still be distinguished even in the semi-circular geometry of Ω GNW. The difference at low N_{inv} could indicate a lower contribution of Coulomb scattering in the case of Ω GNWs, due to additional H_2 anneal process, in contrast with previous study in 3D-stacked GAA NW FETs [3-16,3-30]. The change of Coulomb scattering contribution originating from additional H_2 anneal is also confirmed even in $10\mu\text{m}$ -wide FETs in Fig.3-24.

Chapter 3. Carrier transport characterizations

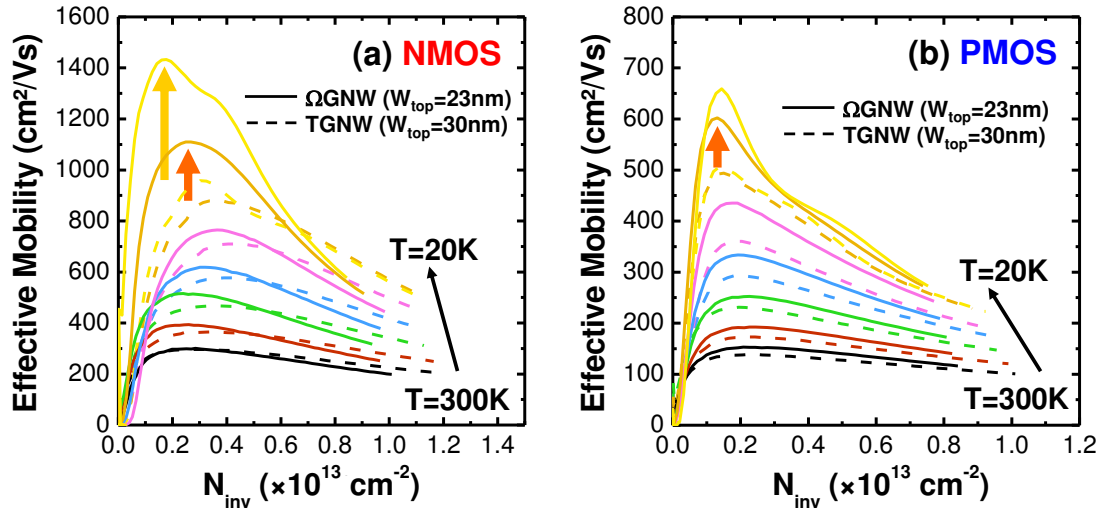


Fig. 3-23. Effective mobility μ_{eff} as a function of N_{inv} extracted at varying temperatures for SOI TG and Ω G NW (a) NMOS and (b) PMOS devices.

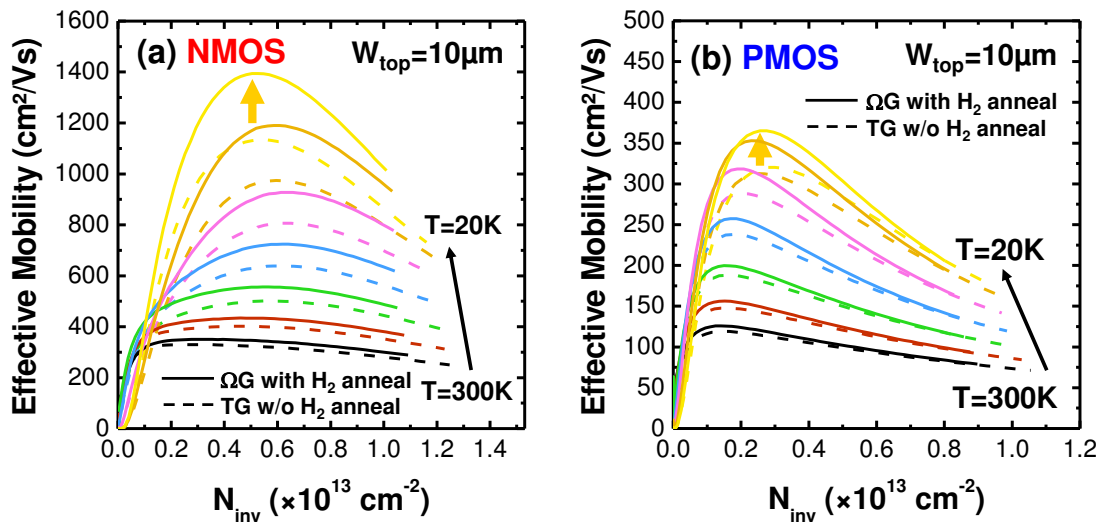


Fig. 3-24. Effective mobility μ_{eff} as a function of N_{inv} extracted at varying temperatures in SOI wide FET with or without additional H_2 anneal process for (a) NMOS and (b) PMOS devices.

3.2.2.3 Impact of tensile strain

In the following, the impact of an additional tensile strain on transport properties is discussed. The tensile strain is expected to be beneficial for electron transport in NMOS FETs. The significant improvement of electron mobility with tensile strain at various

Chapter 3. Carrier transport characterizations

temperatures is confirmed in Fig.3-25a for TGNWs. The maximum mobility values for sSOI FETs, $\mu_{\max} \approx 750 \text{ cm}^2/\text{Vs}$ at $N_{\text{inv}} \approx 0.2 \times 10^{13} \text{ cm}^{-2}$ and $T=100\text{K}$ in TGNW and $\mu_{\max} \approx 950 \text{ cm}^2/\text{Vs}$ at $N_{\text{inv}} \approx 0.7 \times 10^{13} \text{ cm}^{-2}$ and $T=100\text{K}$ in wide FET, are enhanced (Fig.3-25b). In addition, the μ_{\max} peak shift between wide FET and TGNW is similarly observed for sSOI FETs.

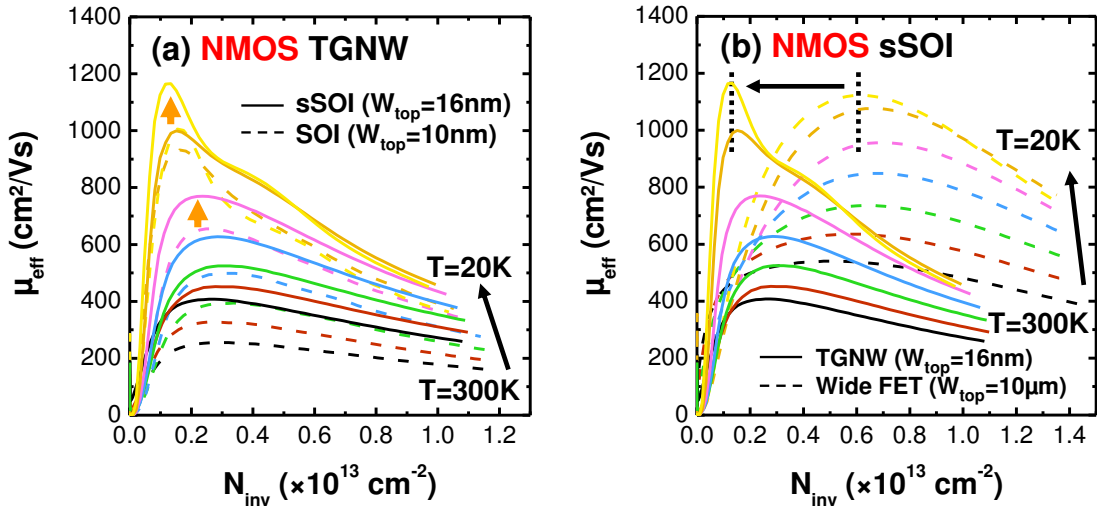


Fig. 3-25. Effective mobility μ_{eff} as a function of N_{inv} extracted at varying temperatures, showing (a) comparison between sSOI wide FET and TGNW devices, and (b) comparison between SOI and sSOI TGNW FETs.

Figure 3-26 shows the μ_{eff} extracted at high $N_{\text{inv}} = 1.0 - 0.8 \times 10^{13} \text{ cm}^{-2}$ as a function of channel width W_{top} with comparison between SOI and sSOI devices in TG and ΩG FETs. For SOI devices, the behavior is well explained by the contribution of top and side-wall mobility and the surface orientation dependence of the mobility (Table 3-1). The Si(110) side-walls are beneficial to hole transport parallel to [110]-oriented channel, while Si(100) top surface is advantageous to electron transport. For NMOS, the mobility is therefore degraded as top surface area decreases, *i.e.* as the W_{top} decreases. On the other hand, the mobility in PMOS is increased as side-wall contribution enlarges. The hole mobility enhancement and the electron mobility degradation as W_{top} decreases is similar in TG and ΩG NWs as already noticed.

Chapter 3. Carrier transport characterizations

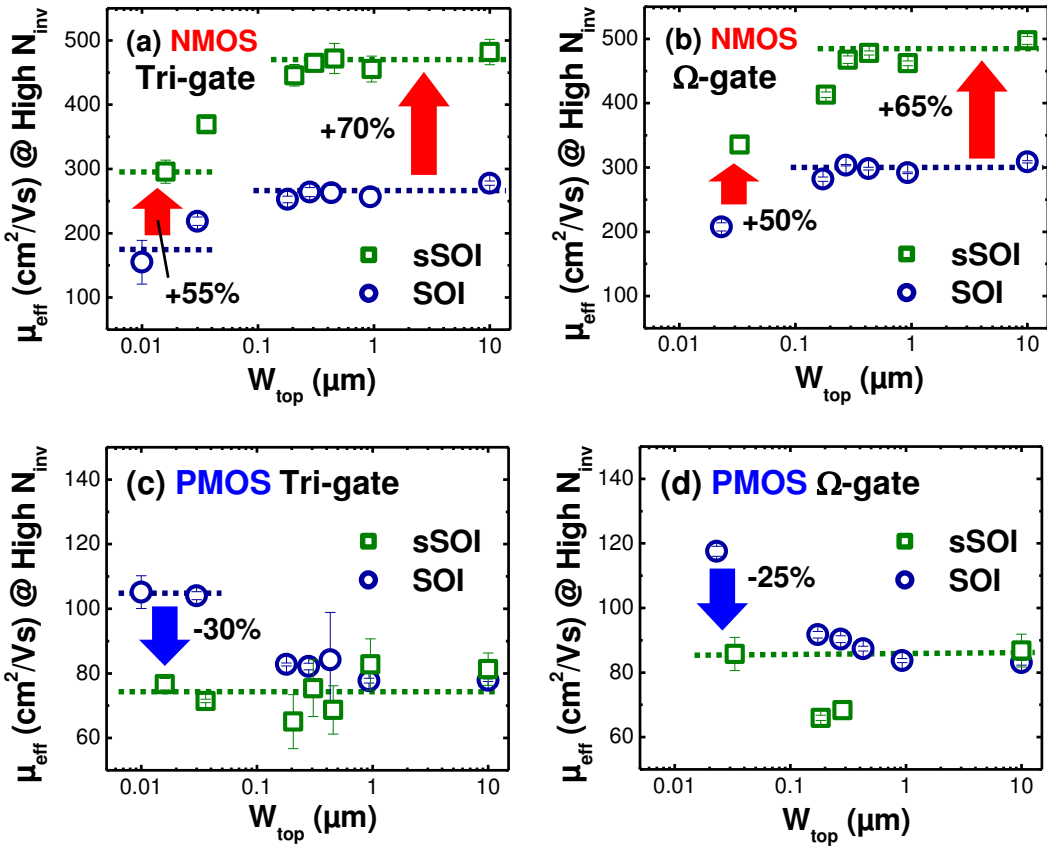


Fig. 3-26. Effective mobility μ_{eff} at high N_{inv} as a function of W_{top} for SOI and sSOI (a,b) NMOS and (c,d) PMOS FETs at room temperature (300K) with comparison between (a,c) TG and (b,d) ΩG devices. The mobility was extracted at $N_{\text{inv}}=10^{13} \text{ cm}^{-2}$ for the both N- and PMOS TG FETs. In ΩG devices, the mobility was extracted at $N_{\text{inv}}=0.9\times10^{13} \text{ cm}^{-2}$ for NMOS, and $N_{\text{inv}}=0.8\times10^{13} \text{ cm}^{-2}$ for PMOS FETs, respectively.

Table 3-1. Brief summary of strain effect on carrier transport along [110]-oriented channel for various stress configurations (mainly established from piezoresistive coefficients and results given in Refs. [3-29,3-31~3-38]).

Strain (transport // [110])	NMOS		PMOS	
	(100)	(110)	(100)	(110)
no strain	0	-	0	+
biaxial tensile	+		- / =	
uniaxial tensile // [110]	++	++	--	-

Chapter 3. Carrier transport characterizations

For sSOI devices the effect of tensile strain for different surface orientations and stress conditions (biaxial vs. uniaxial) has to be taken into account to understand our results. As the width decreases, the biaxial stress in wide (100) plane changes to a uniaxial stress along the [110]-oriented channel direction originating from lateral strain relaxation (cf. Fig.2-19). Physical and electrical characterizations have shown that full lateral relaxation occurs in our NWs for W_{top} below roughly 50 nm [3-19].

Figure 3-26 shows that the addition of a uniaxial tensile strain is very effective in TG devices. In particular we have obtained electron mobility enhancement in NMOS sSi NWs (with up to +55% gain in μ_{eff} for $W_{top}=10\text{nm}$) which overcomes the electron mobility loss inherent to unstrained Si NWs with (110) side-walls (Fig.3-26a,b). On the contrary, for PMOS, the hole mobility is degraded by tensile uniaxial stress along the channel, especially for (100) surface (Table 3-1 [3-31]). In (110) side-wall surface the better hole mobility in unstrained case is counterbalanced by the detrimental effect of a uniaxial tensile strain. As a result, as the width W_{top} is decreased the total hole mobility in sSOI NWs is no more improved as compared to wide transistors, and remains roughly constant with W_{top} variation (Fig.3-26c,d).

We also noticed that both TG and Ω G NWs exhibit roughly the same mobility improvement/degradation for the similar W_{top} , for NMOS as well as for PMOS. This result suggests that the strain relaxation is the same in both geometries, and that the piezoresistive properties are identical in TG and Ω G NWs despite the more complex inversion surface orientations of Ω GNW.

In order to have a better understanding of the physics behind, and a more quantitative model, one must also account for the confinement effect in NWs [3-44~3-47]. For NMOS NWs, a uniaxial tensile strain favors the proportion of fast electrons, and suppresses intervalley scattering, which enhances the mobility. The strain has also significant effects on the transport mass of -z valleys in [110] Si NWs [3-45]. In particular a shear stress breaks the symmetry between transverse mass axes of the Δ_z valleys, leading to the decrease of the transport effective mass for tensile strain ($\varepsilon_{||}>0$). The decrease of effective mass enhances the average velocity of the carriers, reduces intersubband scattering, and therefore increases the mobility. For PMOS, the confinement of Si NWs tends to promote light holes (LH) bands in [110] directions. A compressive strain strengthens the LH character of the highest valence subbands,

Chapter 3. Carrier transport characterizations

pushing heavy hole (HH) subbands down. This leads to a large increase of the mobility. On the contrary, tensile strain brings back up HH subbands which degrade the total mobility.

All these results are in qualitative agreement with the piezoresistance (PR) measurements performed on corresponding NWs, giving the longitudinal piezoresistive coefficients $\pi_L = -545 \times 10^{-12} \text{ Pa}^{-1}$ and $\pi_L = +280 \times 10^{-12} \text{ Pa}^{-1}$ for NMOS and PMOS TGNWs, respectively [3-39,3-43]. In the PR theory, we have $\Delta\mu/\mu = -\pi_L \times \sigma_{\text{stress}}$, with σ_{stress} the applied stress in the longitudinal direction. The sign of π_L denotes an increase or a decrease of mobility with a compressive ($\sigma_{\text{stress}} < 0$) or a tensile ($\sigma_{\text{stress}} > 0$) stress.

Next, the μ_{eff} extracted at a constant high N_{inv} (0.7 and $0.8 \times 10^{13} \text{ cm}^{-2}$ for PMOS and NMOS, respectively) has been plotted as a function of temperature, for both SOI and sSOI FETs (Fig.3-27). Below 100 K, the phonon scattering contribution is negligible, and the mobility at high N_{inv} saturates, as a consequence of the dominant surface roughness scattering contribution. TG and Ω G NWs also exhibit the same mobility behavior in both N- and PMOS case. For NMOS, phonon-limited mobility at high temperature (above 100K) is improved for strained devices. Electron mobility is degraded on the narrowest W_{top} in both SOI and sSOI FETs without correlation to the channel shape, in agreement with dominant (110) side-walls for NWs. For PMOS, the mobility improvement of wide FETs and the degradation of NWs in sSOI FETs are observed in the whole temperature range. The hole mobility is degraded by surface roughness scattering on uniaxial strained NWs in contrast to the improvement in biaxial strained wide FETs.

Chapter 3. Carrier transport characterizations

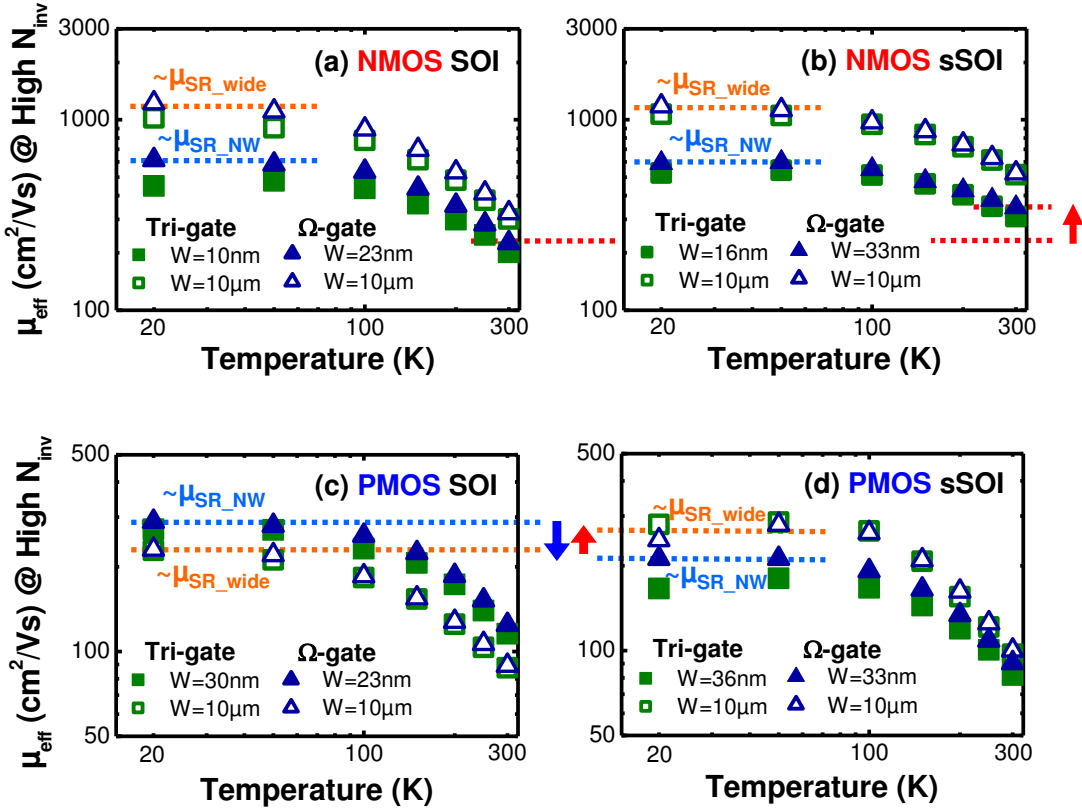


Fig. 3-27. Effective mobility μ_{eff} extracted at high N_{inv} as a function of temperature in (a,c) SOI and (b,d) sSOI devices for (a,b) NMOS and (c,d) PMOS FETs. The mobility was extracted at $N_{\text{inv}}=0.8 \times 10^{13} \text{ cm}^{-2}$ for NMOS and $N_{\text{inv}}=0.7 \times 10^{13} \text{ cm}^{-2}$ for PMOS devices, respectively.

Finally, Fig.3-28 and Table 3-2 show the values of the power law exponent γ of the temperature dependent maximum mobility ($\mu_{\text{max}} \sim T^{-\gamma}$) extracted for all the FETs studied here. Above 77 K, the slope of the temperature dependent mobility is driven by phonon scattering, especially at moderate N_{inv} (typically around μ_{max}). For SOI or sSOI, the values do not differ significantly for each structure: wide, TG or ΩG NW FETs. On the other hand, the temperature dependence changes significantly when comparing unstrained (SOI) and strained (sSOI) devices, especially for NMOS. These results are in good agreement with values of the temperature coefficient which are similar for (100) and (110) planes [3-10]. They also indicate that the temperature dependence of phonon-limited electron mobility and the hole mobility is mainly governed by the strain

Chapter 3. Carrier transport characterizations

effect down to NW with W_{top} of 10nm. A decrease of the values of γ in sSOI NMOS FETs highlights the reduced intervalley phonon scattering by tensile strain. Furthermore, no significant difference in the temperature dependence of μ_{eff} can be observed between TG and Ω G NWs, revealing again no significant influence of cross-sectional shape and dimension of the channel.

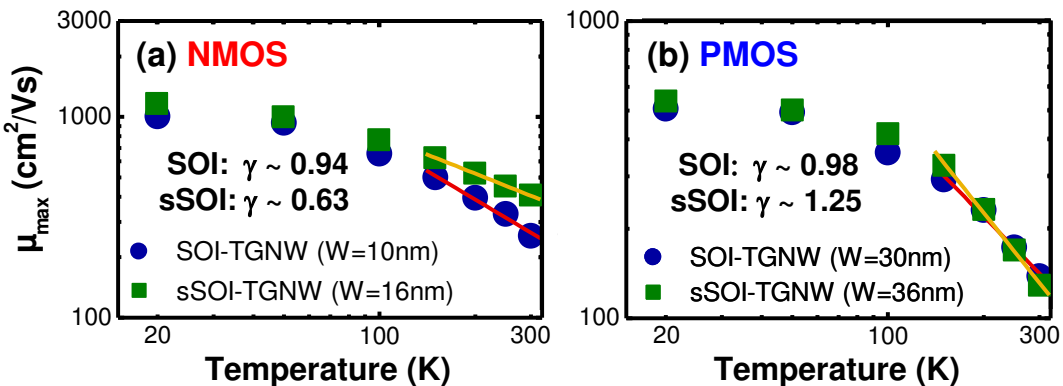


Fig. 3-28. Maximum mobility μ_{max} extracted as a function of temperature in SOI and sSOI (a) NMOS and (b) PMOS TGNW FETs.

Table 3-2. Extracted power law exponent γ in the temperature dependence of maximum mobility $\mu_{max} \sim T^{-\gamma}$.

Values of power law exponent γ		NMOS		PMOS	
		SOI	sSOI	SOI	sSOI
Tri-gate w/o H ₂ anneal	Wide (10μm)	0.95	0.64	1.00	1.18
	NW	0.94	0.63	0.98	1.25
Ω -gate with H ₂ anneal	Wide (10μm)	1.05	0.69	1.03	1.07
	NW	1.05	0.41	1.12	1.13

3.2.3 Low-field mobility

3.2.3.1 Extracted low-field mobility

The μ_0 is extracted using the Y-function method as a function of L_g for the narrowest single-channel NW and widest FETs for reference SOI in Fig.3-29. Both N- and PMOS

Chapter 3. Carrier transport characterizations

devices exhibit a decreasing trend of μ_0 with L_g below 200nm and this trend is in agreement with previous observations on wide bulk and SOI devices [3-26,3-40~3-42]. This degradation with decreasing L_g is often attributed to the enhanced impurity scattering influence due to closer proximity between S/D regions [3-48]. The degradation is more abrupt in NWs, mainly occurring in the range below 100nm. This may be attributed to emphasized one dopant influence in NW, *i.e.* the narrow contact between body and S/D regions. For PMOS case, it should be noticed that NW shows lower μ_0 than wide FET in the degraded region. As mentioned above, studies on effective mobility in 10 μm -long 50-multiple channel tri-gate NW FET with (100) top surface shows mobility improvement compared to the wide FET owing to (110) side-wall contribution with an advantage for hole transport [3-25,3-28]. These extractions seem to indicate that the length dependent μ_0 deterioration is more significant for NW device, compensating and exceeding the mobility advantage by surface orientation contribution.

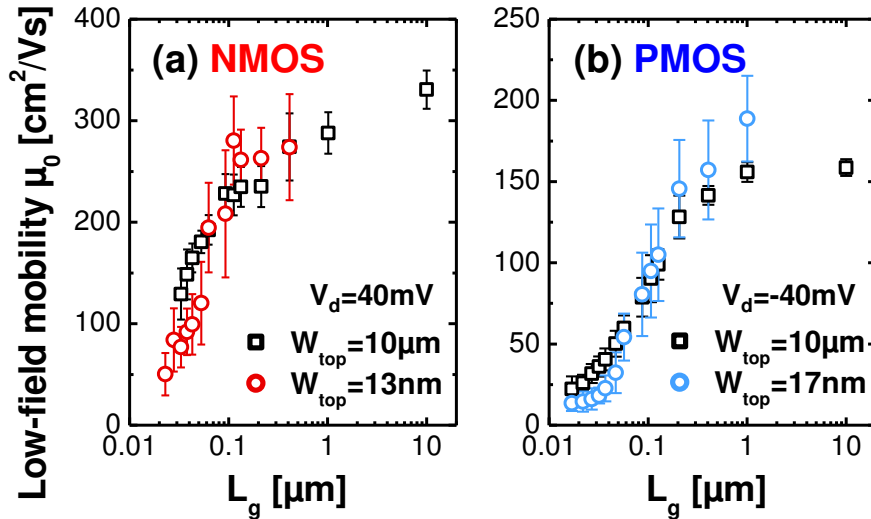


Fig. 3-29. Low-field mobility μ_0 as a function of L_g with comparison between the widest FETs and narrowest NWs in reference SOI (a) NMOS and (b) PMOS devices.

Figure 3-30 demonstrates again that sSOI devices provide great advantage to enhance electron transport compared to the others. For the widest FETs, the mobility gain relative to reference SOI devices is decreased as L_g is shortened (Fig.3-30c), while

Chapter 3. Carrier transport characterizations

the long devices have a μ_0 gain as high as +110% at a maximum. The advantage is sustained in the narrowest NWs, and the gain is maintained in whole L_g range with a value of ~+50% whatever L_g (Fig.3-30d). The difference in the gain behavior between wide FETs and NWs results from the strain configuration: biaxial tensile strain for wide FETs or uniaxial tensile strain for NWs. Additional H₂ anneal process degrades the μ_0 in entire L_g range with the detrimental gain (loss) down to -49% for both widest and narrowest NW FETs. [100]-oriented devices show similar μ_0 level for wide FETs and the narrowest NWs despite a better conduction expected for electrons in the side-walls [3-42].

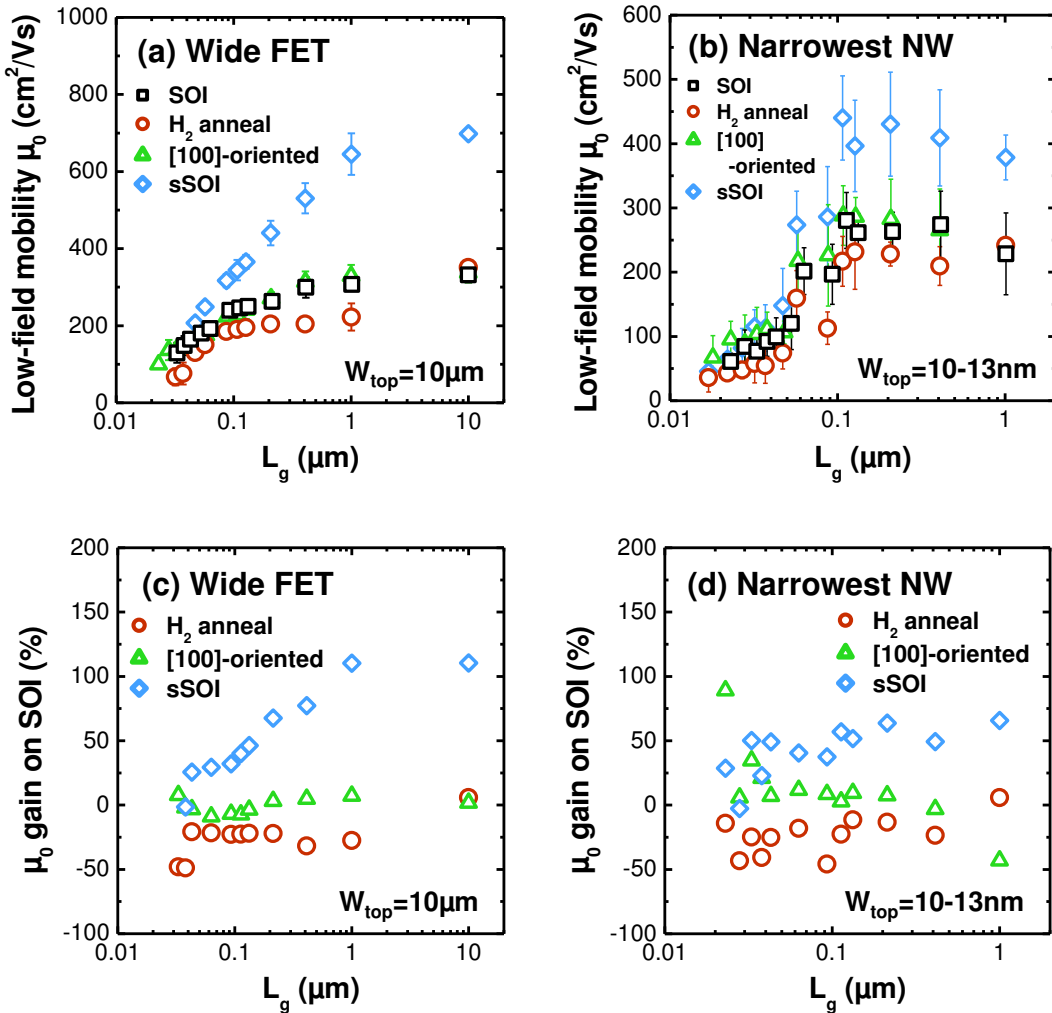


Fig. 3-30. Low-field mobility μ_0 as a function of L_g with comparison among NMOS technological splits in (a) the widest FET and (b) the narrowest NW devices. (c,d) Summary of μ_0 gain compared with reference SOI case.

Chapter 3. Carrier transport characterizations

[Figure 3-31](#) summarizes low-field mobility for PMOS devices. Additional H₂ anneal degrades somewhat the hole mobility in wide FETs, and almost maintains the performance for the narrowest NWs except long devices with L_g=1μm. The 3-types of stressor (SiGe channel, SiGe S/D, and compressive CESL) efficiently improves hole mobility in both wide and NW FETs, especially for NW devices. For wide FETs, all stressors are effective in the devices with shorter L_g than 400nm, and a maximum μ_0 peak is observed at L_g=400nm for n- and cSG-S/D devices. The μ_0 gain compared to reference SOI case is calculated and plotted in [Fig.3-31e](#). We have obtained a gain as high as ~+60-65% for L_g ranging from 32nm to 127nm for cSG-S/D and cSGOI devices.

Strained NWs show a maximum μ_0 around L_g=100nm as a competition between strain enhanced mobility (which could depend on L_g as for cCESL and SiGe-S/D), and mobility degradation with decreasing L_g due to S/D proximity (as in unstrained NWs). An increasing mobility gain is however observed for decreasing L_g ([Fig.3-31f](#)), reaching values as high as ~+525-540% for cSG-S/D and nSGOI NWs. In particular nSGOI NWs exhibit a spectacular μ_0 gain of +333% for the shortest L_g of 17-18nm. This result suggests the higher efficiency of a uniform high uniaxial compressive strain on hole transport, compared to a uniaxial strain which depends on the position under the gate (cCESL or SiGe S/D).

Chapter 3. Carrier transport characterizations

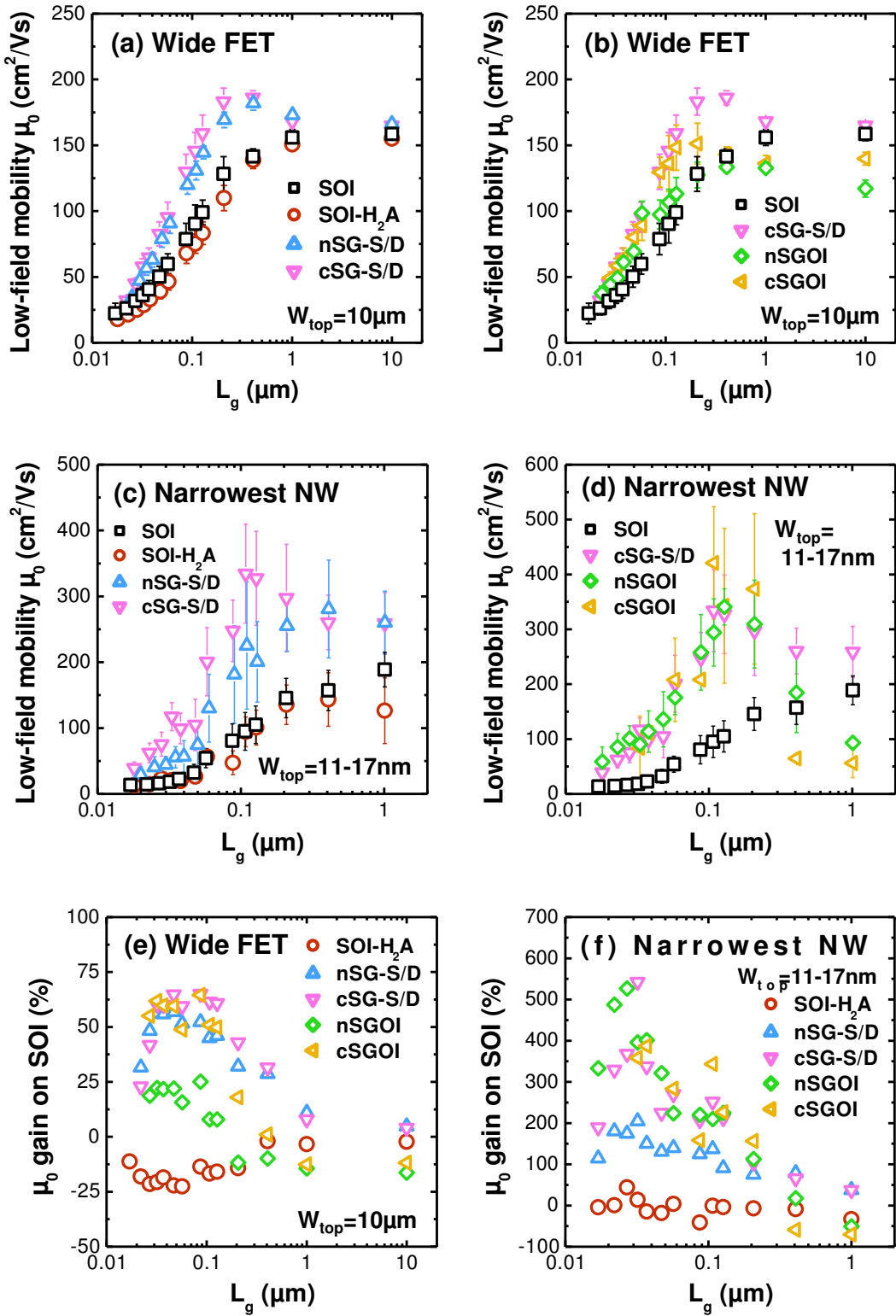


Fig. 3-31. Low-field mobility μ_0 as a function of L_g with comparison among PMOS technological splits in (a,b) the widest FET and (c,d) the narrowest NW devices. (e,f) Summary of μ_0 gain compared with reference SOI case.

Chapter 3. Carrier transport characterizations

3.2.3.2 Mobility degradation factor

We use an empirical model to describe the channel length dependent mobility decrease as following [3-26]:

$$\frac{1}{\mu_0(L_g)} = \frac{1}{\mu_{0_max}} + \frac{\alpha_\mu}{L_g} \quad (3-16)$$

Here, two fitting parameters are defined: μ_{0_max} is the maximum low-field mobility, which is almost equal to the saturated value in long channel case, and α_μ is the mobility degradation factor. The extracted degradation factor α_μ shown in Fig.3-32 is a good indicator of the mobility degradation strength in short channel device: the higher α_μ means the larger degradation.

For all NMOS devices, higher degradation rates are found for NW FETs. PMOS SOI and SOI-H₂A devices show the same trend ($\alpha_{\mu_NW} > \alpha_{\mu_wide}$), however the values are largely higher than NMOS cases. For other PMOS FETs with stressors, the degradation rates in NWs are roughly comparable or slightly lower than wide FETs. It is thus summarized that the attenuation tendency in reference SOI PMOS is much more serious compared to NMOS case. But, the issue is relieved by using the compressive strain technologies.

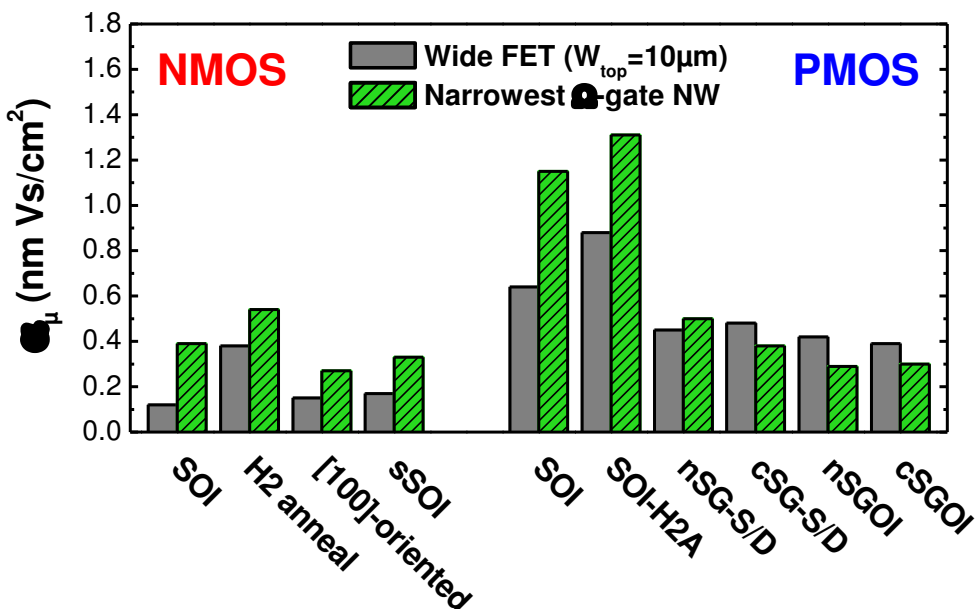


Fig. 3-32. Mobility degradation factor α_μ in the widest FETs and narrowest NWs for all the technological parameters.

Chapter 3. Carrier transport characterizations

3.2.3.3 Evaluation of source/drain series resistance

Normalized source/drain series resistance by the total effective channel width W_{tot} , $R_{\text{SD}}(\Omega \mu\text{m}) = R_{\text{SD}}(\Omega) \times W_{\text{tot}}(\mu\text{m})$, extracted by Y-function method is shown in Fig.3-33. We observed a relatively higher resistivity in PMOS ($\sim 150 \Omega \mu\text{m}$) than NMOS ($\sim 100 \Omega \mu\text{m}$) devices. Our results also show higher values of R_{SD} in both N- and PMOS NWs for reference SOI cases, revealing the need to optimize access regions in our NW devices. This tendency is however not clearly observed in other NMOS devices. The normalized resistance in H_2 annealed SOI and [100]-oriented SOI NWs is ameliorated as compared to reference SOI NW, while wide FET in SOI with H_2 anneal shows the deeply worsened. Furthermore, the both widest and narrowest NW FETs in sSOI are upgraded, therefore the benefit of biaxial and uniaxial tensile strain can be reconfirmed. For PMOS devices, the higher resistance of S/D regions in NWs is found for most of technological splits (except cSG-S/D).

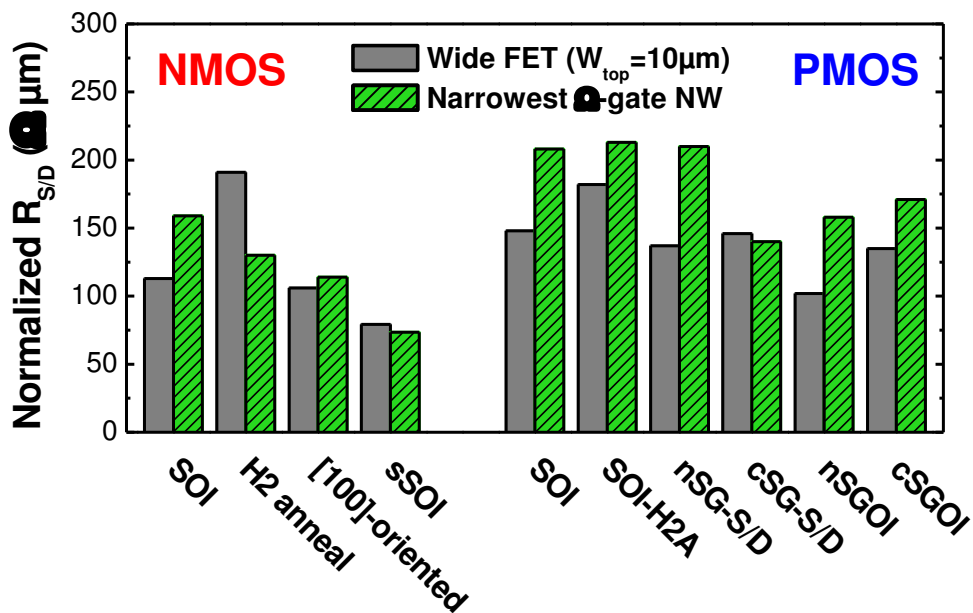


Fig. 3-33. Normalized source/drain resistance R_{SD} in the widest FETs and narrowest NWs for all the technological splits.

Chapter 3. Carrier transport characterizations

3.3 References

- [3-1] S. M. Sze and K. K. Ng: *Physics of Semiconductor Devices*, 3rd Edition, Wiley, Hoboken, 2006.
- [3-2] Y. Taur and T. K. Ning: *Fundamentals of modern VLSI devices*, 2nd Edition, Cambridge Univ. Press, Cambridge, 2009.
- [3-3] D. K. Shroder: *Semiconductor Material and Device Characterization*, 3rd Edition, Wiley-IEEE Press, London, 2005.
- [3-4] F. Balestra: *Nanoscale CMOS: innovative materials, modeling, and characterization*, Wiley-ISTE, London, 2010.
- [3-5] J. Koomen, “Investigation of the MOST channel conductance in weak inversion”, *Solid-State Electron.*, vol. 16, pp. 801-810, 1973.
- [3-6] J. R. Hauser, “Extraction of experimental mobility data for MOS devices,” *IEEE Trans. Electron Devices*, vol. 43, pp. 1981-1988, 1996.
- [3-7] J. R. Hauser, and K. Ahmed, “Characterization of ultra-thin oxides using electrical C-V and I-V measurements,” *Proc. AIP Conf.*, 1998, pp. 235-239.
- [3-8] O. Gunawan, L. Sekaric, A. Majumdar, M. Rooks, J. Appenzeller, J. W. Sleight, S. Guha, and W. Haensch, “Measurement of carrier mobility in silicon nanowires,” *Nano Lett.*, vol. 8, pp. 1566-1571, 2008.
- [3-9] S. Takagi, A. Toriumi, M. Iwase, and H. Tango, “On the universality of inversion layer mobility in Si MOSFET's: Part I - Effects of substrate impurity concentration,” *IEEE Trans. Electron Devices*, vol. 41, pp. 2357-2362, 1994.
- [3-10] S. Takagi, A. Toriumi, M. Iwase, and H. Tango, “On the universality of inversion layer mobility in Si MOSFET's: Part II - Effects of surface orientation,” *IEEE Trans. Electron Devices*, vol. 41, pp. 2363-2368, 1994.
- [3-11] G. Ghibaudo, “New method for the extraction of MOSFET parameters,” *Electron. Lett.*, vol. 24, pp. 543-545, 1988.
- [3-12] P. K. McLarty, S. Cristoloveanu, O. Faynot, V. Misra, J. R. Hauser, and J. J. Wortman, “A simple parameter extraction method for ultra-thin oxide MOSFETs,” *Solid-State Electron.*, vol. 38, pp. 1175-1177, 1995.
- [3-13] G. Reichert and T. Ouisse, “Relationship between empirical and theoretical mobility models in silicon inversion layers,” *IEEE Trans. Electron Devices*, vol. 43, pp. 1394-1398, 1996.

Chapter 3. Carrier transport characterizations

- [3-14] A. Ortiz-Conde, F. J. García Sánchez, J. J. Liou, A. Cerdeira, M. Estrada, and Y. Yue, “A review of recent MOSFET threshold voltage extraction methods,” *Microelectron. Reliab.*, vol. 42, pp. 583-596, 2002.
- [3-15] F. Andrieu, O. Faynot, X. Garros, D. Lafond, C. Buj-Dufournet, L. Tosti, S. Minoret, V. Vidal, J. C. Barbé, F. Allain, E. Rouchouze, L. Vandroux, V. Cosnier, M. Cassé, V. Delaye, C. Carabasse, M. Burdin, G. Rolland, B. Guillaumot, J. P. Colonna, P. Besson, L. Brévard, D. Mariolle, P. Holliger, A. Vandooren, C. Fenouillet-Béranger, F. Martin, and S. Deleonibus, “Comparative scalability of PVD and CVD TiN on HfO₂ as a metal gate stack for FDSOI cMOSFETs down to 25nm gate length and width,” *IEDM Tech. Dig.*, 2006, pp. 313-316.
- [3-16] K. Tachi, M. Cassé, D. Jang, C. Dupré, A. Hubert, N. Vulliet, V. Maffini-Alvaro, C. Vizioz, C. Carabasse, V. Delaye, J. M. Hartmann, G. Ghibaudo, H. Iwai, S. Cristoloveanu, O. Faynot, and T. Ernst, “Relationship between mobility and high-k interface properties in advanced Si and SiGe nanowires,” *IEDM Tech. Dig.*, 2009, pp. 313-316.
- [3-17] L. Hutin, M. Cassé, C. Le Royer, J.-F. Damлencourt, A. Pouydebasque, C. Xu, C. Tabone, J.-M. Hartmann, V. Carron, H. Grampeix, V. Mazzocchi, R. Truche, O. Weber, P. Batude, X. Garros, L. Clavelier, M. Vinet, and O. Faynot, “20nm gate length trigate pFETs on strained SGOI for high performance CMOS,” *Symp. VLSI Tech. Dig.*, 2010, pp. 37-38.
- [3-18] P. Nguyen, S. Barraud, M. Koyama, M. Cassé, F. Andrieu, C. Tabone, F. Glowacki, J.-M. Hartmann, V. Maffini-Alvaro, D. Rouchon, N. Bernier, D. Lafond, M.-P. Samson, F. Allain, C. Vizioz, D. Delprat, B.-Y. Nguyen, C. Mazuré, O. Faynot, and M. Vinet, “High mobility Ω-gate nanowire p-FET on cSGOI substrates obtained by Ge enrichment technique,” *Proc. IEEE S3S Conf.*, 2014.
- [3-19] R. Coquand, M. Cassé, S. Barraud, P. Leroux, D. Cooper, C. Vizioz, C. Comboroure, P. Perreau, V. Maffini-Alvaro, C. Tabone, L. Tosti, F. Allain, S. Barnola, V. Delaye, F. Aussenaс, G. Reimbold, G. Ghibaudo, D. Munteanu, S. Monfray, F. Boeuf, O. Faynot, and T. Poiroux, “Strain-induced performance enhancement of tri-gate and omega-gate nanowire FETs scaled down to 10nm width,” *Symp. VLSI Tech. Dig.*, 2012, pp. 13-14.

Chapter 3. Carrier transport characterizations

- [3-20] S. Barraud, R. Coquand, V. Maffini-Alvaro, M.-P. Samson, J.-M. Hartmann, L. Tosti, M. Cassé, V.-H. Nguyen, F. Triozon, Y.-M. Niquet, C. Tabone, P. Perreau, F. Allain, C. Vizioz, C. Comboroure, F. Aussénac, S. Monfray, G. Ghibaudo, F. Boeuf, B. De Salvo, and O. Faynot, “Scaling of Ω -gate SOI nanowire N- and P-FET down to 10nm gate length: size- and orientation-dependent strain effects,” *Symp. VLSI Tech. Dig.*, 2013, pp. T230-T231.
- [3-21] D. V. Lang, R. People, J. C. Bean, and A. M. Sergent, “Measurement of the band gap $\text{Ge}_x\text{Si}_{1-x}/\text{Si}$ strained-layer heterostructures,” *Appl. Phys. Lett.*, vol. 47, pp. 1333-1335, 1985.
- [3-22] J.-S. Goo Q. Xiang, Y. Takamura, F. Arasnua, E. N. Paton, P. Besser, J. Pan, and M.-R. Lin, “Band offset induced threshold variation in strained-Si nMOSFETs,” *IEEE Electron Device Lett.*, vol. 24, pp. 568-570, 2003.
- [3-23] J.-S. Lim, S. E. Thompson, and J. G. Fossum, “Comparison of threshold-voltage shifts for uniaxial and biaxial tensile-stressed n-MOSFETs,” *IEEE Electron Device Lett.*, vol. 25, pp. 731-733, 2004.
- [3-24] S. Barraud, R. Coquand, M. Cassé, M. Koyama, J.-M. Hartmann, V. Maffini-Alvaro, C. Comboroure, C. Vizioz, F. Aussénac, O. Faynot, and T. Poiroux, “Performance of omega-shaped-gate silicon nanowire MOSFET with diameter down to 8 nm,” *IEEE Electron Device Lett.*, vol. 33, pp. 1526-1528, 2012.
- [3-25] R. Coquand, S. Barraud, M. Cassé, P. Leroux, C. Vizioz, C. Comboroure, P. Perreau, E. Ernst, M.-P. Samson, V. Maffini-Alvaro, C. Tabone, S. Barnola, D. Munteanu, G. Ghibaudo, S. Monfray, F. Boeuf, and T. Poiroux “Scaling of high-k/metal-gate trigate SOI nanowire transistors down to 10nm width,” *Proc. ULIS*, 2012.
- [3-26] G. Bidal, D. Fleury, G. Ghibaudo, F. Boeuf, and T. Skotnicki, “Guidelines for MOSFET device optimization accounting for L-dependent mobility degradation,” *Proc. SNW*, 2009.
- [3-27] F. Andrieu, C. Dupré, F. Rochette, O. Faynot, L. Tosti, C. Buj, E. Rouchouze, M. Cassé, B. Ghyselen, I. Cayrefoureq, L. Brévard, F. Allain, J. C. Barbé, J. Cluzel, A. Vandooren, S. Denorme, T. Ernst, C. Fenouillet-Béranger, C. Jahan, D. Lafond, H. Dansas, B. Previtali, J. P. Colonna, H. Grampeix, P. Gaud, C. Mazuré, and S. Deleonibus, “25nm short and narrow strained FDSOI with TiN/HfO₂ gate stack,” *Symp. VLSI Tech. Dig.*, 2006, pp. 134-135.
- [3-28] J. Chen, T. Saraya, and T. Hiramoto, “Mobility enhancement over universal mobility in (100) silicon nanowire gate-all-around MOSFETs with width and height of less than 10nm

Chapter 3. Carrier transport characterizations

- range," *Symp. VLSI Tech. Dig.*, 2010, pp. 175-176.
- [3-29] M. V. Fischetti, Z. Ren, P. M. Solomon, M. Yang, and K. Rim, "Six-band kp calculation of the hole mobility in silicon inversion layers: Dependence on surface orientation, strain, and silicon thickness," *J. Appl. Phys.*, vol. 94, pp. 1079-1095, 2003.
- [3-30] K. Tachi, M. Cassé, S. Barraud, C. Dupré, A. Hubert, N. Vulliet, M. E. Faivre, C. Vizioz, C. Carabasse, V. Delaye, J. M. Hartmann, H. Iwai, S. Cristoloveanu, O. Faynot, and T. Ernst, "Experimental study on carrier transport limiting phenomena in 10 nm width nanowire CMOS transistors," *IEDM Tech. Dig.*, 2010, pp. 784-787.
- [3-31] H. Irie, K. Kita, K. Kyuno, and A. Toriumi, "In-plane mobility anisotropy and universality under uni-axial strains in n- and p-MOS inversion layers on (100), (110), and (111) Si," *IEDM Tech. Dig.*, 2004, pp. 225-228.
- [3-32] T. Mizuno, N. Sugiyama, T. Tezuka, Y. Moriyama, S. Nakaharai, and S. Takagi, "(110)-Surface strained-SOI CMOS devices," *IEEE Trans. Electron Devices*, vol. 52, pp. 367-374, 2005.
- [3-33] K. Uchida, T. Krishnamohan, K. C. Saraswat, and Y. Nishi, "Physical mechanisms of electron mobility enhancement in uniaxial stressed MOSFETs and impact of uniaxial stress engineering in ballistic regime," *IEDM Tech. Dig.*, 2005, pp. 129-132.
- [3-34] B. Mereu, C. Rossel, E. P. Gusev, and M. Yang, "The role of Si orientation and temperature on the carrier mobility in metal oxide semiconductor field-effect transistors with ultrathin HfO₂ gate dielectrics," *J. Appl. Phys.*, vol. 100, 014504, 2006.
- [3-35] K. Uchida, A. Kinoshita, and M. Saitoh, "Carrier transport in (110) nMOSFETs: Subband structures, non-parabolicity, mobility characteristics, and uniaxial stress engineering," *IEDM Tech. Dig.*, 2006.
- [3-36] A. Teramoto, T. Hamada, M. Yamamoto, P. Gaubert, H. Akahori, K. Nii, M. Hirayama, K. Arima, K. Endo, S. Sugawa, and T. Ohmi, "Very high carrier mobility for high-performance CMOS on a Si(110) surface," *IEEE Trans. Electron Devices*, vol. 54, pp. 1438-1445, 2007.
- [3-37] G. Sun, Y. Sun, T. Nishida, and S. E. Thompson, "Hole mobility in silicon inversion layers: Stress and surface orientation," *J. Appl. Phys.*, vol. 102, 084501, 2007.
- [3-38] Y. Sun, S. E. Thompson, and T. Nishida: *Strain Effect in Semiconductors*, Springer&Verlag, New York, 2010.
- [3-39] M. Cassé, S. Barraud, C. Le Royer, M. Koyama, R. Coquand, D. Blachier, F. Andrieu, G. Ghibaudo, O. Faynot, T. Poiroux, and G. Reimbold, "Study of piezoresistive properties of advanced CMOS transistors: thin film SOI, SiGe/SOI, unstrained and strained tri-gate

Chapter 3. Carrier transport characterizations

- nanowires," *IEDM Tech. Dig.*, 2012, pp. 637-640.
- [3-40] F. Andrieu, T. Ernst, F. Lime, F. Rochette, K. Romanjek, S. Barraud, C. Ravit, F. Boeuf, M. Jurczak, M. Cassé, O. Weber, L. Brévard, G. Reimbold, G. Ghibaudo, and S. Deleonibus, "Experimental and comparative investigation of low and high field transport in substrate- and process-induced strained nanoscaled MOSFETs," *Symp. VLSI Tech. Dig.*, 2005, pp. 176-177.
- [3-41] F. Lime, F. Andrieu, J. Derix, G. Ghibaudo, F. Boeuf, and T. Skotnicki, "Low temperature characterization of effective mobility in uniaxially and biaxially strained nMOSFETs," *Solid-State Electron.*, vol. 50, pp. 644-649, 2006.
- [3-42] A. Cros, K. Romanjek, D. Fleury, S. Harrison, R. Cerutti, P. Coronel, B. Dumont, A. Pouydebasque, R. Wacquez, B. Duriez, R. Gwoziecki, F. Boeuf, H. Brut, G. Ghibaudo, and T. Skotnicki, "Unexpected mobility degradation for very short devices : A new challenge for CMOS scaling," *IEDM Tech. Dig.*, 2006.
- [3-43] M. Cassé, S. Barraud, R. Coquand, M. Koyama, D. Cooper, C. Vizioz, C. Comboroure, P. Perreau, V. Maffini-Alvaro, C. Tabone, L. Tosti, S. Barnola, V. Delaye, F. Aussénac, G. Ghibaudo, H. Iwai, and G. Reimbold, "Strain-enhanced performance of Si-nanowire FETs," *ECS Transactions*, vol. 53, pp. 125-136, 2013.
- [3-44] M. Baykan, S. E. Thompson, and T. Nishida, "Strain effects on three-dimensional, two-dimensional, and one-dimensional silicon logic devices: Predicting the future of strained silicon," *J. Appl. Phys.*, vol. 108, 093716, 2010.
- [3-45] Y.-M. Niquet, C. Delerue, and C. Krzeminski, "Effects of strain on the carrier mobility in silicon nanowires," *Nano Lett.*, vol. 12, pp. 3545-3550, 2012.
- [3-46] R. Kotlyar, T. D. Linton, R. Rios, M. D. Giles, S. M. Cea, K. J. Kuhn, M. Povolotskyi, T. Kubis, and G. Klimeck, "Does the low hole transport mass in <110> and <111> Si nanowires lead to mobility enhancements at high field and stress: A self-consistent tight-binding study," *J. Appl. Phys.* vol. 111, 123718, 2012.
- [3-47] Y.-M. Niquet, C. Delerue, and D. Rideau, "Orientational and strain dependence of the mobility in silicon nanowires," *Proc. ULIS*, 2012, pp. 49-52.
- [3-48] G. Ghibaudo, M. Mouis, L. Pham-Nguyen, K. Bennamane, I. Pappas, A. Cros, G. Bidal, D. Fleury, A. Claverie, G. Benassayag, P.-F. Fazzini, C. Fenouillet-Beranger, S. Monfray, F. Boeuf, S. Cristoloveanu, T. Skotnicki, N. Collaert, "Electrical transport characterization of nano CMOS devices with ultra-thin silicon film," *Proc. IWJT*, 2009, pp. 58-63.

Chapter 4

Low-frequency noise characterizations

4.1 Fundamentals

- 4.1.1 Introduction to main noise sources**
- 4.1.2 Low-frequency noise in MOSFET**
- 4.1.3 Measurement setup**

4.2 Experimental results

- 4.2.1 1/f noise behavior and CNF+CMF model**
- 4.2.2 Flat-band voltage noise**
- 4.2.3 Coulomb scattering parameter**
- 4.2.4 Oxide trap density**
- 4.2.5 Drain bias influence**
- 4.2.6 Comparison with ITRS requirements for 1/f LFN**

4.3 References

Chapter 4. Low-frequency noise characterizations

4.1 Fundamentals

4.1.1 Introduction to main noise sources

Generally, “noise” is referred to as unwanted and detrimental signal mainly appearing in telecommunications, such as sounds and images. Noise usually interferes with communications through transmitting/receiving processes by distorting the raw data. Noise spontaneously and randomly arises in every electronic device, on the current or voltage, and could disrupt the signals. Noise from external sources such as vibrations, lights, interferences from AC power lines, etc... is often considered as a main hindrance, but it can be suppressed or removed by appropriate shielding, filtering, and layout design for electronic devices and circuits. Despite reduction of external noise, inherent noise still exists in each electronic device. Internal noise can be efficiently reduced by optimizing the fabrication process and design of the devices and circuits. From an engineer’s point of view, performance limits of analog circuits and devices are determined by noise properties. From a physicist’s point of view, noise provides insight into the carrier transport mechanisms in the MOSFET’s channel that cannot be revealed by DC characterization. Therefore, measurement and understanding of internal noise are important in order to evaluate the performance and study the carrier transport in MOSFETs.

In general, the study of internal electronic noise in solid-state devices is carried out by measuring the current fluctuations. [Figure 4-1](#) illustrates the time dependent fluctuating current $I(t)$ due to random noise effect through a device [\[4-1\]](#), that can be expressed as:

$$I(t) = \bar{I} + i(t) \quad (4-1)$$

In this expression, \bar{I} is the average value of the current and $i(t)$ is the randomly fluctuating component as a function of time. The average of $i(t)$ monitored over a long time should always equal zero (stationary), since the value of $i(t)$ is completely random at any point in time domain. Noise investigation requires to be performed with mathematical methods based on probability theory, which allows defining the appropriate averages of randomly fluctuating variables. A commonly-used and powerful

Chapter 4. Low-frequency noise characterizations

method to interpret and characterize noise relies on variable transformation from the time domain to the frequency domain by Fourier transform.

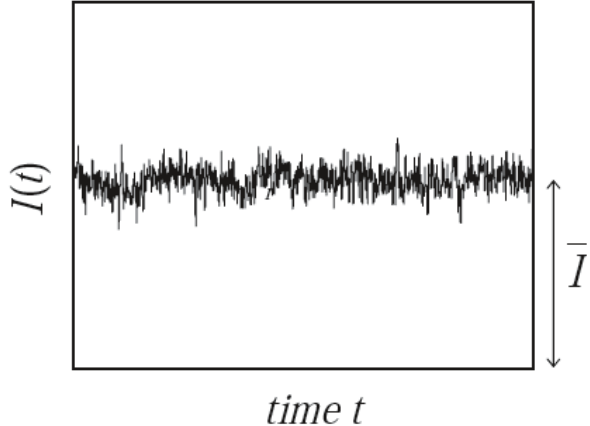


Fig. 4-1. An illustration of typical noise waveform [4-1].

The Fourier transform method is defined as:

$$X(f) = \int_{-\infty}^{\infty} x(t) \exp(-j2\pi ft) dt \quad (4-2a)$$

and reciprocally, inverse Fourier transform:

$$x(t) = \int_{-\infty}^{\infty} X(f) \exp(j2\pi ft) df \quad (4-2b)$$

where $x(t)$ is a stationary variable in time domain and $X(f)$ is the Fourier-transformed variable in frequency domain. The Fourier transform separates the random signal into the sum of simple frequency components represented mathematically as sine and cosine waves. To properly describe the noise distributed within frequency regime, the mean random signal squared (noise power) per unit frequency, named the power spectral density (PSD) $S(f)$ is generally used. The PSD is given by the autocorrelation function $R(s)$ according to the Wiener-Khintchine theorem [4-2,4-3] and can be derived as:

$$S(f) = 4 \int_0^{\infty} R(s) \cos(2\pi fs) ds \quad (4-3a)$$

$$\text{equivalently: } R(s) = \int_0^{\infty} S(f) \cos(2\pi fs) df \quad (4-3b)$$

The PSD can be measured with a spectrum analyzer for the current noise S_I and voltage

Chapter 4. Low-frequency noise characterizations

noise S_V in A^2/Hz and V^2/Hz , respectively.

There are various kinds of noise sources leading to different behaviors in frequency or time domain. In the following, representative fundamentals of the noise sources are described [4-1].

4.1.1.1 Thermal noise

Thermal noise stems from the random thermal motion of electrons in a material. In 1906, A. Einstein predicted that Brownian motion of electrons would cause fluctuations of the material resistance in thermal equilibrium [4-4]. Each time an electron is scattered and the velocity is randomized by the thermal energy. If there are more electrons moving in a certain direction than electrons moving in the other directions, a small net current is flowing. Strength and direction of the current fluctuates, but the average over time is always zero. Thus, thermal noise is nearly constant over frequency, and is also called white noise. It was first experimentally discovered by J. B. Johnson and theoretically explained by H. Nyquist in 1928 [4-5,4-6]. For this reason, thermal noise is also called Johnson or Nyquist noise.

If a piece of material with resistance R and temperature T is considered, the PSD of thermal noise current S_I or the voltage counterpart S_V can be written as:

$$S_I = \frac{4kT}{R} \quad (4-4a)$$

$$S_V = S_I R^2 = 4kTR \quad (4-4b)$$

Thermal noise exists in every resistor and resistive part of devices except at absolute zero point ($T=0\text{K}$), and needs no applied voltage bias. It is thereby frequently used for comparison with other noise sources and temperature measurement characterizing the resistance R . For instance, thermal noise is usually used to calibrate a noise measurement system, because it determines the lower limit of measured noise level in the system.

4.1.1.2 Shot noise

Shot noise is generally observed in the current flowing across a potential barrier, such as p-n junction and Schottky junction. The current is not continuous due to the

Chapter 4. Low-frequency noise characterizations

discrete nature of the charge carriers (electrons) and is given by the number of carriers flowing through the barrier during a period of time. Shot noise was firstly discovered in vacuum tubes by W. Schottky in 1918, and an equation was also derived as the Schottky formula [4-7]. The PSD of shot noise is expressed as:

$$S_I = 2qI \quad (4-5)$$

Shot noise is also considered as a white noise source, since the behavior has no frequency dependence likewise thermal noise. But, the level of shot noise is generally much lower than the thermal noise, thus it cannot be distinguished easily.

4.1.1.3 Generation-recombination (g-r) noise

Generation-recombination (g-r) noise in semiconductors is caused from random generation and recombination of charge carriers (*i.e.* electrons or holes) via trapping sites. It leads to the fluctuation of the number of carriers related to the current flowing. Electronic states localized within the forbidden bandgap are referred to as traps, and exist due to the presence of various defects or impurities in the semiconductor or at the surface [4-8]. The carrier number fluctuations by capturing/emitting the carriers can also induce several fluctuations in the carrier mobility, electric field, barrier height, width of space charge region, etc... The g-r noise PSD can be expressed as:

$$\frac{S_I}{I^2} = \frac{S_N}{N^2} = \frac{\overline{\Delta N^2}}{N^2} \cdot \frac{4\tau}{1 + (2\pi f)^2 \tau^2} \quad (4-6)$$

where N is the averaging number of carriers, $\overline{\Delta N^2}$ is the variance of the fluctuating number of carriers, and τ is the time constant of the transitions. The shape of g-r noise spectrum in Eq. (4-6) is illustrated in Fig.4-2 and is called a Lorentzian [4-1]. In general, the time constant and the relative strength of the traps differ and strongly depend on the trap energy level and spatial location. The g-r noise is only significant when the Fermi energy level is close to the trap energy level (within a few kT), and then the capture time and the emission time are almost equal. On the other hand, when the Fermi level is far above or below the trap level, the trap is occupied or emptied most of the time and few g-r events occur.

Chapter 4. Low-frequency noise characterizations

4.1.1.4 Random-telegraph-signal (RTS) noise

A special case of g-r noise is the random-telegraph-signal (RTS) noise (also called burst noise or popcorn noise), which is monitored as discrete switching events of the I_d level in the time domain in a MOSFET. The RTS noise is commonly observed in MOSFETs with small channel area and is correlated to individual carrier trapping/de-trapping between the Si substrate and traps in the gate oxide [4-9,4-10]. If only one or a few traps in the gate oxide are involved, I_d can switch between two or more states owing to random trapping/de-trapping of carriers.

For a two-level system with step difference ΔI and time durations for the lower state τ_l and for the higher state τ_h , the PSD of the current fluctuations is derived under Poisson distribution (Fig.4-3) as:

$$S_I = \frac{4(\Delta I)^2}{(\tau_l + \tau_h) \cdot \left\{ (\tau_l^{-1} + \tau_h^{-1})^2 + (2\pi f)^2 \right\}} \quad (4-7)$$

Both PSD shapes of RTS noise and g-r noise exhibit a Lorentzian type (Fig.4-2). When the number of traps contributing to the current fluctuations is small, the g-r noise is only observed as a sum of the RTS noise stemming from one or a few traps with identical time constants. In typical RTS noise investigation, the random switching process of the I_d level involved by just one trap, *i.e.* by a single electron, can be studied in the time domain. The trap energy level, spatial location of the trap, and the capture and emission behavior can be derived from the g-r and RTS noise characterizations with measuring the temperature and bias dependencies [4-8, 4-11~4-13].

Chapter 4. Low-frequency noise characterizations

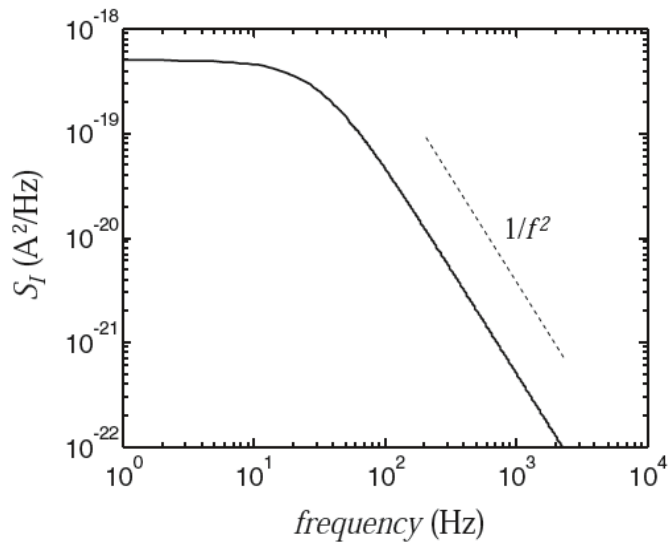


Fig. 4-2. A Lorentzian shaped PSD, plotted for the RTS noise waveform in Fig.4-3 [4-1].

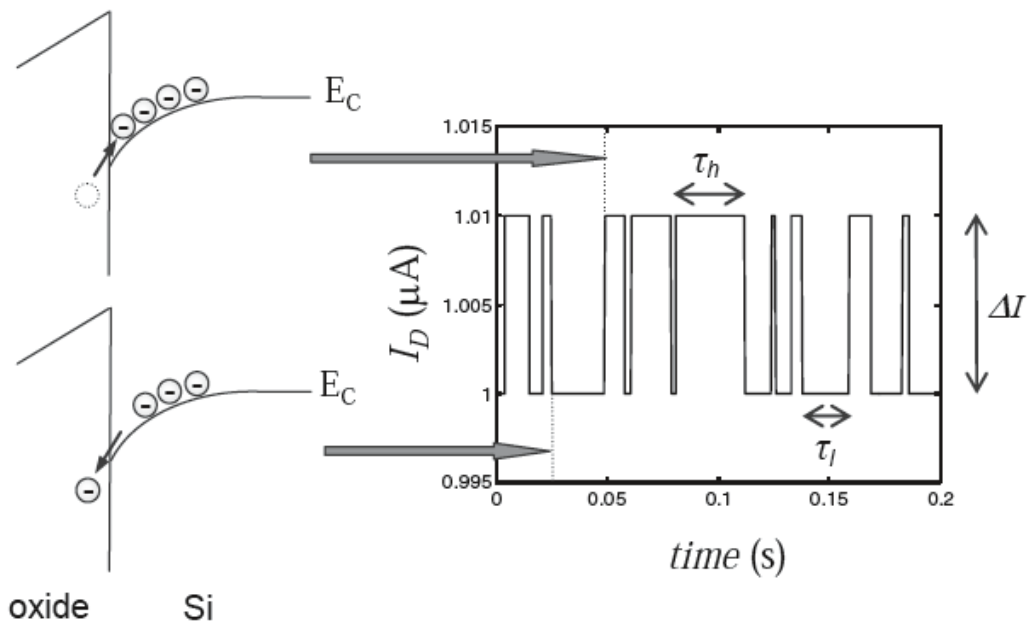


Fig. 4-3. Schematic description of RTS noise, exemplified for a MOSFET. The drain current switches between two discrete levels when a channel electron moves in and out of a trap in the gate oxide [4-1].

Chapter 4. Low-frequency noise characterizations

4.1.1.5 1/f noise

1/f noise, also called flicker noise, is the general name of fluctuations with a PSD being proportional to $1/f^\gamma$ with the value of frequency exponent γ around 1. The general form of PSD for 1/f noise is given as:

$$S_I = \frac{K \cdot I^\zeta}{f^\gamma} \quad (4-8)$$

where K is a proportional constant and ζ is a current exponent. The 1/f noise was firstly observed in vacuum tubes by J. B. Johnson in 1925 [4-14], and then was first interpreted by W. Schottky [4-15]. It has been accepted as the most general noise type in low-frequency regime of the spectrum (10^5 - 10^7 Hz) in most conductive materials and various semiconductor devices up to the present date. In general, the 1/f noise is difficult to find at high-frequency part due to the overlap with thermal noise. There are essentially two physical mechanisms of current fluctuations: fluctuations in the carrier mobility or fluctuations in the number of carriers.

For the carrier number fluctuations, the g-r noise stemming from a large number of traps can produce 1/f noise by the PSD superposition for a certain distribution of various time constants as shown in Fig.4-4. The idea of Lorentzians superposition to yield the 1/f noise behavior was suggested by J. Bernamont in 1937 [4-16] and by M. Surdin in 1939 [4-17]. The 1/f noise from fluctuations of the carrier number has been well described in large area down to small area MOSFETs. However, 1/f noise can be still observed even though the RTS noise is not involved. In such case, the 1/f behavior is attributed to the fluctuations in the carrier mobility. The physical origin of 1/f noise (carrier number fluctuations vs. mobility fluctuations) still remains controversial and the search of mechanisms of this noise is being intensively continued to the present day.

Chapter 4. Low-frequency noise characterizations

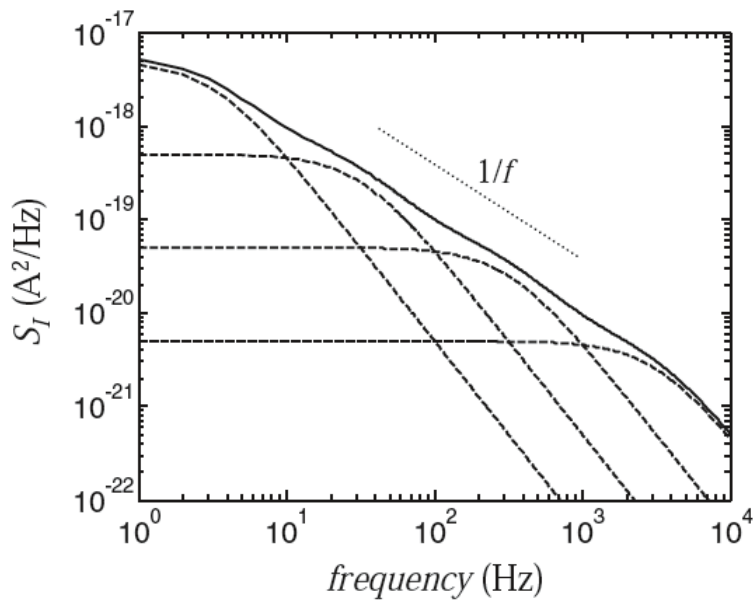


Fig. 4-4. Superposition of 4 Lorentzians giving a total spectrum that approximately exhibits a $1/f$ dependence over several decades of frequency [4-1].

4.1.2 Low-frequency noise in MOSFET

4.1.2.1 LFN measurements as a diagnostic tool

Measurement of LFN appearing in the drain current I_d is an efficient diagnostic tool to characterize the electrical properties of MOSFETs, mainly focusing on the oxide/channel interface properties. In general, LFN spectra in a MOSFET show the frequency dependent components; $1/f$ and/or $1/f^2$ (g-r) components, as mentioned above. Figure 4-5 shows a schematic of the PSDs for the $1/f$, g-r, and thermal noise at low frequency region [4-1].

Chapter 4. Low-frequency noise characterizations

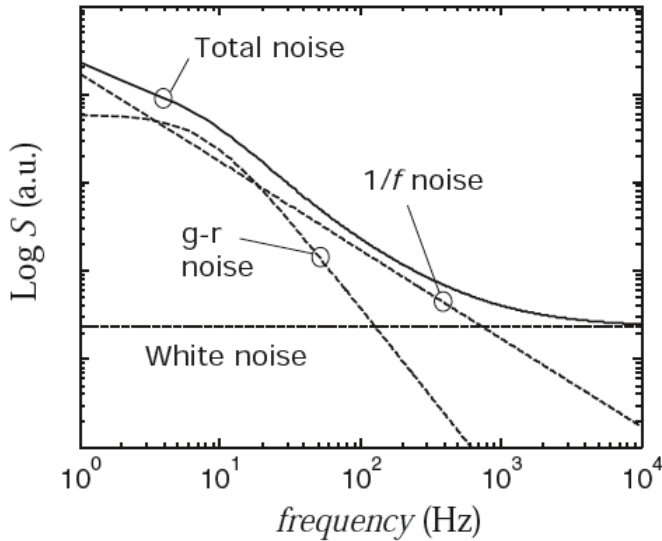


Fig. 4-5. The PSD for low-frequency noise and white noise plotted vs. frequency. The excess noise above the white noise floor is called low-frequency noise and may consist of 1/f noise or g-r noise [4-1].

Even if 1/f noise is considered to be universal for various devices, there have been controversies for its origin. The current fluctuations in materials can be understood as conductivity fluctuations. The conductivity σ is defined for drift of electrons as:

$$\sigma = qn\mu_n \quad (4-9)$$

where n is the carrier (electron) density as carrier and μ_n is the electron mobility. From the idea of conductivity fluctuations, two fluctuation models can be considered; carrier number fluctuations (CNF, Δn) and mobility fluctuations (MF, $\Delta\mu$). Several theories have been proposed to interpret l/f noise in MOSFETs, and there are two most essential frameworks:

- (i) Hooge empirical model, which presumes the MF [4-18~4-22]
- (ii) McWhorter model, which assumes the CNF by the QM tunneling transitions between oxide traps and channel [4-23~4-27]

In MOSFETs, the drain current flows in the channel, *i.e.* a narrow path confined close to the substrate surface beneath the gate oxide. In such case, CNF is mostly expected, and is actually dominant as the 1/f noise source in some reports [4-28~4-31]. Nevertheless, other published works have reported that the MF noise model tends to be better to

Chapter 4. Low-frequency noise characterizations

explain the 1/f noise especially in PMOS FETs [4-32,4-33].

Concerning 1/f noise in recent advanced MOSFETs, such as MG devices (FinFETs [4-34~4-44] and NW devices [4-45~4-54]), the origin is attributed to the carrier number fluctuations with correlated mobility fluctuations (CNF+CMF) [4-55,4-56]. This model assumes that CNF additionally induces fluctuations of the carrier mobility due to Coulomb interactions between charge carriers in the channel and trapped charges. In practice, this CNF+CMF model is suitable for MG devices [4-36,4-39,4-42~4-45,4-49, 4-52,4-54]. Consequently, LFN measurement is thought to be enough powerful even for future device nodes with more complex and ultra-scaled architectures, such as NW MOSFETs.

4.1.2.2 Hooge empirical model - Mobility fluctuations

In 1969, an empirical relation between the conductivity fluctuations showing the 1/f noise and the number of conducting carriers N was proposed by F. N. Hooge [4-18]. It is simply given as [4-18~4-21]:

$$\frac{S_\sigma}{\sigma^2} = \frac{S_R}{R^2} = \frac{S_I}{I^2} = \frac{\alpha_H}{fN} \quad (4-10)$$

where S_σ/σ^2 is the normalized conductivity noise PSD, S_R/R^2 is the normalized resistance noise PSD, and α_H is a dimensionless parameter usually referred to as the Hooge parameter. The Hooge model has successfully explained the 1/f noise in metals and bulk semiconductors. In Eq. (4-10), the factor N^{-1} means that the fluctuations only result from mobility fluctuations of the conducting carriers [4-19]. It was also proposed that only phonon scattering contributes to the mobility fluctuations [4-21].

Unfortunately, the Hooge model does not suggest any physical explanations of the MF, and cannot provide a further explanation for 1/f noise. In spite of the success of the empirical model, the lack of physical principles is a weakness. Several efforts have been made to develop a theory of MF noise model. However, none of them is widely accepted so far. Nevertheless, it has often been used to compare the noise behavior between different devices or materials.

The Hooge MF model was applied for the linear and saturation regions in MOSFET operation [4-57~4-60]. In linear region, the normalized current noise spectral density

Chapter 4. Low-frequency noise characterizations

S_{Id}/I_d^2 can be defined involving the total number of inversion carriers $N=WLQ_{inv}/q$ as:

$$\frac{S_{Id}}{I_d^2} = \frac{q\alpha_H}{fWLQ_{inv}} \quad (4-11)$$

Substituting the definition of μ_{eff} (Eq. (3-1)) into this equation, it can be seen that the S_{Id}/I_d^2 is inversely proportional to I_d as:

$$\frac{S_{Id}}{I_d^2} = \frac{q\alpha_H \mu_{eff} V_d}{fL^2 I_d} \quad (4-12)$$

In saturation region, on the other hand, Q_{inv} is non-uniformly distributed. In fact, it varies parabolically along the channel and reaches zero at the drain region edge. In such case, S_{Id}/I_d^2 is expressed considering the non-uniform inversion charge as:

$$\frac{S_{Id}}{I_d^2} = \frac{q\alpha_H}{fWL^2} \int_0^L \frac{dx}{Q_{inv}(x)} \quad (4-13)$$

Introducing here the gradual channel approximation (GCA) [4-61], the I_d leads to:

$$I_d = W\mu_{eff}Q_{inv}(x) \frac{dV}{dx} \quad (4-14)$$

Substituting the approximated Eq. (4-14) into Eq. (4-13) and assuming a constant mobility along the channel μ_{const} , a similar relationship to Eq. (4-12) is obtained as:

$$\frac{S_{Id}}{I_d^2} = \frac{q\alpha_H}{fWL^2} \int_0^L \frac{dx}{Q_{inv}(x)} = \frac{q\alpha_H}{fWL^2} \int_0^{V_d} \frac{\mu_{eff}W}{I_d} dV = \frac{q\alpha_H \mu_{const} V_d}{fL^2 I_d} \quad (4-15)$$

Therefore, MOSFETs in linear and saturation regions show the same S_{Id}/I_d^2 behavior decreasing in inverse proportion to I_d in the Hooge MF model.

4.1.2.3 McWhorter model - Carrier number fluctuations

In 1957, A. L. McWhorter dealt with 1/f noise spectra observed in germanium-based MOS structure, and proposed the charge fluctuations model caused by the tunneling between the bulk and the oxide defects as the physical mechanism of the 1/f noise [4-23]. This model has been considered as a prototype of the carrier number fluctuations (CNF) model, and accepted widely [4-24~4-27,4-60,4-62]. The CNF in a NMOS FET is schematically illustrated in Fig.4-6 [4-1]. Generally, it is understood that the fluctuations of drain current I_d stem from the fluctuations of the oxide charges, and the oxide charge fluctuations result from the dynamic trapping and de-trapping of carriers between the

Chapter 4. Low-frequency noise characterizations

channel and oxide traps located near the interface. The oxide charge fluctuation δQ_{ox} is equivalent to the flat-band voltage fluctuation δV_{fb} by considering the V_{fb} definition in Eq. (2-7), and it is written as:

$$\delta Q_{ox} = -C_{ox}\delta V_{fb} \quad (4-16)$$

$$\text{with } V_{fb} = \phi_{ms} - \frac{Q_{ox}}{C_{ox}} \quad (2-7)$$

Therefore, the drain current fluctuation δI_d can be derived as [4-60,4-62]:

$$\delta I_d = \frac{\partial I_d}{\partial Q_{ox}} \delta Q_{ox} = \frac{\partial I_d}{\partial V_{fb}} \delta V_{fb} = -\frac{\partial I_d}{\partial V_g} \delta V_{fb} = -g_m \delta V_{fb} \quad (4-17)$$

here noticing that V_g and V_{fb} play a symmetric role. Consequently, a relationship between the S_{Id}/I_d^2 and the flat-band voltage noise PSD S_{Vfb} is given as:

$$\frac{S_{Id}}{I_d^2} = \frac{g_m^2}{I_d^2} S_{Vfb} \quad (4-18)$$

From Eq. (4-18), it is shown that the normalized drain current noise S_{Id}/I_d^2 in the CNF model is proportional to $(g_m/I_d)^2$. The S_{Id}/I_d^2 curve shows a plateau in weak inversion region, whereas the curve decreases in inverse proportion to I_d^2 in strong inversion region. A simulation result of the S_{Id}/I_d^2 behavior difference between CNF and Hooge MF models from subthreshold to strong inversion regions is shown in Fig.4-7 [4-1].

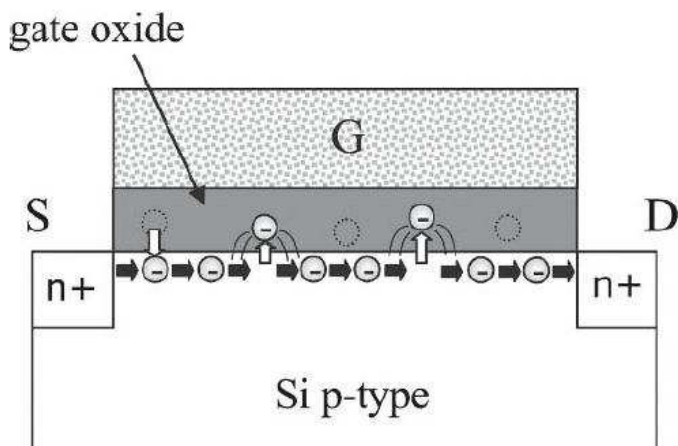


Fig. 4-6. Schematic illustration of electrons in the channel of a MOSFET moving in and out of traps, giving rise to fluctuations in the inversion charge density and thereby the drain current [4-1].

Chapter 4. Low-frequency noise characterizations

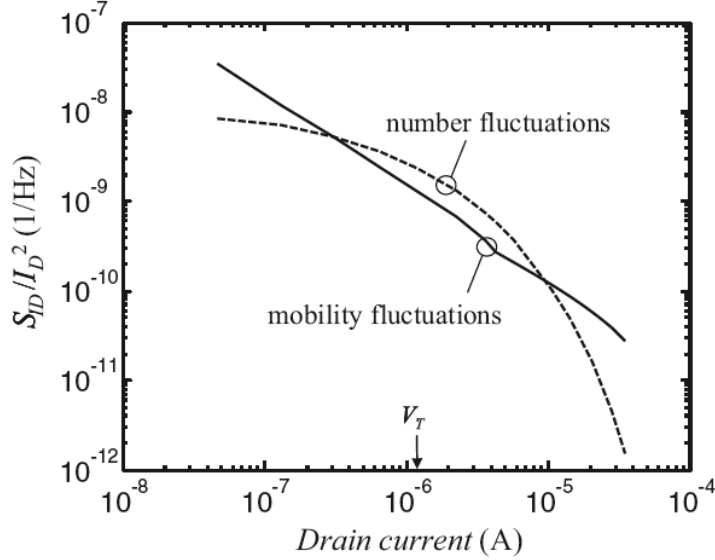


Fig. 4-7. Simulation of the mobility fluctuation noise and carrier number fluctuation noise from subthreshold to the strong inversion regime [4-1].

Equation (4-18) is a common expression without supposing the mechanism of the flat-band voltage fluctuations. Physical carrier trapping and de-trapping between the gate oxide and the channel by the tunneling is assumed as the mechanism, and it is the essence of McWhorter model as the explanation of 1/f noise in MOSFETs. In the tunneling process, the trapping time constant τ_{trap} is given by:

$$\tau_{\text{trap}} = \tau_0(E) \cdot \exp\left(\frac{z}{\lambda}\right) \quad (4-19)$$

where τ_0 is the time constant based on Shockley-Read-Hall (SRH) process and often taken as 10^{-10} s, z is the distance of a trap located in the gate oxide from the interface ($z=0$), and λ is the tunneling attenuation length of the electron or hole wave function in the gate oxide. The value of λ is predicted by the Wentzel-Kramers-Brillouin (WKB) approximation, and is defined as [4-24]:

$$\lambda = \left(\frac{4\pi}{h} \sqrt{2m^* \Phi_B} \right)^{-1} \quad (4-20)$$

where Φ_B is the tunneling barrier height felt by the carriers at the interface, h is the Planck's constant, and m^* is the effective mass of the carriers. The values of λ depends

Chapter 4. Low-frequency noise characterizations

on the gate oxide materials, however the reported values lie in the range of $\approx 0.07\text{-}0.21\text{nm}$ [4-1]. Especially, λ is estimated as $\approx 0.1\text{nm}$ for electron and $\approx 0.14\text{nm}$ for hole in the Si/HfO₂ system with SiO₂ interfacial layer (IL) [4-63~4-65]. For the electron tunneling, this yields $z=2.3\text{nm}$ and 0.9 nm for a frequency of 1Hz and 1MHz , respectively. Thus, oxide traps located near the channel interface are fast, and those located more than 2.5 nm from the interface are slow contributing to high and low frequency range, respectively.

Based on the tunneling process model, S_{Vfb} can be evaluated as:

$$S_{Vfb} = \frac{q^2 kT \lambda N_t}{f^\gamma WLC_{ox}^2} \quad (4-21)$$

where N_t is the gate oxide trap density per volume in unit of $\text{eV}^{-1}\text{cm}^{-3}$. The frequency exponent γ deviates from 1 if the trap density is non-uniformly distributed for the depth [4-66,4-67]. It is noticed that the responsible traps for the fluctuations are those located within $2kT$ range from quasi-Fermi energy level (*i.e.* total $4kT$ range) [4-24].

The band diagram shown in Fig.4-8 illustrates the tunneling transition of carrier (electron) from the Si substrate to the gate oxide, in (i) direct process [4-24] or (ii) indirect one via interface traps as steppingstones [4-68]. The window of traps with $4kT$ range seen at a particular bias point is shown as the shaded area. From the interface trap density D_{it} studies, the D_{it} often shows a U-shaped distribution as a function of energy in the Si band gap, with an increased value toward the conduction or valence band edges [4-69]. Assuming that N_t follows the same behavior as D_{it} , the N_t is predicted to increase with V_g bias, because the quasi-Fermi level approaches the band edge E_C or E_V (*e.g.* the quasi-Fermi level for electron E_{Fn} is close to the E_C in Fig.4-8). Owing to the band bending of the gate oxide, the N_t distribution in the traps window could become non-uniform. Thus, the frequency exponent γ could also deviate from 1 in inversion region.

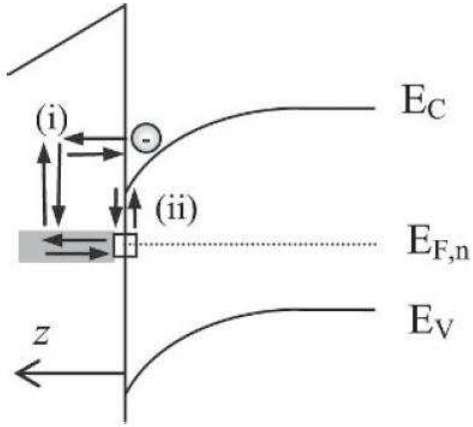


Fig. 4-8. Energy band diagram showing the tunneling transitions of electrons between the conduction band and traps in the gate oxide, (i) corresponds to direct tunneling and (ii) to indirect tunneling via interface traps [4-1].

4.1.2.4 CNF+CMF model

In 1990, Hung *et al.* suggested a unified model which combines the CNF and the MF frameworks [4-55]. In 1991, a more popular definition was proposed by Ghibaudo *et al.* [4-56]. In this advanced theory, the influence on the conduction through the Coulomb interaction with the trapped carriers is also considered. This means that the oxide charge fluctuations, *i.e.* the CNF, can additively induce a change of the mobility which causes an extra I_d variation. Based on this idea for the MF correlated to the CNF, the drain current fluctuations δI_d can be expressed with Eq. (4-17) as:

$$\delta I_d = \frac{\partial I_d}{\partial V_{fb}} \delta V_{fb} + \frac{\partial I_d}{\partial \mu_{eff}} \delta \mu_{eff} = -g_m \delta V_{fb} + \frac{\partial I_d}{\partial \mu_{eff}} \frac{\partial \mu_{eff}}{\partial Q_{ox}} \delta Q_{ox} \quad (4-22)$$

Since I_d is proportional to μ_{eff} (cf. Eq. (3-1)) then this equation yields to:

$$\delta I_d = -g_m \delta V_{fb} + \frac{I_d}{\mu_{eff}} \frac{\partial \mu_{eff}}{\partial Q_{ox}} \delta Q_{ox} = -g_m \delta V_{fb} - \frac{I_d}{\mu_{eff}} \frac{\partial \mu_{eff}}{\partial Q_{ox}} C_{ox} \delta V_{fb} \quad (4-23)$$

Here a scattering parameter can be introduced to reflect the coupling between the oxide charge and the mobility variations. The Coulomb scattering coefficient α_{sc} is defined as:

$$\alpha_{sc} = -\frac{\partial(1/\mu_{eff})}{\partial Q_{ox}} = \frac{1}{\mu_{eff}^2} \frac{\partial \mu_{eff}}{\partial Q_{ox}} \quad (4-24)$$

Substituting Eq. (4-24) into Eq. (4-23), then δI_d is written as:

Chapter 4. Low-frequency noise characterizations

$$\delta I_d = -g_m \delta V_{fb} - I_d \alpha_{sc} \mu_{eff} C_{ox} \delta V_{fb} = -g_m \left(1 + \alpha_{sc} \mu_{eff} C_{ox} \frac{I_d}{g_m} \right) \delta V_{fb} \quad (4-25)$$

Consequently, a definition of S_{Id}/I_d^2 in the “carrier number fluctuations with correlated fluctuations (CNF+CMF)” model can be given by:

$$\frac{S_{Id}}{I_d^2} = \left(\frac{g_m}{I_d} \right)^2 \left(1 + \alpha_{sc} \mu_{eff} C_{ox} \frac{I_d}{g_m} \right)^2 S_{Vfb} \quad (4-26)$$

In Eq. (4-26), the first term corresponds to the CNF component and the second term indicates the CMF factor by trapped charges. If α_{sc} is close to zero, it means that CMF does not influence the LFN and the behavior can be described by the CNF only. In contrast, when the α_{sc} is high enough, the slope of S_{Id}/I_d^2 vs. I_d in strong inversion region is impacted by the CMF and departed from the proportion to I_d^{-2} . However, CMF does not influence the noise behavior in weak inversion region, and CNF is predominant.

A constant α_{sc} has been frequently used in the LFN models, but this is not physically correct for several reasons, such as the screening effect [4-13,4-31]. In practice, α_{sc} is expected to decrease with increasing inversion charge density Q_{inv} due to the screening effect. In addition, the product of $\alpha_{sc} \mu_{eff} = \mu_{eff}^{-1} \delta \mu_{eff} / \partial Q_{ox}$ is anticipated as a key and fairer parameter, which is called Coulomb scattering parameter, in the CMF investigation [4-39,4-70].

The relationship between the drain current noise PSD S_{Id} and the input gate voltage noise counterpart S_{Vg} is expressed as [4-56]:

$$S_{Vg} = \frac{S_{Id}}{g_m^2} = \left(1 + \alpha_{sc} \mu_{eff} C_{ox} \frac{I_d}{g_m} \right)^2 S_{Vfb} \quad (4-27)$$

It is thus confirmed that I_d noise spectrum can be simply transformed to the V_g noise characteristic by the measured g_m .

4.1.3 Measurement setup

LFN measurements were performed at room temperature under a probe level using a semi-automatic noise measurement system by Synergie Concept [4-71]. The system is well configured for delicate measurements. The system is called Programmable Point

Chapter 4. Low-frequency noise characterizations

Probe Noise Measuring System (3PNMS), and was operated by control software NOISYS (version 4.1) with programmable biasing amplifier (PBA2). [Figure 4-9](#) shows a schematic of the LFN measurement system with device under test (DUT) and PBA2. The PBA2 is composed of batteries without AC signals and low-noise amplifiers. Input V_d , V_g , and the measuring steps are finely programmable, and DC and AC components of output I_d are monitored.

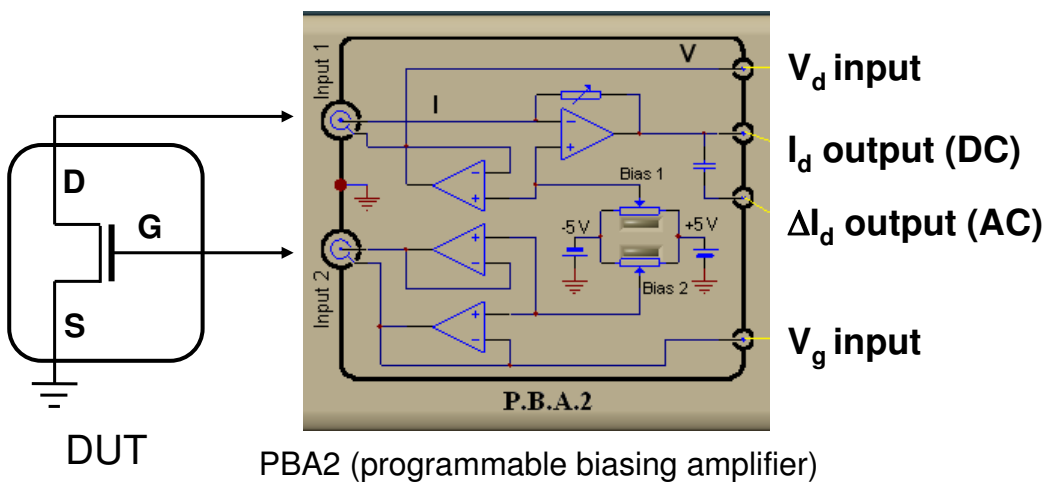


Fig. 4-9. Schematic of the LFN measurement system 3PNMS with PBA2 and DUT.

The noise signal is computed by converting the output AC component (ΔI_d) in time domain into the PSD in frequency domain with fast Fourier transform (FFT). For the accurate measurement of noise characteristic in MOSFETs, the system was shielded by a metal box enclosure and isolated from extrinsic noise sources. In addition, each component of the system was appropriately grounded to prevent an unexpected electric shock from affecting the measurement. The system noise floor of 3PNMS was measured around $\sim 2 \times 10^{-27} \text{ A}^2/\text{Hz}$. It accomplishes the recommended noise floor level below $10^{-26} \text{ A}^2/\text{Hz}$.

In this work, the PSD of drain current noise S_{Id} was acquired at 400 sample points of frequency, and with 32 times averaging. The V_g was varied from subthreshold region (actually with the current lower limit of $|I_d| > 10^{-9} \text{ A}$) up to strong inversion region ($|V_g| > 1.0 \text{ V}$). The V_d bias were varied from linear region ($|V_d| = 40 \text{ mV}$) up to saturation region ($|V_d| = 0.9 \text{ V}$).

Chapter 4. Low-frequency noise characterizations

4.2 Experimental results

4.2.1 1/f noise behavior and CNF+CMF model

Normalized drain current noise S_{Id}/I_d^2 as a function of frequency in the narrowest single-channel SOI and sSOI Ω -gate NMOS NWs is shown in Fig.4-10. Although the single NWs show dispersions of noise level and shape, the averaged spectrum measured for 5 or 6 devices exhibits good 1/f noise behavior from threshold up to strong inversion regions for both SOI and sSOI devices. For PMOS, the 1/f noise curves can be also seen in both reference SOI and nSGOI NWs as shown in Fig.4-11. Although nSGOI NWs show larger dispersion of the noise behavior, the 1/f behavior is sustained on the averaged spectrum for 6 devices. This clearly means that LFN behavior in our both N- and PMOS NWs has the potential to be interpreted by CNF+CMF model even for strain-processed devices.

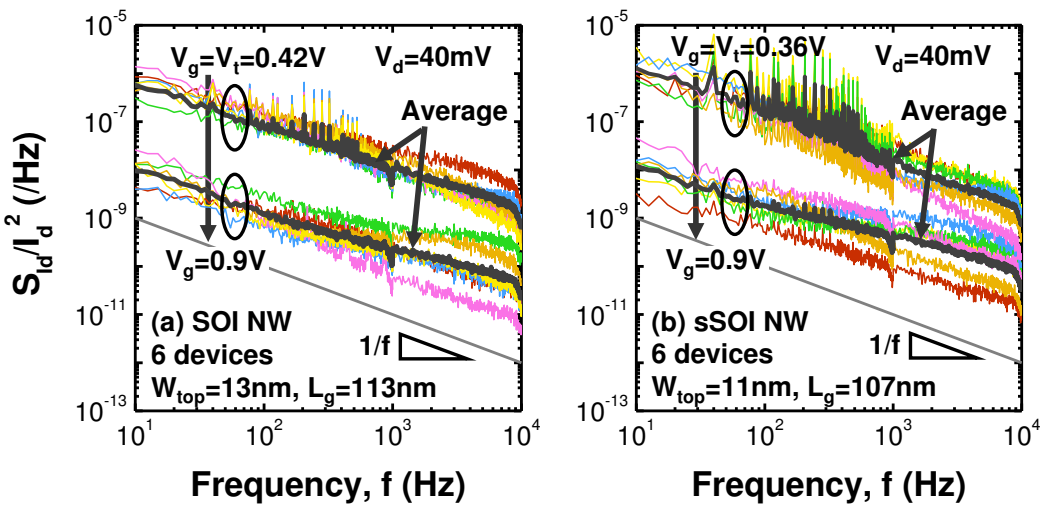


Fig. 4-10. S_{Id}/I_d^2 as a function of frequency in the (a) SOI and (b) sSOI narrowest Ω -gate NW NMOS FETs with $L_g \sim 110$ nm, showing good 1/f behavior at threshold voltage ($V_g = V_t$) up to strong inversion region.

Chapter 4. Low-frequency noise characterizations

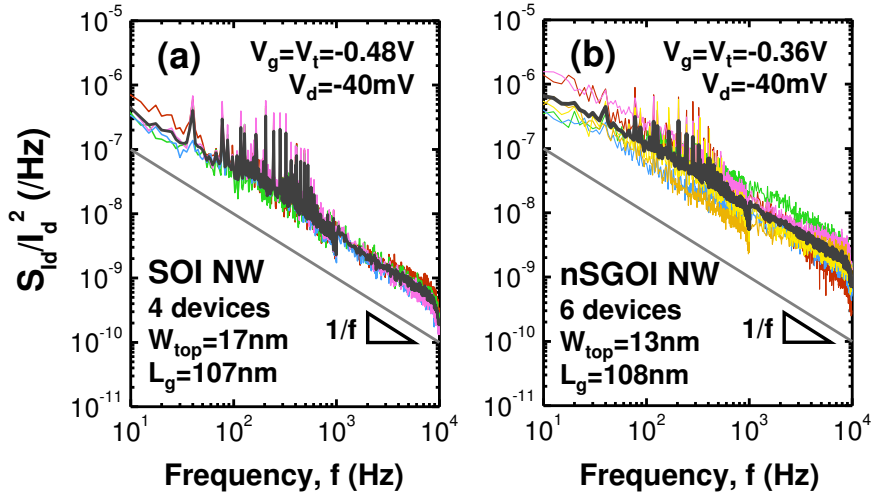


Fig. 4-11. S_{Id}/I_d^2 as a function of frequency in the SOI and nSGOI narrowest Ω -gate NW PMOS FETs with $L_g=107\text{-}108\text{nm}$, showing good $1/f$ behavior at threshold voltage ($V_g=V_t$).

In the following, the presence of g-r and/or RTS noise is more carefully discussed. SOI NMOS NWs with $L_g=113\text{nm}$ exhibits clear $1/f$ noise as shown in Fig.4-10, however some devices include additional $1/f^2$ noise components. Figure 4-12 shows I_d fluctuation measured for the device including a $1/f^2$ -like spectrum in time domain using three sampling frequencies covering the frequency range of noise measurement between 1Hz and 1MHz. No typical RTS is observed at the three sampling frequencies, whereas a small $1/f^2$ noise spectrum is found. This means that the Lorentzian should correspond to g-r noise caused by a charge trap in silicon body as distinct from the interfacial trap event.

Chapter 4. Low-frequency noise characterizations

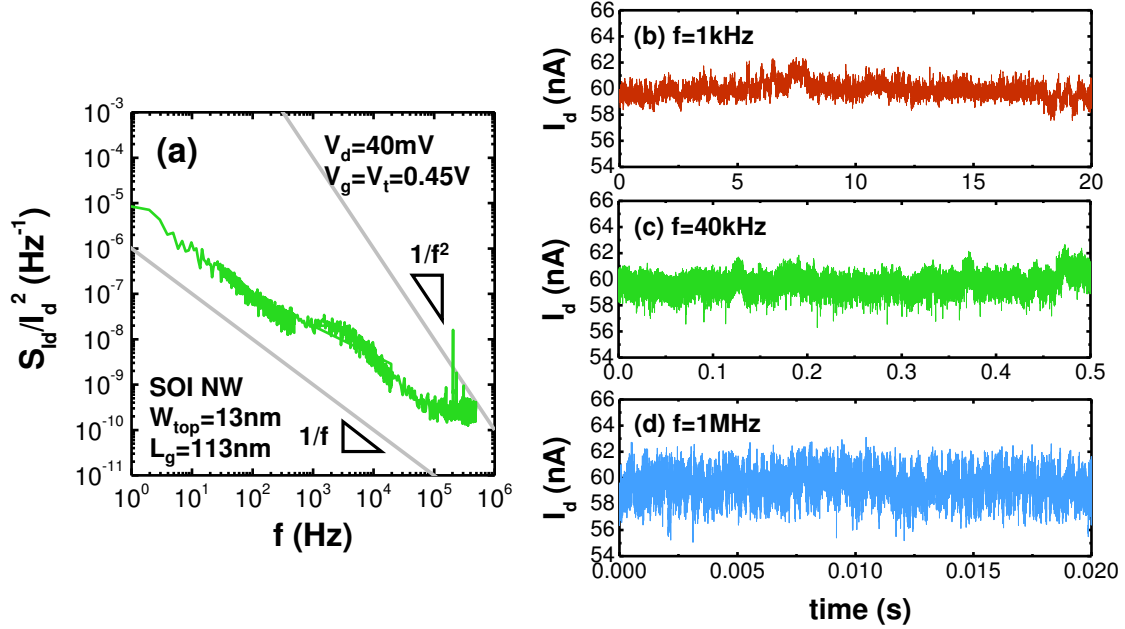


Fig. 4-12. (a) S_{Id}/I_d^2 as a function of frequency in the narrowest SOI Ω -gate NW NMOS FETs with $L_g=113\text{nm}$, showing $1/f$ and additional $1/f^2$ noise components at threshold voltage ($V_g=V_t$). I_d fluctuation as a function of time for sampling frequency of (b) $f=1\text{kHz}$, (c) $f=40\text{kHz}$, and (d) $f=1\text{MHz}$.

On the other hand, I_d fluctuation measurement in time domain for an SOI NMOS NW with short $L_g=28\text{nm}$ exhibiting two large $1/f^2$ noise component (one is at the range of 1Hz-10Hz, and other appears around 100kHz) is shown in Fig.4-13. A clear RTS is observed at sampling frequency of 1kHz corresponding to the lower frequency region (Fig.4-13b). The additional $1/f^2$ noise spectra are more visible also in other short channel NWs than longer device cases, as shown in Fig.4-14. However, it is thereby concluded that $1/f$ noise behavior is basically observed and less RTS noise is found in low-frequency region for most of our devices, even for single short channel NWs.

Chapter 4. Low-frequency noise characterizations

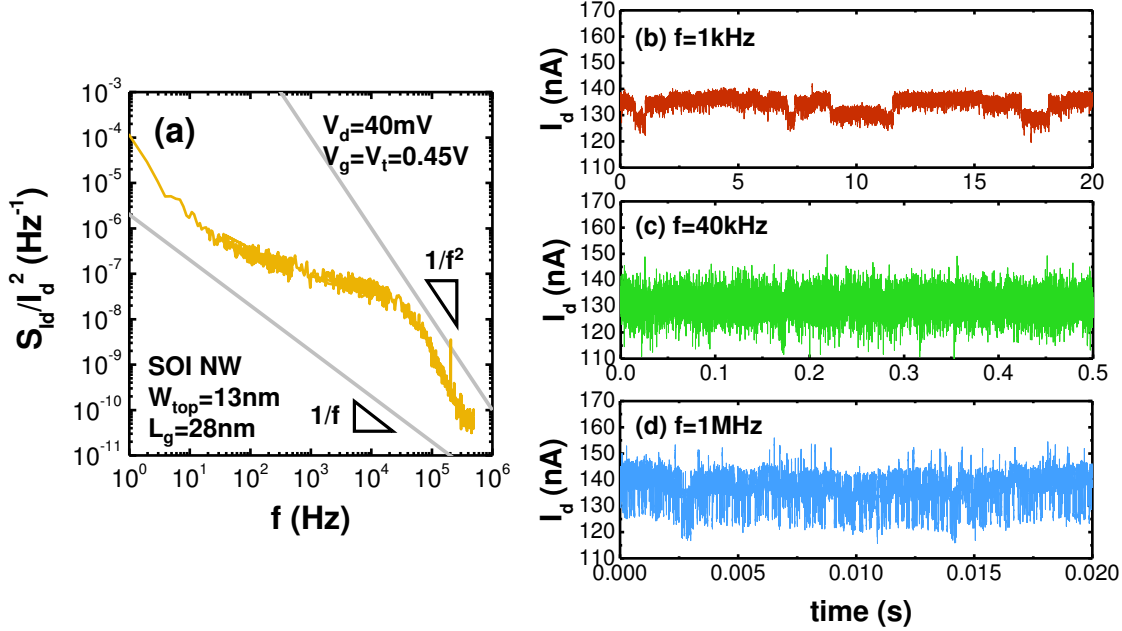


Fig. 4-13. (a) S_{Id}/I_d^2 as a function of frequency in the narrowest SOI Ω -gate NW NMOS FETs with $L_g=28\text{nm}$, showing large $1/f^2$ noise components at threshold voltage ($V_g=V_t$). I_d fluctuation as a function of time for sampling frequency of (b) $f=1\text{kHz}$, (c) $f=40\text{kHz}$, and (d) $f=1\text{MHz}$.

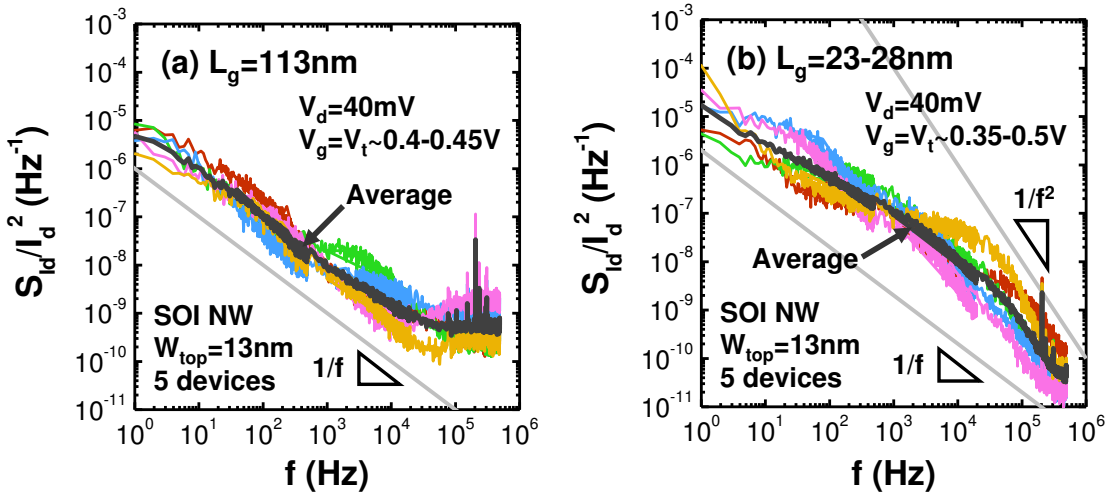


Fig. 4-14. S_{Id}/I_d^2 as a function of frequency in the narrowest SOI Ω -gate NW NMOS FETs with (a) $L_g=113\text{nm}$ and (b) short channel $L_g=23-28\text{nm}$, showing $1/f$ behavior in low-frequency region at threshold voltage ($V_g=V_t$).

Chapter 4. Low-frequency noise characterizations

4.2.1.1 Comparison between experimental data and CNF+CMF model

The measured S_{Id}/I_d^2 extracted at frequency of $f=10\text{Hz}$ as a function of I_d with normalization by the channel area parameters (both W_{tot} and L_g) is shown in [Fig.4-15](#) for a number of NMOS technological splits (channel orientation, H_2 anneal, and strained channel). Actually, good agreement between S_{Id}/I_d^2 plot and the corresponding $(g_m/I_d)^2$ curve is observed in all the devices. This indicates that the LFN properties in all the technological parameters are well described by CNF+CMF model. Furthermore, the almost merged LFN data in [Fig.4-15a](#) indicates that there is no significant influence of the orientation differences ([110]- vs. [100]-orientation [\[4-72\]](#), and (001) top surface vs. (110) side-walls in [110]-oriented SOI [\[4-36,4-51\]](#)). The wide FET processed with additional H_2 anneal shows larger noise level in subthreshold region exhibiting plateaued noise level, whereas the noise curve of NW perfectly agrees with the case w/o H_2 anneal ([Fig.4-15b](#)). In [Fig.4-15c](#), sSOI devices show slight noise level increase in the entire region for both wide and narrowest NW cases. This can be partly attributed to the I_d enhancement.

Chapter 4. Low-frequency noise characterizations

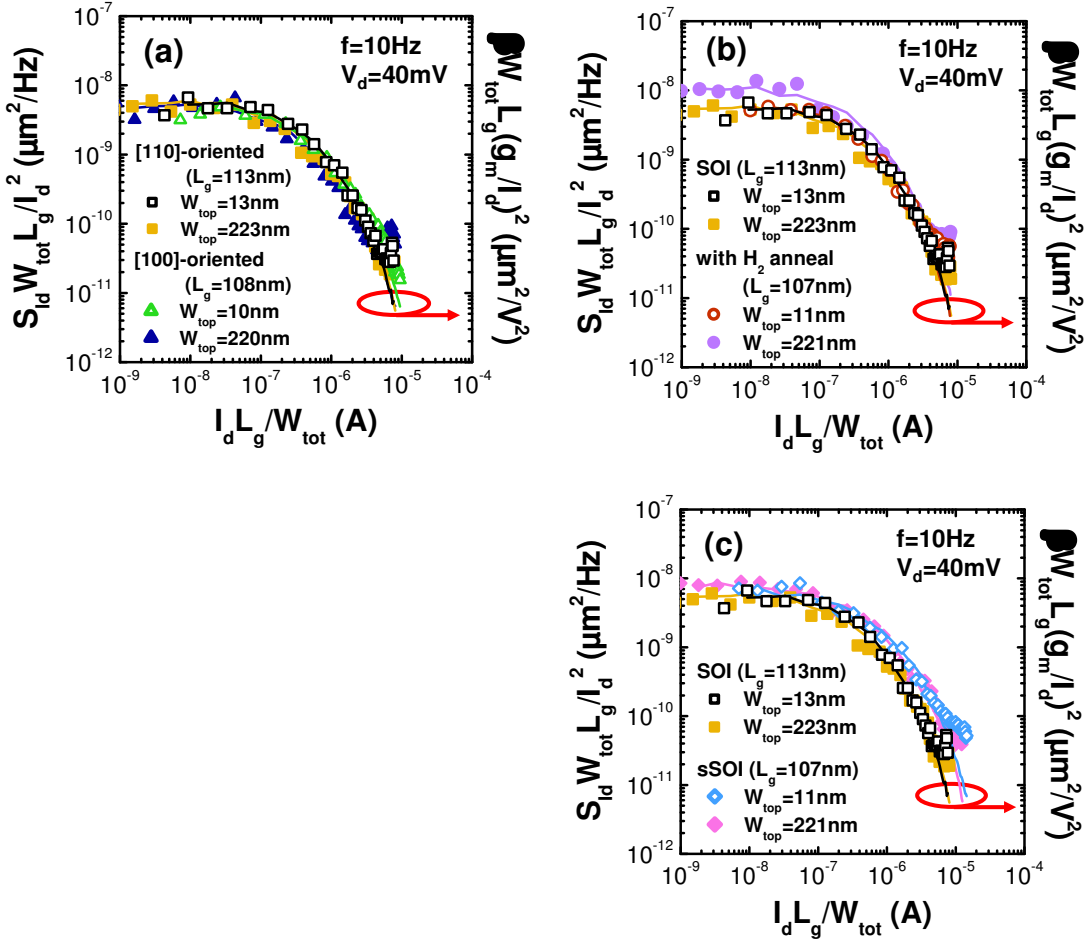


Fig. 4-15. I_d dependent (symbols) S_d/I_d^2 and (lines) corresponding $(g_m/I_d)^2$ curve characteristics normalized by channel size parameters (W_{tot} and L_g) in reference SOI wide FETs and the narrowest NWs compared with (a) [100]-oriented SOI, (b) SOI with additional H_2 anneal, and (c) sSOI for NMOS devices.

Same measurements have been also performed for PMOS (Fig.4-16). Good agreement between noise data and CNF+CMF model is also observed and sustained for reference SOI, nSG-S/D, and nSGOI devices. In SOI devices for both NW and wide FETs, and in nSG-S/D NWs, a large augmentation of the noise level in strong inversion region is observed. This indicates a strong contribution from S/D series resistance R_{SD} [4-29,4-32,4-45]. This phenomenon is discussed in detail in the next section. In Fig.4-17, we compare the 3-types of PMOS technological variants. The noise curves in wide FETs are superposed below the strong inversion region, *i.e.* for $I_d \times L_g / W_{tot} < 10^{-6} \text{ A}$ in

Chapter 4. Low-frequency noise characterizations

[Fig.4-17a](#). On the other hand, the noise curve related to nSGOI NWs exhibit a large shift due to huge I_d (I_{ON}) improvement in the narrowest NWs, whereas the plots corresponding to SOI and nSG-S/D devices are roughly merged ([Fig.4-17b](#)). In both wide and NW FETs, the plateaued noise level in subthreshold region is maintained.

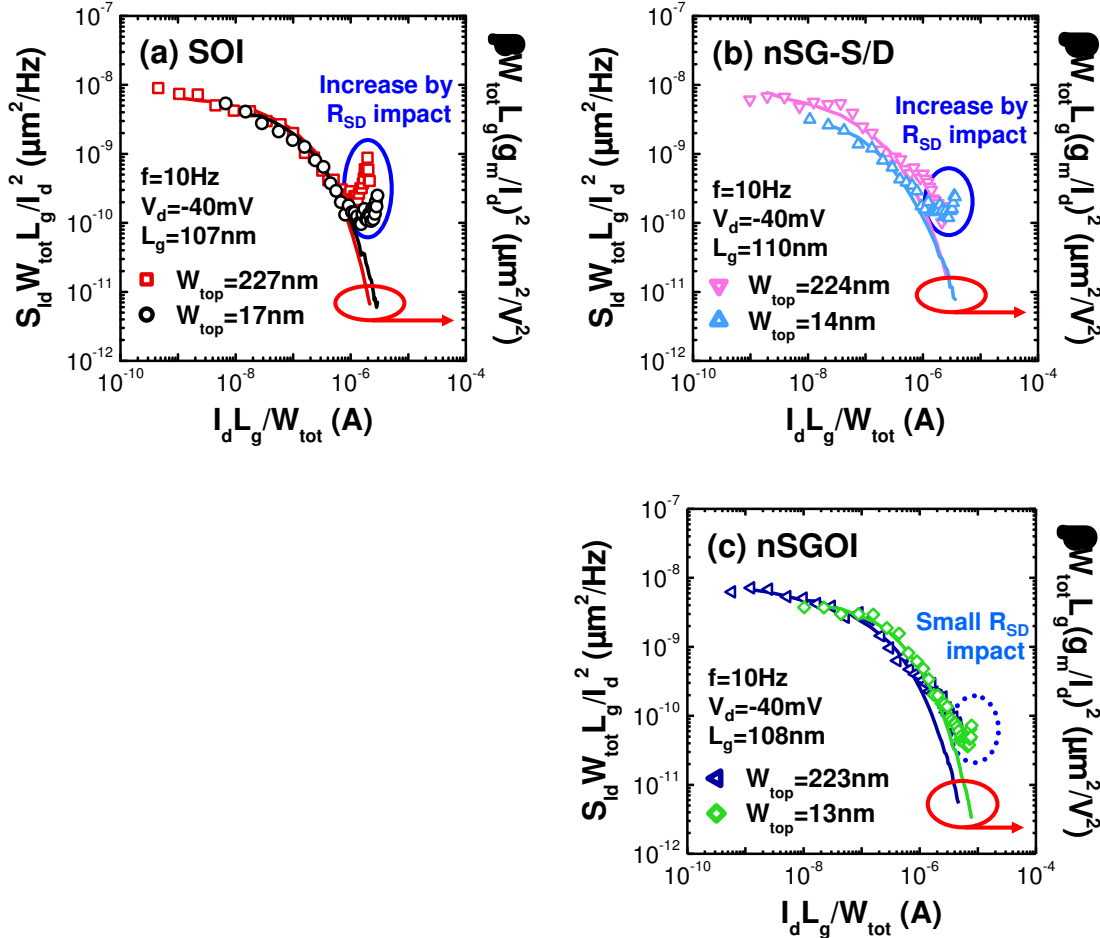


Fig. 4-16. I_d dependent (symbols) S_{Id}/I_d^2 and (lines) corresponding $(g_m/I_d)^2$ curve characteristics normalized by channel size parameters (W_{tot} and L_g) in wide FETs and the narrowest NWs for (a) SOI, (b) nSG-S/D, and (c) nSGOI for PMOS devices.

Chapter 4. Low-frequency noise characterizations

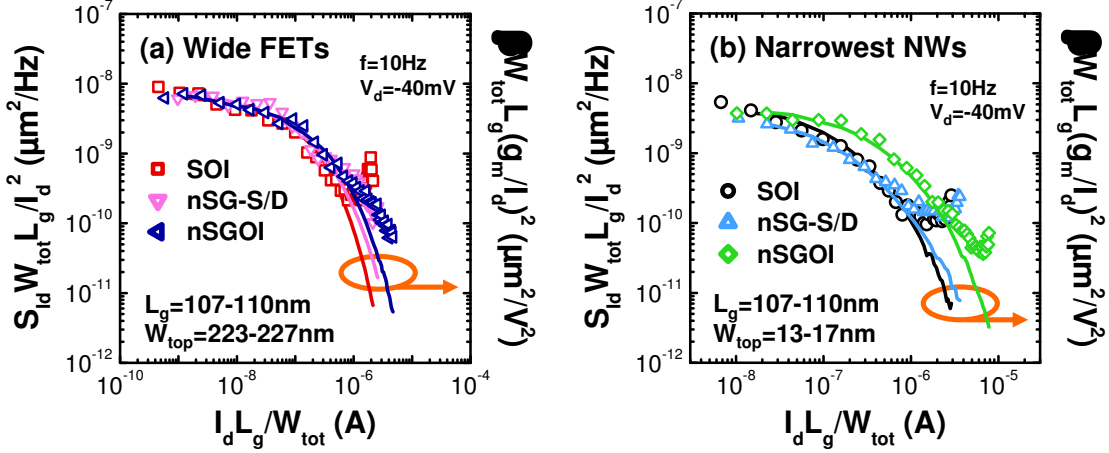


Fig. 4-17. Comparison of 3-types of PMOS device variants; SOI, nSG-S/D, and nSGOI, in I_d dependent (symbols) S_d/I_d^2 and (lines) corresponding $(g_m/I_d)^2$ curve characteristics normalized by W_{tot} and L_g for (a) wide FETs and (b) the narrowest NWs.

It can be noticed that the noise level decrease due to the volume inversion, reported in SOI tri-gate NW FETs with $\text{SiO}_2/\text{poly-Si}$ gate stack [4-51], and in GAA Si NW FETs with *in-situ* steam-generated (ISSG) SiO_2/TiN gate stack [4-52], is not observed in our case. In our SOI-based Ω -gate NWs, the scaling regularity with both W_{tot} and L_g , without much quantum effect, could be attributed to the use of Hf-based high- κ gate oxide (HfSiON) and the carrier transport occurring mainly in 2D surfaces of top and side-walls even in NW geometry.

4.2.1.2 Impact of resistance from source/drain regions

Here, the R_{SD} contribution to 1/f LFN properties is discussed. A large increment of the noise level in strong inversion region, shown in Fig.4-16a and b, stems from the strong contribution of S/D access regions. The R_{SD} is additively fluctuating by trapping/de-trapping events of carriers caused via defects in the spacers 1 and 2 consisting of SiN_x and/or in the silicon film, as illustrated in Fig.4-18. The fluctuations contribute to the rise of 1/f noise level in strong inversion regime, and are distinct from thermal noise which is frequency independent. Worse quality of the S/D regions in PMOS devices than NMOS is generally attributed to less controllability of the boron

Chapter 4. Low-frequency noise characterizations

dopant due to the lighter mass of B than P or Ar. This could explain the higher contribution of R_{SD} to noise observed for PMOS than for NMOS. The CNF+CMF model can be simply completed by considering the additional noise impact caused by the S/D regions as [4-29]:

$$\frac{S_{Id}}{I_d^2} = \left(\frac{g_m}{I_d} \right)^2 \left(1 + \alpha_{sc} \mu_{eff} C_{ox} \frac{I_d}{g_m} \right)^2 S_{Vfb} + \left(\frac{I_d}{V_d} \right)^2 S_{Rsd} \quad (4-28)$$

where S_{Rsd} is the PSD of the R_{SD} fluctuations.

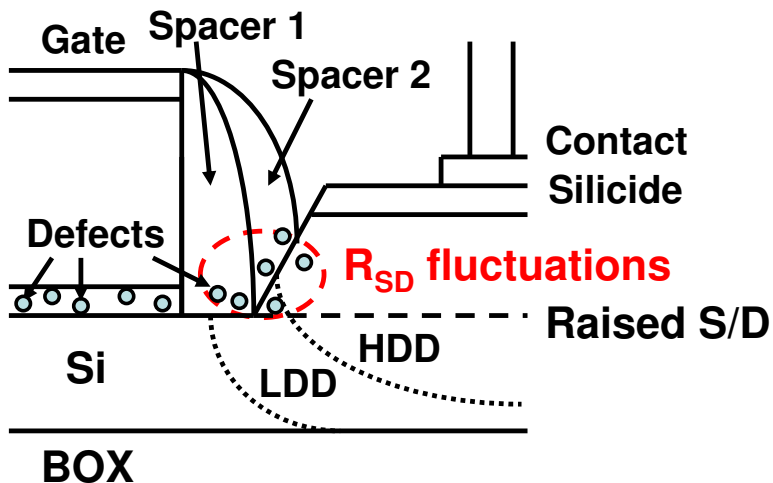


Fig. 4-18. Schematic of defects in spacers 1 and 2 and/or in Si film contributing to R_{SD} fluctuations in SOI MOSFET architecture.

In Fig.4-19, experimental S_{Id}/I_d^2 - I_d plots are shown together with the theoretical expression Eq. (4-28) using two fitting parameters β and S_{Rsd} . The experimental curves above V_t for SOI devices can be perfectly described by the included R_{SD} impact (Fig.4-19a). For both nSG-S/D and nSGOI devices, the spectra in NWs are well interpreted by considering both $\alpha_{sc}\mu_{eff}$ and S_{Rsd} components (Fig.4-19b), whereas for wide FETs, the $\alpha_{sc}\mu_{eff}$ factor is only dominant without the S_{Rsd} term (Fig.4-19c). The values of S_{Rsd} are summarized in Table 4-1. They highlight the advantage of nSGOI device which exhibits much lower impact of R_{SD} , in relation with a lower R_{SD} value by Y-function (cf. Fig.3-33).

Chapter 4. Low-frequency noise characterizations

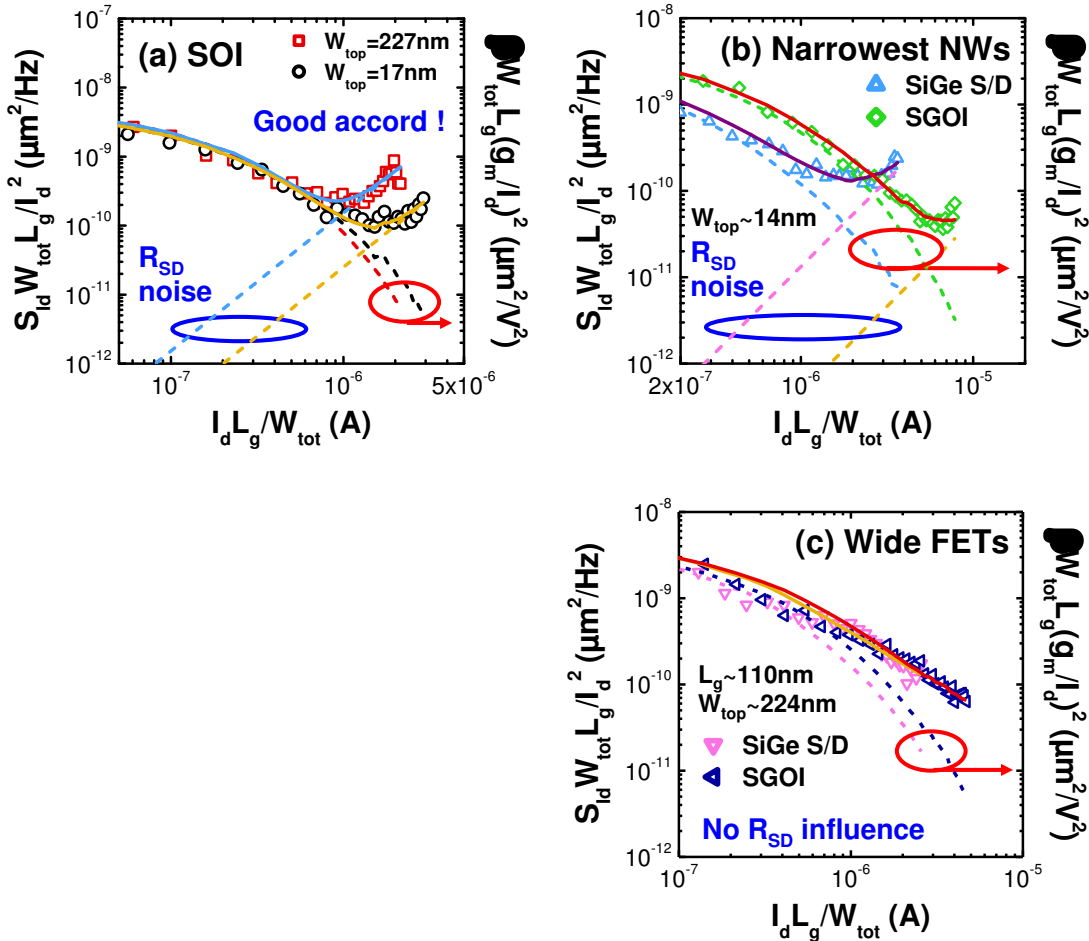


Fig. 4-19. I_d dependent (symbols) S_{Id}/I_d^2 and (lines) corresponding $(g_m/I_d)^2$ curves with consideration of the $\alpha_{\text{sc}}\mu_{\text{eff}}$ and S_{Rsd} term shown in Eq. (4-28), showing (a) the narrowest NW vs. wide FETs in SOI devices, and SiGe S/D vs. SGOI devices in (b) NWs, and in (c) wide FETs.

Table 4-1. Summary of the extracted $\alpha_{\text{sc}}\mu_{\text{eff}}$ and S_{Rsd} values in Fig.4-15 with the extracted S/D series resistance R_{SD} normalized by W_{tot} for NWs in Fig.3-33.

[110]-oriented Ω -gate PMOS	$\alpha_{\text{sc}}\mu_{\text{eff}} (\times 10^6 \text{ cm}^2/\text{C})$		$S_{\text{Rsd}} (\Omega^2/\text{Hz})$		$R_{\text{S/D}} (\Omega \mu\text{m})$
	Wide	NW	Wide	NW	
SOI	No impact	No impact	1.6	50	208
nSG-S/D	1.5	1.1	No impact	65	210
nSGOI	1.4	0.75	No impact	1.7	158

Chapter 4. Low-frequency noise characterizations

4.2.1.3 Evaluation of Hooge parameter

We have also extracted the Hooge parameter α_H (cf. Eq. (4-11)), which is based on an empirical model considering only mobility fluctuations. In fact, Hooge's empirical model has no theoretical argument, even though it has been often able to explain the 1/f noise behavior. Meanwhile, the Hooge parameter α_H has been often reported to discuss the noise behavior difference for technological and structural parameters in overdrive operation. The values of α_H extracted in our NW FETs are shown in Fig.4-20 as a function of the voltage overdrive V_{gt} . Different trends depending on the technological splits can be distinguished.

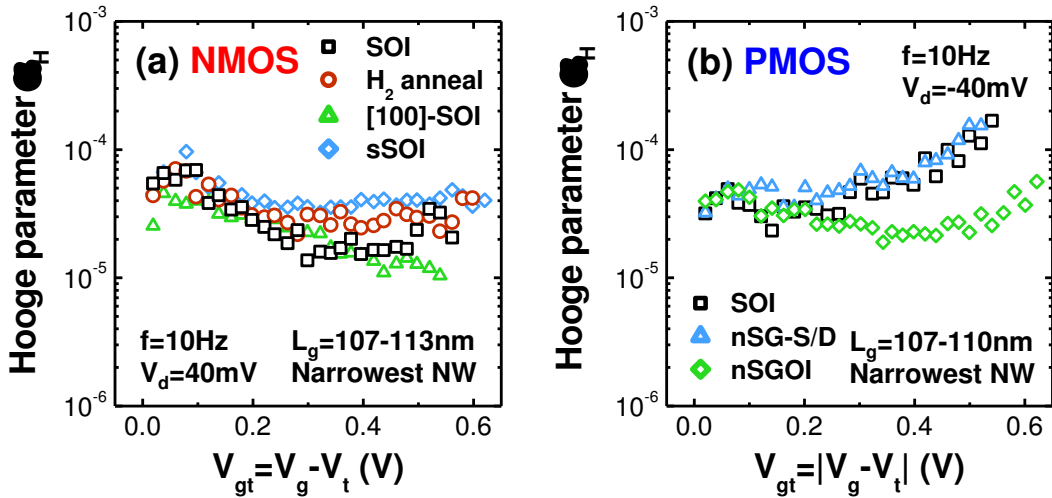


Fig. 4-20. Hooge parameter α_H as a function of gate voltage overdrive V_{gt} for various technological splits in the narrowest (a) NMOS and (b) PMOS NW FETs.

For NMOS, higher values of α_H is observed in SOI NW with additional H₂ anneal process and in sSOI NW, compared to reference SOI NW especially for V_{gt} above 0.2V. It is ascribed to the relatively large influence of CMF component (values of $\alpha_{sc}\mu_{eff}$). On the other hand, [100]-oriented NW exhibits similar or lower values than reference [110]-NW in almost entire V_{gt} range, suggesting no large impact of side-wall orientation. In $V_{gt}>0.5V$ region, it should be noticed that α_H level of reference SOI NW rises and reaches the levels in H₂ annealed SOI and sSOI NWs. This can be attributed to the effect of R_{SD} fluctuations.

For PMOS, level of α_H is equal among the three technological splits in V_{gt} region

Chapter 4. Low-frequency noise characterizations

below 0.2V. Above 0.2V, reference SOI and nSG-S/D NWs show the higher value and steeper upward trend compared to nSGOI device. Lower noise level for nSGOI NW in strong inversion region is here reconfirmed.

We conclude that Hooge's empirical parameter α_H well reflects $\alpha_{sc}\mu_{eff}$ and S_{Rsd} impacts in strong inversion region, even though the noise behaviors are in accordance with CNF+CMF model, not only MF. Moreover, it is visibly concluded that the S_{Rsd} influence in PMOS is much stronger than NMOS devices, and SGOI technology is advantageous for PMOS NW FETs.

4.2.2 Flat-band voltage noise

4.2.2.1 Extraction

For more detailed investigations, two important parameters S_{Vfb} and $\alpha_{sc}\mu_{eff}$ in Eq. (4-27) can be obtained from experimental data. Both parameters are simultaneously extracted from experimental $S_{Vg}^{1/2}$ plot as a function of I_d/g_m as:

$$S_{Vg}^{1/2} = \sqrt{\frac{S_{Id}}{g_m^2}} = \left(1 + \alpha_{sc}\mu_{eff}C_{ox} \frac{I_d}{g_m}\right) S_{Vfb}^{1/2} \quad (4-29)$$

Figure 4-21 shows $S_{Vg}^{1/2}$ versus I_d/g_m characteristics with varying V_g from weak to strong inversion regions. The two parameters, namely $S_{Vfb}^{1/2}$ and $S_{Vfb}^{1/2}\alpha_{sc}\mu_{eff}C_{ox}$ are provided by the intercept with the vertical axis and the slope, respectively [4-70]. The straight line indicates the linear regression calculated for reference wide and 1ch-TGNW FETs. However, lower S_{Vfb} values than the actual values are extracted by the linear regression method for 1ch-NWs, whereas no mismatch is seen in reference wide FETs.

Chapter 4. Low-frequency noise characterizations

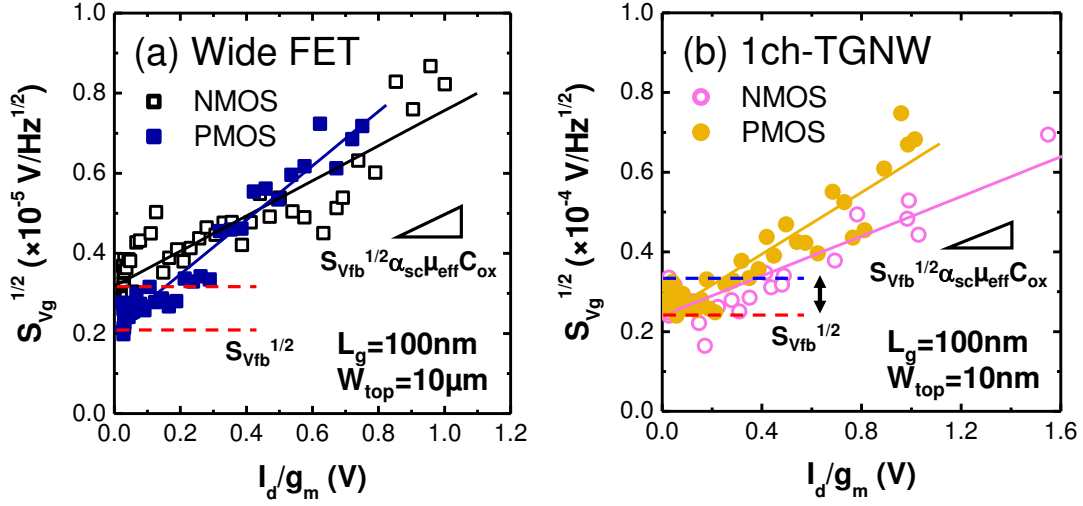


Fig. 4-21. (Symbols) $S_{Vg}^{1/2}$ versus I_d/g_m characteristics and (lines) the linear regression for extraction of S_{Vfb} and $\alpha_{sc}\mu_{eff}$ in (a) wide and (b) 1ch-TGNW both N- and PMOS FETs.

S_{Vfb} value can also be extracted by direct fitting of S_{Id}/I_d^2 versus $(g_m/I_d)^2$ curves, in the subthreshold region showing the plateaued noise level (cf. Figs.4-15~4-17). In this regime where CNF is predominant, the coefficient $(1+\alpha_{sc}\mu_{eff}C_{ox}I_d/g_m)$ in Eq. (4-27) reduces to 1. The proportionality constants β used in Figs.4-15~4-17 and 4-19 thereby corresponds to the value of S_{Vfb} in the plateau region, where CNF noise can be approximated as:

$$\frac{S_{Id}}{I_d^2} \approx \beta \left(\frac{g_m}{I_d} \right)^2 \approx S_{Vfb} \left(\frac{g_m}{I_d} \right)^2 \quad (4-30)$$

This method seems more relevant for NW devices with less mismatched values compared to those obtained by the linear regression method.

4.2.2.2 Influence of scalability

Extracted flat-band voltage noise S_{Vfb} in Fig.4-22 shows roughly simple channel scaling effect, *i.e.* the noise level increases as the inverse of both W_{tot} [4-39] and L_g decreasing, without any large deviation from the different technological parameters for NMOS devices. For PMOS, cSGOI devices in the narrowest NW region exhibit relatively higher noise level than other splits as shown in Fig.4-23a. From Fig.4-23b, we

Chapter 4. Low-frequency noise characterizations

also evidenced that the narrowest PMOS NWs exhibit different noise levels depending on the technological splits, whereas wide FETs have the same level whatever splits. In particular, SiGe channel NWs (n- and cSGOI) show slightly higher noise than Si channels. For the other technological splits within reasonable uncertainty, we conclude that S_{Vfb} in PMOS devices exhibits the simple scaling effect and the unity among the technological parameters in analogy with the NMOS case.

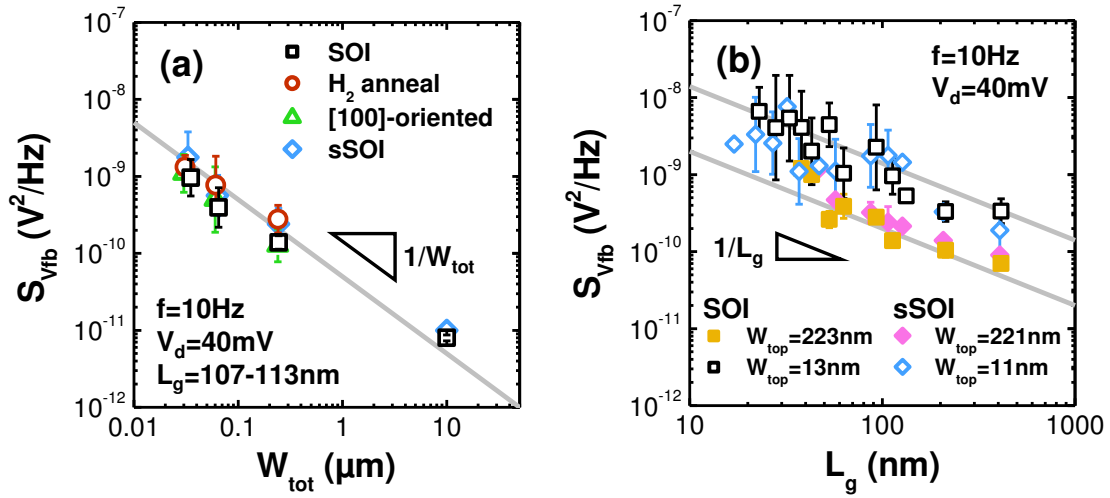


Fig. 4-22. S_{Vfb} as a function of (a) W_{tot} and (b) L_g for all the technological splits in NMOS devices.

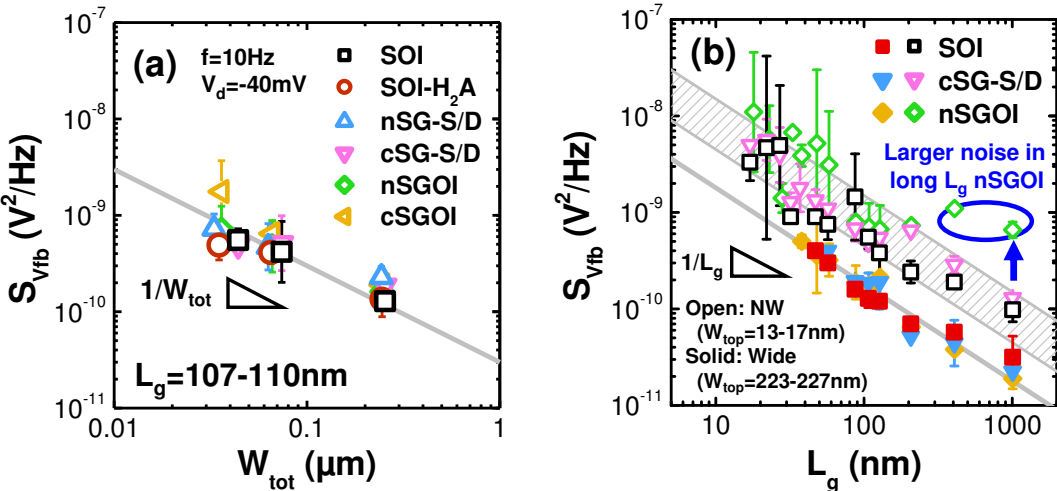


Fig. 4-23. S_{Vfb} as a function of (a) W_{tot} and (b) L_g for all the technological parameters in PMOS devices.

Chapter 4. Low-frequency noise characterizations

4.2.3 Coulomb scattering parameter

4.2.3.1 General feature

The linear relationship between $S_{Vg}^{1/2}$ and I_d/g_m shown in Fig.4-21 suggests that the Coulomb scattering parameter $\alpha_{sc}\mu_{eff}$ is constant from weak to strong inversion regions in agreement with previous works [4-39,4-70], and that this relationship is applicable even in ultra-scaled TGNW devices. The values of $\alpha_{sc}\mu_{eff}$, corresponding to CMF factor, as a function of the device channel area $W_{tot}L_g$ is extracted in Fig.4-24. It is found that the parameter is not altered by scaling effect (W_{top} or L_g downscaling) for both N- and PMOS devices within measurement uncertainty. We conclude that the device-to-device dispersion is only dominant for CMF. Finally, the values of $\alpha_{sc}\mu_{eff}$ roughly agree with previously reported data [4-42,4-70].

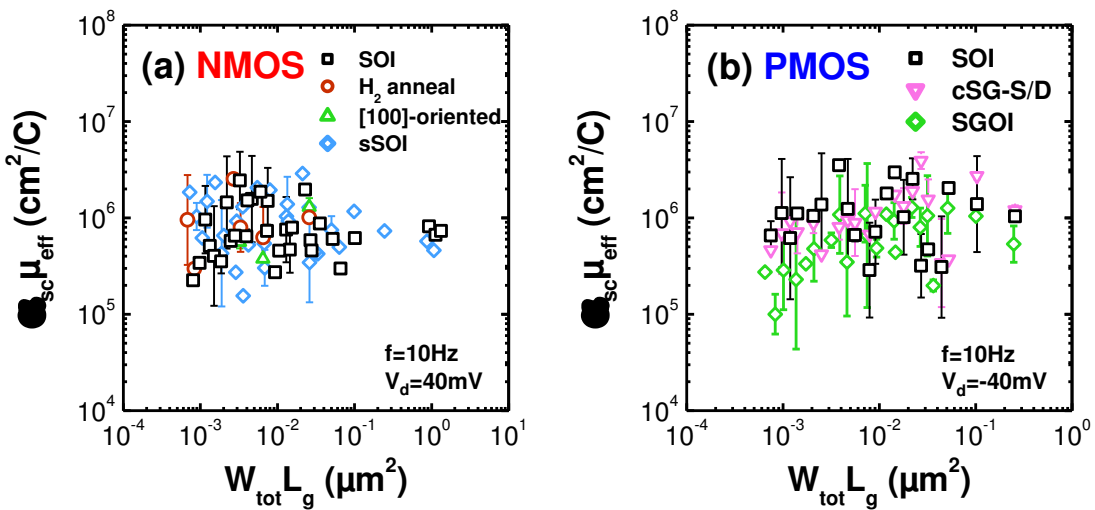


Fig. 4-24. Coulomb scattering parameter $\alpha_{sc}\mu_{eff}$ as a function of the channel area $W_{tot}L_g$ in all the devices with single-channel for (a) NMOS and (b) PMOS FETs.

4.2.3.2 Comparison with transport parameter: low-field mobility

The extracted $\alpha_{sc}\mu_{eff}$ from LFN study is compared with extracted μ_0 by the Y-function method (cf. Section 3.2.3) in the narrowest NW devices. Figure 4-25 shows $\alpha_{sc}\mu_{eff}$ as a function of μ_0 for reference SOI and strained NW devices (sSOI for NMOS, cSG-S/D and nSGOI for PMOS, respectively). It is concluded that $\alpha_{sc}\mu_{eff}$ does not clearly correlate to the mobility behavior in inversion region and the magnitude

Chapter 4. Low-frequency noise characterizations

extracted at low-field regime regardless of the mobility enhancement induced by strain for both N- and PMOS NW FETs.

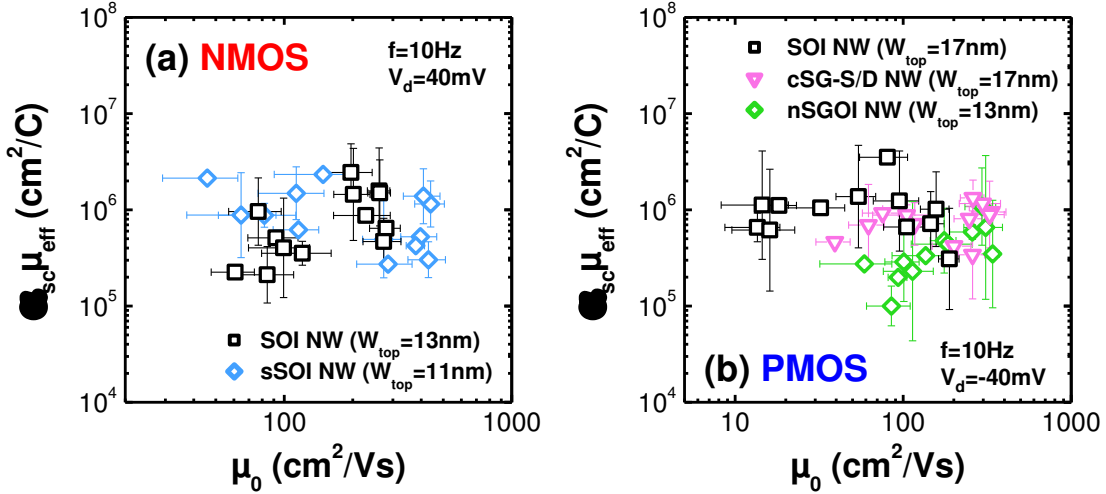


Fig. 4-25. Coulomb scattering parameter $\alpha_{sc}\mu_{eff}$ as a function of low-field mobility μ_0 extracted in Figs.3-30b and 3-31d for the narrowest NW (a) NMOS and (b) PMOS FETs.

4.2.4 Oxide trap density

4.2.4.1 General tendency

The gate oxide trap density N_t ($\text{eV}^{-1}\text{cm}^{-3}$) around quasi-Fermi energy level within $4kT$ range can be written from Eq. (4-21) as:

$$N_t = \frac{fW_{tot}L_g C_{ox}^2 S_{Vfb}}{q^2 kT \lambda} \quad (4-31)$$

The trap density N_t calculated from S_{Vfb} data (Figs.4-22 and 4-23) is shown and discussed here.

Figure 4-26 shows N_t as a function of W_{tot} and L_g in NMOS FETs with $L_g \approx 110\text{nm}$. Again, slightly higher N_t is measured in SOI with H_2 anneal and sSOI as compared with reference SOI (nearly twice higher) (Fig.4-26a). This result is in agreement with a previous work reporting higher interface trap density D_{it} for additional H_2 anneal in 3D-stacked Si NW FETs [4-69]. However, N_t in both SOI and sSOI MOSFETs as a function of L_g is distributed within one decade (10^{17} to $10^{18}\text{eV}^{-1}\text{cm}^{-3}$) due to device-to-device dispersion, especially in the narrowest NWs (Fig.4-26b). Some sSOI NWs thus have similar or lower N_t as compared to SOI NWs. Published LFN studies on

Chapter 4. Low-frequency noise characterizations

sSi MOSFETs fabricated from SiGe virtual layers have reported lower [4-73~4-75], constant [4-1], or higher [4-76~4-79] trap density compared to reference Si devices. Refs.[4-76~4-79] suggest that diffusion of Ge atoms from the SiGe layers into the Si channel and the gate oxide as well as the threading dislocations can severely degrade the gate oxide/channel interface quality (D_{it} increase has been also reported in correlation [4-80]). Therefore, extrinsic process parameters associated with sSOI substrate preparation, such as the SiGe and sSi epitaxial growth, selective etching of the SiGe, and the reliability (*i.e.* device-to-device dispersion), could dominate compared with intrinsic tensile strain impact on the gate oxide/channel interface quality.

For PMOS, the cSGOI NW shows slightly larger N_t value than the other devices in Fig.4-27a. In Fig.4-27b it can be seen that nSGOI NWs with longer $L_g < 400\text{nm}$ have relatively higher N_t . However, the influence of the compressively strained SiGe channel is not large in magnitude, while very high D_{it} [4-87] and N_t [4-48,4-49] were found in previous NW studies due to Ge content.

In literature, some work have reported N_t increase due to SiGe S/D process in FETs with HfO_2 gate oxide [4-74,4-81,4-82], and a slight increase of the noise level and D_{it} in FETs with SiO_2 or nitrided oxide [4-83~4-85]. Fortunately, it has been reported that replacing HfO_2 by HfSiON provides steady noise level with the reference Si S/D device owing to a better robustness against the thermal budget of the SiGe S/D process [4-86]. Our SiGe S/D devices show no large deviation of N_t values from reference SOI devices regardless of the compressive CESL effect. This could be ascribed to the use of HfSiON/TiN gate stack. It could be also attributed to an optimized technological process. As a result, the device-to-device dispersion is only dominant similarly to the NMOS case.

Chapter 4. Low-frequency noise characterizations

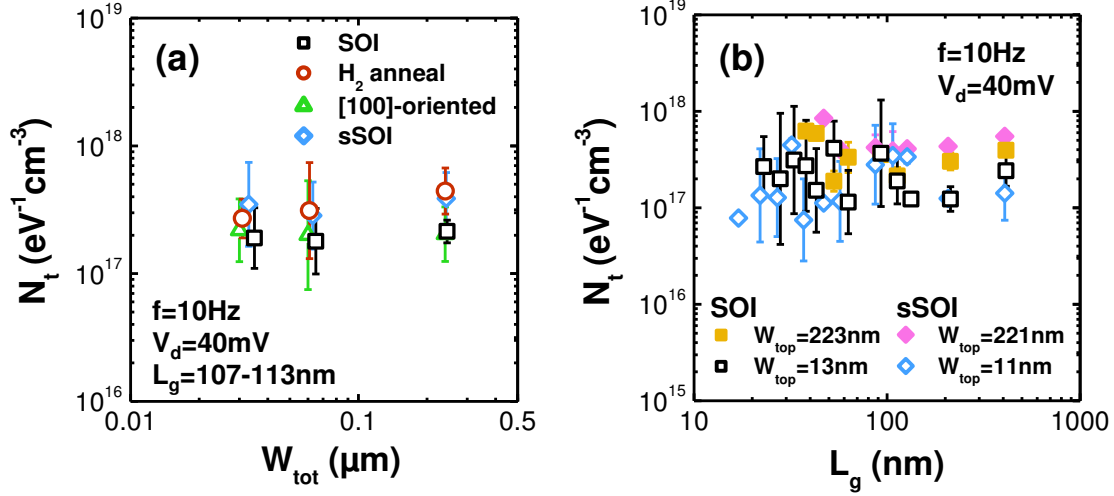


Fig. 4-26. N_t as a function of (a) W_{tot} and (b) L_g for all the technological splits in NMOS devices.

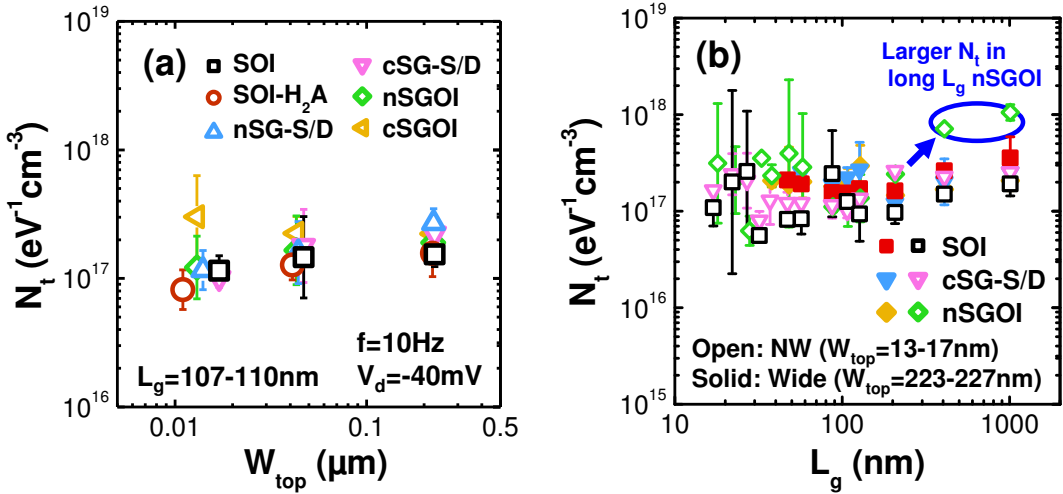


Fig. 4-27. N_t as a function of (a) W_{top} and (b) L_g for all the technological parameters in PMOS devices.

Our most important conclusion is that the mean N_t values for all the devices lie in roughly similar order ($\approx 5 \times 10^{16}$ to 10^{18} eV⁻¹cm⁻³) as the values recently reported for state-of-the-art Hf-based high- κ /metal gate technology [4-43,4-64,4-70,4-88~4-90]. The N_t values averaged over all L_g in NW and wide FETs are shown in Fig. 4-28. Data from reference SOI and strained devices (sSOI for NMOS, cSG-S/D and nSGOI for PMOS,

Chapter 4. Low-frequency noise characterizations

respectively) are compared. NWs exhibit somewhat lower values in most of the devices (except nSGOI with $2.0 \times 10^{17} \text{ eV}^{-1}\text{cm}^{-3}$ for both wide and NW FETs). This clearly indicates that the N_t values are not altered by the scaling effect of W_{top} , *i.e.* by the 2D or 3D architectural impact [4-34,4-35]. As a consequence, it is concluded that the excellent oxide/interface quality is achieved and maintained in all our N- and PMOS devices, especially in NWs with side-wall surfaces which play an increasing role as W_{top} is scaled down.

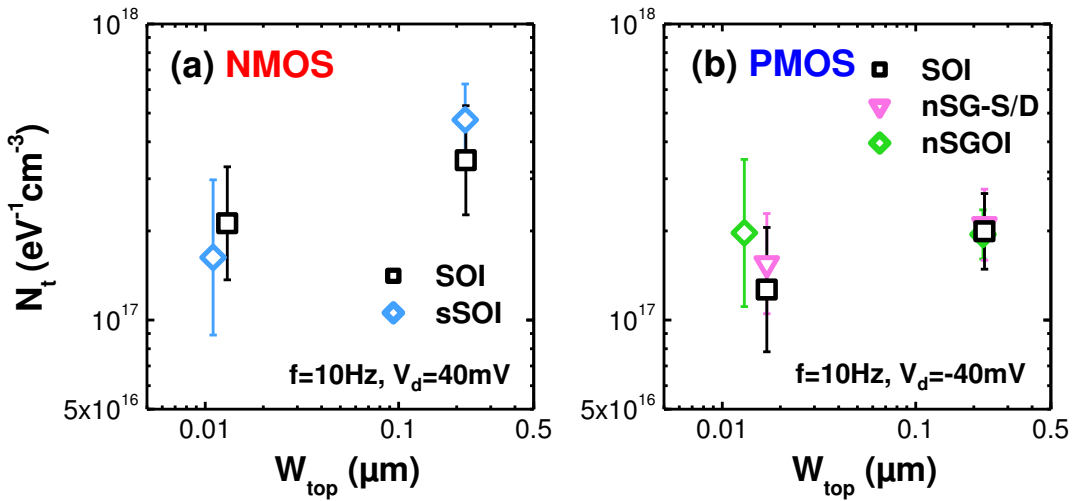


Fig. 4-28. N_t averaged over all L_g in wide and NW FETs for (a) NMOS and (b) PMOS devices, with comparison between SOI and sSOI for NMOS, and among SOI, cSG-S/D, and nSGOI for PMOS.

4.2.4.2 Assessment of the contributions of the different surface orientations

For more rigorous assessment of the interface quality, a separation method of the N_t contribution between top surface (N_{t_top}) and side-walls ($N_{t_side-wall}$) could be introduced as follows:

$$N_{t_tot} = \frac{W_{top}}{W_{tot}} N_{t_top} + \frac{2H_{NW}}{W_{tot}} N_{t_side-wall} \quad (4-32)$$

Using this simple formula, we have extracted N_{t_top} and $N_{t_side-wall}$ for three different width W_{top} ($L_g \approx 110 \text{ nm}$) as shown in Figs.4-29 and 4-30.

For NMOS, the (100) plane, which corresponds to surface orientation of the top surface of reference [110]-oriented SOI, and to the orientation of both the top and

Chapter 4. Low-frequency noise characterizations

side-walls of [100]-oriented SOI (cf. Fig.2-23), show very similar values $\sim 2 \times 10^{17} \text{ eV}^{-1} \text{ cm}^{-3}$. This agreement in (100) planes therefore confirms the reliability of the separating method. Surprisingly, the (110) plane in side-walls of [110]-oriented NW leads to slightly lower $N_{t_side-wall}$ values than the (100) top surface. In the devices performed with additional H₂ anneal, the (100) top surfaces degrades, whereas the quality of (110) side-walls is improved. Tensile strain relatively deteriorates both the top and side-wall surfaces compared to reference SOI devices.

For PMOS, the (110) planes in side-walls also show improved N_t values compared to the (100) planes (except in cSGOI devices). This could indicate that CESL process affects the side-wall quality, and that process optimization is needed. Strain process technologies otherwise (SiGe channel material or SiGe S/D) and additional H₂ anneal degrade somewhat the quality of (100) top surfaces, whereas the quality of (110) side-walls is enhanced. It is further noticed that the H₂ anneal process is less harmful in PMOS than in NMOS case.

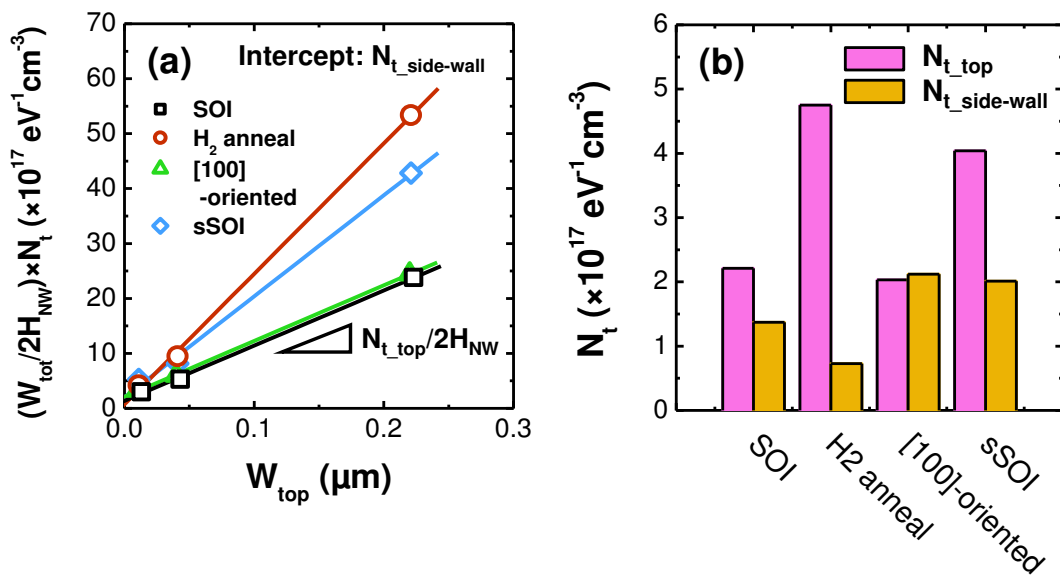


Fig. 4-29. (a) Demonstration of the extraction and (b) the extracted N_t contribution of top surface and side-walls by the N_t separation method for all the NMOS devices.

Chapter 4. Low-frequency noise characterizations

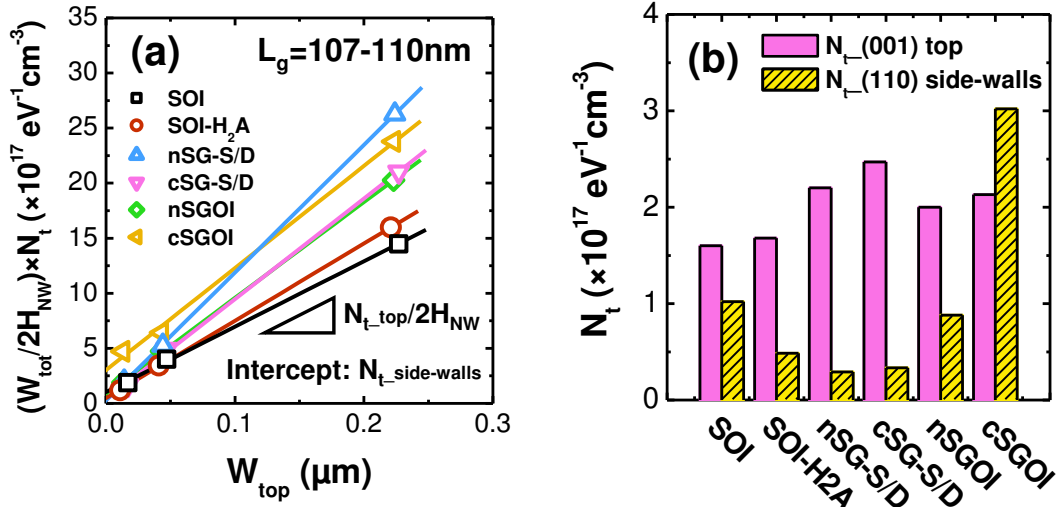


Fig. 4-30. (a) Demonstration of the extraction and (b) the extracted N_t contribution of top surface and side-walls by the N_t separation method for all the PMOS devices.

4.2.4.3 Interface quality comparison with charge pumping measurement

Oxide/channel interface quality evaluated by LFN measurement has been compared with charge pumping (CP) measurement [4-91,4-92]. To perform CP measurement on FD-SOI devices, gated diode structures with N⁺ and P⁺ contacts (P-i-N gated diode) are needed, as illustrated in Fig.4-31 [4-93,4-94]. In the CP technique, a trapezoidal voltage pulse is applied to the gate with a varying base level V_{base} and a constant amplitude ΔV_g greater than the band gap energy of Si ΔE_{g_Si}=1.12eV (here, ΔV_g=1.3eV is fixed). This pulse causes a recombination current flowing in the N⁺ and P⁺ regions by capture/release process of electrons and holes at the interface states. The maximum CP current I_{CP} can be expressed by:

$$I_{CP} = qf_p W_{tot} L_g \overline{D_{it}(E)} \Delta E \quad (4-33)$$

where f_p is the frequency of the pulsed signal, and $\overline{D_{it}(E)}$ is the mean D_{it} over the Si band gap, and ΔE is the swept energy range ($\approx 1\text{eV}$). Note that the mean D_{it} extracted by CP technique takes into account the traps distributed over the Si band gap, and is thus distinct from N_t evaluated from LFN characterization which gives a value at E_F±2kT.

Chapter 4. Low-frequency noise characterizations

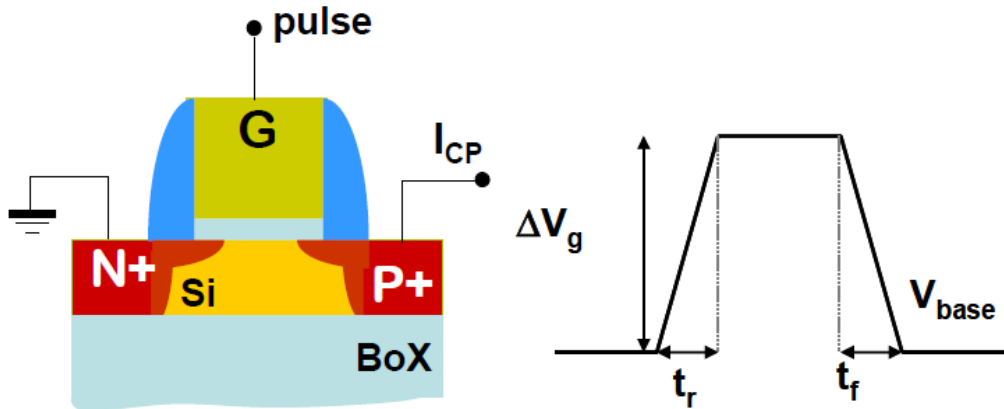


Fig. 4-31. Schematics of the experimental set-up used for charge pumping spectroscopy. A trapezoidal pulse (amplitude ΔV_g , rise and fall time t_r, t_f), with constant amplitude and varying base level V_{base} , is applied to the gate and I_{CP} is measured on the P^+ contact [4-94].

Figure 4-32 shows the extracted mean D_{it} in [110]-oriented SOI devices with $H_{NW}=11\text{nm}$ and $L_g=0.5\mu\text{m}$. Wide device with $W_{top}=2\mu\text{m}$ and multiple channel Ω -gate NWs with 75 fingers varying the W_{top} from 75nm down to 40nm have been measured. All devices exhibit mean D_{it} in the $1-3\times10^{10}\text{eV}^{-1}\text{cm}^{-2}$ range. The NWs exhibit slightly lower D_{it} compared to wide devices in agreement with our results using LFN. This corroborates our conclusions that lower trap density is present in (110) side-walls compared with (100) top surface in most of our MOSFETs.

Chapter 4. Low-frequency noise characterizations

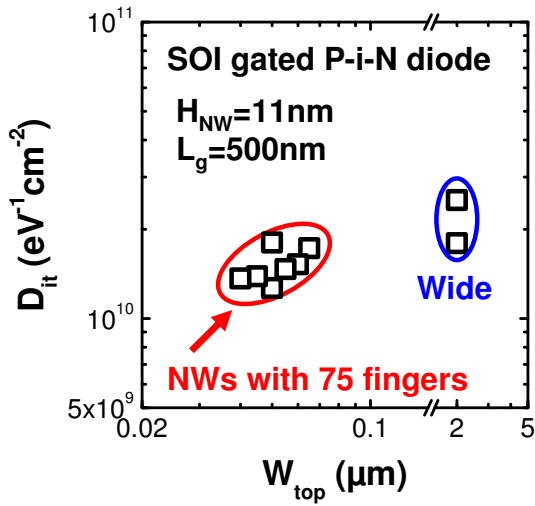


Fig. 4-32. Mean D_{it} obtained by CP measurement as a function of W_{top} in wide gated P-i-N diode and 75-multiple channel NW devices.

4.2.5 Drain bias influence

It was also studied how V_d variation from linear regime up to saturation region impact the LFN properties. $S_{Id}/I_d^2 - I_d$ characteristics have been plotted in Fig.4-33 for SOI and sSOI narrowest NW NMOS FETs. We found that a good agreement with CNF+CMF model is retained from linear ($|V_d|=40\text{mV}$ and 0.2V) to saturation regions ($|V_d|=0.9\text{V}$).

Furthermore, the plateaued noise level in subthreshold region is also maintained regardless of the drain bias variation. Both trends, agreement of CNF+CMF model and constancy of plateaued noise level for varied V_d , are also observed in SOI and nSGOI PMOS NWs, even in the devices with shortest L_g (Fig.4-34). This means that S_{Vfb} and N_t properties are nearly independent of V_d without any strain impact in N- and PMOS NWs.

Chapter 4. Low-frequency noise characterizations

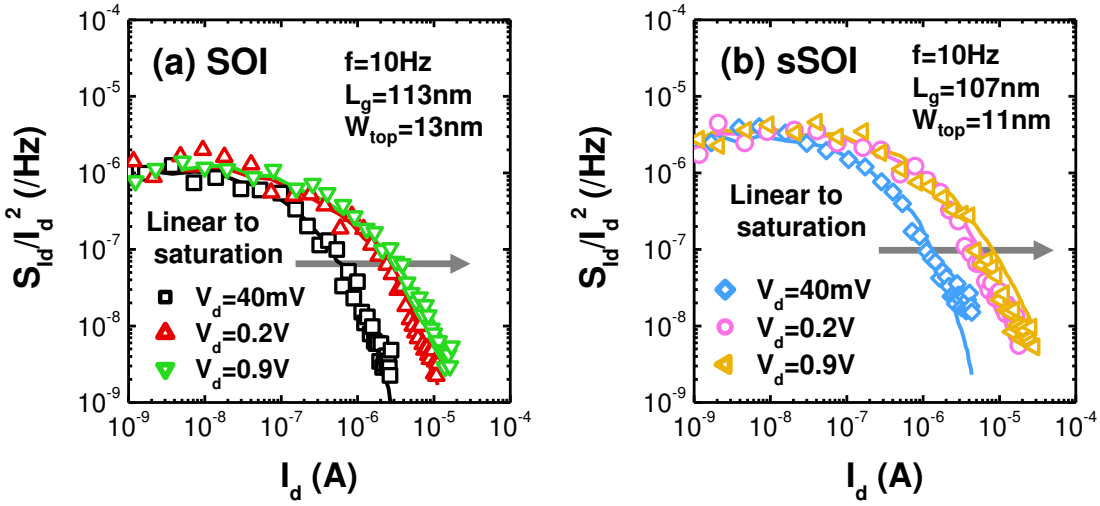


Fig. 4-33. V_d impact for (symbols) S_{Id}/I_{d}^2 - I_d characteristics of the narrowest NW NMOS FETs in (a) SOI ($L_g=113\text{nm}$) and (b) sSOI ($L_g=107\text{nm}$), with (lines) corresponding $(g_m/I_d)^2$ curves.

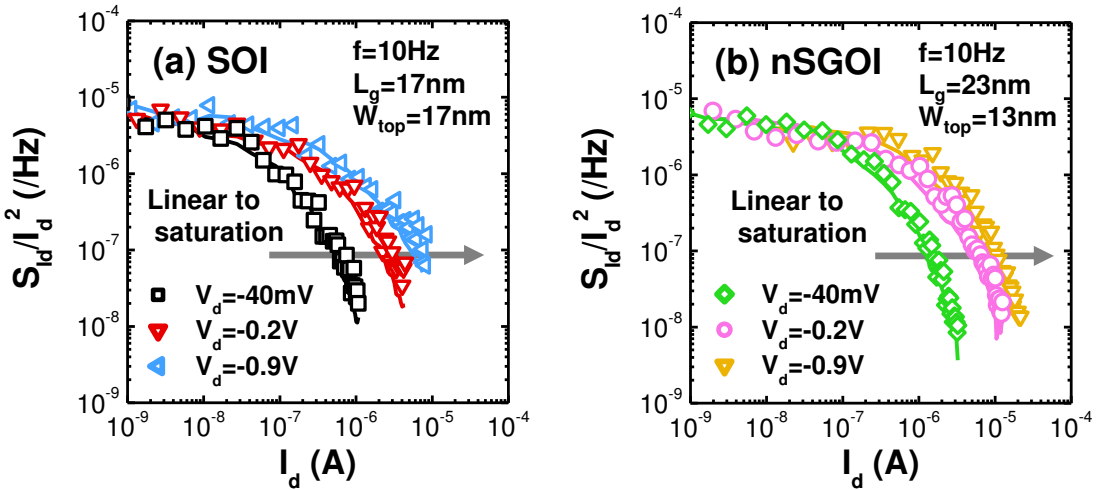


Fig. 4-34. V_d impact for (symbols) S_{Id}/I_{d}^2 - I_d characteristics of the narrowest NW PMOS FETs with short channel in (a) SOI ($L_g=17\text{nm}$) and (b) nSGOI ($L_g=23\text{nm}$), with (lines) corresponding $(g_m/I_d)^2$ curves..

4.2.6 Comparison with ITRS requirements for 1/f LFN

Finally, gate voltage noise S_{Vg} obtained from measured S_{Id} was compared with ITRS requirements for LFN showing 1/f behavior for logic devices [4-95]. S_{Vg} values are extracted at an overdrive operation ($V_g=V_t+0.2\text{V}$ for NMOS, and $V_g=V_t-0.2\text{V}$ for

Chapter 4. Low-frequency noise characterizations

PMOS, respectively), and in saturation regime ($|V_d|=0.3\text{-}0.4\text{V}$). The comparison is shown in [Figs.4-35~4-38](#). [Table 4-2](#) (graphically plotted in [Fig.1-7](#)) summarizes the yearly requirements of L_g , V_{dd} , and V_d (defined as $V_d=V_{dd}/2$) for high performance (HP) and low standby power (LSTP) logic circuits consisting of MG MOSFETs.

For NMOS, The narrowest NWs in both SOI and sSOI with gate length $L_g=22\text{-}28\text{nm}$ already fulfill the noise requirements for year 2015 with approaching $L_g=17\text{-}19\text{nm}$. They also almost satisfy the requirements for future CMOS technology node by 2026. In addition, sSOI shows slightly lower noise level that can help fulfill ITRS requirements more easily ([Fig.4-36](#)). No L_g and V_d dependence of the noise level on L_g range up to 113nm is observed, and device-to-device dispersion influence is just visible in both devices ([Fig.4-35](#)).

For PMOS, L_g and V_d independent behavior as well as device-to-device dispersion effect is similarly observed with NMOS results ([Fig.4-37](#)). The normalized S_{Vg} of NWs with $L_g=22\text{-}23\text{nm}$ satisfy the demands until 2026 whatever technological splits (SOI, SiGe S/D or SiGe channel) ([Fig.4-38](#)). At minimum $L_g=17\text{-}18\text{nm}$, the noise level in SOI and cSG-S/D exceeds the ITRS requirements in 2026, while the three options still fulfill the data in 2015. nSGOI NWs exhibit reduced noise level compared to Si channel NWs, mostly due to reduced R_{sd} fluctuations (cf. [Fig.4-19](#) and [4-20](#)).

It can be thus concluded that both tensile and compressive strain technologies, besides electrical performance improvement (mainly through transport properties), are also attractive features in terms of the future 1/f noise requirements.

Chapter 4. Low-frequency noise characterizations

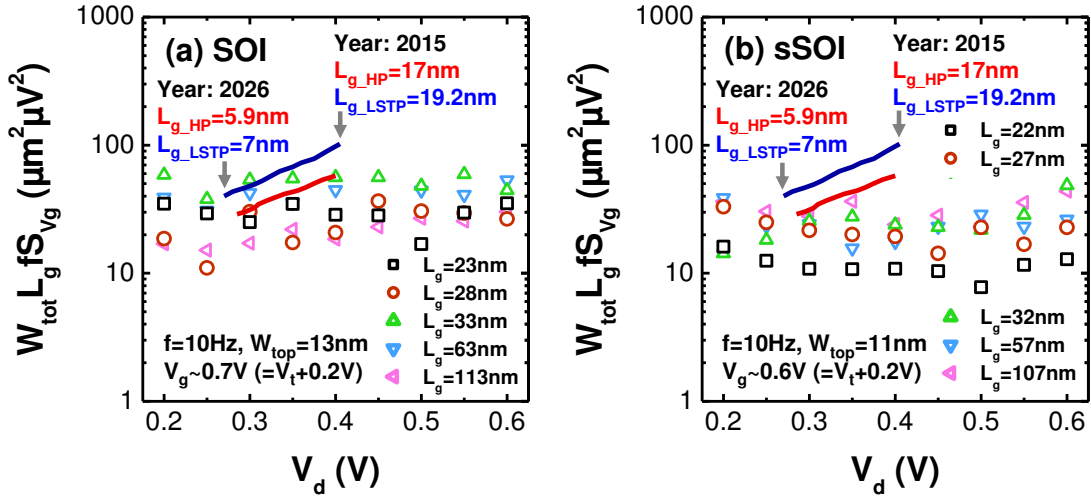


Fig. 4-35. (Symbols) S_{Vg} with normalization by channel size parameters (W_{tot} and L_g) and frequency as a function of V_d in the (a) SOI and (b) sSOI narrowest NW NMOS FETs. These data are compared with (lines) the requirements for 1/f LFN in ITRS 2013 (Table RFAMS1 CMOS technology requirements) for high performance (HP) and low standby power (LSTP) logics MG FETs [4-95].

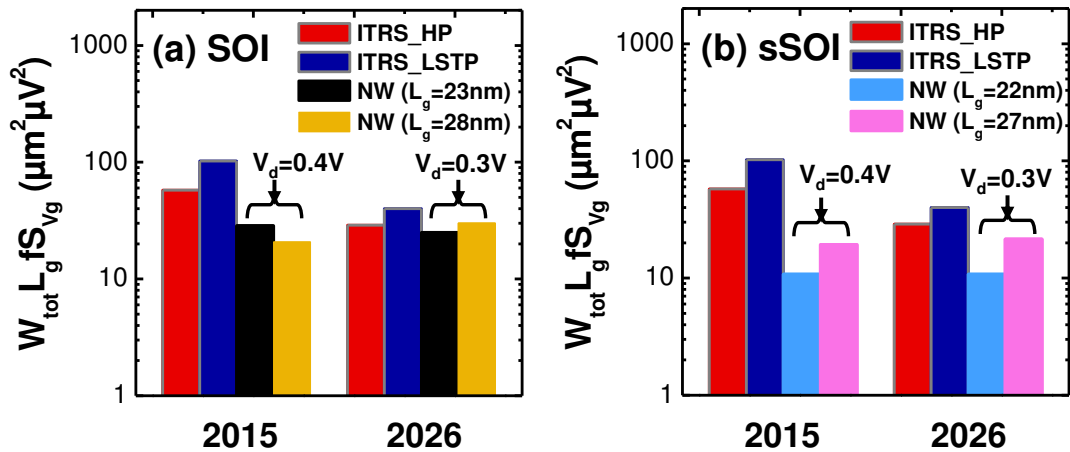


Fig. 4-36. Comparison of the normalized S_{Vg} between our experimental data and ITRS requirements in 2015 and 2026 in NMOS MG FETs [4-95].

Chapter 4. Low-frequency noise characterizations

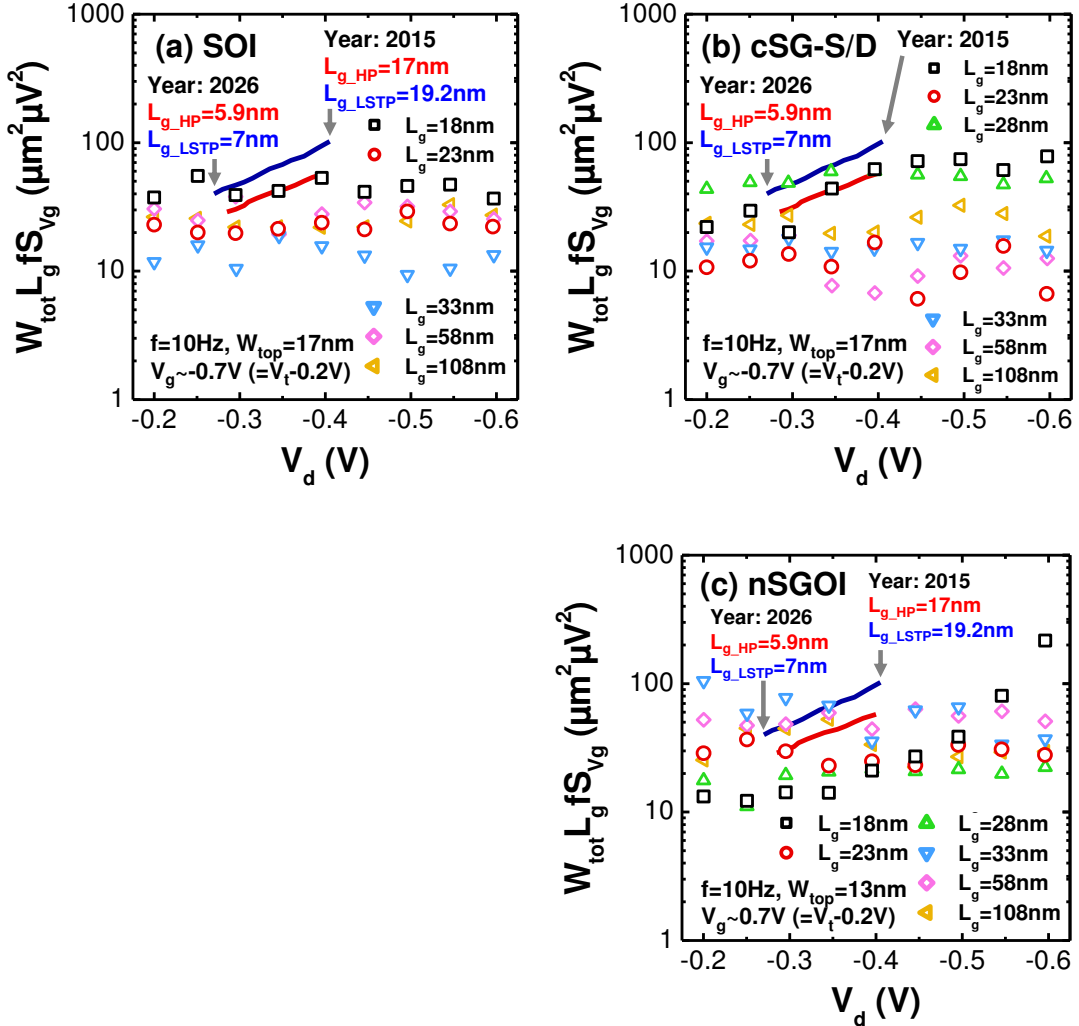


Fig. 4-37. (Symbols) S_{Vg} with normalization by channel size parameters (W_{tot} and L_g) and frequency as a function of V_d in the narrowest NW PMOS FETs for (a) SOI, (b) cSG-S/D, and (c) nSGOI devices. These data are compared with (lines) the requirements for 1/f LFN in ITRS 2013 data [4-95] (cf. Fig.4-35).

Chapter 4. Low-frequency noise characterizations

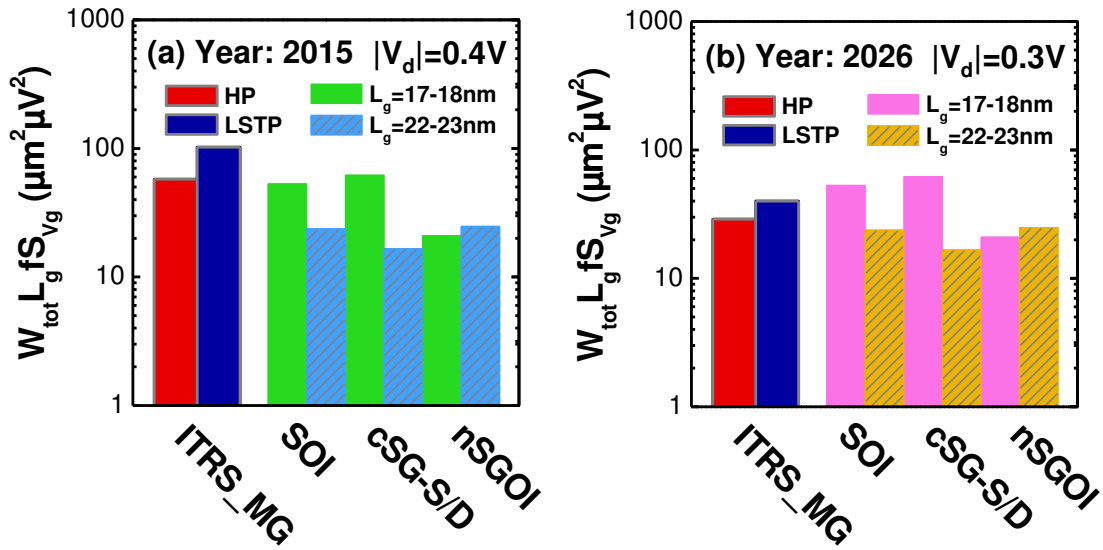


Fig. 4-38. Comparison of the normalized S_{Vg} between our experimental data and ITRS requirements in 2015 and 2026 for PMOS MG FETs [4-95].

Table 4-2. ITRS requirements data of L_g , V_{dd} , and V_d conditions for high performance (HP) and low standby power (LSTP) logic circuits consisting of MG FETs (cf. Fig.1-7) [4-95].

ITRS MG	HP			LSTP		
	Year	L_g (nm)	V_{dd} (V)	V_d (V)	L_g (nm)	V_{dd} (V)
2015	17	0.8	0.4	19.2	0.81	0.41
2016	15.3	0.77	0.39	17.5	0.78	0.39
2017	14	0.75	0.38	16	0.75	0.38
2018	12.8	0.73	0.37	14.6	0.72	0.36
2019	11.7	0.71	0.36	13.3	0.7	0.35
2020	10.6	0.68	0.34	12.1	0.67	0.34
2021	9.7	0.66	0.33	11.1	0.65	0.33
2022	8.9	0.64	0.32	10.1	0.63	0.32
2023	8.1	0.62	0.31	9.2	0.61	0.31
2024	7.4	0.61	0.31	8.4	0.59	0.30
2025	6.6	0.59	0.30	7.7	0.56	0.28
2026	5.9	0.57	0.29	7	0.54	0.27

Chapter 4. Low-frequency noise characterizations

4.3 References

- [4-1] M. von Haartman and M. Östling: *Low-frequency noise in advanced MOS devices*, Springer, Dordrecht, 2007.
- [4-2] N. Wiener, “Generalized harmonic analysis”, *Acta Mathematica*, vol. 55, pp. 117-258, 1930.
- [4-3] A. Khintchine, “Korrelationstheorie der stationären stochastischen Prozesse (Correlation theory of stationary stochastic processes),” *Mathematische Annalen*, vol. 109, pp. 604-615, 1934. [in German]
- [4-4] A. Einstein, “Über die von der molekularkinetischen Theorie der Wärme geforderte Bewegung von in ruhenden Flüssigkeiten suspendierten Teilchen (On the movement of small particles suspended in stationary liquids required by the molecular-kinetic theory of heat),” *Annalen der Physik*, vol. 17, pp. 549-560, 1905. [in German]
- [4-5] J. B. Johnson, “Thermal agitation of electricity in conductors”, *Phys. Rev.*, vol. 32, pp. 97-109, 1928.
- [4-6] H. Nyquist, “Thermal Agitation of Electric Charge in Conductors”, *Phys. Rev.*, vol. 32, pp. 110-113, 1928.
- [4-7] W. Schottky, “Über spontane Stromschwankungen in verschiedenen Elektrizitätsleitern (On spontaneous current fluctuations in various electricity conductors),” *Annalen der Physik*, vol. 57, pp. 541-567, 1918. [in German]
- [4-8] G. Bosman and R. J. J. Zijlstra, “Generation-recombination noise in p-type silicon, *Solid-State Electron.*, vol. 25, pp. 273-280, 1982.
- [4-9] M. J. Uren, D. J. Day, and M. J. Kirton, “1/f and random telegraph noise in silicon metal-oxide-semiconductor field-effect transistors,” *Appl. Phys. Lett.*, vol. 47, pp. 1195-1197, 1985.
- [4-10] P. Restle, “Individual oxide traps as probes into submicron devices,” *Appl. Phys. Lett.*, vol. 53, pp. 1862-1864, 1988.
- [4-11] K. Kandiah, M. O. Deighton, and F. B. Whiting, “A physical model for random telegraph signal currents in semiconductor devices,” *J. Appl. Phys.*, vol. 66, pp. 937-948, 1989.
- [4-12] M. J. Kirton and M. J. Uren, “Noise in solid-state microstructures: A new perspective on individual defects, interface states and low-frequency (1/f) noise,” *Adv. Phys.*, vol. 38, pp. 367-468, 1989.

Chapter 4. Low-frequency noise characterizations

- [4-13] K. K. Hung, P. K. Ko, C. Hu, and Y. C. Cheng, "Random telegraph noise of deep-submicrometer MOSFET's," *IEEE Electron Device Lett.*, vol. 11, pp. 90-92, 1990.
- [4-14] J. B. Johnson, "The Schottky effect in low frequency circuits", *Phys. Rev.*, vol. 26, pp. 71-85, 1925.
- [4-15] W. Schottky, "Small-shot effect and flicker effect," *Phys. Rev.*, vol. 28, pp. 74-103, 1926.
- [4-16] J. Bernamont, "Fluctuations in the resistance of thin films," *Proc. Physical Society*, vol. 49, pp. 138-139, 1937.
- [4-17] M. Surdin, "Fluctuations de courant thermionique et le « Flicker effect » (Thermionic current fluctuations and the « Flicker effect »)," *Journal de Physique et le Radium*, vol. 10, pp. 188-189, 1939. [in French]
- [4-18] F. N. Hooge, "1/f noise is no surface effect," *Phys. Lett.*, vol. 29A, pp. 139-140, 1969.
- [4-19] F. N. Hooge, "Discussion of recent experiments on 1/f noise," *Physica*, vol. 60, pp. 130-144, 1972.
- [4-20] F. N. Hooge, "1/f noise," *Physica*, vol. 83B, pp. 14-23, 1976.
- [4-21] F. N. Hooge and L. K. J. Vandamme, "Lattice scattering causes 1/f noise," *Phys. Lett.*, vol. 66A, pp. 315-316, 1978.
- [4-22] F. N. Hooge, T. G. M. Kleinpenning, and L. K. J. Vandamme, "Experimental studies on 1/f noise," *Rep. Prog. Phys.*, vol. 44, pp. 479-532, 1981.
- [4-23] R. H. Kingston: *Semiconductor Surface Physics*, Univ. Pennsylvania Press, Philadelphia, 1957.
- [4-24] S. Christensson, I. Lundström, and C. Svensson, "Low frequency noise in MOS transistors - I. Theory," *Solid-State Electron.*, vol. 11, pp. 797-812, 1968.
- [4-25] S. Christensson and I. Lundström, "Low frequency noise in MOS transistors - II. Experiments," *Solid-State Electron.*, vol. 11, pp. 813-820, 1968.
- [4-26] F. Berz, "Theory of low frequency noise in Si MOST's," *Solid-State Electron.*, vol. 13, pp. 631-647, 1970.
- [4-27] G. Reimbold, "Modified 1/f trapping noise theory and experiments in MOS transistors biased from weak to strong inversion - Influence of interface states," *IEEE Trans. Electron Devices*, vol. 31, pp. 1190-1198, 1984.
- [4-28] E. Simoen and C. Claeys, "On the flicker noise in submicron silicon MOSFETs," *Solid-State Electron.*, vol. 43, pp. 865-882, 1999.

Chapter 4. Low-frequency noise characterizations

- [4-29] G. Ghibaudo and T. Boutchacha, “Electrical noise and RTS fluctuations in advanced CMOS devices,” *Microelectron. Reliab.*, vol. 42, pp. 573-582, 2002.
- [4-30] C. Claeys, A. Mercha, and E. Simoen, “Low-frequency noise assessment for deep submicrometer CMOS technology nodes,” *J. Electrochem. Soc.*, vol. 151, pp. G307-G318, 2004.
- [4-31] M. von Haartman, J. Westlinder, D. Wu, B. G. Malm, P.-E. Hellström, J. Olsson, and M. Östling, “Low-frequency noise and Coulomb scattering in $\text{Si}_{0.8}\text{Ge}_{0.2}$ surface channel pMOSFETs with ALD Al_2O_3 gate dielectrics,” *Solid-State Electron.*, vol. 49, pp. 907-914, 2005.
- [4-32] M. von Haartman, A.-C. Lindgren, P.-E. Hellström, B. G. Malm, S.-L. Zhang, and M. Östling, “ $1/f$ noise in Si and $\text{Si}_{0.7}\text{Ge}_{0.3}$ pMOSFETs,” *IEEE Trans. Electron Devices*, vol. 50, pp. 2513-2519, 2003.
- [4-33] M. von Haartman, B. G. Malm, and M. Östling, “Comprehensive study on low-frequency noise and mobility in Si and SiGe pMOSFETs with high- κ gate dielectrics and TiN gate,” *IEEE Trans. Electron Devices*, vol. 53, pp. 836-843, 2006.
- [4-34] F. Crupi, B. Kaczer, R. Degraeve, V. Subramanian, P. Srinivasan, E. Simoen, A. Dixit, M. Jurczak, and G. Groeseneken, “Reliability comparison of triple-gate versus planar SOI FETs,” *IEEE Trans. Electron Devices*, vol. 53, pp. 2351-2357, 2006.
- [4-35] E. Simoen, A. Mercha, C. Claeys, N. Lukyanchikova, “Low-frequency noise in silicon-on-insulator devices and technologies,” *Solid-State Electron.*, vol. 51, pp. 16-37, 2007.
- [4-36] K. Bennamane, T. Boutchacha, G. Ghibaudo, M. Mouis, and N. Collaert, “DC and low frequency noise characterization of FinFET devices,” *Solid-State Electron.*, vol. 53, pp. 1263-1267, 2009.
- [4-37] C. Wei, Y.-Z. Xiong, and X. Zhou, “Investigation of low-frequency noise in n-channel FinFETs from weak to strong inversion,” *IEEE Trans. Electron Devices*, vol. 56, pp. 2800-2810, 2009.
- [4-38] M. G. C. de Andrade, J. A. Martino, E. Simoen, and C. Claeys, “Comparison of the low-frequency noise of bulk triple-gate FinFETs with and without dynamic threshold operation,” *IEEE Electron Device Lett.*, vol. 32, pp. 1597-1599, 2011.
- [4-39] C. G. Theodorou, N. Fasarakis, T. Hoffman, T. Chiarella, G. Ghibaudo, and C. A. Dimitriadi, “Flicker noise in n-channel nanoscale tri-gate fin-shaped field-effect transistors,” *Appl. Phys. Lett.*, vol. 101, 243512, 2012.

Chapter 4. Low-frequency noise characterizations

- [4-40] T. Romeo, L. Pantisano, E. Simoen, R. Krom, M. Togo, N. Horiguchi, J. Mitard, A. Thean, G. Groeseneken, C. Claeys, and F. Crupi, “Low-Frequency Noise Assessment of the Transport Mechanisms in SiGe Channel Bulk FinFETs,” *Proc. ESSDERC*, 2012, pp. 330-333.
- [4-41] E. Simoen, T. Romeo, L. Pantisano, A. Luque Rodríguez, J. A. Jiménez Tejada, M. Aoulaiche, A. Veloso, M. Jurczak, R. Krom, J. Mitard, Ch. Caillat, P. Fazan, F. Crupi, and C. Claeys, “Insights in low frequency noise of advanced and high-mobility channel transistors,” *IEDM Tech. Dig.*, 2012, pp. 661–664.
- [4-42] C. G. Theodorou, N. Fasarakis, T. Hoffman, T. Chiarella, G. Ghibaudo, and C. A. Dimitriadis, “Origin of the low-frequency noise in n-channel FinFETs,” *Solid-State Electron.*, vol. 82, pp. 21-24, 2013.
- [4-43] J. W. Lee, M. J. Cho, E. Simoen, R. Ritzenthaler, M. Togo, G. Boccardi, J. Mitard, L.-Å Ragnarsson, T. Chiarella, A. Veloso, N. Horiguchi, A. Thean, and G. Groeseneken, “1/f noise analysis of replacement metal gate bulk p-type fin field effect transistor,” *Appl. Phys. Lett.*, vol. 102, 073503, 2013.
- [4-44] J. W. Lee, E. Simoen, A. Veloso, M. J. Cho, H. Arimura, G. Boccardi, L.-Å. Ragnarsson, T. Chiarella, N. Horiguchi, A. Thean, and G. Groeseneken, “1/f noise analysis of replacement metal gate bulk p-type fin field effect transistor,” *IEEE Trans. Electron Devices*, vol. 60, pp. 2960-2962, 2013.
- [4-45] J. Zhuge, R. Wang, R. Huang, Y. Tian, L. Zhang, D.-W. Kim, D. Park, Y. Wang, “Investigation of low-frequency noise in silicon nanowire MOSFETs,” *IEEE Electron Device Lett.*, vol. 30, pp. 57-60, 2009.
- [4-46] C. Wei, Y.-Z. Xiong, X. Zhou, N. Singh, S. C. Rustagi, G. Q. Lo, and D.-L. Kwong, “Investigation of low-frequency noise in silicon nanowire MOSFETs in the subthreshold region,” *IEEE Electron Device Lett.*, vol. 30, pp. 668-671, 2009.
- [4-47] C. Wei, Y. Jiang, Y.-Z. Xiong, X. Zhou, N. Singh, S. C. Rustagi, G. Q. Lo, and D.-L. Kwong, “Impact of gate electrodes on 1/f noise of gate-all-around silicon nanowire transistors,” *IEEE Electron Device Lett.*, vol. 30, pp. 1081-1083, 2009.
- [4-48] K. Tachi, M. Cassé, D. Jang, C. Dupré, A. Hubert, N. Vulliet, V. Maffini-Alvaro, C. Vizioz, C. Carabasse, V. Delaye, J. M. Hartmann, G. Ghibaudo, H. Iwai, S. Cristoloveanu, O. Faynot, and T. Ernst, “Relationship between mobility and high-k interface properties in advanced Si and SiGe nanowires,” *IEDM Tech. Dig.*, 2009, pp. 313-316.

Chapter 4. Low-frequency noise characterizations

- [4-49] D. Jang, J. W. Lee, K. Tachi, L. Montes, T. Ernst, G. T. Kim, and G. Ghibaudo, “Low-frequency noise in strained SiGe core-shell nanowire p-channel field effect transistors,” *Appl. Phys. Lett.*, vol. 97, 073505, 2010.
- [4-50] R.-H. Baek, C.-K. Baek, H.-S. Choi, J.-S. Lee, Y. Y. Yeoh, K. H. Yeo, D.-W. Kim, K. Kim, D. M. Kim, and Y.-H. Jeong, “Characterization and modeling of 1/f noise in Si-nanowire FETs: effects of cylindrical geometry and different processing of oxides,” *IEEE Trans. Nanotechnol.*, vol. 10, pp. 417-423, 2011.
- [4-51] W. Feng, R. Hettiarachchi, Y. Lee, S. Sato, K. Kakushima, M. Sato, K. Fukuda, M. Niwa, K. Yamabe, K. Shiraishi, H. Iwai, and K. Ohmori, “Fundamental origin of excellent low-noise property in 3D Si-MOSFETs ~Impact of charge-centroid in the channel due to quantum effect on 1/f noise~,” *IEDM Tech. Dig.*, 2011, pp. 630–633.
- [4-52] S.-H. Lee, C.-K. Baek, S. Park, D.-W. Kim, D. K. Sohn, J.-S. Lee, D. M. Kim, and Y.-H. Jeong, “Characterization of channel-diameter-dependent low-frequency noise in silicon nanowire field-effect transistors,” *IEEE Electron Device Lett.*, vol. 33, pp. 1348-1350, 2012.
- [4-53] M. Saitoh, K. Ota, C. Tanaka, and T. Numata, “Systematic understanding of channel-size dependence of low-frequency noise in 10nm-diameter tri-gate nanowire MOSFETs,” *Symp. VLSI Tech. Dig.*, 2013, pp. T228-T229.
- [4-54] S.-H Lee, Y.-R. Kim, J.-H. Hong, E.-Y. Jeong, J.-S. Yoon, C.-K Baek, D.-W. Kim, J.-S. Lee, and Y.-H Jeong, “Investigation of low-frequency noise in p-type nanowire FETs: Effect of switched biasing condition and embedded SiGe layer,” *IEEE Electron Device Lett.*, vol. 35, pp. 702-704, 2014.
- [4-55] K. K. Hung, P. K. Ko, C. Hu, and Y. C. Cheng, “A physics-based MOSFET noise model for circuit simulators,” *IEEE Trans. Electron Devices*, vol. 37, pp. 1323-1333, 1990.
- [4-56] G. Ghibaudo, O. Roux, Ch. Nguyen-Duc, F. Balestra, and J. Brini, “Improved analysis of low frequency noise in field-effect MOS transistors,” *Phys. Status Solidi A*, vol. 124, pp. 571-581, 1991.
- [4-57] F. M. Klaassen “Characterization of low 1/f noise in MOS transistors,” *IEEE Trans. Electron Devices*, vol. ED-18, pp. 887-891, 1971.
- [4-58] A. van del Ziel, “Unified presentation of 1/f noise in electronic devices: Fundamental 1/f noise sources,” *Proc. IEEE*, vol. 76, pp. 233-258, 1988.
- [4-59] E. A. Hendriks and R. J. J. Zijlstra, “1/f noise in (100) n-channel Si-MOSFETs from T=4.2K to T=295K,” *Solid-State Electron.*, vol. 31, pp. 1105-1111, 1988.

Chapter 4. Low-frequency noise characterizations

- [4-60] I. M. Hafez, G. Ghibaudo, and F. Balestra, "A study of flicker noise in MOS transistors operated at room and liquid helium temperatures," *Solid-State Electron.*, vol. 33, pp. 1525-1529, 1990.
- [4-61] H. C. Pao and C. T. Sah, "Effects of diffusion current on characteristics of metal-oxide (insulator)-semiconductor transistors," *Solid-State Electron.*, vol. 9, pp. 927-937, 1966.
- [4-62] G. Ghibaudo, "On the theory of carrier number fluctuations in MOS devices," *Solid-State Electron.*, vol. 32, pp. 563-565, 1989.
- [4-63] P. Srinivasan, E. Simoen, R. Singanamalla, H. Y. Yu, C. Claeys, and D. Misra, "Gate electrode effects on low-frequency (1/f) noise in p-MOSFETs with high- κ dielectrics," *Solid-State Electron.*, vol. 50 pp. 992-998, 2006.
- [4-64] B. C. Wang, S. L. Wu, Y. Y. Lu, S. J. Chang, J. F. Chen, S. C. Tsai, C. H. Hsu, C. W. Yang, C. G. Chen, O. Cheng, and P. C. Huang, "Comparison of the trap behavior between ZrO₂ and HfO₂ gate stack nMOSFETs by 1/f noise and random telegraph noise," *IEEE Electron Device Lett.*, vol. 34 pp. 151-153, 2013.
- [4-65] E. Simoen, A. Veloso, Y. Higuchi, N. Horiguchi, and C. Claeys, "On the oxide trap density and profiles of 1-nm EOT metal-gate last CMOS transistors assessed by low-frequency noise," *IEEE Trans. Electron Devices*, vol. 60, pp. 3849-3855, 2013.
- [4-66] R. Jayaraman and C. G. Sodini, "A 1/f noise technique to extract the oxide trap density near the conduction band edge of silicon," *IEEE Trans. Electron Devices*, vol. 36, pp. 1773-1782, 1989.
- [4-67] N. Lukyanchikova, M. Petrichuk, N. Garbar, E. Simoen, A. Mercha, C. Claeys, H. van Meer, and K. De Meyer, "The 1/f^{1.7} noise in submicron SOI MOSFETs with 2.5 nm nitrided gate oxide," *IEEE Trans. Electron Devices*, vol. 49, pp. 2367-2370, 2002.
- [4-68] H.-S. Fu and C.-T. Sah, "Theory and experiments on surface 1/f noise," *IEEE Trans. Electron Devices*, vol. ED-19, pp. 273-285, 1972.
- [4-69] M. Cassé, K. Tachi, S. Thiele, and T. Ernst, "Spectroscopic charge pumping in Si nanowire transistors with a high- κ /metal gate," *Appl. Phys. Lett.*, vol. 96, 123506, 2010.
- [4-70] E. G. Ioannidis, C. A. Dimitriadis, S. Haendler, R. A. Bianchi, J. Jomaah, and G. Ghibaudo, "Improved analysis and modeling of low-frequency noise in nanoscale MOSFETs," *Solid-State Electron.*, vol. 76, pp. 54-59, 2012.
- [4-71] J. A. Chroboczek, "Automatic, wafer-level, low frequency noise measurements for the interface slow trap density evaluation," *Proc. ICMTS*, 2003, pp. 95-98.

Chapter 4. Low-frequency noise characterizations

- [4-72] P. Gaubert, A. Teramoto, W. Cheng, and T. Ohmi, "Relation between the mobility, 1/f noise, and channel direction in MOSFETs fabricated on (100) and (110) silicon-oriented wafers," *IEEE Trans. Electron Devices*, vol. 57, pp. 1597-1607, 2010.
- [4-73] E. Simoen, G. Eneman, P. Verheyen, R. Delhougne, R. Loo, K. De Meyer, and C. Claeys, "On the beneficial impact of tensile-strained silicon substrates on the low-frequency noise of n-channel metal-oxide-semiconductor transistors," *Appl. Phys. Lett.*, vol. 86, 223509, 2005.
- [4-74] E. Simoen, G. Eneman, P. Verheyen, R. Loo, K. De Meyer, and C. Claeys, "Processing aspects in the low-frequency noise of nMOSFETs on strained-silicon substrates," *IEEE Trans. Electron Devices*, vol. 53, pp. 1039-1047, 2006.
- [4-75] E. Simoen, and C. Claeys, "Impact of strain-engineering on the low-frequency noise performance of advanced MOSFETs," *Proc. ICSICT*, 2006, pp. 120-123.
- [4-76] M. H. Lee, P. S. Chen, W.-C. Hua, C.-Y. Yu, Y. T. Tseng, S. Maikap, Y. M. Hsua, C. W. Liu, S. C. Lu, W.-Y. Hsieh, and M.-J. Tsai, "Comprehensive low-frequency and RF noise characteristics in strained-Si NMOSFETs," *IEDM Tech. Dig.*, 2003.
- [4-77] W.-C. Hua, M. H. Lee, P. S. Chen, S. Maikap, C. W. Liu, and K. M. Chen, "Ge outdiffusion effect on flicker noise in strained-Si nMOSFETs," *IEEE Electron Device Lett.*, vol. 25, pp. 693-695, 2004.
- [4-78] W.-C. Hua, M. H. Lee, P. S. Chen, M.-J. Tsai, and C. W. Liu, "Threading dislocation induced low frequency noise in strained-Si nMOSFETs," *IEEE Electron Device Lett.*, vol. 26, pp. 667-669, 2005.
- [4-79] Y. P. Wang, S. L. Wu, and S. J. Chang, "Low-frequency noise characteristics in strained-Si nMOSFETs," *IEEE Electron Device Lett.*, vol. 28, pp. 36-38, 2007.
- [4-80] G. K. Dalapati, S. Chattopadhyay, K. S. K. Kwa, S. H. Olsen, Y. L. Tsang, R. Agaiby, A. G. O'Neill, P. Dobrosz, and S. J. Bull, "Impact of strained-Si thickness and Ge out-diffusion on gate oxide quality for strained-Si surface channel n-MOSFETs," *IEEE Trans. Electron Devices*, vol. 53, pp. 1142-1152, 2006.
- [4-81] G. Giusi, E. Simoen, G. Eneman, P. Verheyen, F. Crupi, K. De Meyer, C. Claeys, and C. Ciofi, "Low-frequency (1/f) noise behavior of locally stressed HfO₂/TiN gate-stack pMOSFETs," *IEEE Electron Device Lett.*, vol. 27, pp. 508-510, 2006.
- [4-82] B. C. Wang, S. L. Wu, C. W. Huang, Y. Y. Lu, S. J. Chang, Y. M. Lin, K. H. Lee, and O. Cheng, "Correlation between random telegraph noise and 1/f noise parameters in 28-nm pMOSFETs with tip-shaped SiGe source/drain," *IEEE Electron Device Lett.*, vol. 33, pp. 928-930, 2012.

Chapter 4. Low-frequency noise characterizations

- [4-83] C. Y. Cheng, Y. K. Fang, J. C. Hsieh, H. Hsia, Y. M. Sheu, W. T. Lu, W. M. Chen, and S. S. Lin, “Investigation and localization of the SiGe source/drain (S/D) strain-induced defects in PMOSFET with 45-nm CMOS technology,” *IEEE Electron Device Lett.*, vol. 28, pp. 408-411, 2007.
- [4-84] J. J.-Y. Kuo, W. P.-N. Chen, and P. Su, “Investigation of low frequency noise in uniaxial strained PMOSFETs,” *Proc. VLSI-TSA*, 2009, pp. 82-83.
- [4-85] J. J.-Y. Kuo, W. P.-N. Chen, and P. Su, “Impact of uniaxial strain on low-frequency noise in nanoscale PMOSFETs,” *IEEE Electron Device Lett.*, vol. 30, pp. 672-674, 2009.
- [4-86] E. Simoen, P. Verheyen, A. Shickova, R. Loo, and C. Claeys, “On the low-frequency noise of pMOSFETs with embedded SiGe source/drain and fully silicided metal gate,” *IEEE Electron Device Lett.*, vol. 28, pp. 987-989, 2007.
- [4-87] L. Hutin, M. Cassé, C. Le Royer, J.-F. Damlencourt, A. Pouydebasque, C. Xu, C. Tabone, J.-M. Hartmann, V. Carron, H. Grampeix, V. Mazzocchi, R. Truche, O. Weber, P. Batude, X. Garros, L. Clavelier, M. Vinet, and O. Faynot, “20nm gate length trigate pFETs on strained SGOI for high performance CMOS,” *Symp. VLSI Tech. Dig.*, 2010, pp. 37-38.
- [4-88] D. Lopez, S. Haendler, C. Leyris, G. Bidal, and G. Ghibaudo, “Low-frequency noise investigation and noise variability analysis in high-k/metal gate 32-nm CMOS transistors,” *IEEE Trans. Electron Devices*, vol. 58, pp. 2310-2316, 2011.
- [4-89] E. G. Ioannidis, S. Haendler, A. Bajolet, T. Pahron, N. Planes, F. Arnaud, R. A. Bianchi, M. Haond, D. Golanski, J. Rosa, C. Fenouillet-Beranger, P. Perreau, C. A. Dimitriadis, and G. Ghibaudo, “Low frequency noise variability in high-k/metal gate stack 28nm bulk and FD-SOI CMOS transistors,” *IEDM Tech. Dig.*, 2011, pp. 449-452.
- [4-90] C. G. Theodorou, E. G. Ioannidis, S. Haendler, N. Planes, F. Arnaud, F. Andrieu, T. Poiroux, O. Faynot, J. Jomaah, C. A. Dimitriadis, and G. Ghibaudo, “Front-back gate coupling effect on 1/f noise in ultra-thin Si film FDSOI MOSFETs,” *Proc. ESSDERC*, 2012, pp. 223-226.
- [4-91] J. S. Brugler and P. G. A. Jespers, “Charge pumping in MOS devices,” *IEEE Trans. Electron Devices*, vol. 16, pp. 297-302, 1969.
- [4-92] G. Groeseneken, H. E. Maes, N. Beltran, and R. F. De Keersmaecker, “A reliable approach to charge-pumping measurements in MOS transistors,” *IEEE Trans. Electron Devices*, vol. ED-31, pp. 42-53, 1984.

Chapter 4. Low-frequency noise characterizations

- [4-93] T. Elewa, H. Haddara, S. Cristoloveanu, and M. Bruel, “Charge pumping in silicon on insulator structure using gated P-i-N diodes,” *J. Phys. Colloques*, vol. 49, pp. 137-140, 1988.
- [4-94] M. Cassé, X. Garros, O. Weber, F. Andrieu, G. Reimbold, and F. Boulanger, “A study of N-induced traps due to a nitrided gate in high- κ /metal gate nMOSFETs and their impact on electron mobility,” *Solid-State Electron.*, vol. 65-66, pp. 139-145, 2011.
- [4-95] “RF and analog/mixed-signal technologies (RFAMS) 2013 tables,” ITRS 2013 edition. [Online] Available: http://www.itrs.net/Links/2013ITRS/2013Tables/RFAMS_2013Tables.xlsx (accessed on 30 June 2014).

Chapter 5

Conclusions

5.1 Carrier transport characterizations

5.2 Low-frequency noise characterizations

5.3 Feature of strain technologies in advanced NW MOSFETs

5.4 Future perspectives

5.5 References

Chapter 5. Conclusions

In this work, the gate oxide/channel interface properties were experimentally and comprehensively investigated by carrier transport and low-frequency noise (LFN) characterizations in ultra-scaled NW MOSFETs. The purpose and originality of this work are to understand electrical properties of the gate oxide/channel interface mainly by LFN investigations with important concerns as follows;

- (i) CNF+CMF model parameters as a function of channel size down to NW
- (ii) NW FETs with advanced Hf-based high- κ /metal gate stack
- (iii) Contributions of different crystallographic orientations of channel surface
- (iv) Large channel surface/volume ratio in NW
- (v) Strained NW technology;

NMOS - tensile strain

PMOS - compressive strain

Our Si NW MOSFETs were fabricated from advanced fully-depleted SOI (FD-SOI) substrate to efficiently reduce detrimental SCE, resulting in the cross-section as small as 10nm×10nm. As the gate stack, Hf-based high- κ /metal (HfSiON/TiN) was used in order to suppress the gate leakage effects. Furthermore, strain introduction to the channel was additively processed to further improve the MOSFET's on-state performance. Tensile strained-SOI substrate was applied for NMOS, on the other hand, three-types of compressive stressors were used for PMOS devices; strained Si channel by raised SiGe-S/D and CESL formations, and strained SiGe-on-insulator (SGOI) substrate. In addition, impacts on channel direction difference ([110] vs. [100]) and on NW cross-sectional shape (w/ or w/o additional H₂ anneal resulting in the rectangular or rounded shape) were parametrically tested.

5.1 Carrier transport characterizations

Firstly, the most common and important I_d - V_g characteristics were studied in single-channel Ω -gate NW MOSFETs to understand the basic performance. 4-types of

Chapter 5. Conclusions

parameters; threshold voltage V_t , drain induced barrier lowering (DIBL), subthreshold swing (SS), and on-state current I_{ON} were extracted and discussed. The reference SOI NWs successively provided the excellent static control against SCE as shown in DIBL and SS discussions. The stressors dramatically enhanced the I_{ON} owing to a modification of the channel energy-band structure. However, the SCE endurance was negatively affected, especially for PMOS consisted of SGOI NWs. This trade-off relationship thus needs to more optimize the strain processing.

Next, carrier effective mobility μ_{eff} was carefully studied in strained and unstrained Si NWs with the 50-multiple channel fingers along [110]-direction and with the rectangular (TG) or rounded (Ω G) NW cross-sectional shapes. We found that: (i) the μ_{eff} properties in TGNW with (100) top and (110) side-wall surfaces are well described by the separate contribution of inversion surfaces for the rectangular section as small as $10\text{nm} \times 10\text{nm}$; (ii) Ω GNW mainly exhibits the similar μ_{eff} behavior as TGNW, in spite of the more complex geometry with multiple surface orientations, for the top-view width W_{top} down to 23 nm; (iii) lower Coulomb scattering was observed in Ω GNW, as a possible consequence of the additional H_2 anneal process; (iv) uniaxial tensile strain obtained from sSOI substrate was effective in NMOS NWs, independently of the NW geometry, and can thus be exploited to enhance entirely NMOS performance in NW dimension.

Then, low-field mobility μ_0 in the single-channel NW devices was characterized for L_g down to 17nm. We observed that: (i) the L_g dependent μ_0 degradation is appeared in NW devices as with wide MOSFETs, highlighting the specific behavior in NW architecture for both N- and PMOS by degradation factor α_μ discussion; (ii) sSOI NWs for NMOS maintains the advantage of uniaxial tensile strain down to the shortest $L_g=22\text{-}23\text{nm}$ with smaller normalized S/D resistance R_{SD} ; (iii) 4-types of compressive stressors for PMOS NWs largely improve the performance, especially nSGOI NW shows the lowest normalized R_{SD} and the highest μ_0 gain at the shortest $L_g=17\text{-}18\text{nm}$. The μ_0 extraction exhibits the effectiveness for MOSFET's performance evaluation even for ultra-scaled single-channel NW architecture.

Chapter 5. Conclusions

5.2 Low-frequency noise characterizations

The LFN investigation was effectively applied for the evaluation of various technological and architectural parameters. Carrier number fluctuations with correlated mobility fluctuations (CNF+CMF) model can describe the 1/f noise behavior from subthreshold to strong inversion modes in all our devices down to the shortest and narrowest NW MOSFET. The drain current noise behavior is basically similar in both N- and PMOS devices regardless of the technological splits. Larger 1/f noise impact stemming from S/D regions in PMOS devices can be perfectly interpreted by the CNF+CMF model completed with a term of R_{SD} fluctuations. This observation shows the lower S/D region noise in nSGOI NW, and thus the advantage can be clearly found.

The geometrical variations with the W_{top} and L_g alter the CNF component on LFN, the flat-band voltage noise S_{Vfb} , with simple impact of device scaling, which is reciprocal to both W_{tot} and L_g . Any harmful impact of surface orientation difference between the channel (100) top and (110) side-walls is not observed. The scaling regularity with both W_{tot} and L_g , without much quantum effect, could be attributed to the use of HfSiON/TiN gate stack and the carrier transport occurring mainly in 2D surfaces of top and side-walls even in NW geometry. On the other hand, the CMF factor, Coulomb scattering parameter $\alpha_{sc}\mu_{eff}$, is not altered by decreasing dimensions or 3D structure impacts, while the mobility strongly depends on the impacts. It only dominated by device-to-device dispersion. No clear relationship between the $\alpha_{sc}\mu_{eff}$ and μ_0 is observed, also without influence of improved mobility in strained NW FETs.

The oxide trap density N_t extracted from the S_{Vfb} is not also significantly modified by scaling, architecture, and technological parameter impacts. The separation method of the contributions between top surface and side-walls of the channel is demonstrated in order to strictly assess the difference. It reveals that the oxide quality on (100) top and on (110) side-walls is roughly comparable in all the [110]-oriented devices. The N_t values are also roughly steady and same as the recently reported values. Therefore, an excellent quality of the interface with Hf-based high- κ /metal gate stack is sustained for all our technological and geometrical device parameters.

Chapter 5. Conclusions

Variation of the drain voltage bias does not significantly influence the LFN behaviors (CNF+CMF model and oxide trap density) in our NW MOSFETs regardless of L_g scaling and strain effect. Furthermore, the both strained and unstrained NWs accomplish the 1/f LFN requirements for future CMOS logic node with MG FETs stated in the ITRS in 2013. It is thus well demonstrated that strain technology is a powerful booster of the NW FET performances.

5.3 Feature of strain technologies in advanced NW MOSFETs

It is finally concluded that the appropriate strain technologies powerfully provide beneficial features to improve both carrier transport and 1/f LFN properties for future CMOS circuits consisting of NW FETs, without a significant concern on the oxide/channel interface quality. Consequently, the channel interface quality is mainly dominated by the extrinsic fabrication parameters appearing as device-to-device dispersion, in undoped FD-channel technology with HfSiON/TiN gate stack, whereas the carrier transport property strongly depends on intrinsic structural impacts.

5.4 Future perspectives

LFN measurement can be applicable for the characterization of further advanced MG devices, which is GAA junction-less (JL) FET only comprised of uniformly doped body without S/D regions [5-1]. The GAA JL-FET with a short $L_g=3\text{nm}$ can operate without noticeable SCE [5-2]. For characterizations in Schottky S/D device [5-3], thin-film-transistor (TFT) [5-4], nanowire FETs with the different body materials from Si [5-5,5-6], the LFN measurement has been also used. Moreover, the LFN measurement has been applied for characterization of the different concept device from MOSFET such as tunnel-FET (TFET) [5-7~5-10] and high electron mobility transistors (HEMT) [5-11,5-12]. The TFET and HEMT operated under different carrier transport theory from MOSFET, achieving better switching performance with the steeper SS than

Chapter 5. Conclusions

MOSFET's lower limit of 60mV/dec by using TFETs in theory, and with availability for further high-frequency operation by using HEMTs. The different noise theory from CNF+CMF model is expected for TFETs owing to the band-to-band tunneling (BTBT) based carrier transport. Furthermore, LFN investigation can be a powerful diagnosis tool even for future promising devices consisting of novel 1D or 2D materials, such as carbon nanotube (CNT) [5-13~5-16], graphene [5-17,5-18], and molybdenum-disulfide (MoS_2) [5-19~5-24].

Chapter 5. Conclusions

5.5 References

- [5-1] D. Y. Jang, J. W. Lee, C.-W. Lee, J.-P. Colinge, L. Montès, J. I. Lee, G. T. Kim, and G. Ghibaudo, “Low-frequency noise in junctionless multigate transistors,” *Appl. Phys. Lett.*, vol. 98, 133502, 2011.
- [5-2] J.-P. Colinge, C.-W. Lee, A. Afzalian, N. D. Akhavan, R. Yan, I. Ferain, P. Razavi, B. O’Neill, A. Blake, M. White, A.-M. Kelleher, B. McCarthy, and R. Murphy “Nanowire transistors without junctions,” *Nature Nanotechnol.*, vol. 5, pp. 225-229, 2010.
- [5-3] B. G. Malm, M. Olyaei, and M. Östling, “Low-frequency noise in FinFETs with PtSi Schottky-barrier source/drain contacts,” *Proc. ICNF*, 2011, pp. 135-138.
- [5-4] C. G. Theodorou, A. Tsormpatzoglou, C. A. Dimitriadis, S. A. Khan, M. K. Hatalis, J. Jomaah, and G. Ghibaudo, “Origin of low-frequency noise in the low drain current range of bottom-gate amorphous IGZO thin-film transistors,” *IEEE Electron Device Lett.*, vol. 32, pp. 898-900, 2011.
- [5-5] S. Kim, H. Kim, D. B. Janes, and S. Ju, “Interface studies of N₂ plasma-treated ZnSnO nanowire transistors using low-frequency noise measurements,” *Nanotechnol.*, vol. 24, 305201, 2013.
- [5-6] C. J. Delker, Y. Zi, C. Yang, and D. B. Janes, “Low-frequency noise contributions from channel and contacts in InAs nanowire transistors,” *IEEE Trans. Electron Devices*, vol. 60, pp. 2900-2905, 2013.
- [5-7] J. Wan, C. Le Royer, A. Zaslavsky, and S. Cristoloveanu, “Low-frequency noise behavior of tunneling field effect transistors,” *Appl. Phys. Lett.*, vol. 97, 243503, 2010.
- [5-8] J. Wan, C. Le Royer, A. Zaslavsky, and S. Cristoloveanu, “Tunneling FETs on SOI: Suppression of ambipolar leakage, low-frequency noise behavior, and modeling,” *Solid-State Electron.*, vol. 65-66, pp. 226-233, 2011.
- [5-9] S. Richter, S. Vitusevich, S. Pud, J. Li, L. Knoll, S. Trelenkamp, A. Schafer, S. Lenk, Q. T. Zhao, A. Offenhausser, S. Mantl, and K. K. Bourdelle, “Low frequency noise in strained silicon nanowire array MOSFETs and tunnel-FETs,” *Proc. ESSDERC*, 2013, pp. 256-259.
- [5-10] R. Bijesh, D. K. Mohata, H. Liu, and S. Datta, “Flicker noise characterization and analytical modeling of homo and hetero-junction III-V tunnel FETs,” *Proc. DRC*, 2012, pp. 203-204.

Chapter 5. Conclusions

- [5-11] M. Silvestri, M. J. Uren, N. Killat, D. Marcon, and M. Kuball, “Localization of off-stress-induced damage in AlGaN/GaN high electron mobility transistors by means of low frequency 1/f noise measurements,” *Appl. Phys. Lett.*, vol. 103, 043506, 2013.
- [5-12] M. Silvestri, M. J. Uren, N. Killat, D. Marcon, and M. Kuball, “Physics-based analysis of low frequency drain noise-current in $\text{Al}_x\text{Ga}_{1-x}\text{N}/\text{GaN}$ HFETs,” *J. Phys. D: Appl. Phys.*, vol. 47, 085104, 2014.
- [5-13] J. Appenzeller, Y.-M. Lin, J. Knoch, Z. Chen, and P. Avouris, “1/f noise in carbon nanotube devices - On the impact of contacts and device geometry,” *IEEE Trans. Nanotechnol.*, vol. 6, pp. 368-373, 2007.
- [5-14] S. Kim, S. Kim1, D. B Janes, S. Mohammadi, J. Back, and M Shim, “DC modeling and the source of flicker noise in passivated carbon nanotube transistors,” *Nanotechnol.*, vol. 21, 385203, 2010.
- [5-15] M.-K. Joo, U. J. Kim, D.-Y. Jeon, S. J. Park, M. Mouis, G.-T. Kim, G. Ghibaudo, “Static and low frequency noise characterization of densely packed CNT-TFTs,” *Proc. ESSDERC*, 2012, pp. 129-132.
- [5-16] M.-K. Joo, M. Mouis, D.-Y. Jeon, G.-T. Kim, U. J. Kim, and G. Ghibaudo, “Static and low frequency noise characterization of N-type random network of carbon nanotubes thin film transistors,” *J. Appl. Phys.*, vol. 114, 154503, 2013.
- [5-17] G. Liu, S. Rumyantsev, M. S. Shur, and A. A. Balandin, “Origin of 1/f noise in graphene multilayers: Surface vs. volume,” *Appl. Phys. Lett.*, vol. 102, 093111, 2013.
- [5-18] A. A. Balandin, “Low-frequency 1/f noise in graphene devices,” *Nature Nanotechnol.*, vol. 8, pp. 549-555, 2013.
- [5-19] V. K. Sangwan, H. N. Arnold, D. Jariwala, T. J. Marks, L. J. Lauhon, and M. C. Hersam, “Low-frequency electronic noise in single-layer MoS₂ transistors,” *Nano Lett.*, vol. 13, pp. 4351-4355, 2013.
- [5-20] J. Na, M.-K. Joo, M. Shin, J. Huh, J.-S. Kim, M. Piao, J.-E. Jin, H.-K. Jang, H. J. Choi, J. H. Shim, and G.-T. Kim, “Low-frequency noise in multilayer MoS₂ field-effect transistors: the effect of high- κ passivation,” *Nanoscale*, vol. 6, pp. 433-441, 2014.
- [5-21] H.-J. Kwon, H. Kang, J. Jang, S. Kim, and C. P. Grigoropoulos, “Analysis of flicker noise in two-dimensional multilayer MoS₂ transistors,” *Appl. Phys. Lett.*, vol. 104, 083110, 2014.
- [5-22] J. Renteria, R. Samnakay, S. L. Rumyantsev, C. Jiang, P. Goli, M. S. Shur, and A. A. Balandin, “Low-frequency 1/f noise in MoS₂ transistors: Relative contributions of the channel and contacts,” *Appl. Phys. Lett.*, vol. 104, 153104, 2014.

Chapter 5. Conclusions

-
- [5-23] X. Xie, D. Sarkar, W. Liu, J. Kang, O. Marinov, M. J. Deen, and K. Banerjee, “Low-frequency noise in bilayer MoS₂ transistor,” *ACS Nano*, vol. 8, pp. 5633-5640, 2014.
 - [5-24] S. Ghatak, S. Mukherjee, M. Jain, D. D. Sarma, and A. Ghosh, “Microscopic origin of low frequency noise in MoS₂ field-effect transistors,” *APL Materials*, vol. 2, 092515, 2014.

Résumé de la thèse en français

Introduction générale

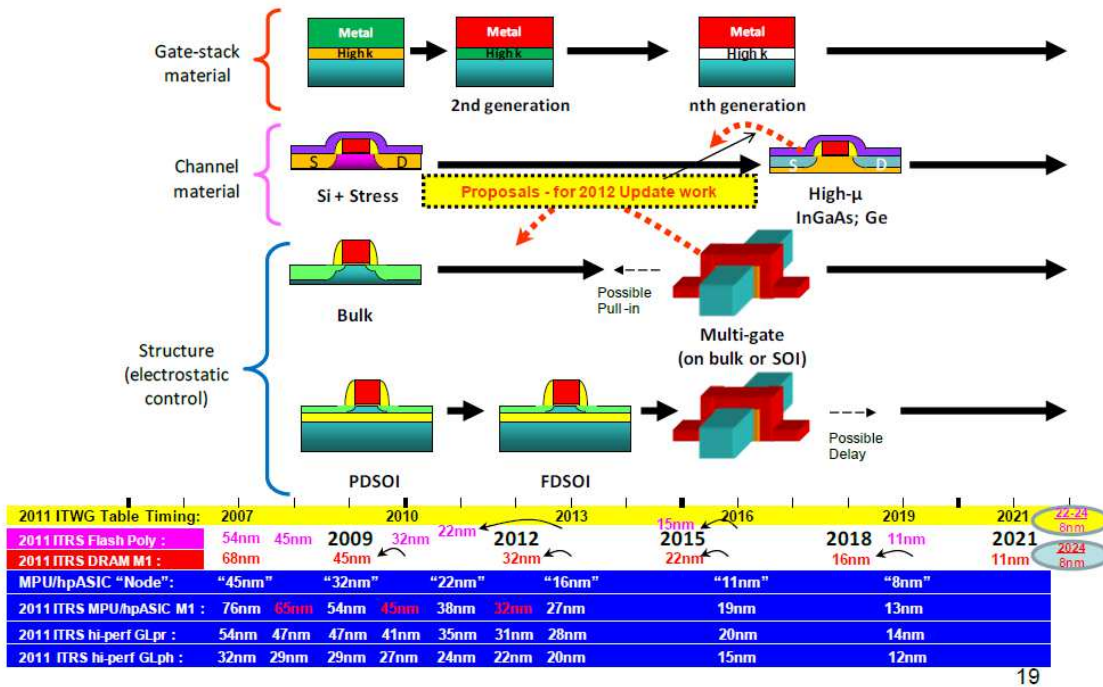


Fig. 6-1. Feuille de route de l'ITRS 2011 pour les technologies CMOS, avec les différents noms des nœuds technologiques correspondants [1-19].

Les futurs nœuds technologiques CMOS devraient exiger des architectures de transistors multigrilles (MG) (Fig.6-1). Par ces transistors MG, les transistors nanofilms dont les dimensions ont été réduites jusqu'à quelques nanomètres pour la section, représentent une alternative sérieuse. Cependant, la qualité de l'interface oxyde de grille/canal pose question pour transistors dont l'architecture s'étend dans les 3 dimensions, en raison du fort rapport surface/volume inhérent à ces transistors, des différentes orientations cristallographiques de ces interfaces, ou encore des matériaux contraints utilisés pour améliorer les performances électriques. La compréhension des liens entre les propriétés de transport des porteurs dans le canal, qui garantissent en grande partie les performances électriques des transistors, et la qualité de l'interface avec l'oxyde de grille est primordiale pour optimiser les transistors nanofilms.

Pour ces nouvelles architectures MG, en particulier pour les dispositifs nanofilms (NW), il est devenu difficile d'utiliser rigoureusement les caractérisations électriques conventionnelles, comme les méthodes de caractérisation basées sur une mesure de capacité (comme par exemple les mesures split-CV pour caractériser le transport). Le

Résumé de la thèse en français

bruit basse fréquence (LFN) permet de caractériser précisément les propriétés électriques de l'interface oxyde de grille / canal dans les MOSFETs [1-22]. De plus les mesures de bruit basse fréquence n'ont pas de limite minimale de surface de dispositif mesurable, contrairement aux mesures de capacité. Par conséquent, la mesure de bruit peut être une technique de caractérisation puissante pour les MOSFETs nanofils sans être limité par la taille ultra-réduite de ces transistors.

Du point de vue des circuits les circuits RF / analogiques, le bruit basse fréquence peut représenter un problème. En effet le bruit ne peut pas être complètement éliminé et fixe une limite inférieure de détection de signaux dans les dispositifs et les circuits analogiques. Par conséquent, les mesures et la compréhension du bruit basse fréquence sont très importants afin d'évaluer (*i*) les propriétés de l'interface canal/oxyde de grille, et (*ii*) les performances des MOSFETs.

Aujourd'hui, un grand nombre de travaux ont été publiés sur les mesures de bruit, y compris dans les dispositifs MG (que ce soit des FinFETs [1-23~1-35] ou des transistors nanofils [1-36~1-45]). Concernant les caractérisations de bruit dans les dispositifs MG récents, l'origine du bruit 1/f est principalement attribuée aux fluctuations du nombre de porteurs corrélées aux fluctuations de mobilité (CNF + CMF). Hung *et al.* ont suggéré le modèle CNF + CMF en 1990 [1-46], puis Ghibaudo *et al.* ont proposé une définition plus populaire [1-47]. Dans la pratique, le modèle est principalement approprié pour les dispositifs MG. Peu d'études approfondies ont été publiées sur l'évolution de chaque paramètres définis dans le modèle CNF + CMF en fonction de la taille des MOSFETs (largeur de canal W_{TOP} et longueur de grille L_G), de l'architecture (planaire *vs.* MG), et de différents paramètres technologiques (comme l'orientation du canal, la contrainte, etc ...).

Dans cette thèse, les propriétés électriques de transistors à nanofils de silicium liées à l'interface oxyde de grille/canal ont donc été étudiées par le biais de mesures de bruit basse fréquence (bruit 1/f) et de transport dans le canal. Les propriétés de transport ont également été abordées dans cette étude, dans la mesure où le paramètre principal du transport – la mobilité des porteurs dans le canal en inversion – apparaît dans le modèle de bruit (fluctuations de mobilité des porteurs) et dans la mesure où la mobilité est également très sensible à l'interface oxyde / canal. Cette thèse s'attache en

Résumé de la thèse en français

particuliers à étudier en détail certains points importants pour les MOSFETs nanofils :

- (i) les paramètres du modèle CNF + CMF en fonction de la taille du canal, des transistors planaires (W_{top} large) jusqu'au nanofils (W_{top} de l'ordre de quelques nm)
- (ii) le bruit dans les transistors nanofils intégrant un empilement de grille métal / oxyde de grille à forte permittivité (à base de Hf).
- (iii) les contributions des différentes orientations cristallographiques du canal des transistors.
- (iv) L'influence du rapport surface / volume dans les transistors nanofils.
- (v) L'influence des contraintes mécaniques (contrainte en *tension* pour les NMOS, contrainte en *compression* pour les PMOS).

Ce résumé est composé de deux grandes parties qui donnent une vue générale de mon travail de thèse.

Une première partie décrit brièvement la technologie de fabrication des transistors nanofils étudiés dans cette thèse, ainsi que les différentes caractérisations du transport en lien avec l'interface oxyde de grille / canal pour les différents MOSFETs nanofils (chapitre 3 du manuscrit de thèse). En particulier l'évolution de la mobilité effective (μ_{eff}) en fonction de la température et la mobilité à faible champ (μ_0) extraite en fonction de la longueur de grille sont présentées.

La deuxième partie présente les mesures de bruit $1/f$ (chapitre 4 du manuscrit). Les valeurs des densités spectrales de bruit S_{Id}/I_d^2 , l'évaluation des paramètres basés sur le modèle de bruit $1/f$ avancé (bruit de tension de bandes-plates S_{Vfb} , paramètre de Coulomb $\alpha_c \mu_{eff}$, et la densité de pièges dans l'oxyde N_t), la dépendance en fonction de la tension de drain (S_{VG-V_d}), sont caractérisés. Enfin le comportement de toutes les variantes de transistors nanofils par rapport aux exigences ITRS est analysé.

Partie I : Les transistors nanofils et la caractérisation du transport

A. Les transistors nanofils FDSOI

Résumé de la thèse en français

Les transistors nanofils étudiés ont été fabriqués à partir de substrats minces SOI ou sSOI, et intègrent un empilement de grille HfSiON/TiN, qui permet de réduire les dimensions tout en conservant les mêmes propriétés électrostatiques ([Fig 6.2](#)).

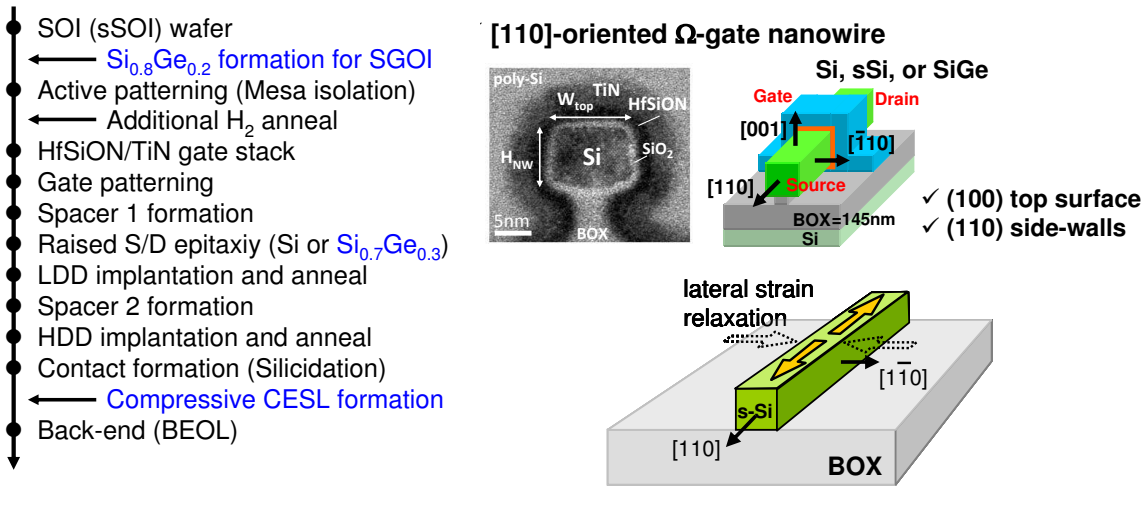


Fig. 6-2. (a) Schéma des principales étapes technologiques utilisées pour la fabrication des transistors nanofils FDSOI. (b) La relaxation de la contrainte dans la direction latérale (largeur du nanofils) permet d'obtenir un nanofils de Si en tension uniaxiale à partir d'un substrat sSOI (contrainte initiale biaxiale).

Pour gagner en performances, des contraintes mécaniques ont été introduites dans le canal en silicium : en tension pour les NMOS, par le biais de substrat contraint (sSOI, tension biaxiale de 1.4GPa), et en compression pour les PMOS ([Fig. 6-3](#)). Un canal en compression uni-axiale peut être obtenu par l'intégration de source/drain en SiGe et/ou par l'utilisation de couches contraintes de type CESL. Des transistors à canal SiGe sur isolant en compression (20% et 30% de Ge soit respectivement 1.4GPa et 2.1GPa) ont également été fabriqués et étudiés ([Fig. 6-4](#)). Pour les transistors nanofils la contrainte initialement biaxiale dans le cas des substrats SiGeOI et sSOI se réduit à une contrainte uniaxiale dans la direction du canal en raison de la relaxation de celle-ci en bord de zone active ([Fig. 6-2b](#)).

L'ensemble de variantes technologiques étudiées ici est résumé dans la [Fig.6-5](#). Pour les NMOS, quatre types de paramètres technologiques ont été étudiés: deux orientations de canal selon [110] ou [110], un recuit supplémentaire H_2 , un canal [110] en tension uniaxiale (sSOI). Pour les PMOS, six variantes ont été étudiées: une référence SOI, un

Résumé de la thèse en français

recuit supplémentaire H₂ (SOI-H2A), une architecture S/D surélevés Si_{0.7}Ge_{0.3} (NSG-S/D), une architecture S/D SiGe et CESL en compression (CSG-S/D), le canal Si_{0.8}Ge_{0.2}OI en compression (nSGOI), et enfin le canal SGOI avec CESL en compression (cSGOI). Tous les PMOS ont un canal orienté selon [110].

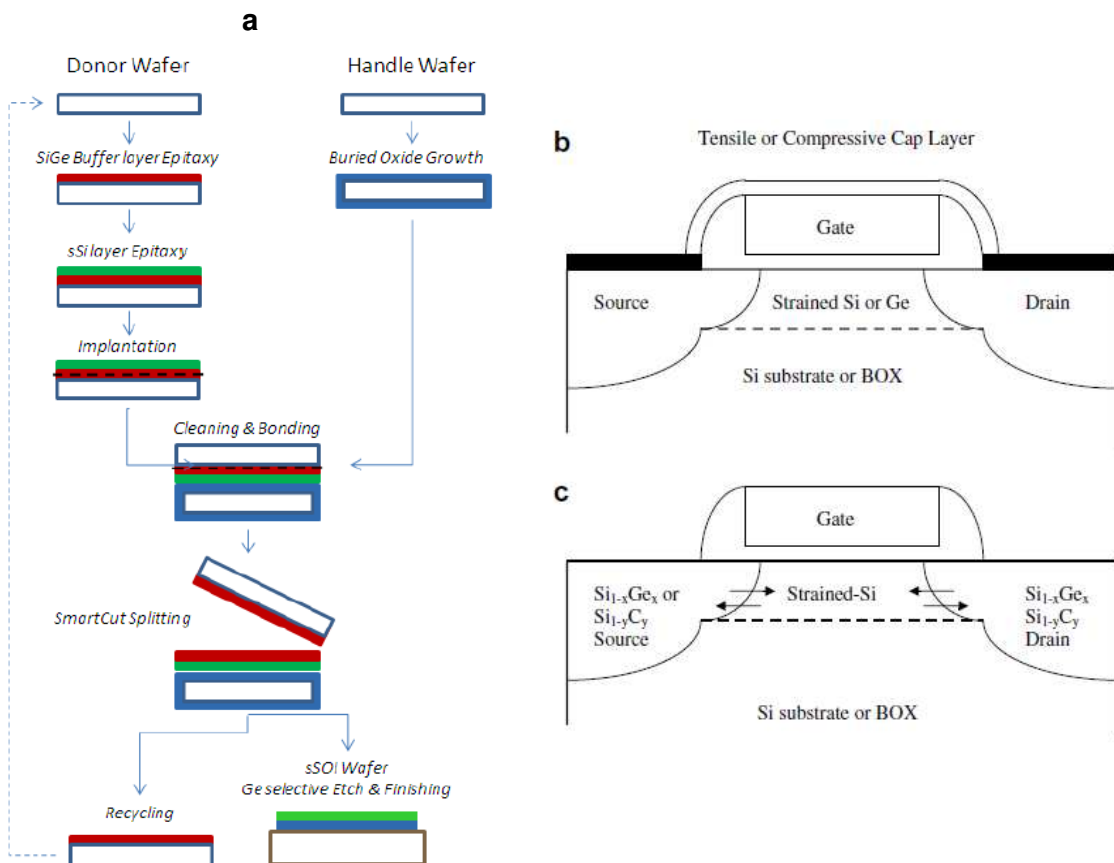


Fig. 6-3. Illustration des différentes stratégies utilisées pour implémenter une contrainte dans les transistors : (a) à partir d'un substrat sSOI [2-89] obtenu par épitaxie de silicium constraint sur un substrat *virtuel* de Si_{1-x}Ge_x; (b) contrainte locale du canal en tension ou compression obtenue par transfert de contrainte d'une couche déposée au-dessus de la grille (CESL); (c) contrainte locale du canal en tension ou compression obtenue à partir de source/drain fabriqués en SiGe (PMOS en compression) ou SiC (NMOS en tension).

Résumé de la thèse en français

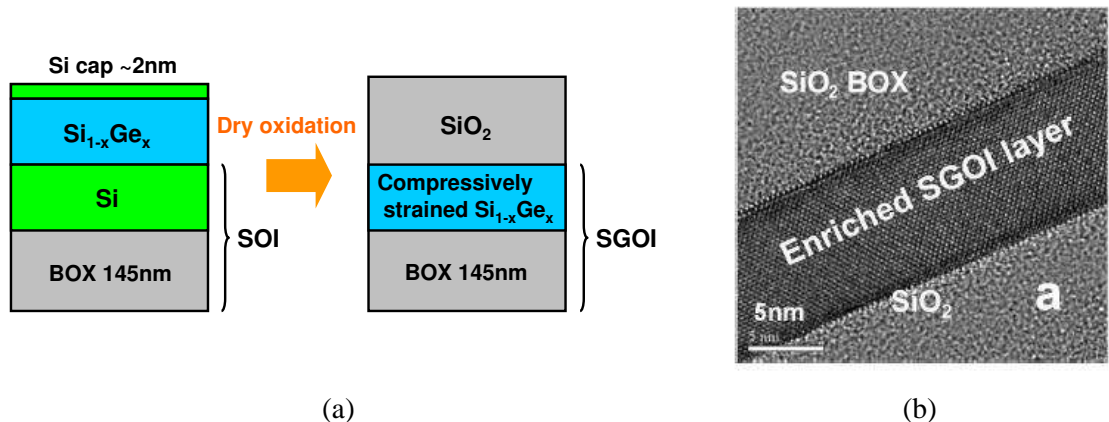


Fig. 6-4. Schéma de principe de la préparation d'un substrat de SiGe en compression sur isolant (SGOI) par la technique de condensation de Ge. La structure SiGe initialement épitaxiée sur Si permet d'enrichir cette couche en Ge par oxydation de la couche supérieure de Si. (b) Image TEM de la structure finale SGOI ($\text{SiO}_2/\text{SiGe}/\text{BOX}$) obtenue par condensation [2-95].

Ω-gate NW NMOS FETs	Channel		H ₂ anneal	NW height H _{NW}	Narrowest NW top width W _{top}
	Material	Direction			
Reference SOI	Si	[110]	No	11nm	13nm
SOI with H ₂ anneal	Si	[110]	Yes	10nm	11nm
[100]-oriented SOI	Si	[100]	No	10nm	10nm
Strained-SOI (sSOI)	sSi	[110]	No	11nm	11nm

[110]-oriented Ω-gate PMOS	Undoped channel	Raised S/D with B dope	C-CESL	H ₂ anneal	NW height H _{NW}	Narrowest NW top width W _{top}
SOI	Si	Si	No	No	13.5nm	17nm
SOI-H ₂ A	Si	Si	No	Yes	12nm	11nm
nSG-S/D	Si	Si _{0.8} Ge _{0.3}	No	No	9.5nm	14nm
cSG-S/D	Si	Si _{0.7} Ge _{0.3}	Yes	No	13.5nm	17nm
nSGOI	Si _{0.8} Ge _{0.2}	Si _{0.7} Ge _{0.3}	No	No	11.5nm	13nm
cSGOI	Si _{0.8} Ge _{0.2}	Si _{0.7} Ge _{0.3}	Yes	No	11.5nm	13nm

Fig. 6-5. Résumé de l'ensemble des variantes technologiques testées dans cette thèse.

Les caractéristiques électriques des divers transistors nanofils (courbes I_d - V_g , compromis I_{on} - I_{off} , mobilité des porteurs) démontrent l'excellent contrôle électrostatique dû à l'architecture 3D, ainsi que l'efficacité de l'ingénierie de contraintes dans les nanofils jusqu'à de faibles longueurs de grilles (~17nm).

B. La caractérisation du transport

La mobilité des porteurs est un paramètre important du fonctionnement des MOSFETs, qui intervient dans la définition du courant de drain I_d . Ce paramètre a été extrait par la technique conventionnelle split-CV [3-5~3-8] pour les transistors à canal long (typiquement $L=10\mu\text{m}$). Pour les transistors à canal plus court l'évaluation de la mobilité faible champ μ_0 basée sur la méthode de la fonction Y permet d'étudier l'évolution du transport en fonction de la longueur de grille [3-4,3-11~3-13].

Résumé de la thèse en français

La mobilité effective μ_{eff} des porteurs a été systématiquement mesurée en fonction de la température, de la température ambiante (300K) jusqu'à 20K, afin d'étudier les différents mécanismes d'interactions impliqués dans le transport des électrons et des trous (Fig.6-6). Pour les nanofils NMOS comme pour les PMOS, avec une orientation de canal [110], la mobilité des porteurs est significativement différente de celle des transistors planaires larges, surtout à basse température ($T < 100\text{K}$). Ce comportement démontre la contribution non négligeable des parois latérales pour les transistors nanofils, en accord notamment avec une mobilité différentes pour des surfaces d'inversion (100) et (110).

Les contributions des surfaces supérieure et latérale sur la mobilité des transistors TG ont été extraites en utilisant l'expression de la mobilité totale suivante [3-25,3-28]:

$$\mu_{TG} = \frac{W_{top}}{W_{tot}} \mu_{top}^{(100)} + \frac{2H_{NW}}{W_{tot}} \mu_{side-wall}^{(110)} \quad (3-15)$$

où μ_{top} et $\mu_{side-wall}$ représentent la mobilité correspondant à chaque orientation de la surface d'inversion des nanofils, à savoir (100) pour la surface supérieure, et (110) pour les parois latérales. En utilisant cette équation et en faisant l'hypothèse raisonnable que la mobilité pour la surface (100) supérieure μ_{top} est simplement donnée par la mobilité des transistors larges ($W=10\mu\text{m}$), les contributions respectives de la surface supérieure et des parois latérales peuvent être dé-corréllées simplement (Fig.6-7).

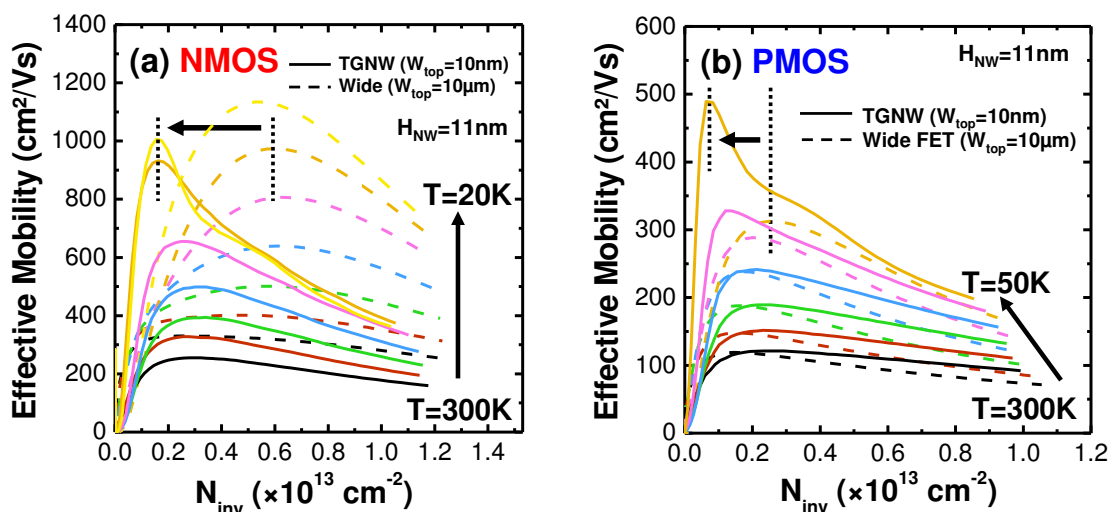


Fig. 6-6. Mobilité effective extraite en fonction de la charge d'inversion N_{inv} pour des transistors nanofils (TGNW) et des transistors larges, pour différentes températures (de 300 K à 20K) pour des dispositifs (a) NMOS, et (b) PMOS.

Résumé de la thèse en français

La mobilité latérale $\mu_{\text{side-wall}}$ pour les NMOS et PMOS est en bon accord avec les données expérimentales de référence pour une orientation Si-(110), montrant que les propriétés de transport des transistors nanofils TG en régime de forte inversion sont principalement régies par chaque surface d'inversion (faces supérieure et latérales) indépendamment les unes des autres.

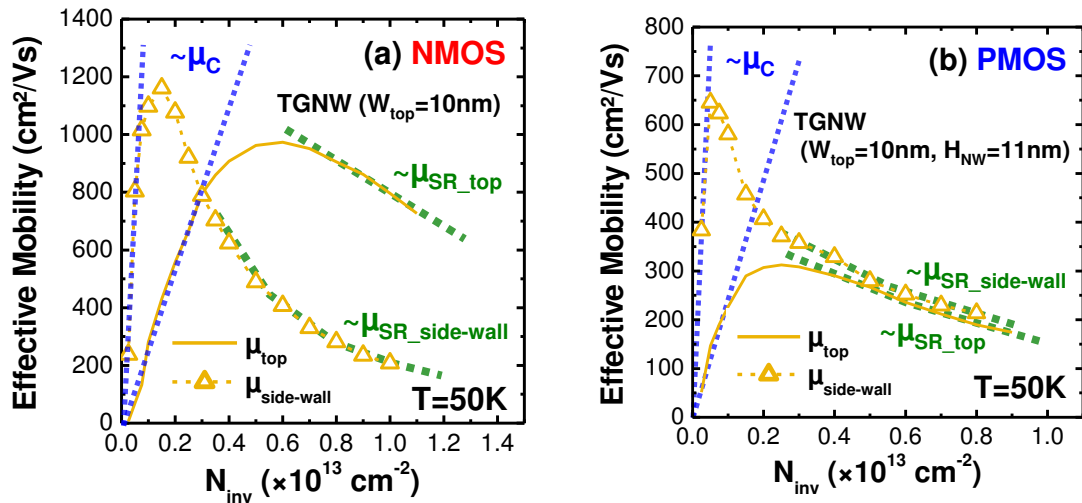


Fig. 6-7. Extraction des contributions latérale ($\mu_{\text{side-wall}}$) et supérieure (μ_{top}) à partir des mesures de mobilité à 50K pour des dispositifs nanofils (TGNW) de largeur $W_{\text{top}}=10\text{nm}$: (a) NMOS, et (b) PMOS.

Pour les NMOS, la contribution due à la rugosité de surface est considérablement augmentée dans les nanofils en raison de la contribution de la surface latérale, en bon accord avec les données publiées pour la mobilité des électrons dans des surfaces (110) / [110] [3-10,3-29]. En outre, le maximum de mobilité μ_{max} dans les nanofils est décalé aux plus faibles N_{inv} , et pourrait indiquer une moindre contribution des interactions coulombiennes (μ_C) pour les faces latérales. Pour les PMOS, la mobilité limitée par la rugosité de surface μ_{SR} dans des faces latérales est légèrement améliorée, conduisant à une meilleure mobilité à forte densité de porteurs N_{inv} pour les transistors NW par rapport aux MOSFETs planaires larges. De même que pour les NMOS, la contribution des interactions coulombiennes μ_C pour les surfaces d'inversion latérales orientées (110) est considérablement réduite (Fig. 6-7b).

Résumé de la thèse en français

L'impact d'une contrainte additionnelle sur le transport a également été étudié à partir de mesures effectuées sur des transistors nanofils sSOI. Théoriquement, une contrainte en tension uniaxiale est bénéfique pour le transport des électrons dans les NMOS. Au contraire pour les PMOS cette même contrainte uniaxiale dégrade la mobilité des trous. Les mobilités mesurées dans les transistors nanofils sSOI sont en bon accord avec ces considérations théoriques, en considérant les différentes surfaces d'inversion latérales et supérieures ou bien un modèle plus quantitatif prenant en compte l'effet de confinement dans les transistors nanofils [3-44~3-47].

L'addition d'une contrainte uniaxiale modifie la structure de bandes (décalage énergétique des sous-bandes). L'effet d'une contrainte se traduit ainsi principalement sur les interactions avec les phonons (transitions inter et intra sous-bandes). Des mesures en température de nos transistors sSOI nous ont permis d'étudier plus finement l'effet d'une forte contrainte uniaxiale sur le transport dans les transistors nanofils (Fig. 6-8).

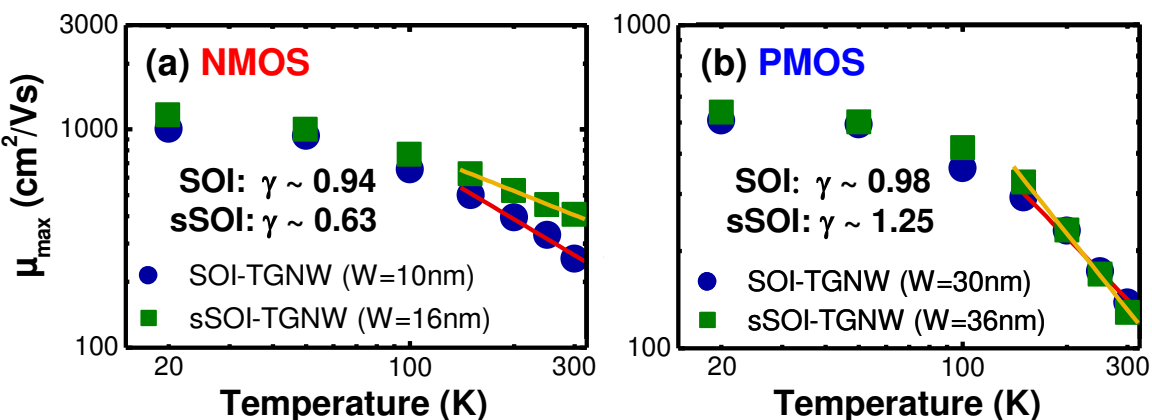


Fig. 6-8. Mobilité maximale μ_{max} extraite en fonction de la température pour des transistors nanofils SOI et sSOI : (a) NMOS, et (b) PMOS.

Le tableau 6-1 montre les valeurs de l'exposant γ de la loi en puissance du maximum de mobilité en fonction de la température ($\mu_{max} \sim T^{-\gamma}$) extraites pour tous les transistors étudiés ici. Au-dessus de 77 K, la mobilité en fonction de la température est dominée par les interactions avec les phonons, en particulier pour des densités de porteurs N_{inv} modérées (typiquement pour μ_{max}). Pour les transistors SOI ou sSOI, les valeurs ne sont pas significativement différentes pour chaque structure: transistors planaires larges, TG

Résumé de la thèse en français

ou ΩG . D'autre part, la dépendance en température change de façon très significative lorsque l'on compare les transistors non contraints (SOI) et les transistors contraints (sSOI) indépendamment de l'architecture, en particulier pour les NMOS. Ces résultats sont en bon accord avec les valeurs du coefficient de température γ qui sont semblables pour les plans (100) et (110) [3-10]. Ils indiquent également que la dépendance en température de la mobilité des électrons et des trous est principalement dominée par l'effet de la contrainte jusqu'à des largeurs de nanofils W_{TOP} de l'ordre de 10 nm.

Tableau 6-1. Valeurs du paramètre γ extraits pour tous les dispositifs SOI et sSOI étudiés, correspondant au coefficient en température défini par $\mu_{max} \sim T^{-\gamma}$.

Values of power law exponent γ		NMOS		PMOS	
		SOI	sSOI	SOI	sSOI
Tri-gate w/o H ₂ anneal	Wide (10μm)	0.95	0.64	1.00	1.18
	NW	0.94	0.63	0.98	1.25
Ω -gate with H ₂ anneal	Wide (10μm)	1.05	0.69	1.03	1.07
	NW	1.05	0.41	1.12	1.13

La mobilité faible champs μ_0 a été extraite en utilisant la méthode de la fonction Y. L'évolution de μ_0 en fonction de la longueur de grille L_g a été mesurée pour l'ensemble des variantes technologiques (transistors nanofils et planaires). La Figure 6-9 montre les résultats pour les dispositifs non contraints. Une dégradation plus abrupte de μ_0 avec L_g a été observée pour les nanofils, cette dégradation étant généralement attribuée à la proximité des régions source/drain très dopées et possiblement avec des défauts dus à l'implantation [3-26,3-40~3-42]. Cette dégradation plus prononcée pourrait s'expliquer par une influence électrostatique plus importante des dopants pour des géométries étroites.

Pour les dispositifs contraints (NMOS sSOI, PMOS SGOI et SG-S/D), un fort gain en mobilité est observé jusqu'aux faibles longueurs de grille (17-18nm) montrant l'efficacité de ces techniques de contraintes pour améliorer les performances des transistors, même pour des géométries très agressives. Des gains de mobilité¹ records supérieurs à +333% ont pu être obtenus pour les PMOS avec $L_g=17\text{nm}$ intégrant à la

¹ par rapport à des nanofils non contraints de référence

Résumé de la thèse en français

fois un canal SiGe est des S/D SiGe cumulant ainsi les sources de contraintes. Pour les NMOS ce gain peut atteindre +50% aux dimensions les plus agressives sur des dispositifs sSOI.

Enfin, à partir de cette méthode de la fonction Y on peut également extraire le facteur de dégradation de la mobilité α_μ [3-26]:

$$\frac{1}{\mu_0(L_g)} = \frac{1}{\mu_{0_max}} + \frac{\alpha_\mu}{L_g} \quad (3-16)$$

Les valeurs de ce facteur confirment une plus grande dégradation de la mobilité avec la longueur de grille pour les nanofils que pour les transistors planaires.

Les valeurs de résistance d'accès R_{SD} apparaissent aussi notamment plus élevées sur les nanofils que sur les transistors planaires, et nécessitent donc une réelle optimisation.

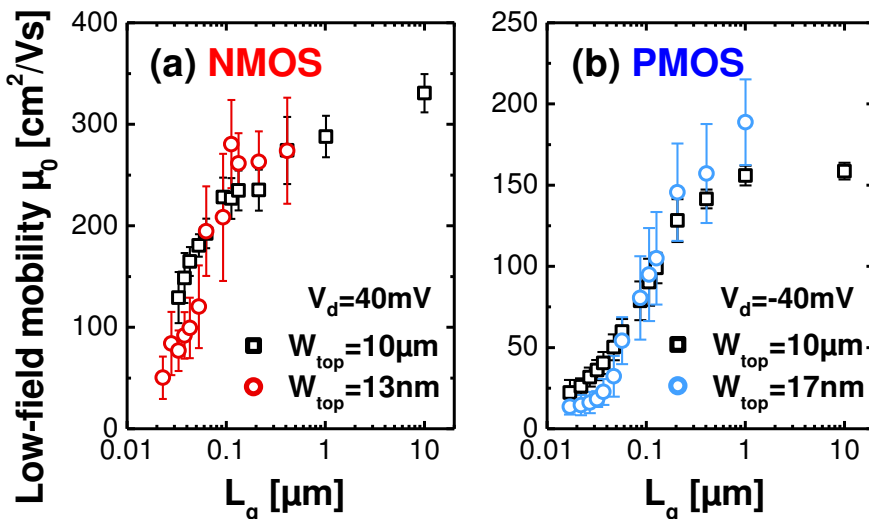


Fig. 6-9. Mobilité à champ faible μ_0 extraite en fonction de la longueur de grille L_g . Comparaison entre les transistors planaires larges ($W_{top}=10\mu\text{m}$) et les transistors nanofils ($W_{top}=10-13\text{nm}$) : (a) NMOS, et (b) PMOS.

Partie II: Les mesures de bruit basse fréquence

Des mesures de bruit basse fréquence ont été réalisées sur ces mêmes dispositifs et analysées en fonction des paramètres géométriques de l'architecture nanofils (largeur W , forme de la section, longueur de grille L), et des diverses variantes technologiques.

Résumé de la thèse en français

Ces mesures ont été effectuées à température ambiante en utilisant un système de mesure du bruit semi-automatique² conçu par Synergie Concept [4-71] (Fig. 4-9). Le bruit est calculé en convertissant la composante de sortie AC (ΔI_d) dans le domaine temporel en la densité spectrale de puissance (PSD) dans le domaine fréquentiel grâce à une transformée de Fourier rapide (FFT). Le niveau de bruit minimal mesurable du système 3PNMS a été mesuré autour $\sim 2 \times 10^{-27} \text{ A}^2/\text{Hz}$.

Dans ce travail, la densité spectrale du bruit de courant de drain S_{Id} a été acquise à partir de 400 points de fréquence, moyenné 32 fois. La tension de grille V_G appliquée varie de la région sous le seuil (en tenant compte de la limite inférieure de courant $|I_d| > 10^{-9} \text{ A}$) jusqu'à la région de forte inversion ($|V_g| > 1.0 \text{ V}$). La tension de drain V_d varie de région linéaire ($|V_d| = 40 \text{ mV}$) jusqu'à la région de saturation ($|V_d| = 0.9 \text{ V}$).

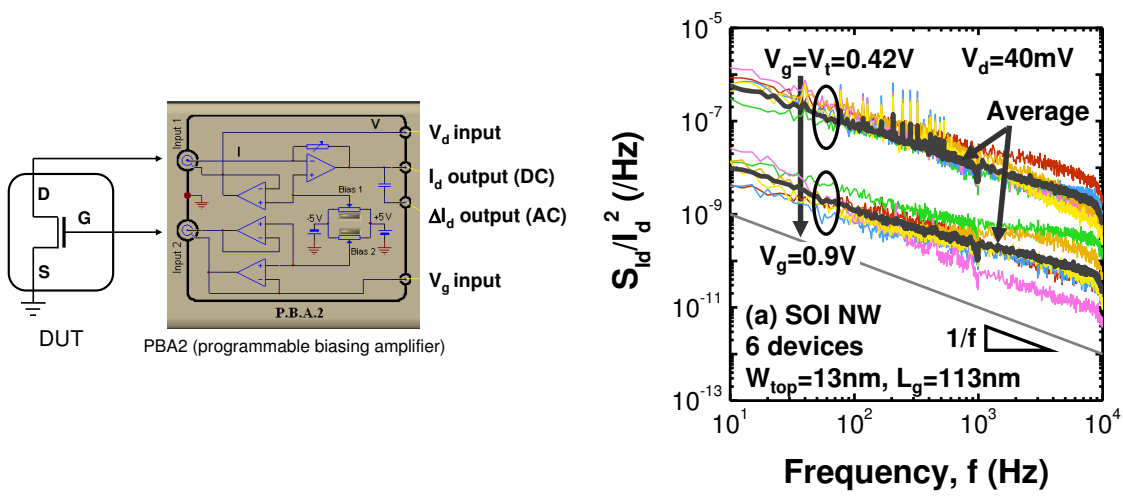


Fig. 6-10. (a) Schéma du système de mesure de bruit 3PNMS. (b) Densité spectrale S_{Id}/I_d^2 en fonction de la fréquence mesurée sur des transistors nanofils SOI ($W_{top}=13\text{nm}$, $L_g \sim 110\text{nm}$), montrant un bon comportement en $1/f$ de la région autour de la tension de seuil ($V_g=V_t$) jusqu'à la région de forte inversion.

Le bruit en courant de drain normalisé S_{Id}/I_d^2 en fonction de la fréquence dans le cas de transistors nanofils SOI NMOS est tracé sur la Figure 6-10. Bien que certains dispositifs nanofils montrent une dispersion de niveau de bruit et de la forme, le spectre moyen mesuré pour 5 ou 6 dispositifs présente un bon comportement de bruit 1/f, du régime

² Appelé Programmable Point Probe Noise Measuring System (3PNMS) et contrôlé par le logiciel NOISYS (version 4.1)

Résumé de la thèse en français

de fonctionnement sous le seuil jusqu'en forte inversion. Le même comportement a été observé pour les dispositifs PMOS et les dispositifs contraints. Ce résultat démontre clairement que les transistors nanofils ont bien un comportement de bruit en $1/f$, quelles que soient les variantes technologiques.

Nous avons par la suite analysé ce bruit en utilisant le modèle CNF + CMF basé sur l'équation suivante [4-55, 4-56] :

$$\frac{S_{Id}}{I_d^2} = \left(\frac{g_m}{I_d} \right)^2 \left(1 + \alpha_{sc} \mu_{eff} C_{ox} \frac{I_d}{g_m} \right)^2 S_{Vfb} \quad (4-26)$$

Dans cette équation, le premier terme correspond à la composante de fluctuation du nombre de porteurs (CNF) et le second terme indique le facteur de corrélation de la fluctuation de mobilité (CMF) due aux charges piégées. Si α_{sc} est proche de zéro, cela signifie que le terme CMF n'a pas d'influence sur le bruit, et le comportement peut être décrit seulement par le premier terme. En revanche, lorsque le α_{sc} est assez grand, la pente de S_{Id}/I_d^2 en fonction de I_d dans la région de forte inversion est impactée par le terme CMF, et s'éloigne du comportement en I_d^{-2} . Dans tous les cas, le terme CMF n'a pas d'influence sur le bruit dans la région de faible inversion, et celui-ci est décrit parfaitement par le terme de fluctuations du nombre de porteurs.

Un α_{sc} constant est fréquemment utilisé dans les modèles de bruit $1/f$, mais ce n'est physiquement pas correct, notamment à cause de l'effet d'écrantage [4-13,4-31]. Dans la pratique, α_{sc} devrait diminuer avec l'augmentation de la densité de charge d'inversion Q_{inv} en raison de l'écrantage électrostatique. Le produit $\alpha_{sc} \mu_{eff} = \mu_{eff}^{-1} \delta \mu_{eff} / \partial Q_{ox}$ apparaît plus pertinent pour caractériser les interactions coulombiennes dans la théorie CMF [4-39,4-70].

Résumé de la thèse en français

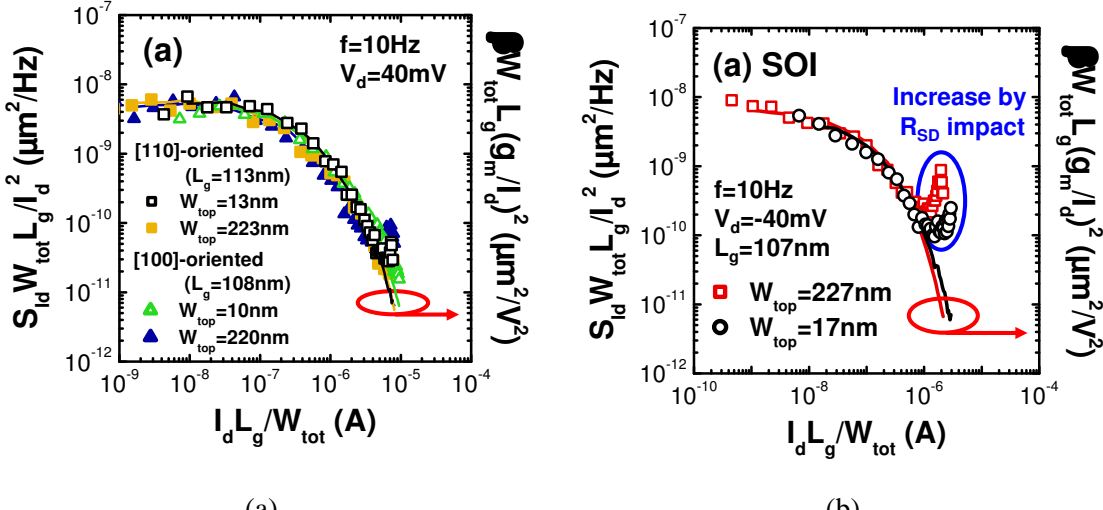


Fig. 6-11. (a) densité spectrale de bruit S_{Id}/I_d^2 et ratio $(g_m/I_d)^2$ correspondant (ligne) en fonction du courant I_d normalisé par les paramètres géométriques W_{tot} et L_G (symboles) pour des transistors planaires et nanofils SOI: (a) NMOS, et (b) PMOS.

La densité spectrale de bruit S_{Id}/I_d^2 extraite à la fréquence $f=10\text{Hz}$ en fonction de I_d normalisé par les paramètres géométriques du canal (W_{tot} et L_G) est représentée sur la Figure 6-11 pour des transistors NMOS et PMOS. Un bon accord entre S_{Id}/I_d^2 et la quantité correspondante $(g_m/I_d)^2$ est observée pour tous nos dispositifs. Ces résultats indiquent que les propriétés de bruit sont bien décrites par le modèle CNF + CMF pour les transistors planaires FDSOI et les transistors nanofils, ainsi que pour toutes les variantes technologiques étudiées (contraintes mécaniques, orientation du canal, ...). En particuliers, nous n'avons pas observé d'influence significative de l'orientation du canal [110] ou [100] [4-72], et des différentes orientations cristallographiques des couches d'inversion (001) et (110) sur le bruit [4-36,4-51].

Un bon accord entre la densité spectrale de bruit et le modèle CNF + CMF est également observée pour tous les dispositifs PMOS étudiés (Fig.6-11b) : référence SOI, S/D SiGe, et dispositifs SGOI. Toutefois pour les dispositifs à canal Si, une augmentation du niveau de bruit dans la région de forte inversion est observée, indiquant une contribution des résistances d'accès R_{SD} [4-29,4-32,4-45]. En effet, la résistance d'accès R_{SD} fluctue en raison du piégeage/dépiégeage des porteurs provoqués par des défauts dans les espaces en nitride SiN et/ou dans le film de silicium (Fig.6-12a). Ces fluctuations contribuent à l'augmentation du niveau de bruit 1/f en

Résumé de la thèse en français

régime de forte inversion, et sont distinctes du bruit thermique indépendant de la fréquence. La qualité moindre de ces régions S/D pour les dispositifs PMOS est généralement attribué à la moins bonne contrôlabilité des dopant bore en raison de leur masse plus légère que les espèces P ou Ar.

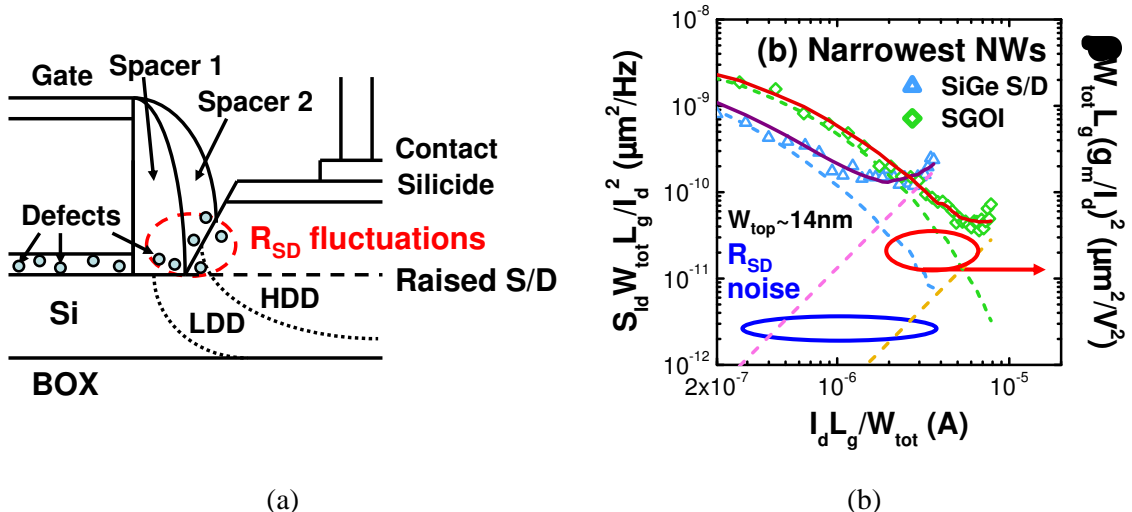


Fig. 6-12. (a) Représentation schématique des défauts dans les espaces contribuant aux fluctuations de R_{SD} dans les architectures FDSOI. (b) Courbes S_{Id}/I_d^2 en fonction de I_d (symboles) et modèle (ligne en pointillés) intégrant les paramètres $\alpha_{sc}\mu_{eff}$ et S_{Rsd} (Cf. équation 4-28).

Ce bruit associé aux régions S/D peut être intégré dans le modèle en ajoutant une contribution supplémentaire [4-29]:

$$\frac{S_{Id}}{I_d^2} = \left(\frac{g_m}{I_d} \right)^2 \left(1 + \alpha_{sc}\mu_{eff} C_{ox} \frac{I_d}{g_m} \right)^2 S_{Vfb} + \left(\frac{I_d}{V_d} \right)^2 S_{Rsd} \quad (4-28)$$

où S_{Rsd} est la densité spectrale de puissance PSD des fluctuations de R_{SD} . Les courbes expérimentales $S_{Id}/I_d^2 - I_d$ peuvent ainsi être décrites parfaitement par l'impact des R_{SD} au-dessus du V_t (Fig. 6-12b), en utilisant deux paramètres d'ajustement β and S_{Rsd} . Nous avons pu ainsi montrer que pour les dispositifs nanofil NSG-S/D et nSGOI, les spectres sont bien reproduits en tenant compte à la fois des termes $\alpha_{sc}\mu_{eff}$ et S_{Rsd} (Fig. 6-12b), alors que pour les transistors larges, seul le facteur $\alpha_{sc}\mu_{eff}$ est dominant. Les valeurs de S_{Rsd} extraites mettent en évidence l'avantage des dispositifs nSGOI qui présentent un

Résumé de la thèse en français

impact beaucoup plus faible des fluctuations des R_{SD} , en relation avec une valeur inférieure de R_{SD} (extrait par la fonction Y).

Nous avons également extrait le paramètre de Hooge α_H donné par l'équation :

$$\frac{S_{Id}}{I_d^2} = \frac{q\alpha_H}{fWLQ_{inv}} \quad (4-11)$$

basée sur un modèle empirique ne considérant que les fluctuations de mobilité. En fait, le modèle empirique de Hooge n'a aucun argument théorique, même si celui-ci a souvent été en mesure d'expliquer le comportement de bruit $1/f$. Cependant, le paramètre de Hooge a souvent été utilisé pour discuter de la différence de comportement de bruit en fonction des paramètres technologiques et structurels en régime de fonctionnement.

Les valeurs de α_H extraites pour les transistors nanofils nous ont amené à conclure que le paramètre empirique de Hooge α_H reflète l'impact des paramètres $\alpha_{sc}\mu_{eff}$ et S_{Rsd} dans la région de forte inversion, même si les comportements de bruit sont en conformité avec le modèle CNF + CMF, et non seulement avec les fluctuations de mobilité.

Pour une étude plus détaillée, deux paramètres importants S_{Vfb} – lié aux fluctuations du nombre de porteurs – et $\alpha_{sc}\mu_{eff}$ – lié au transport – ont été extraits à partir de données expérimentales en utilisant la relation

$$S_{Vg}^{1/2} = \sqrt{\frac{S_{Id}}{g_m^2}} = \left(1 + \alpha_{sc}\mu_{eff}C_{ox} \frac{I_d}{g_m}\right) S_{Vfb}^{1/2} \quad (4-29)$$

Les deux paramètres $S_{Vfb}^{1/2}$ $\alpha_{sc}\mu_{eff}C_{ox}$ sont obtenus grâce respectivement à l'ordonnée à l'origine et à la pente des courbes expérimentales ([Fig.6-13a](#)) [4-70]. Le paramètre S_{Vfb} peut également être extrait par l'ajustement direct de S_{Id}/I_d^2 en fonction de $(g_m/I_d)^2$ dans la région sous le seuil, montrant un plateau dans le niveau de bruit. Dans ce régime où la fluctuation du nombre de porteurs domine, le coefficient $(1 + \alpha_{sc}\mu_{eff}C_{ox}I_d/g_m)$ se réduit à 1. Cette méthode paraît plus pertinente pour les dispositifs nanofils.

Résumé de la thèse en français

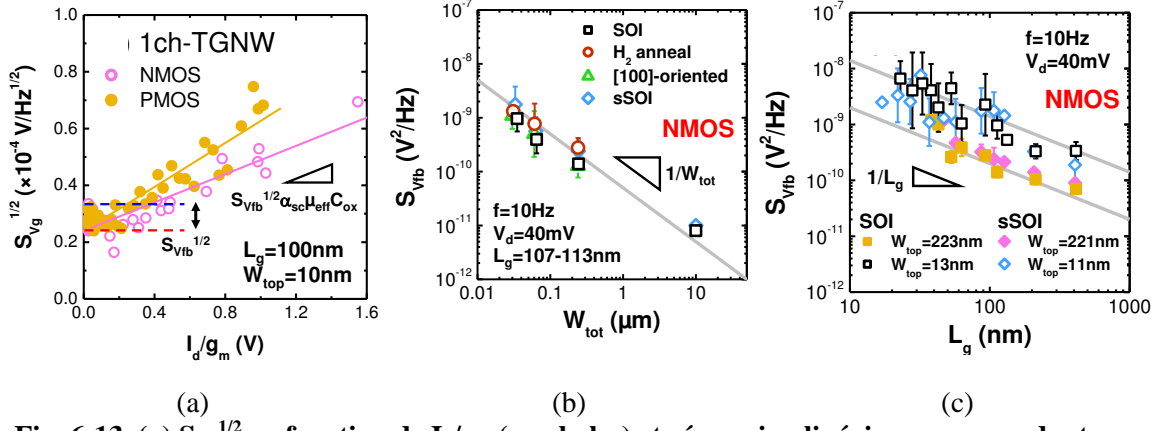


Fig. 6-13. (a) $S_{Vg}^{1/2}$ en fonction de I_d/g_m (symboles) et régression linéaire correspondante (lignes) utilisée pour l'extraction de S_{Vfb} et $\alpha_{sc}\mu_{eff}$ pour des transistors nanofils (NMOS et PMOS). S_{Vfb} en fonction de (b) W_{tot} , et (c) L_g pour toutes les variantes technologiques des dispositifs NMOS.

Alors que les différentes variantes technologiques ont peu d'effet sur facteur S_{Vfb} , les variations de géométrie en L et W changent la composante de bruit liée aux fluctuations du nombre de porteurs de manière inversement proportionnelle à la surface totale $\sim 1/WL$ (Fig. 6-13b,c pour les NMOS) [4-39].

La relation linéaire entre $S_{Vg}^{1/2}$ et I_d/g_m montré dans la Figure 6-13a suggère que le paramètre de Coulomb $\alpha_{sc}\mu_{eff}$ est constant de la région de faible inversion à la région de forte inversion en accord avec les travaux précédents [4-39,4-70], et que ceci reste même dans les dispositifs nanofils TG aux dimensions ultra-réduites. Le facteur α_{sc} représente le couplage entre la variation de la charge piégée dans l'oxyde δQ_{ox} et les variations de mobilité induite, et peut-être défini par

$$\alpha_{sc} = -\frac{\partial(1/\mu_{eff})}{\partial Q_{ox}} = \frac{1}{\mu_{eff}^2} \frac{\partial \mu_{eff}}{\partial Q_{ox}} \quad (4-24)$$

Nous avons pu montrer que le paramètre $\alpha_{sc}\mu_{eff}$ n'est pas modifié par les dimensions du transistor (W_{TOP} ou L_g) à la fois pour les NMOS et les PMOS, dans l'incertitude de mesure (dispersion de dispositifs à dispositifs). En outre, les valeurs de $\alpha_{sc}\mu_{eff}$ sont en bon accord avec les données précédemment rapportés dans la littérature [4-42,4-70]. Nous n'avons cependant pas pu mettre en évidence de corrélation avec la mobilité μ_0

Résumé de la thèse en français

extraite précédemment, indépendamment de l'amélioration de la mobilité induite par la contrainte que ce soit pour les NMOS ou les PMOS.

Le piégeage et dépiégeage des porteurs entre l'oxyde de grille et le canal par effet tunnel est supposé être le mécanisme responsable du bruit en $1/f$ dans les MOSFETs ; il constitue l'essence même du modèle McWhorter. Dans ce formalisme, la densité de piège dans l'oxyde de grille N_t (exprimée en $\text{eV}^{-1} \text{cm}^{-3}$) dans un intervalle d'énergie $4kT$ autour du quasi-niveau de Fermi est donnée par l'équation suivante, en considérant une distribution uniforme des pièges dans l'épaisseur de l'oxyde [4-66,4-67,4-24] :

$$N_t = \frac{fW_{tot}L_g C_{ox}^2 S_{Vfb}}{q^2 kT \lambda} \quad (4-31)$$

où λ est la longueur d'atténuation de la fonction d'onde des électrons ou des trous dans l'oxyde de grille. La valeur de λ dépend des matériaux constituant l'oxyde de grille. Cependant les valeurs généralement rapportées se situent dans la plage $\approx 0.07\text{-}0.21\text{nm}$ [4-1]. En particulier, λ est estimée à $\approx 0.1\text{nm}$ pour les électrons et $\approx 0.14\text{nm}$ pour les trous pour un empilement Si/SiO₂/HfO₂ [4-63 ~ 4-65]. La densité de pièges N_t peut ainsi être calculée à partir des mesures de S_{Vfb} (Fig.6-14).

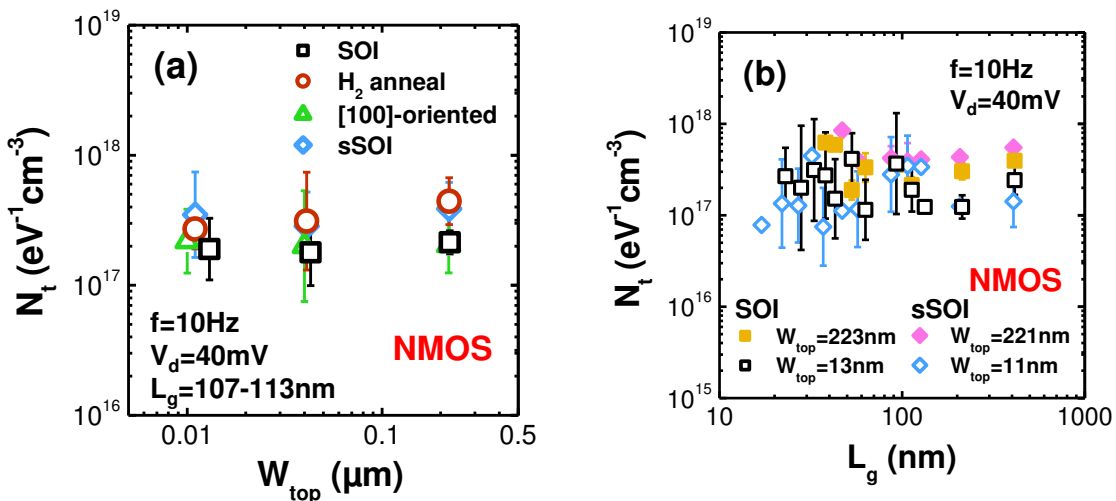


Fig. 6-14. Densité de pièges dans l'oxyde N_t mesurée en fonction de (a) W_{tot} et (b) L_g pour toutes les variantes technologiques des transistors NMOS.

La conclusion la plus importante est que les valeurs moyennes de N_t pour tous les dispositifs se situent dans le même ordre de grandeur ($\approx 5\times 10^{16}\text{-}10^{18} \text{ eV}^{-1}\text{cm}^{-3}$) que l'état

Résumé de la thèse en français

de l'art des valeurs reportées pour des empilement grille métal / diélectrique à forte permittivité à base de Hf [4-43,4-64,4-70,4-88~4-90]. Les transistors nanofils présentent des valeurs légèrement inférieures aux MOSFETs planaires dans la plupart des cas, indiquant clairement que les valeurs de N_t ne sont pas modifiées par la réduction des dimensions de la zone active (W_{TOP}), ni par l'architecture 3D [4-34,4-35]. La bonne qualité de l'interface oxyde/canal est ainsi maintenue dans tous nos dispositifs N- et PMOS, en particulier dans les nanofils pour lesquels les parois latérales jouent un rôle important dans le transport.

Pour une évaluation plus rigoureuse de la qualité de l'interface, une méthode de séparation de la contribution de la surface supérieure (N_{t_top}) et des parois latérales ($N_{t_side-wall}$) à la densité totale de pièges a été introduite comme suit:

$$N_{t_tot} = \frac{W_{top}}{W_{tot}} N_{t_top} + \frac{2H_{NW}}{W_{tot}} N_{t_side-wall} \quad (4-32)$$

En utilisant cette formule simple, nous avons extrait N_{t_top} et $N_{t_side-wall}$ pour trois largeurs différentes W_{TOP} ($Lg \approx 110\text{nm}$) (Fig. 6-15).

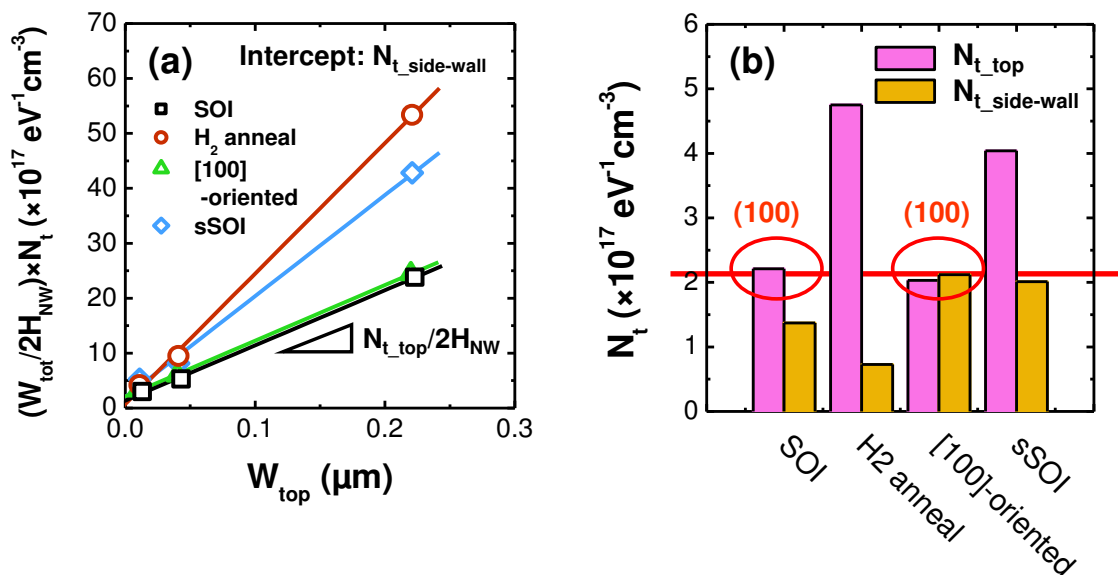


Fig. 6-15. (a) Démonstration de l'extraction de la contribution des surfaces supérieure (N_{t_top}) et latérales ($N_{t_side-wall}$) à la densité de pièges totale, et (b) valeur de ces contributions pour tous les dispositifs NMOS testés.

Pour les NMOS, les plans (100), qui correspondent à l'orientation de la surface supérieure pour les transistors nanofils orientés [110], et aux surfaces supérieure et

Résumé de la thèse en français

latérales pour les transistors nanofils orientés [100], montrent des valeurs très semblables $\sim 2 \times 10^{17} \text{ eV}^{-1} \text{ cm}^{-3}$. Cette même valeur pour tous les plans (100) confirme la fiabilité de la méthode de séparation. Étonnamment, les plans (110) (parois latérales pour les nanofils orientés [110]) montrent des valeurs $N_{t_side-wall}$ légèrement inférieures aux surfaces (100). La même constatation a pu être établie pour les PMOS. Dans tous les cas (NMOS et PMOS) l'introduction de contraintes (sSOI, canal SiGe ou S/D SiGe) ainsi que le recuit additionnel H₂ détériore légèrement les interfaces.

Ces résultats sont en bon accord avec les mesures de pompage de charges [4-91,4-92] effectuées sur des dispositifs similaires. Tous les transistors présentent une densité moyenne de piége d'interface (D_{it}) dans la gamme $1\text{--}3 \times 10^{10} \text{ eV}^{-1} \text{ cm}^{-2}$. Les nanofils présentent un niveau de D_{it} légèrement inférieur aux dispositifs planaires larges en accord avec nos mesures de bruit.

Finalement, les mesures de bruit 1/f ont été comparées aux spécifications ITRS 2013 pour les transistors multi-grilles en vue des futurs nœuds technologiques de la logique CMOS, et démontrent que nos transistors nanofils satisfont les exigences en la matière (Fig.6-16).

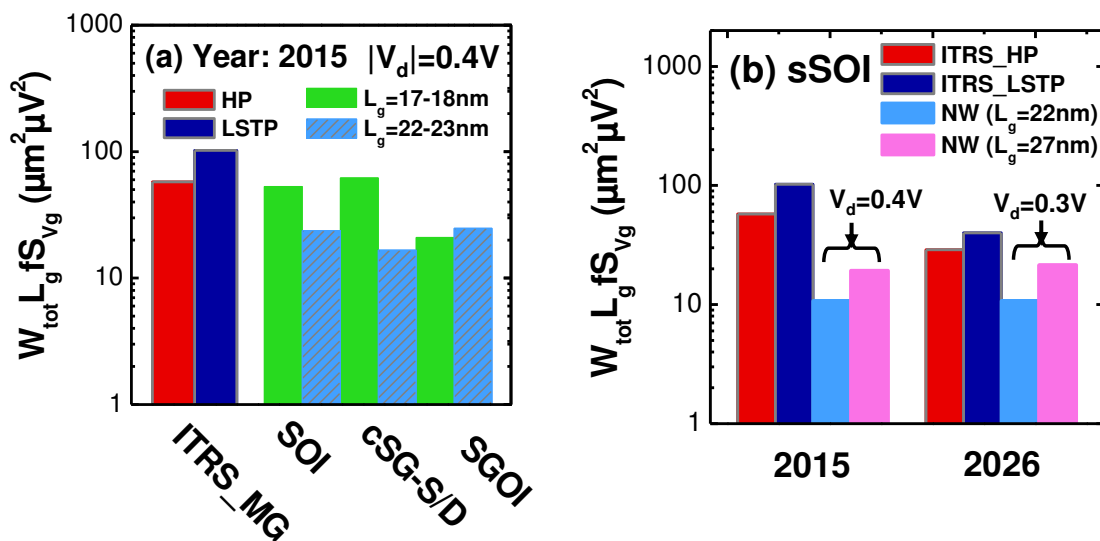


Fig. 6-16. (a) Comparaison des valeurs expérimentales de S_{VG} normalisées pour nos transistors nanofils PMOS et des exigences ITRS pour l'année 2015 pour les PMOS multi-grilles [4-95]. (b) Même chose pour les nanofils NMOS sSOI comparés aux exigences ITRS pour les années 2015 et 2026.

Résumé de la thèse en français

Conclusion générale

Dans ce travail, les propriétés de l'interface oxyde de grille/canal ont été étudiées expérimentalement par des mesures de transport et de bruit de basse fréquence ($1/f$) dans des transistors nanofils FDSOI aux dimensions ultra-réduites. Le but et l'originalité de ce travail était de comprendre les propriétés électriques de cette interface par une approche croisée mesures de bruit / transport

Nous avons démontré que le bruit $1/f$ dans les transistors nanofils peut être décrit par le modèle de fluctuations du nombre de porteurs (CNF) corrélées aux fluctuations de mobilité (CMF). Le bruit associé aux régions S/D a pu également être intégré dans ce modèle en ajoutant une contribution, en particulier pour les PMOS. Alors que les différentes variantes technologiques ont peu d'effet sur le bruit $1/f$, les variations de géométrie en L et W changent la composante de bruit liée aux fluctuations du nombre de porteurs (CNF) de manière inversement proportionnelle à la surface totale ($\sim 1/WL$). Cette augmentation du bruit est le reflet du transport qui se produit à proximité des interfaces avec l'oxyde. Les différentes orientations des interfaces supérieures et latérales (110) ou (100) présentent la même quantité de pièges d'interface (extrait à partir des mesures de bruit $1/f$, en séparant les contributions des différentes faces du nanofil) bien qu'ayant une rugosité différente essentiellement liée au process technologique. En revanche la composante CMF n'est pas altérée par la réduction des dimensions contrairement à la mobilité des porteurs qui décroît fortement avec L.

Nous avons également conclu qu'une ingénierie des contraintes appropriée permet d'améliorer grandement les performances des transistors nanofils (transport et exigences ITRS en matière de bruit) pour les futurs circuits CMOS, sans impact significatif sur la qualité de l'interface oxyde/canal.

Les mesures de bruit basse fréquence peuvent évidemment être appliquées à la caractérisation d'autres dispositifs avancés, comme par exemple les transistors sans jonction à grille totalement enrobante (GAA *junctionless*) composés seulement d'une zone de Si fortement dopée [5-1], les transistors à contact Schottky [5-3], les transistors

Résumé de la thèse en français

à film mince (TFT) [5-4], ou encore des dispositifs tunnel-FET (TFET) [5-7 ~ 5-10] ou à haute mobilité d'électrons (HEMT) [5-11,5-12]. Pour les TFETs un modèle théorique de bruit différent de CNF + CMF est prévue en raison de l'effet tunnel bande à bande (BTBT). Enfin, les mesures de bruit représentent un outil de diagnostic puissant, notamment pour des dispositifs plus exploratoires constitués de matériaux 1D ou 2D, tels que des nanotubes de carbone (CNT) [5-13 ~ 5-16], le graphène [5-17,5-18] et le molybdène-disulfure (MoS_2) [5-19 ~ 5-24].

List of Publications and Presentations

My publications and presentations between October 2011 and November 2014 as first author are only listed.

Journal papers

- [1] M. Koyama, M. Cassé, R. Coquand, S. Barraud, C. Vizioz, C. Comboroure, P. Perreau, V. Maffini-Alvaro, C. Tabone, L. Tosti, S. Barnola, V. Delaye, F. Aussenac, G. Ghibaudo, H. Iwai, and G. Reimbold, “Study of carrier transport in strained and unstrained SOI tri-gate and omega-gate silicon nanowire MOSFETs,” *Solid-State Electronics*, vol.84, pp.46-52, March 2013.

- [2] M. Koyama, M. Cassé, S. Barraud, G. Ghibaudo, H. Iwai, O. Faynot, and G. Reimbold, “Assessment of technological and geometrical device parameters by low-frequency noise investigation in SOI omega-gate nanowire NMOS FETs,” *Solid-State Electronics*, 2015. (accepted, to be published)

Oral presentations in international conferences

- [3] M. Koyama, M. Cassé, S. Barraud, P. Nguyen, G. Ghibaudo, H. Iwai, and G. Reimbold, “Study of Si- and SiGe-on-Insulator Ω -gate Nanowire PMOS FETs by Low-frequency Noise Measurements,” *46th International Conference on Solid State Devices and Materials (SSDM 2014)*, Tsukuba, Japan, September 2014, pp. 864-865.

- [4] M. Koyama, M. Cassé, R. Coquand, S. Barraud, G. Ghibaudo, H. Iwai, and G. Reimbold, “Influence of Technological and Geometrical Parameters on Low-frequency Noise in Omega-gate Nanowire NMOSFETs,” *21st International Symposium on VLSI Technology, Systems and Applications (VLSI-TSA 2014)*, Hsinchu, Taiwan, April 2014, pp. 27-28.

List of Publications and Presentations

- [5] M. Koyama, M. Cassé, S. Barraud, G. Ghibaudo, H. Iwai, and G. Reimbold, “Assessment of Technological Device Parameters by Low-frequency Noise Investigation in SOI Omega-gate Nanowire NMOS FETs,” *15th International Conference on Ultimate Integration on Silicon (ULIS 2014)*, Stockholm, Sweden, April 2014, pp. 57-60.
- [6] M. Koyama, M. Cassé, R. Coquand, S. Barraud, G. Ghibaudo, H. Iwai, and G. Reimbold, “Influence of Device Scaling on Low-frequency Noise in Tri-gate N- and P-type Si Nanowire MOSFETs,” *43rd European Solid-State Device Research Conference (ESSDERC 2013)*, Bucharest, Romania, September 2013, pp. 300-303.
- [7] M. Koyama, M. Cassé, R. Coquand, S. Barraud, G. Ghibaudo, H. Iwai, and G. Reimbold, “Study of Low-frequency Noise in SOI Tri-gate Si Nanowire MOSFETs,” *22nd International Conference on Noise and Fluctuations (ICNF 2013)*, Montpellier, France, June 2013.
- [8] M. Koyama, M. Cassé, R. Coquand, S. Barraud, H. Iwai, G. Ghibaudo, and G. Reimbold, “Study of Carrier Transport in Strained and Unstrained SOI Tri-gate and Omega-gate Si-Nanowire MOSFETs,” *42nd European Solid-State Device Research Conference (ESSDERC 2012)*, Bordeaux, France, September 2012, pp. 73-76.

Poster presentation in French national conference

- [9] M. Koyama, “Study of low-frequency noise in silicon nanowire MOSFETs,” *Journées Nationales du Réseau Doctoral en Micro-nanoélectronique (JNRDM 2013)*, Grenoble, France, June 2013.